The University of Nottingham

FLUTE
FLUID AND THERMAL
ENGINEERING RESEARCH
GROUP

Computational investigation of boiling flows within micro-pin fin evaporators for thermal management of high-power density micro-electronics

by

Ismail El Mellas

Thesis Supervisors	Dr. Mirco Magnini
	Dr. David Hann
	Dr. Matteo Icardi

Fluids and Thermal Engineering Research Group

Department of Mechanical, Materials and Manufacturing Engineering

The University of Nottingham

Dissertation submitted in partial fulfillment of the requirements
for the degree of Doctor of Philosophy in Mechanical Engineering

December 2023

Acknowledgments

I extend my sincere gratitude to my supervisor, Dr. Mirco Magnini, for providing me with the invaluable opportunity to embark on this doctoral journey. His unwavering support, constant guidance, and engaging discussions have been instrumental in shaping my research endeavours. Mirco's mentorship, both academically and personally, has been a source of inspiration, and I am thankful for the friendship we've cultivated throughout this experience. I would also like to express my appreciation to my second supervisor, Dr. Matteo Icardi, whose insights and different perspectives have enriched the depth of my research. His guidance has been invaluable, contributing to a broader understanding of my work. A special mention goes to Dr. Alex Stroh, who gave me the opportunity to spend a few months as a visiting student at the ISTM in Germany. This experience broadened my horizons and added a valuable dimension to my academic pursuits. Lastly, I offer heartfelt thanks to my family for their unwavering support.

Abstract

Recent advancements in micro-manufacturing and microelectronic technologies have enabled the large-scale production of high-power-density devices, such as fuel cells, batteries, and electronic chips. The exponential growth in the power output of these devices has created a compelling need for efficient cooling systems. Traditional single-phase cooling systems, typically limited to heat fluxes of less than $1\,\mathrm{MW/m^2}$, are ill-equipped to handle the substantial heat fluxes, often on the order of several $\mathrm{MW/m^2}$, generated by these high-power devices [1]. In contrast, multiphase flows with phase change offer viable technological solutions, allowing for the dissipation of additional heat in the form of latent heat. Boiling flows maintain uniform surface temperatures, a critical factor in the proper functioning of components, and can respond positively and passively to localised hot spots as the heat transfer coefficient increases with heat flux. One promising technology in this regard is the use of pin-fin micro-evaporators, which, compared to conventional straight channels, have the added advantage of disrupting the flow field. This promotes flow mixing, enhances the local surface area, and increases the local heat transfer coefficient, ultimately leading to improved thermal and hydraulic performance. Despite numerous experimental studies on boiling heat transfer in micro-pin fins, ongoing debates persist regarding the underlying dynamics. This is partly due to the limitations of existing experimental techniques, which cannot provide sufficient resolution to investigate the small spatial and temporal scales of the flow. In this study, a comprehensive numerical investigation of two-phase flows propagating through arrays of pin-fins is presented. The study comprises two main parts: one conducted under adiabatic conditions and the other under diabatic conditions. The simulations were performed via the Volume of Fluid (VOF) method implemented in OpenFOAM. Various conditions relevant to heat exchangers for industrial applications were tested, including low-viscosity fluids (e.g., water, refrigerants), laminar flows, and uniform heat loads of hundreds of $\mathrm{kW/m^2}$. Different configurations of the

obstacles were also tested in the investigation.

The thesis aims to unveil the dynamics of two-phase flow propagating across micro-pin fin arrays and, more generally, non-straight channels, with a focus on understanding how the flow is affected by the pin-fins. This involves studying bubble behaviour, the size and morphology of the liquid film, and heat transfer performances. The simulations reveal that the dynamics of two-phase flows through pin-fins differ significantly from those observed in straight channels. As bubbles traverse the arrays of pin-fins, the pin walls tend to be covered, and lateral extension occurs in the gap between adjacent obstacles. The shape of the bubbles and the morphology of the liquid film are directly linked to the pin shape, resulting in entirely different outcomes. Heat transfer performances are significantly influenced by the initialisation spot of the bubbles; generally, higher performances are observed when the bubble nucleates in a downstream region where the fluid is stagnant, leading to the generation of multiple bubbles and coverage of a larger surface area by the two-phase flow.

Keywords: flow boiling, micro-pin fin evaporators, volume of fluid.

Contents

List of Tables

List of Figures

Nomenclature

Acronyms

CFD   Computational Fluid Dynamics

CHT   Conjugate heat transfer

CLSVOF   Coupled Level-Set and Volume Of Fluid

DNS   Direct Numerical Simulation

FT   Front Tracking

FVM   Finite Volume Method

HTC   Heat transfer coefficient

LS   Level Set

MULES   Multidimensional Universal Limiter for Explicit Solution

PLIC   Piecewise Linear Interface Calculation

RDF   Reconstructed distance function

SLIC   Simple Line Interface Method

Greek Letters

α volume fraction $-$

β contact angle   deg

Δ Delta $-$

δ	interface area		$\mathrm{m^{-1}}$
$\dot{\rho}$	volumetric mass flux		$\mathrm{kg\,m^{-2}s^{-1}}$
$\dot{\rho}_0$	smoothed volumetric mass flux		$\mathrm{kg\,m^{-2}s^{-1}}$
γ	evaporation coefficient		$-$
κ	local interface curvature		$-$
λ	thermal conductivity		$\mathrm{W\,m^{-1}\,K^{-1}}$
μ	dynamic viscosity		$\mathrm{kg\,m^{-1}\,s^{-1}}$
ν	kinematic viscosity		$\mathrm{m^2\,s^{-1}}$
ϕ	generic fluid variable		$-$
ψ	reconstructed distance function (rdf)		$-$
ρ	density		$\mathrm{kg\,m^{-3}}$
σ	Surface tension coefficient		$\mathrm{N\,m^{-1}}$
τ	stress tensor		$-$
θ	angle		deg

Roman Letters

$\dot{m}$	mass flux due evaporation		$\mathrm{kg\,m^{-2}\,s^{-1}}$
$\dot{q}$	heat flux due evaporation		$\mathrm{J\,m^{-2}s^{-1}}$
Bo	Bond number	$g\Delta p D^2/\sigma$	$-$
Ca	Capillary number	$\mu U/\sigma$	$-$
Co	Courant number	$U\Delta t/\Delta x$	$-$
La	Laplace number	$\rho\sigma D/\mu^2$	$-$
Ma	Mach number	$U/\sqrt{\beta R_g T}$	$-$

Nu	Nusselt number	$h_w D/\lambda$	—
Re	Reynolds number	$\rho U D/\mu$	—
We	Weber number	$\rho U^2 D/\sigma$	—
$\mathbf{I}$	Identity matrix		—
x	steamwise coordinate		m
y,z	cross-stream coordinate		m
A	area		m^2
c	indicator function		—
c_p	pressure specific heat		$J\,kg^{-1}\,K^{-1}$
d	distance		m
d_h	hydraulic diameter		m
e	specific energy		$J\,kg^{-1}$
f	friction factor		—
G	mass flux		$kg\,m^{-2}\,s^{-1}$
g	Gravitational acceleration		$m\,s^{-2}$
H	height		m
h	liquid film thickness		m
h_w	heat transfer coefficient		$W\,m^{-2}\,K^{-1}$
h_{lv}	latent heat of vaporisation		$J\,kg^{-1}$
L	length		m
M	molecular mass		$kg\,mol^{-1}$
N	normalisation factor		—

P	perimeter	m
p	pressure	Pa
q	heat flux	$\mathrm{J\,s^{-1}\,m^{-2}}$
R	radius	m
r_b	bubble radius	m
R_g	universal gas constant	$\mathrm{J\,K^{-1}\,mol^{-1}}$
T	temperature	K
t	time	s
U	velocity	$\mathrm{m\,s^{-1}}$
V	volume	$\mathrm{m^3}$
W	width	m

Subscripts/Superscripts

c	centre or cell
ch	channel
f	face
inl	inlet
int	interface
l	liquid phase
max	maximum
min	minimum
N	nose
n	normal

out outlet

pin pin-fin

R rear

s surface

sat saturation

t tangential

v, g vapour (gas) phase

w wall

Chapter 1

Introduction

The continuous evolution of micro-manufacturing techniques and the integration of electronic devices has led to a significant escalation in heat dissipation requirements per unit surface area for electronic components. This surge in demand is particularly pronounced in various applications, including computer chips, satellites, nuclear reactors, electric vehicles, batteries, and miniature fuel cells. Notably, these applications now necessitate heat dissipation exceeding levels of $1\,\mathrm{MW/m^2}$, as highlighted by Karayiannis in 2017 [2]. Back in 1965, Moore [3] made a forward prediction, anticipating that the performance of computer chips would double every 18 months. While the pace of computational power growth has subsided somewhat since then, it remains on a consistent upward trajectory. Consequently, an increasing number of components are being densely packed into confined spaces, resulting in a substantial increase in the dissipated heat flux. Data centres, see Fig. 1.1, stand as critical hubs for processing, storing, and computing vast amounts of information. It has become a focal point for a new wave of investment and construction. Masanet et al. [4] underscored the significant impact of data centres, revealing that in 2018, these facilities consumed approximately $205\,\mathrm{TWh}$ of power, equivalent to around 1% of global power consumption. Alarmingly, this power consumption continues to rise, increasing by 6% annually [4]. According to IDC (Internet Data Centre), as of 2020, about 4.98 million racks were deployed in data centres worldwide, consuming $299\,\mathrm{TWh}$ of power. Projections suggest that by 2030, global data centres will consume a staggering $974\,\mathrm{TWh}$ of power, constituting 8% of total global power consumption [6]. This enormous power consumption primarily stems from communication and network equipment, power supply and distribution systems, lighting systems, auxiliary equipment, as well as

1

Figure 1.1: Data centre, from Swallow [5].

heat dissipation and cooling systems [7]. It is worth noting that nearly 40% of this power is allocated to heat dissipation and cooling. Hence, advancing cooling technology is paramount. Enhancing heat dissipation efficiency promises a substantial boost in overall data centre efficiency. Within the server, the basic data centre building block, heat-generating components include processors, storage units, voltage regulators, chips, and power supply equipment. Presently, processor manufacturing has advanced to the $7\,\mathrm{nm}$ era, with high-power server CPUs sporting a Thermal Design Power (TDP) starting at $200\,\mathrm{W}$. Notably, the Intel Core i9-13900k processor realised in 2022 reaches a staggering $300\,\mathrm{W}$[1] and, when pushed to their limits, can consume as much as $700-900\,\mathrm{W}$. Chips typically have a temperature limit of less than $70\,^{\circ}\mathrm{C}$ (or a maximum of $85\,^{\circ}\mathrm{C}$). Any increase in temperature by $2\,^{\circ}\mathrm{C}$ reduces their reliability by 10% [9], posing significant challenges to the electronics and information technology industry. In light of these facts, the development of high-efficiency cooling technology holds immense significance. It ensures the safe and efficient operation of electronic devices and conserves power in data centres, leading to enhanced energy utilisation. Cooling methods can be categorised into active cooling, which includes forced air cooling, forced liquid cooling, refrigeration, and thermoelectric cooling, and passive cooling, which encompasses natural convection through air or liquid and phase change heat transfer techniques such as evaporation, condensation, boiling, and phase change materials. Nowadays, most data centres apply air cooling and electric car batteries are cooled by liquid. These technologies are economical and are easy to construct and maintain, but are not energy efficient as they can handle usually $100\,\mathrm{kW/m^2}$.

---

[1]Given the die size of the processor ($257\,\mathrm{mm^2}$ [8]), it corresponds to a power density approximately of $1160\,\mathrm{kW/m^2}$.
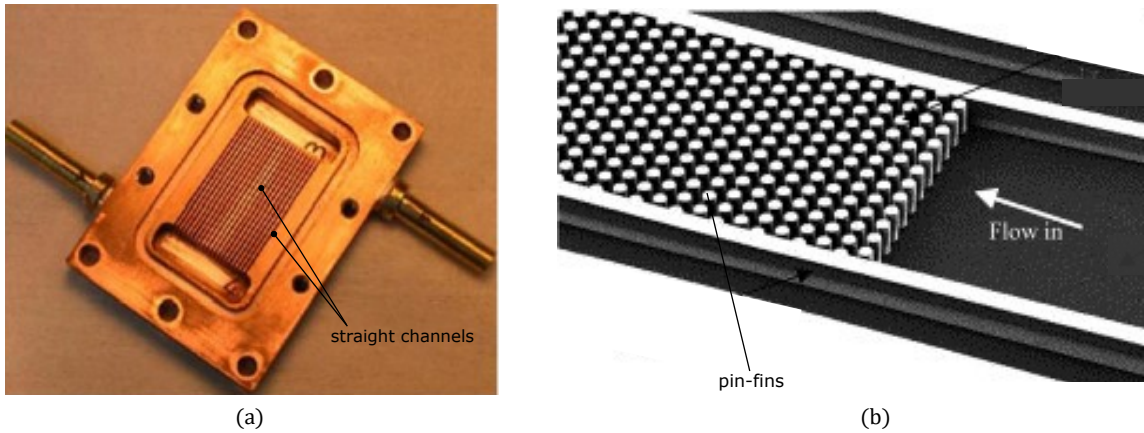
Figure 1.2: (a) Copper micro-channel heat sinks 0.5×4.0 mm, from Park [14]. (b) Fabricated heat-sinks, with micro-pin fins, of diameter of $50\,\mu$m, from Peles et al. [15].

Flow boiling in multi-microchannel evaporators has emerged as an efficient thermal management solution for these high power-density applications due to the advantages of two-phase flow characteristics such as uniform temperature field, high heat transfer coefficients owing to the removal of the latent heat, and the possibility of adopting dielectric refrigerants in direct contact with the surface to be refrigerated [10]. Within multi-micro-channel evaporators, the flow is arranged in parallel micro-channels with a standard inlet and outlet manifold; see Fig. 1.2(a). Flow boiling in micro-channels has been studied extensively in recent years, and several review papers have been dedicated to the underlying fluid dynamics and heat transfer aspects [11, 12, 2, 13]. Pin-fin micro-evaporators represent an alternative geometry to micro-channels. Unlike conventional micro-channel structures where the fluid flows through straight, isolated channels, pin-fin micro-evaporators feature an array of obstacles with various shapes, resulting in a cross-flow configuration [15]. In Fig. 1.2(b), an example of a micro-pin fin heat-sink employing cylindrical pins is presented. Compared with straight channels, the pin-fins create a disturbance on the flow field and promote the flow mixing, thus potentially enhancing the heat transfer coefficient with respect to traditional straight channels [15]. However, the specific investigation of thermal and fluid dynamics for micro-pin fin evaporators in two-phase systems has received far less attention than the conventional boiling in multi-micro-channel evaporators. Despite the large number of experimental studies conducted on pin-fin heat sinks, there is still a strong disagreement on the underlying dynamics because the existing experimental

procedures hardly succeed in capturing the small spatial and temporal scales of the flow with sufficient resolution. For instance, the time response for thermocouples in point-wise temperature measurements is usually larger than the characteristic time of the investigated phenomena and also because the research has mainly focused on reducing the pressure drop in the evaporator while increasing the heat transfer performance. Traditionally, empirical or semi-empirical correlations have been the most common approach for predicting boiling flows. However, due to the limitations of both empirical correlations and theoretical models, there is growing interest in using computational fluid dynamics (CFD) simulations to predict two-phase flows and phase-change processes. The main advantages of this technique are its capability to predict transient fluid flow and heat transfer behaviour and to provide detailed spatial and temporal distributions of phase velocities, pressure, and temperatures. However, while CFD has demonstrated great precision and effectiveness in predicting single-phase flows, its full potential in the context of two-phase scenarios is yet to be fully realised.

Research objective and thesis outline

While reviews have been published on these topics under single-phase and two-phase flow conditions, the substantial scatter observed in experimental results is one of the main challenges in flow boiling within micro-pin fin evaporators.

The thesis investigates the dynamics of two-phase flows within micro-pin fin evaporators through numerical simulations. The goal is to unravel the intricate mechanism governing two-phase flows in non-straight geometries and to provide a deeper understanding of the elaborate interplay among different variables. Accordingly, a list of thesis objectives can be formulated:

- Conduct a comprehensive analysis of typical configurations and conditions of micro-pin fin evaporators found in current literature to determine the optimal numerical framework for simulating two-phase flows in non-straight geometries (Ch. 2).

- Validate the numerical framework resolving benchmark problems to assess the accuracy of the solver (Ch. 4).

- Reveal fluid dynamics in micro-pin fin geometries under adiabatic conditions by investigating the influence of the fluid properties, the impact of the flow regime

and the configuration of the pin-fins. To understand the flow dynamics and the film's morphology, which will be valuable for the subsequent analysis with heat transfer (Ch. 5).

- Advance the investigation by integrating the effects of heat transfer into the physics of the problem. Assess the impact of key parameters, including flow rate, nucleation site of bubbles, and inlet subcooling, on the two-phase flow behaviour, liquid film size and morphology and overall heat transfer performance of the system (Ch. 6).

- Examine the influence of diverse pin-fin shapes on the dynamics of two-phase flows within micro-pin fin evaporators, with a specific emphasis on understanding the flow dynamics, pressure drop as well as the size and shape of the formed liquid films, and how these variations impact system efficiency and performance (Ch. 7).

The present thesis is organised as follows:

Chapter 1 Introduction

Chapter 2 Reviews existing experimental and numerical studies, specifically focusing on two-phase flows within micro-pin fin heat exchangers.

Chapter 3 The governing equations used to model two-phase flows are introduced, along with explanations of the simplifications made. Following that, the numerical framework is presented, delivering specific details about the solvers adopted during the investigation.

Chapter 4 Presents the validation process for the numerical framework, encompassing various benchmark cases. The objective is to evaluate the stability and accuracy of the solvers adopted for the subsequent investigations.

Chapter 5 Delivers the results of adiabatic simulations for the flow of elongated bubbles through arrays of inline cylindrical pin-fins, covering a wide range of conditions commonly encountered in micro-heat exchangers. The primary objective is to unveil how fluid properties, flow rate, and pin fin arrangement influence the propagation of bubbles within these complex geometries, along with the structure of the liquid film trapped at the walls.

Chapter 6 Provides the results of simulations for boiling flows in a heated micro-pin evaporator composed of arrays of inline cylindrical pin-fins. The objective is to understand the heat transfer mechanism during flow boiling by investigating the influence of flow rate, nucleation site, and subcooling level on bubble propagation, liquid film morphology, and heat transfer performances.

Chapter 7 Presents the findings of the study on boiling flows in heated micro-pin fin evaporators, where the arrangement and shape of the pin fins are varied. The objective is to report the impact of the pin shape on the pressure drop, the propagation of the bubbles, film generation, and heat transfer performances.

Chapter 8 Draws conclusions from the study and provides recommendations for future research endeavours.

Chapter 2

Literature review

This section briefly discusses the significant achievements in two-phase flow research related to micro-pin fin evaporators. For clarity, the section is subdivided first into a brief introduction to the boiling phenomena and then into related experimental and numerical work.

2.1   Boiling phenomena

Boiling has been a subject of research interest since the early 20th century, owing to its extensive industrial applications in areas such as power plants, oil refineries, and refrigeration. However, theoretical analysis of this phenomenon has progressed relatively slowly due to its inherent complexity. The heat exchanged by the heated walls and the bulk fluid, typically, is expressed as the product between the heat transfer coefficient, the heat transfer area, and the wall superheat.

$$Q = h_w A (T_w - T_{fluid}) \tag{2.1}$$

To enhance heat transfer, three viable strategies are available: increasing the heat transfer coefficient h_w, expanding the heat transfer area A, or augmenting the temperature difference $(T_w - T_{fluid})$ between the fluid and the wall. Boosting the temperature difference between the wall and the fluid is achievable by cooling the fluid before it enters using a sub-cooler device (by entering with under-saturation conditions). However, this method can harm the overall heat exchanger efficiency, as it demands additional energy to operate the sub-cooler device. Expanding the heat transfer area

7

is typically limited by constraints related to the size and cost of evaporators. Nevertheless, recent advances in micro-fabrication techniques for surface modifications, such as incorporating pin-fins allow for increased surface area [10]. The third option is to enhance the heat transfer coefficient itself. One of the most significant accomplishments of experimental and numerical research is identifying and differentiating the governing heat transfer mechanisms in boiling. However, even today, the understanding of transient heat transfer during boiling remains incomplete and is the subject of ongoing debates within the scientific community. Different boiling flow regimes can be distinguished as described by Nukiyama [16]. Typically, any industrial application will seek to stay in the so-called nucleate boiling regime at moderate or high heat fluxes. Isolated bubbles characterise this regime, where they grow and detach at the heating wall without interacting with each other. Nucleate boiling allows the transfer of high heat fluxes at moderate wall superheats. Minimising the wall superheat is generally one measure to optimise the overall performance of a power generation cycle or a cooling device. The size of the domain also plays a crucial role in this context. It has been found that the typical flow patterns characterising flow boiling in microchannels are, namely bubbly flow, slug flow, annular flow, and dry-out region [17, 18], see Fig. 2.1. The heat transfer mechanism of the bubbly flow regime is acknowledged to be nucleate boiling dominant, and the rest are more forced convection dominant. Since the whole flow boiling process is very complex and each flow pattern has different characteristics, it is not uncommon for researchers to focus on one flow regime at a time. Kandlikar [19] has analysed the similarities and differences between micro and macro channels. It has been found that the differences are generated by the interplay of the relative magnitude of the five forces exerted on the two-phase flow, namely evaporation momentum force, gravity, inertia, shear and surface tension. Typically, the evaporation momentum force causes the interface to push the liquid away backward against the flow, thereby increasing the dry surface of the heater. In contrast, the inertia, viscous, and surface tension forces restore the liquid on the dry patch (rewetting). As the scale decreases, surface tension and shear force increase, gravity falls, and inertia and evaporating momentum are unaffected. Consequently, it becomes clear that the models and correlations developed for the macro-scale cannot be applied in such micro-scale applications. In the micro-domain, the competition of viscous and surface tension forces plays a crucial role, as it gives the origin to thin liquid films that remain trapped between the bubble surface and the walls of the con-
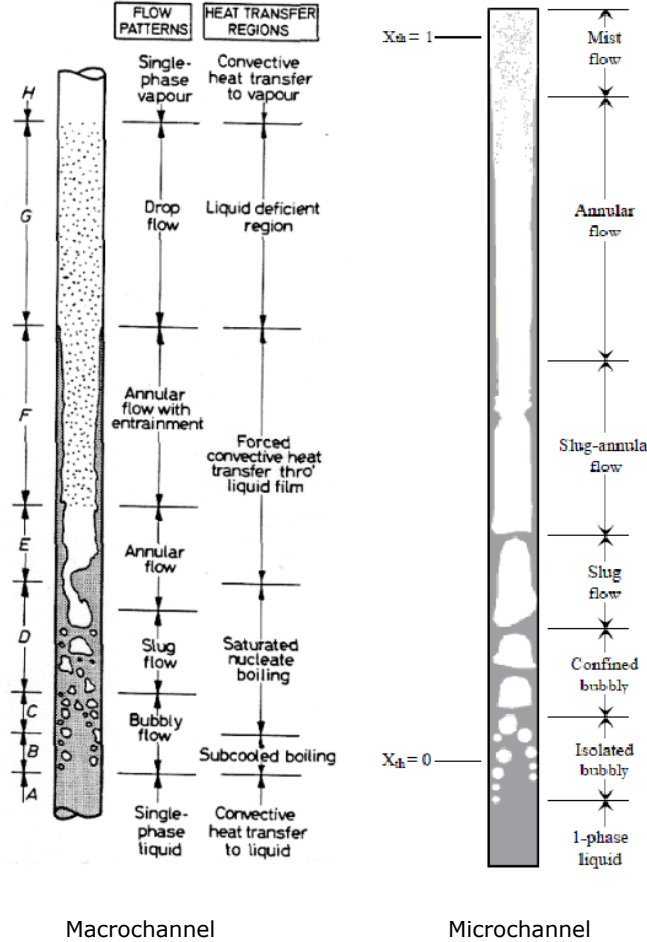
Figure 2.1: The development of a two-phase flow in a vertical tube with a uniform wall heat flux, from Liu [20].

fining medium [21]. The thickness and topography of this liquid film depend on the flow conditions and the fluid properties, but are also strongly impacted by the shape of the gap through which the bubble is advancing [22]. Nonetheless, the thickness and topography of this liquid film have an important impact on the wall-fluid exchanges because cross-stream diffusion typically dominates over other transport phenomena across the liquid film, and thus, the resistance to heat and mass transport offered by the liquid film is inversely proportional to its thickness [23]. For example, the heat transfer coefficient in the correspondence of an evaporating film is often estimated as λ/h, with λ being the thermal conductivity of the liquid and h the local film thickness [24, 25].

2.2 Experimental work

Starting with adiabatic two-phase flows without phase change, extensive research has been conducted in straight channels over the years. The dynamics of bubbles and thin liquid films within confined geometries have been a long-standing topic in fluid mechanics. The works of [21, 26, 22, 27, 28, 29, 30] have resulted in the development of established correlations to predict geometrical features of this liquid film, typically in the form $h/R \sim \mathrm{Ca}^{2/3}/(1 + \mathrm{Ca}^{2/3} - \mathrm{We})$. Here, R denote the tube radius, Ca denotes the capillary number of the flow, $\mathrm{Ca} = \mu U/\sigma$, with μ being the liquid dynamic viscosity, U the liquid or bubble speed and σ the surface tension, and We is the Weber number, $\mathrm{We} = \rho U^2 D/\sigma$, with ρ being the liquid density and D the tube diameter.

Contrarily, the dynamics of two-phase flows propagating through complex and non-straight channels have received far less attention from the fundamental perspective of measurement and topography of the lubricating film, particularly when heat transfer is considered. In this scenario, there are no available correlations to predict the flow dynamics or the morphology and thickness of the liquid film. Comprehensive reviews covering heat transfer enhancement using pin-fin micro-evaporators, including their fabrication, geometrical arrangements, single- and two-phase heat transfer and pressure drop, have been published by Mohammadi and Kosar [31], and Deng et al. [32]. The research on pin-fin heat sinks has mainly focused on reducing the pressure drop in the evaporator while increasing the heat transfer performance. From the available literature, it can be found that experiments in micro-pin fin evaporators have been carried out for various pin-fin shapes, as depicted in Fig. 2.2, such as circular, triangular, square, diamond-shaped, and piranha fins [1, 33, 34, 35, 36]. These studies have shown that triangular and rhomboidal pin-fins tend to outperform other shapes in terms of heat transfer performance. However, circular pin-fins may result in a more homogeneous flow distribution, which can benefit heat transfer performance. Additionally, pin-fin density has been identified as a significant factor affecting the two-phase pressure drop. Kosar et al. [38, 39] investigated the thermal and hydraulic performances of circular and hydrofoil-shaped pin-fins, with the diameter of the circular obstacles, $d_h = 99.5 \, \mu\mathrm{m}$, matching the thickness of the hydrofoils, using R123 as the working fluid, for heat and mass flux in the range $q = 30 - 3120 \, \mathrm{kW/m^2}$ and $G = 976 - 2349 \, \mathrm{Kg/(m^2 s)}$. Heat transfer coefficients (HTC) were reported to
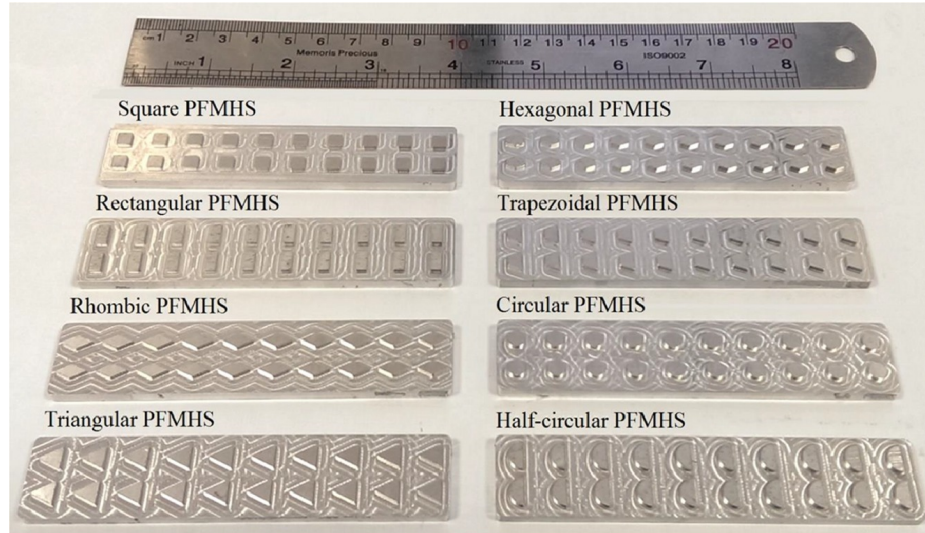
Figure 2.2: Fabricated micro pin-fins heat sinks, from Khoshvaght et al. [37].

increase with the applied heat flux at lower heat flux levels, which was associated with the nucleate boiling behaviour, whereas they decreased when increasing heat flux at high heat flux values, which was associated with the convective boiling behaviour. The qualitative trends of the HTC versus heat and mass fluxes are reported in Fig. 2.3 on the top left. Krishnamurthy et al. [40] performed experiments with staggered arrays of circular micro-pin fins of $d_h = 100\,\mu$m using water as working fluid. The working conditions analysed by the experiment involved a range of mass fluxes of $G = 346 - 794\,\mathrm{Kg/(m^2s)}$ and heat fluxes of $q = 200 - 3500\,\mathrm{kW/m^2}$. They found that the two-phase heat transfer coefficient was moderately dependent on the mass flux and independent of the heat flux, suggesting that convective boiling was the dominant heat transfer mechanism, supported by the observation of annular flow during flow visualisation. The relation between the HTC and mass and heat fluxes is depicted in Fig. 2.3 on the top right. Law et al. [41] experimentally compared the pressure drop and heat transfer of a conventional multi-microchannel evaporator with an evaporator with oblique-finned microchannels, i.e. where the straight parallel channels were communicating via oblique passages so that the overall configuration could be interpreted as that of arrays of rhomboidal pin-fins. They performed the investigation using the refrigerant FC-72 as working fluid, in the range of mass flues of $G = 175 - 350\,\mathrm{Kg/(m^2s)}$, and the heat flux increased until the incipience of critical heat flux (CHF). They reported that the heat transfer coefficient, critical heat flux
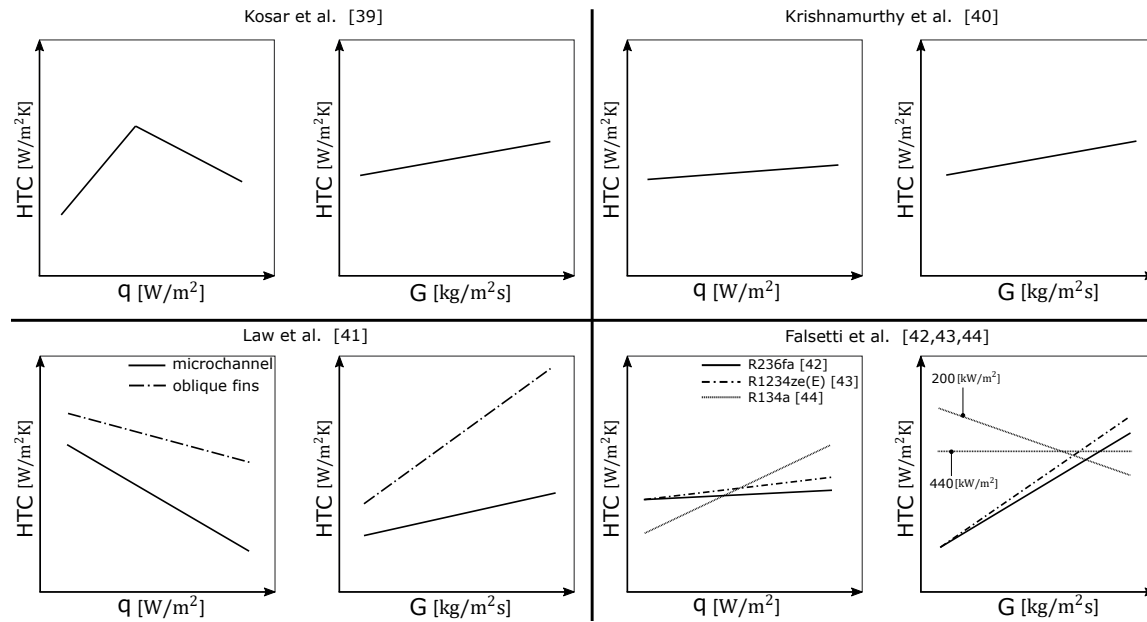
Figure 2.3: Heat transfer trends versus heat and mass fluxes for pin-fin studies, documented by Kosar et al. [39] (top left), Krishnamurthy et al. [40] (top right), Law et al. [41] (bottom left) and Falsetti et al. [42, 43, 44] (bottom right).

and pressure drop were significantly higher for the oblique-finned channels (up to 6 times compared to straight channels), which was attributed to a disruption of the thin liquid film developing over the channel walls. The comparison in HTC trends between the two configurations is drawn in Fig. 2.3 on the bottom left. Falsetti et al. [42, 43, 44] characterised the heat transfer performance of a micro-evaporator with arrays of inline cylindrical pin-fins of diameter of $50\,\mu$m, for different refrigerant fluids, $q = 200 - 480\,$kW/m^2 and $G = 500 - 2500\,$Kg/(m^{2}s). Vapour bubbles were observed to nucleate over the surface of the pin-fins and grow along the gaps in between the pin-fins arrays [44]. Contrasting heat transfer coefficient trends were observed as a function of heat and mass flux depending on the fluid. For R1234ze(E) [43] the heat transfer coefficient was weakly dependent on heat flux for mass fluxes up to $G = 1500\,$kg/(m^{2}s), but increased with heat flux for $G = 1700\,$kg/(m^{2}s); moreover, the heat transfer performances were observed to improve when increasing the mass flux across the entire range of heat fluxes tested ($q = 280 - 440\,$kW/m^2). For R134a [44], the heat transfer coefficient was enhanced when increasing the mass flux but was reduced when increasing the heat flux. However, when plotting the heat transfer coefficient as a function of the streamwise coordinate along the evaporator rather

than as a function of the vapour quality, the heat flux was observed to have only a minor effect. When employing fluid R236fa, the heat transfer coefficient increased with increasing heat flux, and decreased with increasing mass flux for $q = 200 \, \text{kW/m}^2$, whereas it was weakly dependent on the mass flux for $q = 440 \, \text{kW/m}^2$ [42]. In Fig. 2.3 on the bottom right, the relationship between heat transfer coefficient and heat and mass flux for these last experiments is reported. The trends drawn in Fig. 2.3 distinctly reveal that heat transfer trends vary significantly under different operational conditions. This lack of consensus poses a significant obstacle to developing universally accepted correlations for this flow type. It is important to note that the results presented in the figure aim to provide qualitative insight into the heat transfer coefficient trends rather than definitive outcomes. For more comprehensive details, refer to the referenced papers. Chang et al. [45] investigated the effect of the inlet subcooling on flow boiling in square pin-fin evaporators and reported that increasing the level of subcooling had the effect of delaying boiling incipience to higher heat flux, reducing the bubble diameter and departure frequency and thereby slightly reducing the subcooled flow boiling heat transfer coefficient.

2.3   Numerical work

With advancements in computing hardware and algorithms, CFD has become a popular tool for studying two-phase flows and boiling phenomena. There are several advantages of using CFD over experimental and modelling studies. One key advantage is its ability to examine flow phenomena at microscopic scales and in very short time intervals. However, the implementation of models to describe these complex flows is not straightforward. One of the critical challenges is the numerical description of two-phase flows, particularly the interface reconstruction. The discretisation of the heat-mass transfer and surface tension force models are highly linked to the numerical interface representation. Comprehensive reviews covering both aspects have been published, including the work by Chirag et al. [46], Guo et al. [47] and Popinet [48]. Various methods are available today to simulate two-phase flows and boiling problems, and are typically divided into two categories: interface tracking methods, where the formulation of the surface tension and interphase heat-mass transfer effects are straightforward, as the interface is represented by the mesh faces separating the two fluids. One of the early approaches is the **Marker and Cell (MAC)** method

developed by Welch et al. [49], where the interface is marked by weightless particles that are transported with the velocity field in a fixed grid. Afterwards, Tryggvason improved the algorithm by developing the **Front Tracking (FT)** method and applied it to simulations of boiling flows [50, 51, 52]. Another method, introduced by Hirt et al. [53], is the **Arbitrary Langragian-Euler (ALE)** method, where a dynamic mesh follows the motion of the interface, and the interface of the two fluids coincides with the boundary of the computational domain. However, these methods involve very complex formulations and are computationally expensive; therefore, are typically avoided in the treatment of highly deformed surfaces (e.g. slug flows, bubbly flows). The second category is the interface-capturing methods. Most popular among these are the **Phase Field (PF)** method [54], **Level-Set (LS)** method by Sussman et al. [55] and the **Volume of Fluid (VOF)** method developed by Hirt and Nichols [56]. While interface-capturing methods efficiently handle complex deformations of the interface, the implementation of the interface effects (phase change heat-mass transfer and surface tension) is not straightforward. Every method has its own strengths and weaknesses. In the Phase Field method, the transport equation governing the phase indicator incorporates physical effects that govern thin interfaces (the surface tension effect is implicitly included in the formulation). Typically, the method is based on the Cahn-Hilliard or the Allen-Cahn equations [54] and requires handling a fourth-order spatial derivative, which is complicated. In the Level-set method, a signed distance function is used to define the distance from the interface; hence, the interface location is known implicitly from the distance function, allowing for precise discretisation of the interface topology. Despite the proven success of the Level-Set model in handling multiphase systems with large interfacial deformation and discontinuities, the method is characterised by a violation of local mass conservation, which can lead to wrong results or divergence of the solution. On the other hand, in recent years, the VOF method has become more popular due to its simplicity and accuracy (it is globally mass-conserving) and, therefore, is one of the most used methods. The main bottleneck of the VOF method is that the fluid domain is described with a colour function (called volume fraction function), which is not continuous at the interface. Thus, the estimation can become inaccurate when the interface is severely deformed, and the surface tension becomes the dominant force (when the channel diameter is smaller than a few millimetres). At this scale, the interface curvature is large enough to produce spurious currents around it, which are non-physical velocities. A consider-

able number of studies have been published to overcome this problem by developing new algorithms on the body force calculation [57, 58, 59, 60]. To tackle both inaccurate interface representation of the VOF method and mass conservation errors of the LS method, an improved Coupled Level-set/Volume of fluid (CLSVOF) method has been proposed by Sussaman and Puckett [61]. Another, frequently encountered method in recent years is the Lattice-Boltzmann (LB) method [62], which is based on mesoscale formulation where instead of the Navier-Stokes equation, the discrete Boltzmann equation is solved. It popularly derives from its simplicity and does not require explicitly the tracking of the interface.

From here, a list of the most notorious numerical works on two-phase flows and boiling is provided, with a particular interest in the studies performed in a VOF framework, which is the model adopted to perform the study presented in this thesis. Welch and Wilson [63] implemented a model for phase change in a VOF method and simulated one-dimensional test cases and film boiling. Welch and Rachidi [64] extended the model by studying the film boiling with prescribed heat flux, including Conjugate Heat Transfer (CHT). Hardt and Wondra [65] presented an interface heat resistance model for implementing phase change in a VOF or LS framework based on the Schrage work[66]. They performed simulations of film boiling and droplet evaporation. Flow boiling in microchannels has been studied extensively in recent years, dedicated to the underlying fluid dynamics and heat transfer aspects. Mukherjee and Kandlikar [67] studied a vapour bubble growing in superheated liquid inside a microchannel using the level set method. They found that the bubble initially grows continuously, while its length increases rapidly when it fills the channel cross-section and expands in a longitudinal direction. This increase in growth rate is due to the thin layer of liquid between the walls and its interface, where a high rate of evaporation is measured. Kulkelmann et al. [68] implemented a VOF solver on OpenFOAM, including contact line evaporation, with a new class of phase change models called direct heat flux, which was found to be more accurate compared to the model of Hardt and Wondra. Magnini et al. [69] developed a height function algorithm to capture the gas-liquid interface. They used this to study an elongated bubble in a microchannel using a phase change model proposed by Hardt and Wondra [65]. Ling et al. [70] investigated bubble growth and merging in microchannel flow boiling. They adopted a coupled VOF and level set method. Their results showed that the merging can produce a temporal growth in heat flux, while the thin liquid film between the bubble

and the wall is the main reason for the high heat flux in microchannel boiling flow. Nabil and Rattener [71] published a VOF framework for phase change heat transfer modelling, enabling the simulation of diverse phenomena, like film condensation, Taylor flows and nucleate boiling. A considerable number of studies of flow boiling in micro-channels have been published by the group at the University of Brighton. Georgoulas et al. [72, 73] developed an enhanced VOF formulation in OpenFOAM, to investigate bubble detachment in pool boiling. The model presents a new formulation for the interface curvature, using a smoothed volume fraction to reduce the level of spurious currents. They observed that the wall superheat and the level of gravity are very influential on the bubble growth and detachment process. Andredaki et al. [74, 75] studied break-up phenomena of accelerating, elongated bubbles in circular micro-channels. They observed that the applied heat flux does not influence the resulting break-up regimes. Magnini et al. [76] investigated the impact of the channel shape on flow boiling. They found that square channels exhibit the highest heat transfer coefficients at low flow rates due to a very thin liquid film. Municchi et al. [77] examined the effects of conjugate heat transfer and the aspect ratio of microchannels on the bubble and evaporative film dynamics.

While all these motioned studies have extensively examined the hydrodynamics and heat transfer on two-phase flows in straight channels, their application to the analysis of two-phase flows across pin-fin arrays, and more generally, non-straight channels, is scarce. Muradoglu et al. [78] conducted an in-depth investigation into the motion of elongated bubbles in curved channels, utilising theoretical frameworks and numerical simulations. They proposed modifications to Bretherton's law to estimate the inner and outer thickness of the lubricating film. Other studies have focused on bubble and droplet flows in sinusoidal and corrugated channels [79, 80, 81]. Lorenzini and Joshi [82] examined the development of flow patterns and heat transfer performances in evaporators with variable pin densities. Recent years have seen an increasing interest in the study of multiphase phase flow in porous media. Ferrari and Lunati [83] have studied two-phase flow in porous media by modelling the pore geometries from a two-dimensional packing of circles. Understanding multiphase flow in porous media is essential in various fields, such as enhanced oil recovery [84, 85], groundwater remediation, fuel cells [86, 87] and geological sequestration of CO_2 [88]. Micro-pin fin configurations can be considered a simplified approximation of unsaturated porous media. However, these works primarily focused on investigating the overall dynam-

ics of flow and studying the distribution of the phases in the complex geometry, whereas heat transfer has been overlooked. Moreover, they lack systematic data on film thickness, failing to offer comparisons between film thickness with straight channels, thereby restricting their application in micro-pin fin evaporators. In the absence of established methods to predict liquid film thickness through such complex geometries, flat-plate models and Bretherton's law for circular channels are still utilised to model the two-phase dynamics [89, 90].

2.4   Summary

In summary, the experimental studies on the two-phase flow mentioned above emphasise that micro-pin fins enhance flow boiling heat transfer by increasing the available surface area and considerably affecting the flow development and bubble dynamics. However, the contrasting heat transfer trends observed by the different studies when varying the operating conditions further complicate the advancement and understanding of flow boiling phenomena in these complex geometries. This can be mainly ascribed to the high uncertainties in evaluating the wall temperatures, which is due to difficulties in capturing all spatial and temporal scales of the flow with sufficient resolution. Moreover, it has demonstrated that the correlations for the macro-scale cannot predict the hydrodynamic and thermal behaviours in micro-scale domains adequately. Over the past two decades, numerical modelling of two-phase flows has advanced significantly. However, each of the models mentioned above exhibits several limitations. Interface-tracking methods such as MAC, FT, and ALE involve complex formulations and are computationally intensive, particularly in 3-D, which limits their application to specific conditions and configurations. Notably, boiling simulations in complex geometries remain challenging for many of these algorithms. Despite this, interface-capturing methods are promising, although they face challenges in implementing interface effects and complexities due to divergence of the solution by violation of mass conservation for the LS method, and numerical diffusion and high computational demands for the additional differential equations required by the PF method. On the other hand, the VOF method offers a compromise by providing better interface sharpness and being less prone to numerical diffusion and computationally less demanding. This is crucial for simulations where interface dynamics, such as boiling, are essential. Nevertheless, as discussed above, the litera-

ture on two-phase flows through micro-pin fins is insufficient due to the intricate fluid dynamics involved. Additional work is needed to create a more extensive numerical database, with the ultimate aim of revealing the intricate flow dynamics and developing new models to predict bubble behaviours, liquid film size and morphology, and the thermohydraulic performance of micro-pin fin heat sinks. This is the primary goal of the current study.

Chapter 3

Numerical modelling of two-phase flows

This thesis undertakes a comprehensive exploration of two-phase flows, with a specific focus on their behaviour in micro-pin fin heat exchangers, making use of the open-source library OpenFOAM. The research is divided into two main sections. The first part of the study involves an adiabatic investigation of two-phase flow characteristics within micro-pin fins and the results will be shown in Ch. 5. In the second part, the scope broadens to encompass the intricate interplay of interphase heat and mass transfer phenomena presented in Ch. 6 and 7. Two different solvers were employed for these investigations. This chapter provides a concise overview of two-phase flow physics and the numerical model employed for the thesis simulations, organised as follows: the general methods for two-flows are briefly introduced in Sec. 3.1. Subsequently, the numerical framework is presented, including a brief introduction to OpenFOAM and an overview of the chosen solvers for this study in Sec. 3.2.

3.1   Governing equations two-phase flows

Multiphase flows are characterised by the coexistence of multiple fluids or a single fluid in various phases, separated by interfaces. Common examples encompass scenarios such as the dispersion of water droplets in air or the formation of steam bubbles in liquid water. The behaviour of multiphase flow exhibits significant variability and is influenced by various factors, including fluid and phase properties, system geometry, temperature, fluid velocities, and other relevant parameters. Consequently, multi-

phase flows can manifest in diverse configurations, as introduced previously in the introduction. The primary focus of this thesis centres on the investigation of two-phase flows, with a particular emphasis on scenarios involving two phases of the same fluid. This includes situations where one fluid is dispersed within another, such as the advection of a single bubble after the nucleation. In the study of multiphase flows, significant attention is dedicated to the characterisation of the interface, which represents one of the most intricate aspects. In the literature, the interface between two fluids can be approached from both a microscopic and a macroscopic perspective. Generally, in CFD simulations, a macroscopic point of view of the interface is preferred, where the interface is considered massless, and an abrupt change in properties occurs. Regardless of whether the shape of the interface is known or not, various methods can be employed to discretise and model it. Typically, the methods with *surface tracking* are preferred when dealing with flows characterised by complex interface deformations, such as plug, slug, and annular flows. These approaches do not assume any specific interface shape, but instead calculate the interface advection as an integral part of the solution, tracked within a fixed computational grid. The formulation based on surface tracking is commonly referred to as Direct Numerical Simulation (DNS) of the interface. In this approach, there is no necessity for closure equations to account for interfacial effects [91]. These methods are necessary when dealing with scenarios where a distinct interface separates two phases, and the interfacial effects are of significant importance. In such cases, relying on empirical calculations is not feasible due to the need for precise computational accuracy. A *single-fluid formulation* approach is used to describe the interface, where a single set of equations is solved throughout the entire domain. The interfacial effects are integrated as source terms within the governing equations. Between these methods, there is a category called interface capturing methods, which are the most notorious, such as *Phase Field* [54], *Level-Set* [55] and *Volume Of Fluid* algorithm [56]. The various methodologies differ from each other in how the interface is defined, leading to an interface representation which can be categorised as diffusive (Phase Field) or sharp (VOF and LS). In recent years, the VOF method has become one of the dominant methods for two-phase flow in micro-geometries and has already been implemented in OpenFOAM and well tested. For these reasons, the model presented in this thesis is developed within a VOF framework, and a focus on this method is made in Sec. 3.1.3.

3.1.1   Mass, momentum and energy transport

The model's foundation for simulating two-phase flows is established upon the continuity equation and the conservation equations for momentum and energy. Within the framework of the single-fluid formulation, the governing equations for mass, momentum, and energy balances are integrated across the interface. This integration results in a unified set of equations applicable to both the liquid (l) and vapour (v) phases and is solved throughout the entire domain. As previously mentioned, interfacial effects are incorporated into this formulation as source terms; these effects will be introduced Sec. 3.1.2.

$$\frac{\partial \rho}{\partial t} + \nabla \cdot (\rho \vec{u}) = 0 \tag{3.1}$$

$$\frac{\partial (\rho \vec{u})}{\partial t} + \nabla \cdot (\rho \vec{u} \vec{u}) = \nabla \cdot \tau + \vec{F} \tag{3.2}$$

$$\frac{\partial (\rho e)}{\partial t} + \nabla \cdot (\rho e \vec{u}) = \nabla \cdot (\tau : \vec{u}) - \nabla \cdot \vec{q} + \vec{F} \cdot \vec{u} \tag{3.3}$$

where ρ the mixture fluid density, $\vec{u}$ is the velocity, t the time, p the pressure, τ the stress tensor, $\vec{F}$ the force vector, e the specific energy, $\vec{q}$ the heat flux. The vector force $\vec{F}$ in the momentum equation represents external forces acting on the fluid, such as gravitational forces, body force or surface tension force. For the term in the energy equation, external heat can be included, such as heat generated internally by chemical reactions or externally applied heat sources. The following assumptions are applied in order to simplify the set of equations:

- **Incompressible fluid:** The liquid phase is incompressible, as the vapour phase. The maximum velocity of the vapour is not more than some meter per second. As a consequence, the Mach number $\text{Ma} = u/\sqrt{\beta R_g T}$ (where β is heat capacity ratio and R_g universal gas constant) is small enough to neglect compressibility effects. Therefore, both phases can be treated as incompressible, and the velocity field is divergence-free.

$$\nabla \cdot \vec{u} = 0 \tag{3.4}$$

The specific energy e of an incompressible fluid with constant capacity c is a

linear function of temperature. It is assumed, for the sake of simplicity, that the reference value of specific energy is defined as $e_0 = 0\,\mathrm{J/kg}$ at the reference temperature of $T_0 = 0\,\mathrm{K}$. The differences in kinetic and potential energy are minimal in the present study, so they can be neglected. Since the heat capacity at constant pressure is equal to the partial derivative of enthalpy with respect to temperature at constant pressure, the heat capacity at constant pressure of an incompressible fluid is equal to the heat capacity at constant volume. Therefore, it is fair to say that $c = c_v = c_p$. Thus, the specific energy is only a function of the temperature:

$$e = e_0 + c_p(T - T_0) = c_p T \tag{3.5}$$

- **Newtonian fluid:** All the fluids examined during this project are Newtonian, the stress tensor τ in Eq. (3.2) depends linearly on the pressure, the divergence of the velocity field and the deformation speed.

$$\tau = -(p + \frac{2}{3}\mu\nabla \cdot \vec{u})\mathbf{I} + \mu[\nabla\vec{u} + (\nabla\vec{u})^T] \tag{3.6}$$

As the velocity field is free of divergence:

$$\tau = -p\mathbf{I} + \mu[\nabla\vec{u} + (\nabla\vec{u})^T] \tag{3.7}$$

- **Fourier's law for the heat flux:** According to Fourier's law the heat flux $\vec{q}$ in Eq. (3.3) depends linearly on the temperature gradient and thermal conductivity λ of the fluid as follows:

$$\vec{q} = -\lambda\nabla T \tag{3.8}$$

- **Viscous dissipation and power exchange due to volumetric forces are negligible:** The flow velocity, and as a consequence, the shear stress is low. Thus, the effect of viscous dissipation $\nabla \cdot (\tau : \vec{u})$ and power supply or release due to volumetric forces $\vec{F} \cdot \vec{u}$ in Eq. (3.3) are insignificant compared to the convective and conductive heat transport and the heat consumption due to evaporation (and condensation).

- **Gravitational force is negligible:** Within the range of conditions simulated, the Bond number ($Bo = \Delta\rho g d_h^2/\sigma$, where $\Delta\rho$ is the density difference between the two phases, g is the gravitational acceleration, σ is the surface tension) of

the flow is very small $<< 1$, which supports the approximation of negligible gravitational forces.

- **Surface tension effects dominant:** The difference in pressure between two phases is the difference between the recoil pressure and surface tension effect. Generally, the recoil pressure is negligible compared to the surface tension at the interface. More details will be provided in Sec. 3.1.4 where the effects at the interface are introduced.

A general formulation of mass, momentum, and energy equation can be rewritten with the assumption described above:

$$\nabla \cdot \vec{u} = 0 \tag{3.9}$$

$$\frac{\partial \rho \vec{u}}{\partial t} + \nabla \cdot (\rho \vec{u}\,\vec{u}) = -\nabla p + \nabla \cdot \tau + \vec{F}_\sigma \tag{3.10}$$

$$\frac{\partial \rho c_p T}{\partial t} + \nabla \cdot (\rho \vec{u}\, c_p T) - \nabla \cdot (\lambda \nabla T) = 0 \tag{3.11}$$

Furthermore, when considering transient conduction within the heating wall, referred to as Conjugate Heat Transfer (CHT), the conservation equation for energy also needs to be solved within the solid phase. In the solid phase, the convective term is non-existent, and the energy equation for the solid domain comprises solely of transient and diffusive terms.

$$\frac{\partial \rho c_p T}{\partial t} - \nabla \cdot (\lambda \nabla T) = 0 \tag{3.12}$$

where λ is the thermal conductivity. However, it is worth mentioning that all the results presented in this thesis do not account for the effects of CHT, but the heat flux is directly applied as a boundary condition.

Turbulence

Turbulence is not modelled in the simulations performed during the present thesis. Typically, in microchannels with low Reynolds numbers, the flow is generally laminar. Considering the typical maximum velocity magnitude ($u = 10 - 15\,\text{m/s}$, observed inside the vapour phase, near the bubble front, see Ch. 6), a typical diameter equivalent

of a channel (which is the characteristic length used in this formulation) $d_h = 0.0001\,\text{m}$ and a representative kinematic viscosity ($\nu = 5.5 \times 10^{-7}\,\text{m}^2/\text{s}$), the Reynolds number $\text{Re} = ud_h/\nu$ is much smaller than 3000. This allows to disregard the implementation of the turbulence model because a fine mesh is enough to fully characterise the flow characteristics and thermal boundary layer around the geometry.

Nucleation

The nucleation is a thermodynamic process that determines the phase separation in both natural and technological processes. Nucleation is influenced by both the temperature and supersaturation level of the liquid. When the nucleation is controlled by temperature, like in the case of boiling, the change in temperature causes changes in local pressure that favours the formation of vapour nuclei. In supersaturated systems, such as gas evolution on electrodes, the condition of the fluid is 20 to $40\,^\circ\text{C}$ above the saturation condition, the nucleation happens because the system attempts to recover equilibrium by phase separation at a constant temperature. To describe gas bubble nucleation, different mechanisms are available as Jones et al. [92] describe:

- Type 1 or homogeneous nucleation occurs in the liquid bulk at high levels of supersaturation. The nucleation process initiates spontaneously without the presence of any foreign particles or surfaces. It is a relatively rare and less common process because it requires precise conditions for nucleation to occur uniformly throughout the substance.

- Type 2 or heterogeneous nucleation happens at the surface or in imperfections like pits and cavities at lower levels of supersaturation compared to homogeneous ones. The presence of defects reduces the energy required for nucleation.
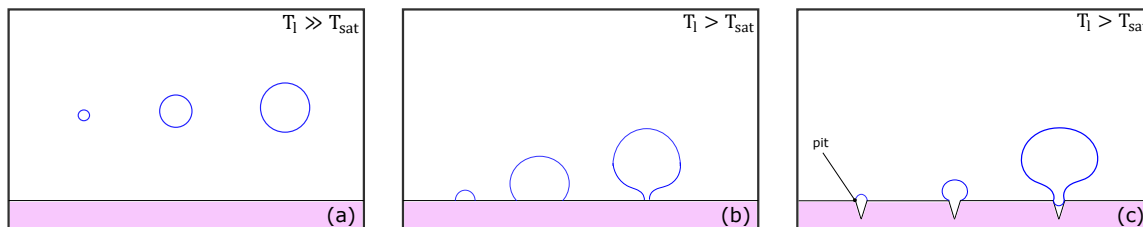
Figure 3.1: Nucleation mechanism. (a) Homogeneous nucleation, (b) Heterogeneous nucleation from a perfect surface and (c) Heterogeneous nucleation from a cavity.

In Fig. 3.1, a visual explanation of two types of nucleation processes is presented. During the present thesis, boiling in micro-channels has been analysed, and the typical conditions closely approach saturation. Therefore, the most suitable mechanism to describe nucleation is type 2. Nucleation often occurs more readily at imperfections on the surface, as the presence of defects reduces the energy required for nucleation. Consequently, potential sites can be identified where micro-cavities are present in the wall due to the microfabrication process. However, the criteria for the activation of a nucleation site and their dependence on the geometry of the nucleation site are still not fully understood. As a consequence, implementing a physically based sub-model for the nucleation process into the two-phase model is not straightforward. To compensate for this lack in the model adopted in the numerical framework used for this thesis, an artificial nucleation has been adopted and will be discussed in detail for the specific simulations. Typically, nucleation is described either through empirical correlations derived from experimental data or by using stochastic models. Recently, Gallo et al. [93] published a new mesoscale approach capable of describing flow boiling from stochastic nucleation up to macroscopic bubble dynamics.

3.1.2 Interface treatment

Up to this point, the equations described do not account for what transpires at the interface. Carey [94] introduced control volumes to derive the general equations for the conservation of mass, momentum, and energy across the interface, as illustrated in Fig. 3.2. Since the interface is infinitesimally thin and lacks mass; therefore can be negligible accumulation of mass, momentum, or energy within it. The position of the interface, denoted as $x_{int}(t)$, is a function of time and is determined by the balance between the fluxes of these quantities entering and leaving through the interface. The movement of the interface, described as $u_i = dx_{int,n}/dt$, gives rise to equations governing the transport of mass, normal momentum, tangential momentum, and energy across the liquid-vapour interface. These equations are commonly referred to as jump conditions, which typically are applied as boundary conditions within the *two-fluid formulation*. Note that the sign convention was adopted arbitrarily by which coordinates and velocities are positive to the right in Fig. 3.2. The transport of mass at the interface is sketched in Fig. 3.2(a), which can be defined as follows:

$$\dot{m}_l - \dot{m}_v = \rho_l u_{l,n} - \rho_v u_{v,n} = (\rho_l - \rho_v)u_{int} \tag{3.13}$$
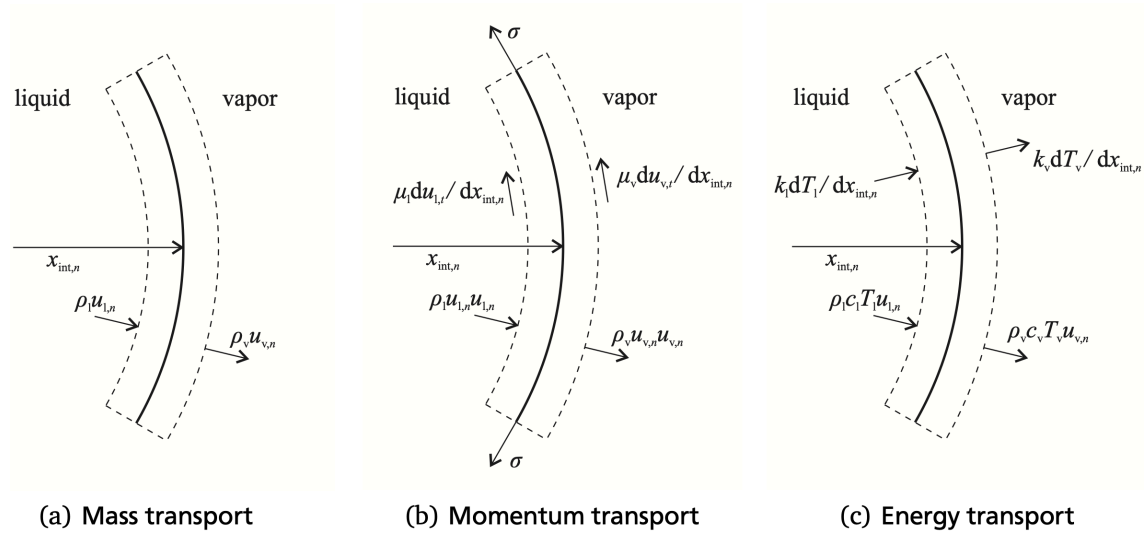
Figure 3.2: Calculation of mass, momentum, and energy transport across a liquid-vapour interface [94].

The two terms represent the rate of liquid mass flow toward the control volume and the rate of vapour mass flow rate out of the control volume moving with the interface. The transport of momentum normal and tangential to the interface are depicted in Fig. 3.2(b), where the subscript n and t, refer to the normal and tangential direction of the interface, respectively. As a consequence of the motion of the interface, the normal momentum is convected into the control volume with the interface at the velocity of the fluid relative to the interface. In the momentum balance, at the liquid-vapour interface, the pressure difference between the two phases can be detected as the difference in the recoil pressure due to evaporation or condensation at the interface and the effects of the surface tension; therefore, the normal momentum is defined as follows:

$$p_v - p_l = \sigma\kappa + \rho_l u_{l,n}(u_{l,n} - u_{int}) - \rho_v u_{v,n}(u_{v,n} - u_{int}) \tag{3.14}$$

The interface motion is usually relatively slow, and the two terms on the right-hand side of Eq. (3.14) can be considered negligible, compared to the effect of the surface tension on the interface and the equation reduces to the *Young-Laplace Equation* [94]:

$$\Delta p = p_v - p_l = \sigma \left(\frac{1}{r_1} + \frac{1}{r_2} \right) = \sigma \kappa \tag{3.15}$$

where r_1 and r_2 are the principal radii of curvature of the interface and κ is twice the mean curvature. The curvature is defined as positive if the interface is convex with respect to the vapour phase, e.g. for a vapour bubble within a bulk liquid. Similarly to the normal contribution, the tangential contribution of the momentum is convected into the control volume at the velocity of the fluid relative to the interface. Including the effects of shear stresses at the interface and considering constant surface tension along the interface, the tangential momentum balance at the interface reduces to the balance of the shear stress in the two fluids on either side of the interface:

$$\mu_l \frac{du_{l,t}}{dx_{int,n}} - \mu_v \frac{dv_{l,t}}{dx_{int,n}} = 0 \tag{3.16}$$

The balance of energy at the interface is depicted in Fig. 3.2(c). As for the transport of mass and momentum, the energy is convected into the control volume moving with the interface at the velocity of the fluid relative to the interface. The transported energy includes the fluid enthalpy and kinetic energy associated with the velocity field in the fluid. The energy can be transported to or from the interface by Fourier conduction, or in the vapour, by radiative transport. Typically, the effects of radiation in the vapour are small. Therefore, a conservation equation for the energy can be defined as follows:

$$\rho_l(u_{l,n} - u_i)\Delta h_v - \rho_v(u_{v,n} - u_i)\Delta h_v = -\lambda_l \frac{dT_l}{dx_{i,n}} + \lambda_v \frac{dT_v}{dx_{i,n}} \tag{3.17}$$

The first two terms on the right-hand side are the heat flux terms.

On the other hand, within the framework of the *single-fluid formulation*, an integration of the governing equations for mass, momentum, and energy balances is carried out across the interface. This integration results in a unified set of equations solved throughout the entire domain. The interface that demarcates the bulk liquid and vapour phases is assumed to be infinitely thin and can be conceptually

represented as a surface. Notably, fluid properties undergo an abrupt change across the interfacial region. In this approach, the interfacial effects are included as source terms and are modelled using delta functions δ, which replace the conventional jump conditions:

$$\nabla \cdot \vec{u} = \dot{m}\delta_{int}(x) = \int_{\Gamma(t)} \dot{m}\delta(x - x_{int})ds \tag{3.18}$$

$$\frac{\partial \rho \vec{u}}{\partial t} + \nabla \cdot (\rho \vec{u}\,\vec{u}) = -\nabla p + \nabla \cdot \tau + \int_{\Gamma(t)} \sigma\kappa\delta(x - x_{int})ds \tag{3.19}$$

$$\frac{\partial \rho c_p T}{\partial t} + \nabla \cdot (\rho \vec{u} c_p T) - \nabla \cdot (\lambda \nabla T) = \dot{q}\delta_{int}(x) = \int_{\Gamma(t)} \dot{q}\delta(x - x_{int})ds \tag{3.20}$$

where $\Gamma(t)$ is the phases interface, $\dot{m}$ and $\dot{q}$ are the interphase mass and heat flux. $\delta(x - x_{int})$ is a multidimensional delta function which is different from zero only at the interface $x = x_{int}$ (where x_{int} is a parametrisation of the phases interface $\Gamma(t)$). A detailed discussion of these terms is performed in Sec. 3.1.4.

Within the single-fluid formulation, to fully close the problem, additional features are required:

- A definition of the marker function $c(\vec{x}, t)$ to describe the fluids and their properties and a method to update the marker function with the interface evolution (advection);

- Approximation of the delta function on the grid;

- Reconstruction of the interface in terms of the curvature (κ) and normal vector ($\vec{n}$) in order to evaluate the surface tension effects.

Generally, the marker function is defined by the δ function and takes values between 0 and 1, depending on the phase present in $\vec{x}$ at time t:

$$c(\vec{x}, t) = \int_V \delta(x - x_{int})dV \tag{3.21}$$

where V is the control volume. The gradient of the indicator function is different

from zero only if the domain (V) contains parts of the interface:

$$\nabla c = \int_\Gamma \delta(x - x_{int})ds = \vec{n}\delta_{int}(x) \tag{3.22}$$

With this definition, a generic expression for fluid material property can be defined:

$$\phi(x,t) = \phi_2 + (\phi_1 - \phi_2)c(\vec{x},t) \tag{3.23}$$

where ϕ_i is a generic property of the fluids. The fluid properties change abruptly across the interface (by the definition of the indicator function); therefore, this can lead to numerical instabilities of the flow, which will be amplified by high density and viscosity ratio between the phases. To avoid these problems, it is usual to employ a smoothed version of the marker function. When it comes to the advection of the marker function, various methods can be found in the literature. Each method employs its own approach to approximate the delta function and calculate the interface geometry. For the interface capturing methods, the topology of the interface is implicit in the indicator function field (c). This indicator function is advected by solving a conservation equation. As the numerical model adopted for the entire thesis is based on the VOF method to discretise the two-phase flow, a detailed description of the method is presented in the next sub-section.

3.1.3   Volume of Fluid method

As previously mentioned, the Volume of Fluid method has been selected as the primary approach for discretising two-phase flow in all the work presented in this thesis. The VOF method, originally developed by Hirt and Nichols [56], is favoured for its simplicity and its capacity to handle relatively complex flow configurations characterised by substantial deformations of the interface. In the VOF method, the indicator function is represented as a step function, as defined in Eq. (3.21). The interface between phases can be identified where $\nabla c \neq 0$. The spatial integration of c within the computational cell volume (V_c) is referred as the volume fraction α:

$$\alpha = \frac{1}{V_c} \int_{V_c} c(\vec{x})dV_c \tag{3.24}$$
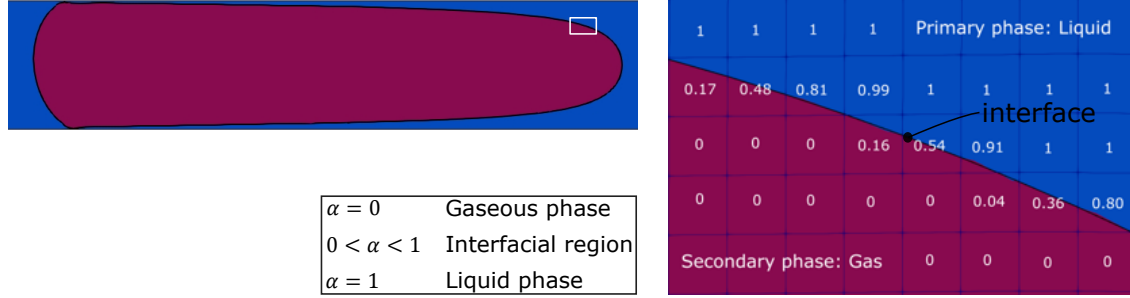
Figure 3.3: Illustration of Volume of Fluid method in a horizontal plane applied to a bubble translating in a straight rectangular channel immersed in a liquid with a sharp interface.

The volume fraction defines how the cell volume is distributed between the phases. In this work, only two phases (liquid and vapour) are considered within the computational domain. Therefore, the volume fraction of the liquid phase in a specific cell is defined as follows:

$$\alpha = \frac{V_l}{V_c} \tag{3.25}$$

Consequently, α has a value of 1 in the liquid phase (cell completely filled by the liquid phase), 0 in the vapour phase (empty cell) and $0 < \alpha < 1$ (jump between the constant values in the bulk phases) for the cells in the interfacial region, as illustrated in Fig. 3.3. The sum of the volume fractions of all phases in a cell has to be equal to 1. Established the volume fraction amount of the cell, the generic fluid properties ϕ can be evaluated as described in Eq. (3.23), by weighting the individual fluid properties with the volume fraction:

$$\phi = \alpha\phi_1 + (1 - \alpha)\phi_2 \tag{3.26}$$

In the VOF method to describe the morphology of the interface, two main parameters are used, the curvature κ and the interface normal vector $\vec{n}$, calculated as follows:

$$\vec{n} = \frac{\nabla\alpha}{|\nabla\alpha|} \tag{3.27}$$

$$\kappa = -\nabla \cdot \vec{n} = -\nabla \cdot \frac{\nabla\alpha}{|\nabla\alpha|} \tag{3.28}$$

A smoothed delta function is used to identify a transition region, where the fluid properties vary smoothly and where the interfacial effects are concentrated. Using this last definition for the interface normal vector and the definition of the gradient

of indicator function Eq. (3.22), a new discrete formulation for the delta function can be found:

$$\delta(\alpha) = |\nabla\alpha| \tag{3.29}$$

For flow without phase change, the volume fraction field is transported exclusively by the velocity field. Therefore, the transport equation for α presents only the transient and convective term:

$$\frac{\partial\alpha}{\partial t} + \vec{u} \cdot \nabla\alpha = 0 \tag{3.30}$$

When phase change occurs, the addition of a source term on the right-hand side of the equation is required. Details will be provided in the subsection dedicated to the phase change modelling in Sec. 3.1.4.

The VOF method offers significant advantages compared to the other interface-capturing methods, primarily its relative simplicity, as it only requires one additional transport equation compared to the single-phase case. It is inherently conservative, allowing for mass conservation close to machine accuracy. However, it also comes with a significant drawback related to its accuracy in discretising the liquid-vapour interface. The transport of the volume fraction field, as described in Eq. (3.30), can lead to challenges due to the definition of the step function. The α field must remain bounded (between 0 and 1), and the change of the volume fraction at the interface should be as sharp as possible. However, adhering to both criteria can lead to problems when solving the transport equation with standard differencing schemes within a Finite Volume Method (FVM) framework. The interface often exhibits a discontinuous change in the volume fraction (where $\nabla\alpha \neq 0$), resulting in excessive interface diffusion. This problem arises from the interpolation of the volume fraction value from cells to face centroids. Consequently, the discretisation of the convective term, which quantifies the volume fraction fluxes across cell faces, requires non-conventional algorithms to avoid issues such as smearing or non-physical oscillations of the interface. Therefore, the choice of solution methods and discretisation schemes is a delicate part of obtaining a correct solution, as it has a significant impact on the results. Low-order discretisation schemes generate a very stable solution but are highly diffusive, while high-order schemes provide a sharp interface and accurate solution (precise calculation of κ and $\vec{n}$) but may be unstable [95]. To address the challenge of balancing accuracy and stability in the VOF method, a commonly embraced solution involves the geometric calculation of volume fraction fluxes across cell faces within the in-

terface and its vicinity. This approach, initially introduced by Noh and Woodward [96], has led to the development of so-called Geometric methods. Consequently, two primary categories of VOF methods exist, distinguished by their approach to interface advection: the Algebraic and Geometric Methods. Both of these methods are available in the OpenFOAM solvers used for the simulations presented in this thesis.

Algebraic methods

The algebraic techniques, as implied by their name, employ algebraic manipulations such as high-resolution or compressive differencing schemes. Some well-known examples include the Flux Corrected Transport (FCT) scheme developed by Rudman et al. [97], the Donor-Acceptor scheme by Hirt and Nichols [56] and the Compressive Interface Capturing Scheme for Arbitrary Meshes (CICSAM) by Ubbink and Issa [98]. In these approaches, the volume fraction varies across a finite-thickness interface. Equation (3.30) can be solved using various combinations of upwind and/or downwind schemes, resulting in an interface that appears diffused across multiple cells and possesses a finite thickness. In OpenFOAM, an example of an algebraic method is the Multidimensional Universal Limiter for Explicit Solution (MULES) algorithm introduced by Weller [99].
An implementation of this algorithm can be found in the solver *interFoam*[1]. However, in the actual computation in OpenFOAM, the advection term in Eq. (3.30) is modified to compress the surface and thereby reduce the smearing, as Deshpande et al. [100] describe. The scheme is obtained by firstly rewriting the advection equation to integral form. Then the equation is discretised, for the transient term any time-stepping (e.g. forward Euler) can be used, while the advection term appears as a summation over cell faces (f) of Ω_i:

$$\frac{\alpha_i^{n+1} - \alpha_i^n}{\Delta t} = -\frac{1}{\Omega_i} \sum_{f \in \partial\Omega_i} (F_u + \lambda_M F_c)^n \tag{3.31}$$

F_u and F_c are the advective fluxes and λ_M is the delimiter, which gets a value of 1 only in the transition region and 0 elsewhere. At the end, the following expression can be written:

$$\frac{\partial\alpha}{\partial t} + \vec{u}\cdot\nabla(\alpha) + \underbrace{\nabla\cdot[\alpha(1-\alpha)\vec{u}_r]}_{\text{anti-diffusion term}} = 0 \tag{3.32}$$

---

[1]Solver for 2 incompressible, isothermal immiscible fluids using a VOF

where the so-called anti-diffusion term operates the interface compression. The compressive term is built in such a way that, due to the presence of the factor $\alpha(1-\alpha)$, it is different from zero in the interfacial cells. $\vec{u}_r$ is an artificial compression velocity and is given by:

$$\vec{u}_r = \min \left[C_\gamma \frac{|\vec{u} \cdot \vec{S}|}{|\vec{S}|}, \left(\frac{|\vec{u} \cdot \vec{S}|}{|\vec{S}|} \right)_{\text{max}} \right] \cdot \vec{n} \tag{3.33}$$

where $\vec{S}$ is the cell boundary face normal vector in such a way that $\vec{u} \cdot \vec{S}$ is the volume flux across the cell face. The coefficient C_γ controls the compression level. A value of zero indicates no compression, a unitary value corresponds to conservative compression (a typical value), while higher values ensure a sharp interface. However, caution is advised against choosing values for the compression coefficient greater than unity. As α becomes steeper, such values may lead to erroneous computations of the interface topology $(\vec{n}, \kappa)$, as mentioned above.

Geometric reconstruction techniques

Geometric methods involve the reconstruction of interfaces using assumed functional forms, followed by Lagrangian advection to compute volume fluxes. This approach comprises an interface reconstruction step, where a linear piecewise approximation of the interface within a cell is constructed. The significant difference from Algebraic methods is that these schemes represent the interface with zero thickness. They are particularly useful when the topology of the interface is determined geometrically by computing volume fraction fluxes across cell faces, especially for cells near the interface. In the original SLIC (Simple Line Interface Calculation) method developed by Noh and Woodward [96], the advection of the volume fraction is solved by splitting it into two (or three) spatial directions. In this approach, the interface is treated as a vertical line during advection in the horizontal direction, and vice versa for the other direction. The entire portion of the cell is defined using the cell's volume fraction gradient. Hirt and Nichols [56], later modified this method by imposing a unique orientation for the interface line when advecting the volume fraction in the different directions, according to the volume fraction gradient, representing the interface norm vector $\vec{n}$. On the other hand, Young [101] introduced the Piecewise Linear Interface Calculation (PLIC), where the straight interface line within each interface cell can be arbitrarily oriented with respect to the x- or y-axis of the domain (sidewalls of
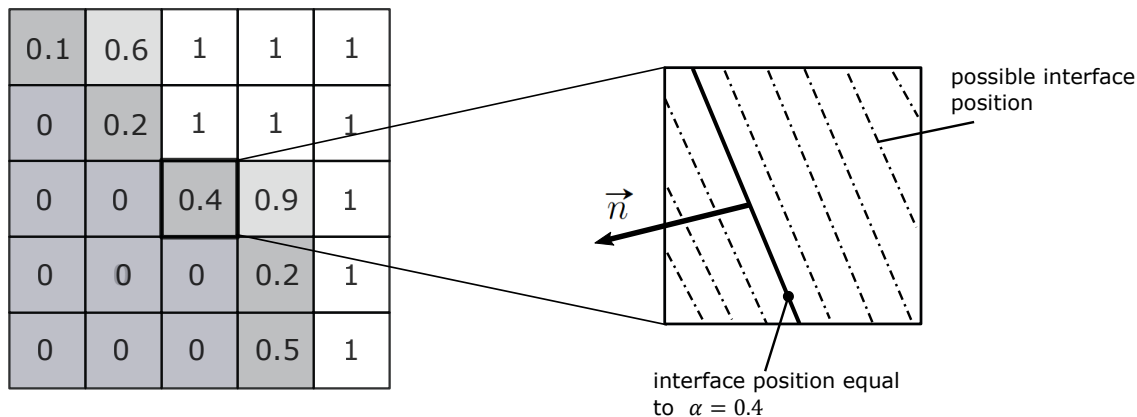
Figure 3.4: Classical reconstruction of the volume fraction field α. $\vec{n}$ is the normal vector to the interface.

rectangular mesh cells). The selection of orientation is determined by the volume fraction gradient, as depicted in Fig. 3.4. Once the interface is reconstructed, the advection step of Eq. (3.30) is performed to proceed with the numerical solution. Then, in an interface advection step the volume fraction crossing each cell during the timestep is calculated, under the assumption that the previously reconstructed interface translates steadily across the cell face; the combination of these fluxes represents the discretised version of the convection term in Eq. (3.30). Roenby et al. [58] implemented a new method called isoAdvector. First, a piecewise planar approximation of the interface is performed with the isosurface, which cuts the cell into two sub-volumes corresponding to the cell's volume fraction. Then, in an interface advection step, the volume fraction crossing the control volume during the time step is calculated, under the assumption that the interface reconstructed in the first step moves steadily across the cell's face. In OpenFOAM, there are different reconstruction methods to obtain a better estimation of interface topology. A comparison of the methods available is performed in the chapter dedicated to the validation of the numerical framework in Ch. 4.

Surface tension calculation

The curvature κ and the resulting surface tension are calculated according to the Continuum Surface Force (CSF) method, which has been developed by Brackbill et al. [102]. Surface tension acts on a surface. As all control-volume-based numerical methods, can only handle volumetric forces, surface tension has to be converted into a

volumetric force (N/m^3) which contributes to the source term F_σ in Eq. (3.19). This is done by multiplying the pressure difference due to surface tension with the gradient of the volume fraction, which represents a volumetric distribution of the interface as discussed above.

$$F_\sigma = \sigma \kappa \nabla \alpha \tag{3.34}$$

The curvature can be evaluated as the divergence of the interfacial normal vector, as explained in Eq. (3.28).

Several hybrid methods are present in literature to better estimate the curvature based on the coupling of the different formulations:

1. To overcome the limitation regarding the poor accuracy on the computation of surface tension effects of the VOF and the LS limitation on the not preservation of mass, Sussman and Puckett [61] developed a *Coupled Level-set and Volume of Fluid algorithm* (CLSVOF). The two formulations are solved simultaneously; the fluid material properties and the terms in the surface tension force are updated according to the LS field. A PLIC advection of the interface is conducted by considering the interface as a linear segment orthogonal to the norm vector computed from the level-set function $\vec{n} = \frac{\nabla \phi}{|\nabla \phi|}$. At this point, the reinitialisation of the LS function is performed by a reconstruction of an exact signed distance function from the volume fraction updated;

2. *Smoothing methods* allow to obtain with a simple implementation a better estimation of the curvature, using a smoothed version of the volume fraction.

$$\alpha^* = \frac{\sum_f \alpha_f S_f}{\sum_f S_f} \tag{3.35}$$

$$\alpha^*(x) = \int_V \alpha(x') K(x - x', h) dx \tag{3.36}$$

The first one is the *Laplacian smoother* and the second is the *Smoothing kernel.* h is the smoothing length. The advantage of these methods is that they are flexible for all types of meshes (also unstructured), but the improvements in performance are limited;

3. Another method is the *Height function*, developed by Owkes et al. [103], a 2°order scheme method, where the curvature is computed with the continuous

field of local interface height $H(x)$. One example, where this method is applied can be found in the Basilisk code [104].

$$H_i = \frac{1}{\Delta x_i} \int_{x_i}^{x_{i+1}} f(x)dx \tag{3.37}$$

Being a second-order scheme is very precise and also avoids numerical instabilities, but the main drawback is that it is not suitable for unstructured meshes.

3.1.4 Phase change

To finally close the problem, the effects related to phase change need to be included in the formulation of the mass, and energy equations (Eqs. (3.18) and (3.20)) and advection of the volume fraction (Eq. (3.30)). Therefore, the calculation of the interphase mass and heat flux needs to be done, respectively $\dot{m}$ and $\dot{q}$. The sub-model for phase change typically involves two distinct steps:

- *Calculation of the local evaporation (or condensation) rate:* In this step, the rate of evaporation or condensation at the liquid-vapour interface is computed based on the local temperature field. This calculation results in determining the mass that evaporates or condenses in each interfacial cell.

- *Calculation of the source terms for the conservation equations:* This step involves calculating the source terms for the conservation equations based on the local mass flux obtained in the previous step. These source terms are essential for accounting for the effects of phase change in the governing equations.

The subsequent sub-sections will address these two steps separately. In principle, it is possible to alter or modify either of these two aspects independently of the other. This flexibility allows for fine-tuning the phase change modelling to meet specific requirements or adapt to particular conditions without necessarily affecting the other step.

Calculation of the local rate of phase change

In general, the choice of the most suitable phase change model is closely tied to the length scale of the domain under consideration. Many phase change models for boiling flows operate under the assumption of thermodynamic equilibrium at the interface,

where both the liquid and vapour phases are considered to be at the same temperature
[52]. This assumption simplifies the modelling process and is often applicable in
practical scenarios.

$$T_{sat}(p_l) = T_l \approx T_v = T_{sat}(p_v) \tag{3.38}$$

The interphase mass flux $\dot{m}$ can be evaluated using the considerations on the inter-
facial transport of energy Eq. (3.17):

$$\dot{m} = \frac{1}{h_{lv}}(\vec{q}_l - \vec{q}_v) \cdot \vec{n} = \frac{1}{h_{lv}}(-\lambda_l \frac{dT_l}{dx_{i,n}} + \lambda_v \frac{dT_v}{dx_{i,n}}) \tag{3.39}$$

where h_{lv} is the latent heat of evaporation. While this is an acceptable hypothesis for
many macro-scale boiling problems, a significant deviation from the thermodynamic
equilibrium may exist at the micro-scale where interfacial resistance, disjoining and
capillary pressures tend to create an interfacial superheating above the saturation
temperature.

Schrage [66] developed a more suitable approach for micro-scale boiling phenomena
based on departure from thermal equilibrium at the interface. The two phases are
assumed to be at their thermodynamic equilibrium saturation values, with a jump at
the interface.

$$T_{sat}(p_l) = T_l \neq T_v = T_{sat}(p_v) \tag{3.40}$$

In all conditions examined in the present thesis, the capillary pressure is small enough
to be considered negligible. Considering, for example, fluid R236fa, vapour bubbles
at $T_{sat} = 30°C$, in a micro-channel with characteristic length of $d_h = 0.0001\,\mathrm{m}$, are
interested by a pressure jump at the interface of $\Delta p \approx 4\sigma/d_h = 357\,\mathrm{Pa}$. This pressure
jump causes an increase in the T_{sat} in the vapour of about $0.05\,\mathrm{K}$, which is negligible
compared to the pressure of the surrounding liquid. Therefore, the assumption of
$T_v = T_{sat}(p_\infty)$ is reasonable.

The Schrage model has already been well-tested in different numerical studies [65,
68, 77] and, as a consequence, is the one implemented in the solver adopted for
the simulations with phase change. Schrage [66] applied the kinetic theory at the
molecular level to obtain a relationship between the local evaporation rate at the
liquid-vapour interface (net flux of molecules crossing the interface) as a function
of the local temperature and pressure jump. Afterwards, Tanasawa [105] simplified
the relationship by assuming that for small interface superheating over local vapour

equilibrium saturation temperature ($\frac{T_v - T_l}{T_v} << 1$), the local interphase mass flux depends linearly on the local temperature jump. Therefore, the interface mass flux per unit interfacial area can be defined as:

$$\dot{m} = \frac{T_i - T_{sat}(p_v)}{R_{int}} \tag{3.41}$$

where R_{int} represents the interfacial resistance to evaporation, defined as follows:

$$R_{int} = \left[\frac{2\gamma}{2 - \gamma} \left(\frac{M}{2\pi R_g} \right)^{1/2} \frac{\rho_v h_{lv}}{T_{sat}^{3/2}(p_v)} \right]^{-1} \tag{3.42}$$

where γ is the accommodation factor, M is the molecular weight of the liquid, R_g is the universal gas constant. The accommodation coefficient represents the fraction of molecules crossing the interface during evaporation. A theory for predicting this accommodation coefficient does not yet exist, and therefore, the appropriate value needs to be extracted from experiments. Various experimental sources and preliminary test benchmarks indicate a value equal to unity [106, 77]. The idea behind the interfacial heat resistance is based on considerations at a much smaller length scale than what is typically resolved in CFD simulation. The primary advantage of using Eq. (3.41) instead of Eq. (3.39) lies in its more straightforward implementation.

Calculation of the source terms for the conservation equations

The evaporating (or condensating) mass flux is transferred through the liquid-vapour interface calculated in the first step according to Eq. (3.41), which needs to be included in the conservation equations. This is achieved by introducing a volumetric source term. The mass flux across the liquid-vapour interface can be converted into a volumetric source term using the interfacial density δ_s. This density serves to identify the transition region and takes non-zero values only at the interface. In the VOF method, it is defined as in Eq. (3.29). For each superheated interfacial cell, an amount of vapour (approximately $\dot{m}\delta_s$) is generated, while an equivalent amount of liquid disappears. Consequently, the local evaporation rate can be expressed as:

$$\dot{\rho} = \dot{m}\delta_s = \frac{T_i - T_{sat}(p_v)}{R_{int}} |\nabla \alpha| \tag{3.43}$$

(a) $\dot{\rho}_0$ (b) $\dot{\rho}_1$ (c) $\dot{\rho}$
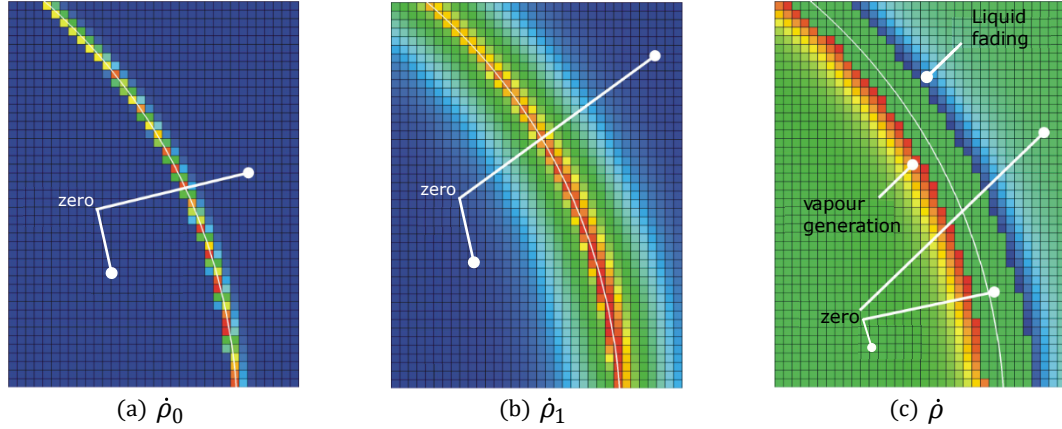
Figure 3.5: Illustration of the smeared source term distribution around a liquid-vapour interface growing in a superheated liquid:(a) initial sharp source term, (b) smeared source term obtained after solving the steady diffusion equation Eq. (3.46), and (c) final source term distribution, scaled in a way to have negative values at the liquid side and positive in the vapour side. The interface ($\alpha = 0.5$) is represented by the white curves in the pictures.

The stability and convergence of the solution process for conservation equations can be quite sensitive to source terms. The source term defined by Eq. (3.43) may have very large values at the interface, while being zero elsewhere. Therefore, it is not used directly. In this thesis work, a modification to the source term proposed by Hardt and Wondra [65] and Kunkelmann and Stephan [68] is employed, to transform the sharp distribution of source terms into a smooth distribution, making it numerically more manageable. The fundamental idea behind this approach is to redistribute the source terms in pure cells (those containing only liquid or vapour) near the liquid-vapour interface. When considering evaporation, a negative mass source is applied on the liquid side of the interface, while a positive mass source is applied on the vapour side. The magnitudes of these positive and negative source terms are selected such that mass is conserved globally. The procedure to obtain the smoothed source term field involves four steps, which are detailed as follows:

- **Step 1**
  A first source term is calculated according to Eq. (3.43), which can be visualised in Fig. 3.5(a). Since the evaporation takes place only in the liquid:

$$\dot{\rho}_0 = \alpha N \dot{m} |\nabla \alpha| \qquad (3.44)$$

where α is equal to 1 on the liquid side and N is a normalisation factor, which allows the preservation of the evaporation rate:

$$N = \frac{\int_V |\nabla\alpha|dV}{\int_V \alpha|\nabla\alpha|dV} \tag{3.45}$$

- **Step 2**

  The source term calculated in the first step is then smeared by resolving a diffusion equation as explained by Hardt and Wondra [65].

$$D\nabla^2\dot{\rho}_1 = (\dot{\rho}_1 - \dot{\rho}_0) \tag{3.46}$$

  This diffusion problem is solved across the entire flow domain while imposing Neumann boundary conditions at all boundaries ($\vec{n} \cdot \nabla\dot{\rho}_{1|\partial V} = 0$). These boundary conditions ensure that the volume integrals of both $\dot{\rho}_0$ and $\dot{\rho}_1$ remain identical despite the smearing process. The diffusion constant, denoted as D, serves as a parameter for diffusion and relies on the mesh resolution. The length scale over which the initial source term is smeared is directly proportional to this diffusion constant and an artificial time increment, and is given by $(D\Delta t)^{1/2}$. This time increment, denoted as Δt, defines the time interval between the two source terms. The value of the diffusion constant is adjusted in relation to the mesh resolution in a manner that ensures the source term is spread over several computational cells on each side of the interface, as illustrated in Fig. 3.5(b).

- **Step 3**

  The presence of the source term in the interfacial region can lead to problems in the advection. Therefore, a cropping is applied to the source term that appears in the smeared interfacial region. Through cropping, the source term in all mixture cells, where $\alpha_{\text{cut}} < \alpha < 1 - \alpha_{\text{cut}}$, is set to zero. α_{cut} is a volume fraction cut-off[2]. The remaining source term field is then redistributed across the interface, both on the vapour and liquid sides, to prevent any loss of mass. The interface itself is not subjected to any source terms and is solely transported by the velocity field, remaining undisturbed by the source term field.

- **Step 4**

---

[2] $\alpha_{\text{cut}} = 10^{-3}$ was adopted in all the simulations presented in this thesis

To ensure global mass conservation, the source term calculated in the first step is integrated over the entire computational domain, to obtain the net mass flow across the liquid-vapour interface.

$$\dot{m}_{net} = \int_V \dot{\rho}_0 dV \tag{3.47}$$

The remaining source term field is scaled individually on the liquid and the vapour side in order to make sure that the mass is globally conserved and that the evaporating or condensating mass flow corresponds globally to the net mass flow through the interface:

$$N_v = \frac{\dot{m}_{net}}{\int_{V_v} \alpha \dot{\rho}_1 dV_v} \tag{3.48}$$

$$N_l = \frac{\dot{m}_{net}}{\int_{V_l} \alpha \dot{\rho}_1 dV_l} \tag{3.49}$$

where V_l, V_v are the pure liquid and vapour domain (where $\alpha < \alpha_{\text{cut}}$ and $\alpha > 1 - \alpha_{\text{cut}}$ respectively). Using the scaling coefficients, the final source term can be calculated as follows:

$$\dot{\rho} = N_v(1 - \alpha)\dot{\rho}_1 - N_l\alpha\dot{\rho}_1 \tag{3.50}$$

$$\dot{\rho} = \begin{cases} N_v(1 - \alpha)\dot{\rho}_1 & \alpha < \alpha_{cut} \\ -N_l\alpha\dot{\rho}_1 & \alpha > 1 - \alpha_{cut} \\ 0 & \alpha_{cut} < \alpha < 1 - \alpha_{cut} \end{cases} \tag{3.51}$$

Figure 3.5(c) presents an example of final source term distribution.
Calculated the final source term, the effects of phase change at the interface can be added to the right-hand side of the conservation Eqs. (3.18), (3.20) and Eq. (3.30). The source term added in the continuity equation accounts for the divergence of the velocity field in cells where the mass is changed.

$$\nabla \cdot \vec{u} = \frac{\dot{\rho}}{\rho} \tag{3.52}$$

The only effect of the phase change in the momentum balance is the pressure recoil, which is already accounted in the continuity equation. The pressure recoil is the pressure drop required to drive the acceleration of the fluid when phase

change occurs. If the velocity field in the vicinity of the interface is correct, the pressure recoil is implicitly considered in the momentum balance [65] as demonstrated by considering a 1D evaporation process by Kunkelmann [107], see Eq. (3.14), where considering a flat surface the surface tension effects are not considered because the interface is not curved.

For the energy equation, the source term consists of two contributions: the first contribution is due to the use (or release) of energy due to evaporation (or condensation) at the interface, which depends on the enthalpy of evaporation (h_{lv}) and sharp source term ($\dot{\rho}_0$). The second contribution is a correction resulting from the removed or added mass in the pure liquid and vapour cells, which results in a not-free divergence velocity field. This term is associated with a certain amount of sensible heat $c_p T$ which is added or removed due to the source term. Therefore, an additional source term, proportional to the smeared source term ($\dot{\rho}$) is added to compensate for this effect.

$$\frac{\partial \rho c_p T}{\partial t} + \nabla \cdot (\rho \vec{u} c_p T) - \nabla \cdot (\lambda \nabla T) = -\dot{\rho}_0 h_{lv} - \dot{\rho} c_p T \qquad (3.53)$$

Since the velocity field is not free of divergence in the interfacial cells where the source term can be present, an additional source term is added to the transport equation of the volume fraction:

$$\frac{\partial \alpha}{\partial t} + \vec{\alpha} \cdot \nabla \alpha = \frac{\dot{\rho}}{\rho} \alpha \qquad (3.54)$$

The inclusion of a source term in the transport equation for the volume fraction is crucial for preventing unbounded volume fraction values, which can result in cell values that are either smaller than 0 or larger than 1. This issue arises due to the convective flux of α across cell faces, which is calculated based on the velocity field. When the velocity field is divergent, often due to a positive source term, the net flux of α entering a cell may not be equivalent to the flux of α exiting the cell as it should be. Instead, the dominant effect is the amount leaving the cell. This can lead to negative values of the volume fraction within the cell, depending on the size of the time step used in the simulation. The source term helps counteract this effect and ensures that the volume fraction remains bounded within the physically meaningful range of 0 to 1.

3.2   OpenFOAM solvers

In this section, the OpenFOAM solvers used during the investigation of two-phase flows in micro-pin fins heat sinks are presented and discussed. First, a brief introduction to OpenFOAM and its structure is presented, and then the solvers adopted are explained.

3.2.1   OpenFOAM structure

The software OpenFOAM is an object-oriented open-source CFD software package built on the C++ programming language. OpenFOAM is a complete tool using different libraries to solve complex fluid dynamics problems. OpenFOAM uses the Finite-Volume-Method to discretise the computational domain spatially and to transfer the partial differential equations into a linear algebraic system of equations. OpenFOAM offers a wide range of solvers for various physical applications, including incompressible and compressible flows, combustion, heat transfer, multiphase flows, and more. OpenFOAM's popularity stems from its accessibility and the opportunity it provides for developing new models. The OpenFOAM layout consists of two main directories:

- ThirdParty: a set of third-party libraries for different purposes, for pre-processing such as meshing and parallel computing. OpenFOAM does not include any specific post-processing software. The user must, therefore, install a post-processing software in order to analyse the data retrieved from the simulations. ParaView is the most commonly used tool for this task and is adopted in this work.

- OpenFOAM libraries: the simulations are configured by several plain text input files located across three main directories; the basic directory structure for an OpenFOAM case is as follows:

    1. *system/:* for setting parameters associated with the solution procedure itself. It contains at least the following 3 files: controlDict where run control parameters are set including start/end time, time step and parameters for data output; fvSchemes where discretisation schemes used in the solution may be selected at run-time; fvSolution where the equation solvers, tolerances, and other algorithm controls are set for the run.

2. *constant/:* that contains a full description of the case mesh in a subdirectory polyMesh and files specifying physical properties for the application concerned, e.g. transportProperties.

3. *0/ (or another initial time directory):* containing individual files of data for particular fields. The data are initial values and boundary conditions that the user must specify to define the problem.

The detailed structure of the tool can be found in the user guide [108]. The solvers in OpenFOAM are organised in a structured manner using classes, enabling mathematical expressions in terms of operators like divergence, gradient, laplacian, rotational operators, temporal derivatives, and others. Therefore, the partial differential equations are comfortably recognisable. For instance, considering the energy equation for the temperature field T with phase change Eq. (3.53) in OpenFOAM can be implemented as follows:

```
1 TEqn (
2          fvm::ddt(rhoCp,T)
3        +fvm::div(rhoCpPhi,T)
4        -fvm::Sp(fvc::ddt(rhoCp) + fvc::div(rhoCpPhi),T)
5        -fvm::laplacian(lambda,T)
6        -fvm::Sp(energySource,T)
7        ==
8        -energySource*Tsat
9     );
```

Listing 3.1: Energy equation Eq. (3.53) implemented in boilingFoam.

The PDE's are stored in sparse matrices that employ two main discretisation approaches: implicit indicated by the namespace fvm (finite volume method) and explicit indicated by fvc (finite volume calculus). ddt (time derivative), div (divergence), laplacian, and Sp (source term) are mathematical operators. The different discretisation methods are coded in classes for each operator and can be specified directly when the simulation is performed[3].

For the generation of the computational domain, different parameters influence the

---

[3]The different discretisation methods can be defined in the system/fvSchemes file.

quality of the mesh; e.g. the orthogonality, for example, plays a crucial role. In the present thesis, the meshes are generated with *blockMesh*[4]. There is no general rule to generate the optimal mesh, which usually depends on the particular simulation and the characteristics interested in the study. It is normal to perform a mesh refinement study along with each study to investigate the influence of the mesh on the results. However, for the generation of complex geometries, *blockMesh* is not enough. It is common in this case to make use of the library *snappyHexMesh*[5], which allows the generation of three-dimensional geometries with simple obstacles (cubic or cylindrical) or directly uploading existing surface geometries in STL format. For the majority of the simulation results presented in this thesis, a refinement of the mesh is performed. The refinement is done near the wall region, where the mesh characteristics can have a huge impact on the results, for example near the micro-pin fin walls. OpenFOAM also allows the use of different tools for the generation of the mesh (e.g. ANSYS, CFX 4, GAMBIT), where the points file can be converted in OpenFOAM format.

As aforementioned, the research presented in this thesis can be divided into two main parts. In the first part, an adiabatic investigation of the two-phase flow behaviour in micro-pin fin geometries has been performed. In the second part, the study has been expanded to include heat transfer. Two different solvers have been employed.

- **Adiabatic study:** interFlow, a solver implemented in the TwoPhaseFlow library for OpenFOAM v1812 released by Scheufler and Roenby [60], has been adopted.

- **Diabatic study:** boilingFoam a solver implemented in OpenFOAM v2106 by Municchi et al. [77], has been employed.

In the forthcoming subsections, concise overviews of these two solvers will be presented, outlining their principal characteristics, governing equations, and computational methods. In Chapter 4, a validation of the two solvers is presented where different benchmark test cases are resolved, to test the performance of the solvers and the phase change model.

---

[4]Mesh generation utility of the OpenFOAM that can be used to generate meshes.

[5]The snappyHexMesh utility generates 3-D meshes containing hexahedra (hex) from triangulated surface geometries in STL format

3.2.2 interFlow

InterFlow is an isothermal incompressible solver without heat transfer, implemented in the TwoPhaseFlow library released by Scheufler and Roenby [60] for OpenFOAM v1812. A single set of governing equations for mass and momentum is formulated and solved over the entire computational domain, as expressed in Eqs. (3.9) and (3.10). The volume fraction is evolved in time by solving the transport equation Eq. (3.30). Only the surface tension effects are considered in the right-hand side of the momentum equation Eq. (3.10). The surface tension force is formulated according to the Continuum Surface Force method [102] and computed as described in Eq. (3.34). As introduced in Sec. 3.1.3, different strategies are available to solve the transport equation of the volume fraction. The solver is based on the geometric VOF isoAdvector [58], where Eq. (3.30) is solved in a two-step procedure. The library comprises two main classes: one for the volume fraction advection scheme and one for the interface reconstruction scheme. The advection scheme base class allows the integration of other advection schemes, such as level-set or phase field methods. This way, the user can select whether to run the solver using the algebraic VOF (interFoam mode) or to use the geometric VOF (isoAdvector mode) with any of the built-in interface reconstruction methods (isoAlpha, isoRDF, plicRDF; see [59]). The accuracy of the computation of the curvature κ has a significant influence in this type of simulation [109], where the surface tension dominates the dynamics of the flow. Numerical errors lead to the generation of spurious velocity fields, whose intensity is higher as the flow is slower because the spurious currents' magnitude is inversely proportional to the capillary number $\text{Ca} = \mu U / \sigma$. The TwoPhaseFlow library provides multiple options to calculate κ based on geometrical approximation:

- RDF (Reconstructed Distance Function) algorithm based on an implementation of the model proposed by [57];

- fitParaboloid estimates the curvature by fitting a local function to the neighbour interface centre provided by the interface reconstruction scheme;

- HF (Height Function Method) is a simple and second-order accurate method for the computation of curvature [110].

Scheufler and Roenby provide further details about the methods [60]. For the work presented in this thesis reported in Ch. 5, a RDF model was selected. The RDF model

shares many similarities with coupled Level Set and Volume of Fluid (CLSVOF) models, the main difference being that, in the RDF, the signed distance function ψ is not found solving a transport equation as in LS methods, but it is constructed geometrically based on the α field [60]. The algorithm, in the first step, calculates the ψ in the cell centre of a narrowband of cells around the interface:

$$\psi_{cc} = \vec{n}_s \cdot (\vec{x}_{cc} - \vec{x}_s) \tag{3.55}$$

where ψ_{cc} denotes the distance from the cell centre ($\vec{x}_{cc}$) to an interface segment ($\vec{x}_s$). The interface normal $\vec{n}_s$ is approximated with a least-squares fit as $\vec{n}_s = \nabla\psi$. The gradient of the signed function is then evaluated as $\vec{n}_\psi = \nabla\psi/|\nabla\psi|$. After that, the curvature is computed by interpolating $\vec{n}_\psi$ from the cell centres to cell faces and applying the Gauss-Green gradient method:

$$\kappa = \nabla \cdot \vec{n}_\psi \rightarrow \kappa_{cc} \approx \frac{1}{V_{cc}} \sum_f \vec{n}_{\psi,f} \cdot \vec{S_f} \tag{3.56}$$

where the V_{cc} is the cell volume and $\vec{S_f}$ is the face area vector pointing out of the cell. The drawback of this method appears in the case of unstructured grids, where inaccuracies may arise due to interpolation errors. These can be reduced by computing κ with the use of a least-squares gradient method. Further details about the algorithm are provided by [60]. A comparison of the different surface tension modules available in the library TwoPhaseFlow with OpenFOAM's interFoam and isoAdvector built-in methods is provided in Sec. 4.1 and in [111].

3.2.3   boilingFoam

BoilingFoam solver is part of a self-developed library in OpenFOAM-v2106 developed by Municchi et al. [77]. The numerical model adopts the Volume Of Fluid method to track the interface between liquid and vapour, using the built-in geometric VOF library based on the work of Roenby et al. [58] and Scheufler and Roenby [59]. The fluid model implemented in this solver is based on the solution of the Navier-Stokes equations, as well as the energy equations for the two immiscible phases as described in Eqs. (3.52),(3.10),(3.53) and transport equation for the volume fraction Eq. (3.54). As for interFlow, the surface tension force is formulated according to the Continuum Surface Force method [102]; however, specific libraries to improve surface tension and

calculate the liquid-vapour mass transfer due to evaporation have been added:

$$\vec{F}_\sigma = \sigma \kappa |\nabla \alpha| \frac{2\rho}{\rho_v + \rho_l} \tag{3.57}$$

The term added in the surface tension formulation represents a density-correction factor that does not change the integral of the surface tension across the interface but redistributes it towards the denser fluid to avoid non-physical accelerations in the region occupied by the lighter fluid [102]. The impact of the density term has been provided in [77]. The interface curvature is calculated based on the gradient of a smoothed volume fraction field $\tilde{\alpha}$.

$$\kappa = \nabla \cdot \left(\frac{\nabla \tilde{\alpha}}{|\nabla \tilde{\alpha}|} \right) \tag{3.58}$$

The smoothed volume fraction field is calculated by interpolating the sharp volume fraction from the cell centres to the face centres and by averaging the resulting α_f field back to cell centres according to:

$$\tilde{\alpha} = \frac{\sum_f \alpha_f S_f}{\sum_f S_f} \tag{3.59}$$

Chapter 4

The OpenFOAM code validation

In this chapter, the results of validation benchmarks for interFlow and boilingFoam are presented[1]. For the adiabatic study (Ch. 5), the performance of the interFlow solver is assessed. This involves a comparative analysis of different surface tension modules available in the TwoPhaseFlow library and the native algebraic VOF method, interFoam, as implemented in OpenFOAM. To evaluate solver accuracy and stability, the classical static bubble benchmark [110] is utilised as a reference, facilitating the quantification of potential issues related to spurious currents and curvature errors. Subsequently, for the diabatic study (Ch. 6 and 7), the validation of the phase change model incorporated into the boilingFoam solver is performed. This validation process encompasses three benchmark problems, each of which has been analytically or semi-analytically solved, serving as benchmarks for evaluating the precision of the evaporation model. The first benchmark problem is the Stefan problem [63], a one-dimensional test case that examines heat transport through the vapour phase to an interface. The second benchmark problem, known as the Sucking interface [63], is also one-dimensional and focuses on the evaporation of a liquid film. Last, the third benchmark problem involves the study of a spherical bubble's growth within a super-heated liquid, commonly referred to in the literature as the Scriven problem [112]. These benchmark cases collectively serve as robust standards for assessing both the performance and accuracy of the phase change model. Further case-specific validation will be presented in Ch. 5 and 6.

---

[1]The results presented in this section served as validation of interFlow and boilingFoam have been published in Magnini et al. [111] and Municchi et al. [77].

4.1 Spurious currents validation

The different surface tension models implemented in the TwoPhaseFlow library [60] were tested on the traditional two-dimensional *static bubble under zero-gravity* problem, which enables quantifying the magnitude of the spurious currents generated by numerical instabilities in the surface tension calculation. The configuration simulated is taken from Gamet et al. [113]. A circular gas bubble (Fluid 1 Air) is initialised inside a continuous liquid phase (Fluid 2 Water). The computational domain has a size of $L \times L = 1\,\mathrm{m}$, the bubble has a radius of $r_{b,0} = 0.4\,\mathrm{m}$. Only a quarter of the two-dimensional geometry is simulated, and a bubble is placed at the correspondence of the coordinate system origin (in the bottom left corner); see Fig. 4.1. The fluid properties are $\rho_l = \rho_g = 1\,\mathrm{kg/m^3}$, $\sigma = 1\,\mathrm{N/m}$, the viscosities of the two phases are the same. During the study, different conditions were examined by varying the viscosity to achieve different Laplace numbers ($\mathrm{La} = \rho\sigma 2r_{b,0}/\mu$). Here are reported the results for the viscosity values of the two fluids to match a Laplace number of $\mathrm{La} = 120$. As the density (ρ) and surface tension (σ) of the two fluids are both taken as a unitary constant value, an increase of the La will correspond to a reduction of the viscosity. Note that the fluid dynamics investigated in this benchmark test case is governed by physics (N-S eqs.) that remains consistent under scaled conditions. Therefore, by maintaining fundamental dimensionless numbers such as Reynolds, Capillary, and Laplace numbers, the physical behaviours observed at the investigated scale can be directly compared to those relevant to the applications of interest, as presented in the following studies in Ch. 5, 6 and 7.

The list of the solvers and algorithm compared during the study are outlined in Tab. 4.1, where gradAlpha holds for $\kappa = \nabla \cdot (\nabla\alpha/|\nabla\alpha|)$, RDF stands for Reconstructed Distance Function, fitParboloid for the parabolic fitting method and HF

VOF Solvers	Category	κ
interFOAM	Algebraic [99]	gradAlpha
isoAdvector	Geometric [58]	gradAlpha
PLIC-RDF	Geometric [59]	RDF
PLIC-RDF	Geometric [60]	fitParaboloid
PLIC-RDF	Geometric [60]	HF

Table 4.1: List of VOF solvers compared in the spurious currents validation study.
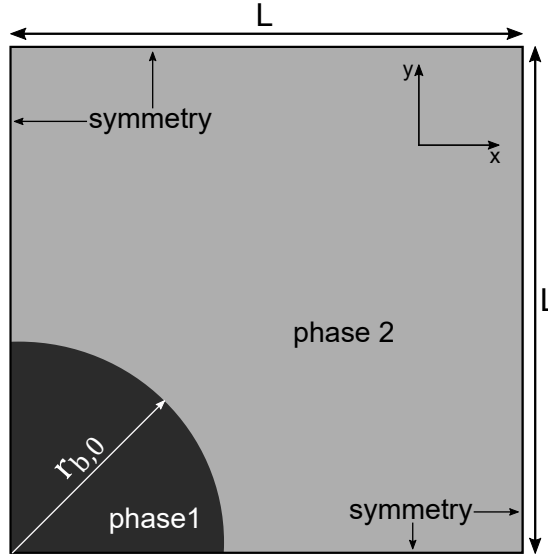
Figure 4.1: Configuration and boundary conditions for 2D static bubble case under zero gravity.

stands for Height Function method. The bubble shape is initialised with the Open-FOAM *setAlphaField* utility to guarantee an accurate initial value for the volume fraction field. Symmetric boundary conditions are applied on all sides of the computational domain. The domain is meshed with a structured mesh, with an identical number of cells along x and y directions. Different mesh resolutions were tested, in the range of 25×25 elements to the finer one with 64×64 elements. The simulation is run with a constant time step of 10^{-3} s and stopped at $t = 71.5$ s, which is large enough to allow an accurate analysis of the spurious currents [114]. The test case is ideally not supposed to generate any velocity field, and the pressure field should follow the Laplace pressure jump at the liquid-gas interface. Therefore, Eq. (3.10) will result in the simple balance between pressure gradient and surface tension force. The spurious currents can appear from numerical instabilities between the discretisation error of those two terms. The numerical imbalance generates a source term in the momentum equation, which causes vortices to appear at the interface (parasitic currents). Figure 4.2 shows a qualitative view of the spurious currents generated by the different solvers/algorithms tested. The snapshots of the velocity vectors are extracted at the end of the simulation for a Laplace number of La = 120 and a grid resolution of 32×32. The velocity vectors are rescaled by a scaling factor to make the

velocity vectors visible, with respect to the isoAdvector results, considering gradAlpha as the method for the calculation of the curvature κ, as is the case that resulted in the higher relative error between the cases tested. Near the interface, represented with a blue line (corresponding to $\alpha = 0.5$), the effects of spurious currents can be detected. To monitor the results of the problem, Popinet [110] defined different time and velocity characteristic scales. Abadie et al. [109] proposed a capillary timescale defined as follows:

$$t_\sigma = \sqrt{\frac{\rho 2 r_{b,0}^3}{\sigma}} \tag{4.1}$$

and a capillary-viscous velocity scale as $u_\sigma = \sigma/\mu$. With these definitions, a non-dimensional Capillary number (Ca) can be defined as follows:

$$Ca_{max} = \frac{\mu U_{max}}{\sigma} = \frac{U_{max}}{u_\sigma} \tag{4.2}$$

The time can be normalised by scaling it with the capillary time scale $t^* = t/t_\sigma$. The temporal evolution of the maximum value of the spurious currents generated (Ca_{max}) is presented in Fig. 4.3 for a Laplace number La $= 120$, on a grid with resolution 32×32, for the different algorithms tested. The results for various grid sizes have not been included in the graph to prevent clutter, but it was observed that the trends in
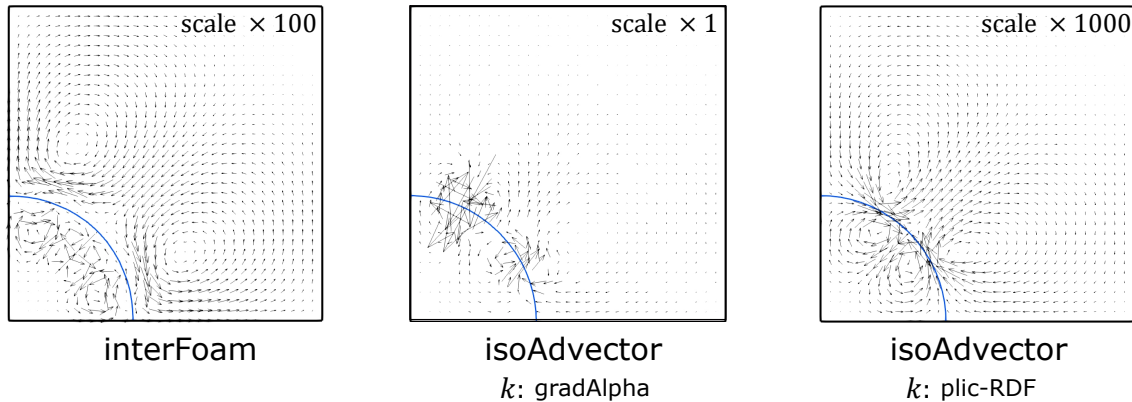
Figure 4.2: Snapshots of velocity for different VOF solvers extracted at the non-dimensional time $t^* = t/t_\sigma = 100$, for the case with Laplace number La $= 120$. The results refer to a grid resolution 32×32. The velocity vectors are rescaled by a factor with respect to isoAdvector results (with κ calculated with gradAlpha). The interface ($\alpha = 0.5$) is highlighted with a blue line.

the results remain consistent. As observed in the velocity vectors, OpenFOAM's built-in isoAdvector solver, which evaluates interface curvature based on volume fraction gradients, exhibits the highest velocity magnitude, reaching nearly 10^{-2}. On the other hand, interFoam outperforms it, generating spurious vectors that are at least two orders of magnitude smaller. This difference can be attributed to the fact that, even though the geometrical methods bring improvements to the evaluation of α in the interfacial cells, the curvature in the solvers is always defined as the gradient of the volume fraction. However, with a piecewise linear reconstruction, the solver sharpens α, making $\nabla\alpha$ sharp, leading to instability. The exclusive use of the plic-RDF method does not yield improved results, except when combined with a different option for calculating κ. When the RDF algorithm is selected, a reduction in spurious currents is observed (10^{-5}). However, the best performances are achieved when the Parabolic reconstruction (10^{-8}) and the Height function (10^{-10}) methods are chosen. It is noteworthy that the spurious velocities remain relatively constant in all solvers and do not converge to machine accuracy, even after a long simulated time. These results suggest that OpenFOAM's parasitic currents are continually sustained due to an imbalance between pressure gradient and surface tension forces. However, it is
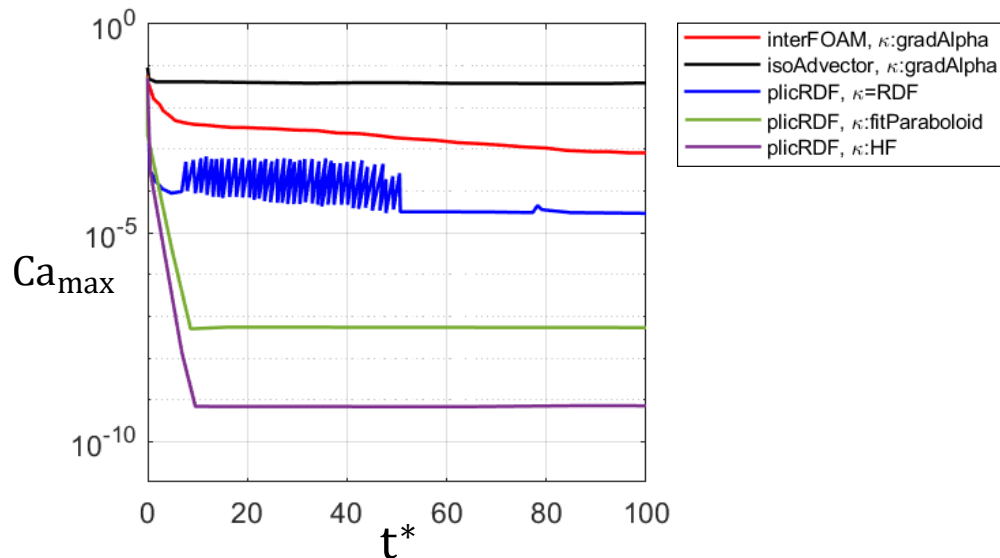
Figure 4.3: Maximum capillary numbers, $\text{Ca}_{\text{max}} = \mu U_{max}/\sigma$, versus non-dimensional time $t^* = t/t_\sigma$, for the different advection and curvature algorithms tested. The results refer to a case with Laplace number La $= 120$ and grid resolution 32×32.

important to note that the parabolic reconstruction requires additional computational resources compared to the other methods, and the Height function method is limited to square/cubic mesh cells. Consequently, these two methods are not considered. The isoAdvector with the plic-RDF method is the chosen algorithm for conducting all simulations reported in Ch. 5.

4.2 Phase change validation

As explained in the introduction of this chapter, the validation of the phase change model incorporated into the boilingFoam solver is carried out and presented in this section. The validation of three benchmark problems is conducted to investigate the accuracy and performance of the phase change model implemented in the solver.

4.2.1 Stefan problem

The Stefan problem has already been studied by Welch and Wilson [63] and Hardt and Wondra [65]. This problem revolves around the evaporation-driven motion of a planar interface caused by the heat transfer from superheated vapour, as illustrated in Fig. 4.4. Within this domain, the boundaries are impermeable, prohibiting any inflow or outflow of fluid. The temperature of the left wall exceeds the saturation temperature T_{sat}, driving the liquid to evaporate, thereby resulting in the movement of the interface. It is assumed that the interface remains flat during the evaporation process, simplifying the problem to one dimension. The interface's motion is solely driven by mass transfer, a valid assumption for phases with equal density; otherwise, an open boundary would be necessary to allow outflow. The temperature boundary conditions at the wall and interface are:

$$T(x = 0, t) = T_w$$
$$T(x = x_i(t), t) = T_{sat}$$

The analytical solution of this problem for the interface motion is given by Hardt and Wondra [65] as follows:

$$x_i(t) = 2\beta\sqrt{k_v t} \tag{4.3}$$

$$T(x, t) = T_w + \frac{T_{sat} - T_w}{erf(\beta)} erf(\frac{x}{2\sqrt{k_v t}}) \tag{4.4}$$

Phase	ρ	λ	c_p	R_g	h_{lv}
	kg/m^3	W/(m K)	J/(kg K)	J/kgK	kJ/kg
gas	0.581	0.025	2030	461.4	2260
liquid	958.4	0.671	4216		

Table 4.2: Thermophysical properties of the water at $T_{sat} = 100°$C.

where $k_v = \lambda_v/(\rho_v c_p)$ is thermal diffusivity, λ_v is the thermal conductivity, c_p is the specific heat capacity and ρ_v is the density of the vapour phase. β is a constant computed from the transcendental equation:

$$\beta \exp(\beta^2) = \frac{c_p(T_w - T_{sat})}{\sqrt{\pi} h_{lv}}$$

Water is considered as working fluid and the vapour and liquid proprieties are listed in Tab. 4.2. The saturation temperature is $T_{sat} = 373.15$ K, the wall is super-heated by 5 K. The one-dimensional domain is long 0.1 mm. The initial position of the interface is set close to the wall $x_i(t = 0) = 0.01$ mm. The domain is meshed with a uniform mesh. Three different mesh resolutions have been tested: 200, 500, and 800. The simulation is performed with a time step size controlled by the Courant number and is stopped at $t = 1$ s. The results of the simulations are presented in Fig. 4.5 in terms of the time evolution of the interface position for the different mesh resolutions tested. The graph also contains the analytical solution results obtained using Eq. (4.3). The simulation results exhibit remarkable agreement with the exact solution, even when using the coarsest mesh.
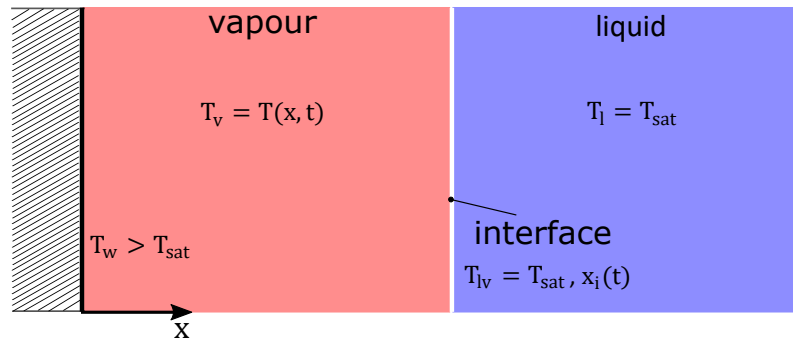
Figure 4.4: Stefan problem configuration.
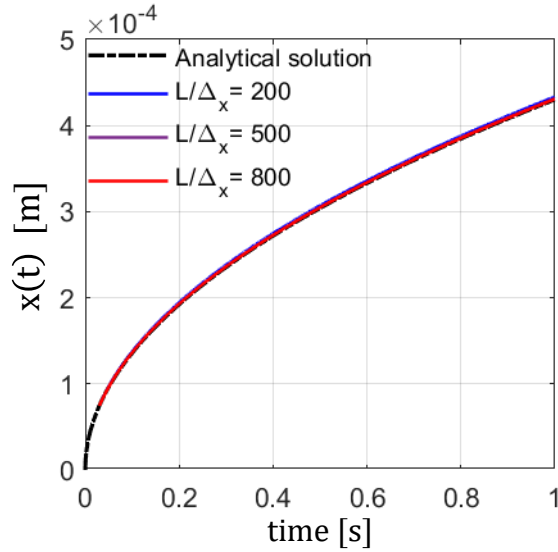
Figure 4.5: Stefan problem results. Interface position as a function of time.

4.2.2 Sucking interface

Another popular validation test is the Sucking Interface problem introduced by Welch and Wilson [63]. Like the Stefan problem, this problem is set up in one dimension. It involves predicting the motion of a planar interface that separates two phases. However, in this scenario, the liquid is superheated, and both the vapour and the wall are at the saturation temperature. The evaporation of the superheated liquid, in this case, leads to a pressure drop, also known as pressure recoil. Also for this problem, an analytical solution for the evaluation of the time-evolution of the interface position exists:

$$x_i(t) = 2\eta\sqrt{k_v t} \tag{4.5}$$

where the constant η can be obtained from the solution of an equation as described in [63]. The incompressibility condition, coupled with the density difference between the two phases, leads to the acceleration of the liquid, pushing it away from the wall. The fluid properties utilised for the simulations are detailed in Tab. 4.2. In the simulation set-up, the liquid is superheated by $5\,\mathrm{K}$. Similar to the Stefan problem, the domain has a length of $0.1\,\mathrm{m}$ and has been discretised with mesh made of 200, 500, and 800 elements. As the initial sharp temperature step at the interface cannot be resolved on a discrete mesh, the initial condition for the simulation is the temperature
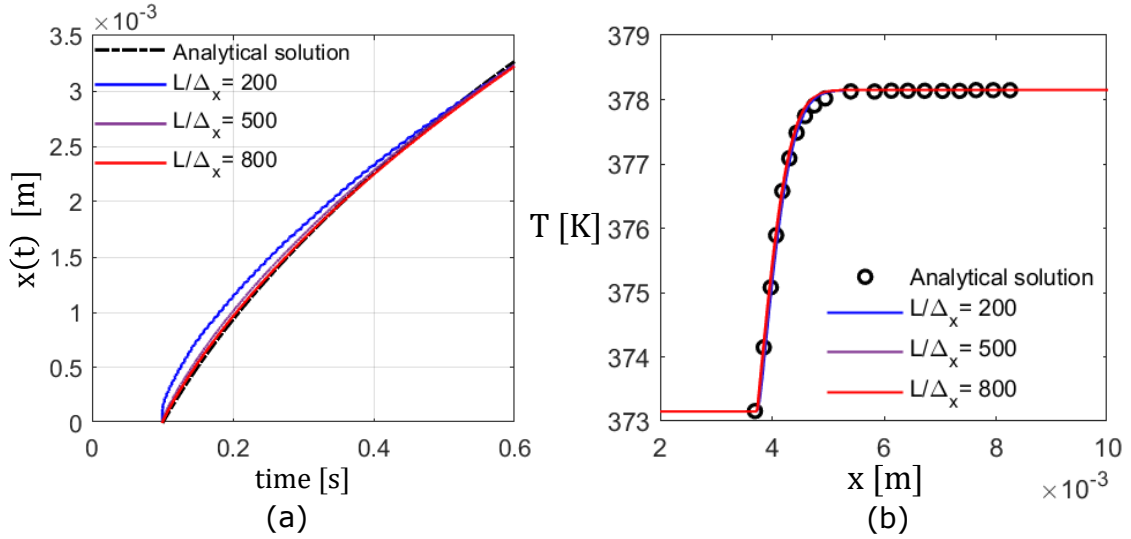
Figure 4.6: Sucking interface problem results. (a) Interface position as a function of time. (b) Temperature profile extracted at the end of the simulation, $t = 0.6\,\text{s}$.

profile and interface position at $t = 0.1\,\text{s}$ extracted from the analytical solution. The evolution of the interface position with time is shown in Fig. 4.6(a). The simulation results show a strong alignment with the analytical solution, except for the simulation conducted with the coarsest mesh ($\Delta x = 0.05\,\text{mm}$), where notable discrepancies become apparent, especially during the initial moments of the simulation. For further insight, the interface position and its absolute error relative to the analytical solution at $t = 0.6\,\text{s}$ are detailed in Tab. 4.3. As the evaporation process takes place, the initial sharp temperature step at the liquid-vapour interface becomes more and more smooth, which is due to thermal diffusion. The smoothing of the temperature profile is illustrated in Fig.4.6(b). Based on the results, it is reasonable to conclude that,

	interface position [mm]	error %
analytical solution	0.003255	-
case 1 ($\Delta x = 0.05\,\text{mm}$)	0.003249	0.5
case 2 ($\Delta x = 0.02\,\text{mm}$)	0.003253	0.04
case 3 ($\Delta x = 0.0125\,\text{mm}$)	0.003255	0

Table 4.3: Sucking interface problem results. Interface position and its absolute error extracted at $t = 0.6\,s$.

for this benchmark problem, the solver consistently predicts the analytical solution accurately. This remarkable accuracy is evident starting from case 2 ($\Delta x = 0.02\,\text{mm}$), where the error between the simulation and the exact solution remains below 0.05%.

4.2.3   Growth of a spherical bubble in a superheated liquid

The third benchmark test case involves the growth of a spherical bubble in superheated liquid. When a bubble nucleates in a pool of superheated liquid where the liquid temperature is greater than the saturation temperature ($T_l = T_\infty > T_{sat}$), and it is not influenced by a wall, the growth of the bubble can be divided into two main stages:

1. **Initial growth stage:** During this stage, the bubble's growth is primarily controlled by surface tension and the inertia effects of the surrounding liquid being pushed aside. The bubble radius follows a linear trend as time elapses.

2. **Second growth stage:** As the bubble continues to grow, it eventually reaches a certain size where the vapour temperature and pressure decrease $T_v \approx T_{sat}(p_l)$ and $p_v \approx p_l$. This marks the beginning of the second growth stage, where the growth rate is controlled by the transfer of latent heat from the superheated liquid to the bubble interface. During this stage, the bubble radius follows an approximately square root of time ($\approx t^{1/2}$) law, as described by Carey [94].

Scriven [112] has derived an analytical solution for this phase, which is employed to predict the growth rate of a bubble in superheated liquid. Similar to the Sucking Interface problem, this analytical solution allows for the evaluation of initial conditions for simulations and the validation of results. The flow domain is represented using a two-dimensional axisymmetric geometry. OpenFOAM's *wedge* utility is employed to simulate a square box with a side length of $1 \times 1\,\text{mm}$. Only one-quarter of the domain is simulated, and symmetric boundary conditions are applied at the sides of the domain. A spherical vapour bubble with an initial radius of $r_{b,0} = 50\,\mu\text{m}$ and temperature $T_v = 373.15\,\text{K}$ is initialised at the centre of the coordinated system, by manipulating the volume fraction and temperature fields[2]. The bubble is placed in a pool of superheated water at atmospheric pressure $p_l = 1\,\text{atm}$ and temperature

---

[2]Using setFields dictionary in OpenFOAM.

$T_l = 374.15$ K. An initial thin thermal boundary layer is imposed around the bubble. The temperature profile of the liquid is extracted using the analytical solution derived by Scriven [112], at the time when the predicted bubble radius is $50\,\mu$m. The analytical evolution of the bubble radius is quite similar to the Stefan problem and is given as follows:

$$R(t) = 2\beta_s \sqrt{k_l t} \qquad (4.6)$$

where β_s is a constant obtained from the solution of a transcendental equation [112], and k_l is the liquid thermal diffusivity. Once the temporal evolution and the growth constant of bubble radius are known, the radial temperature distribution in the liquid can be evaluated at any time with the following considerations: for $r \leq R$, the initial temperature is defined as $T = T_{sat}$, for $r > R$. The initial thermal boundary layer thickness is about $16\,\mu$m. The simulations were run until $t = 0.0047$ s, where the bubble is nearly 4 times its initial size. The vapour and liquid proprieties are listed in Tab. 4.2. During the simulation, the surface tension is set to $\sigma = 0$, thus allowing to test only the influence of the phase-change model. The numerical solver boilingFoam described in the previous chapter can run in both algebraic and geometric VOF modes, but here, only the results using the *isoAdvector* mode (geometric
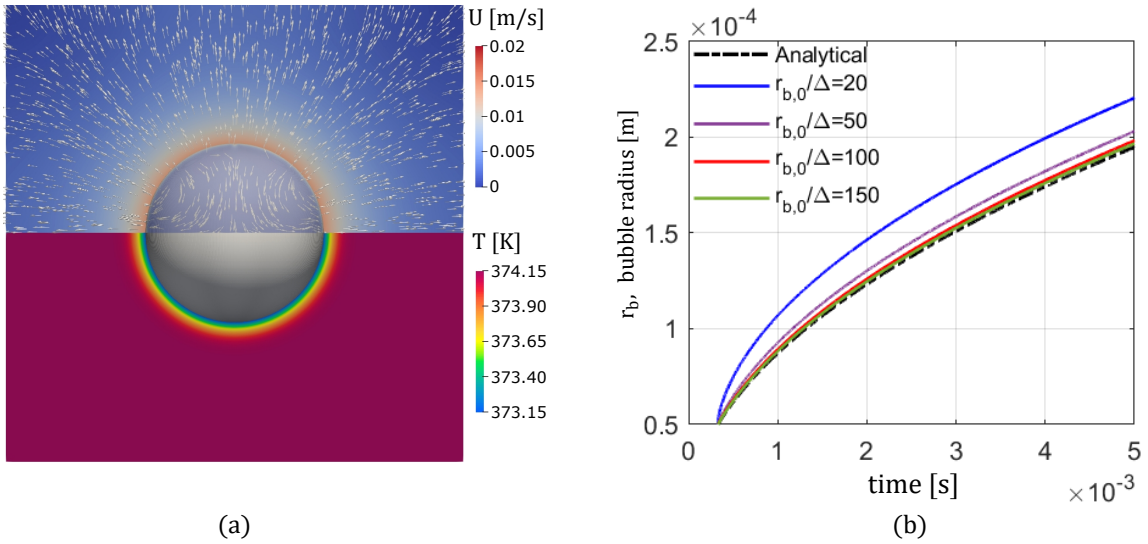
Figure 4.7: Growth of a bubble in a superheated liquid. (a) Snapshot of the bubble, velocity (top half) and temperature (bottom half) contours, at the end of the simulation for $r_{b,0}/\Delta = 100$. (b) Bubble radius (r_b) as a function of time. Δ indicates the cell size.

VOF) are presented. A comparison between the two modes is included in the work of Municchi et al. [77]. The domain is discretised with a structured mesh composed of orthogonal and uniform hexahedrons, where each cell has a side length of Δ. The parameter $r_{b,0}/\Delta$ represents the number of cells per initial bubble radius, and four different meshes were tested with $r_{b,0}/\Delta = 20, 50, 100$ and 150. In Fig. 4.7(a), a snapshot of the bubble growth dynamics is presented. It includes velocity field contours (top half) and temperature contours (bottom half) at the end of the simulation for the case of $r_{b,0}/\Delta = 100$. The bubble tends to maintain a spherical shape throughout its growth, and the thermal boundary layer surrounding the bubble is clearly visible. The velocity of the liquid points outwards the bubble, with maxima detected at the liquid-vapour interface. The growth of the bubble radius (r_b) is shown in Fig. 4.7(b) as a function of time. The bubble radius is evaluated as the equivalent radius corresponding to the instantaneous volume of the bubble ($r_b = \sqrt[3]{3V/4\pi}$, where V is the bubble volume). As a reference, the graph also contains results from the analytical solution. The evolution of the bubble radius is accurately predicted by the numerical model. The results converge towards the analytical solution as the mesh becomes finer. For coarser meshes, there is a faster growth rate during the initial stages, which can be attributed to the poor resolution of the initial thermal boundary layer surrounding the bubble. The evaporation rate is determined based on the temperatures at the centroids of the first few liquid cells (2-3 cells) near the interface. At the beginning of the simulation, when the mesh is coarse, the selected cells are quite far from the interface in a region where high temperatures are present, leading to higher evaporation rates. The agreement with the analytical solution becomes satisfactory when $r_{b,0}/\Delta = 100$, with an over-prediction on the growth rate of less than 2%; the solutions become almost identical when $r_{b,0}/\Delta = 150$. As mentioned earlier, the solver in interFoam mode has also been tested and provided results closer to the exact solution for coarser meshes but identical results for higher resolutions. It is important to note that simulations run with algebraic VOF were faster than those with the geometric mode, which can be explained by the additional reconstruction steps required by isoAdvector. For the finest mesh tested, the computational domain consisted of 2,560,000 cells ($r_{b,0}/\Delta = 150$); the simulation was performed using a workstation with 32 cores and the computational time required was approximately 1500 CPU hours.

A few tests were also performed with a surface tension value of $\sigma = 0.072\,\text{N/m}$ to

assess the influence of the solver's performance on the effects of surface tension. The spurious currents generated at the liquid-vapour interface were small enough not to affect the solution, resulting in a similar bubble growth speed. The results are not reported to avoid overcrowding the results plot.

4.3   Conclusion

This chapter presents the results of validation benchmarks for the two solvers adopted for the subsequent investigations in this thesis. The solver interFlow, employed in the adiabatic study in Ch. 5, has been tested to assess the accuracy and stability of surface tension models concerning the generation of spurious currents. The results demonstrate that, in OpenFOAM, parasitic currents are continually sustained. However, the plicRDF method, which utilises the RDF algorithm for curvature evaluation, shows the best compromise in terms of accuracy and computational cost.

Following the validation of the solver boilingFoam used in the diabatic studies in Ch. 6 and 7, the phase-change model underwent validation through three benchmark problems. The simulation results show significant agreement with the exact solutions of the problems, even with a coarse mesh, confirming the robustness and precision of the phase-change model implemented in the solver. Additionally, the effects of surface tension were examined together with phase-change; the spurious currents generated at the interface were sufficiently small, ensuring no impact on the solution and resulted in similar bubble growth rates. In conclusion, it is reasonable to state that both solvers perform adequately under all conditions of interest for subsequent analyses and are sufficient to confirm the accuracy of the numerical model. Nevertheless, further case-specific validations will be introduced in upcoming investigation.

Chapter 5

Isothermal dynamics of long bubbles translating in micro-pin fin arrays

This chapter is dedicated to the investigation of the dynamics of elongated gas bubbles and thin films as they propagate through arrays of inline cylindrical pins of circular shape in a cross-flow environment. The primary goal of this study is to comprehend how bubbles propagate in these complex geometries under typical conditions for heat exchangers (although in an isothermal case). The objective is to understand the morphology and size of the liquid film that forms on the walls. This understanding will be instrumental for the subsequent analysis of heat transfer in Ch. 6 and 7. This research covers a range of capillary and Reynolds numbers, which are pertinent to applications in heat transfer and porous media flow. Various pitches of the cylinders and initial bubble lengths are considered[1]. To perform this study, three-dimensional numerical simulations of the two-phase flow are performed using the interFlow solver. Systematic analyses are carried out across a range of capillary numbers (Ca $= 0.04 - 1$), Reynolds numbers (Re $= 1 - 1000$), streamwise pitches of the cylinders ($s_x = 0.125R - 2R$, with R representing the radius of the pin-fins), and initial bubble lengths ($L_b = 2.5R - 12R$). The simulations reveal that as bubbles propagate through arrays of pin-fins, they tend to partially coat the cylinders and expand laterally within the gap between adjacent cylinders. It is noteworthy that

---

[1]The results presented in this chapter have been published by El Mellas et al. [115]

the liquid film formed on the cylinders is considerably thinner in comparison to what is observed in straight channels with similar wall thickness and cross-stream grap. As the streamwise distance between the cylinders decreases, the flow configuration approaches that of a straight channel. Conversely, larger distances lead to excessive lateral expansion of the bubble in the cross-stream direction, with an eventual arrest when $s_x > 2R$. Inertial effects play a significant role in shaping the dynamics of the bubbles when $\mathrm{Re} > 500$, giving rise to time-dependent patterns that result in bubble fragmentation and the formation of substantially thicker liquid films.

Solver option

The solver interFlow has been adopted for this study, implemented in OpenFOAM v.1812 [60]. These simulations rely on a geometric Volume of Fluid method to capture the interface dynamics. OpenFOAM's PIMPLE algorithm, which is a combination of PISO (Pressure Implicit with Splitting of Operator) [116] and SIMPLE (Semi-implicit Method for Pressure-Linked Equations) [117] is used for the pressure-velocity coupling, with 3 correction steps (nCorrectors). The different discretisation methods selected for the various terms of the governing equation solved are reported in Tab. 5.1. Transient simulations represent the fluid flow examined in this study and, as a consequence, require an optimal resolution (size mesh and time step) to capture the relevant physical process. Therefore, the time step size is controlled and limited using the time control entry *adjustTimeStep*. This allows OpenFOAM to change the time step according to the maximum Courant number (Co) every time step. The Courant number is an indicator of the propagation speed of information

Term		Scheme
Time derivative	$\partial\phi/\partial t$	Crack-Nicolson (0.9)
Gradient	$\nabla\phi$	Gauss linear
Divergence	$\nabla\cdot(\rho\vec{u}\,\vec{u})$	Gauss limitedLinearV (1)
Divergence	$\nabla\cdot(\alpha\vec{u})$	Gauss vanLeer
Divergence	$\nabla\cdot\mu[\nabla\vec{u} + (\nabla\vec{u})^T]$	Gauss linear
Interpolation		Linear
Surf-norm Grad		Corrected

Table 5.1: Discretisation methods for the solver interFlow.

Field	Solver	smooter/precond.	Tolerance
α	smoothSolver	symGaussSeidel	10^{-8}
p	GAMG	DICGaussSeidel	10^{-8}
u	smoothSolver	symGaussSeidel	10^{-8}
momentumPredictor	yes		
nCorrectors	3		

Table 5.2: Solution methods for the solver interFlow.

on the numerical mesh:

$$\text{Co} = \frac{u\Delta t}{\Delta x} \tag{5.1}$$

where Δx is the cell size and Δt is the time step. In particular, for these types of simulations, the Co is restricted to very low numbers (typically not higher than 0.25). The different solution methods for the flow equations are reported in Tab. 5.2, together with residual thresholds.

5.1 Validation

The present numerical framework has already been tested in Chap. 4 and also in the work of Magnini et al. [111] with the simulation of long gas bubbles propagating in straight rectangular channels of different aspect-ratio, and comparison against benchmark liquid film thickness data from the literature. No literature data is available for the isothermal flow of long bubbles between pin fin arrays, and thus, we have performed new validation tests by considering a confined, elongated gas bubble travelling steadily into straight 2D and circular (axisymmetric) channels. Even though the flow configuration differs from the flow past cylindrical obstacles, we expect that the validation of the numerical framework over a broad range of geometrical configurations is sufficient to verify the accuracy of the numerical model. Furthermore, the dynamics of long bubbles in 2D configurations (flow between parallel plates or within circular pipes) is well established and will serve as a comparison for the simulations of flow past pin-fins presented in the next sections.

The flow configuration analysed in this validation is exemplified in Fig. 5.1(a), which provides a snapshot of a long bubble passing through a 2D straight channel, at steady-state. We consider the benchmark Bretherton problem [21], where a long

gas bubble propagates in a straight channel under the effect of a net liquid inflow. Owing to the competition of viscous and capillary forces, the bubble traps a thin liquid film against the wall. The main parameter describing the profile and thickness of this film is the capillary number, which compares viscous and capillary effects, $\mathrm{Ca} = \mu_l U / \sigma$, with U being either the bubble U_b or the cross-sectional average liquid velocity U_l. Inertial forces may have a role on the bubble dynamics [30], and these are described by the Reynolds number $\mathrm{Re} = 2 \rho_l U R / \mu_l$, with R being the channel radius (pipe flow) or semi-height (2D flow). Gravitational effects are neglected in this study, as we are interested in microfluidic conditions where the Bond number (Bo) is much
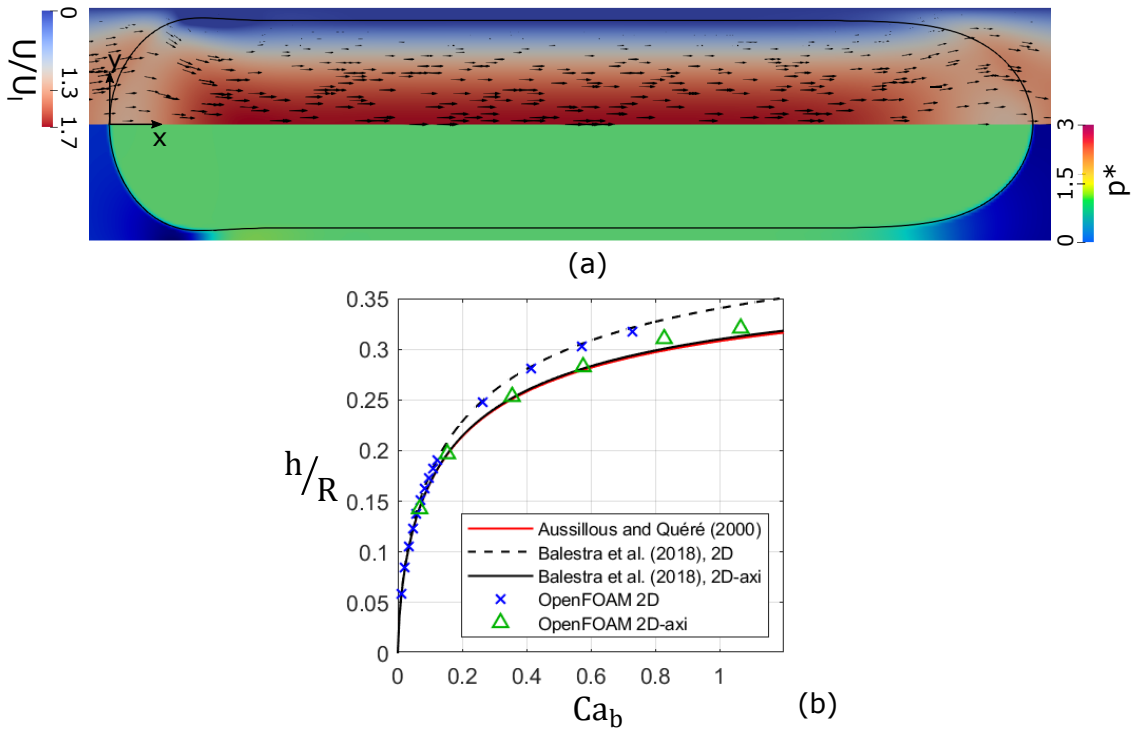
Figure 5.1: Results for the validation case of a long bubble translating in a 2D and 2D axisymmetric channel. (a) Snapshot of a confined elongated bubble passing through a 2D straight channel, considering the results for capillary number $\mathrm{Ca_l} = 0.03$. In the image, pressure (bottom half) and velocity fields (top half) are displayed. The velocity field is rescaled by the average liquid speed (U_l); the pressure field is rescaled by the capillary pressure $p_{ref} = \sigma / R$. (b) Dimensionless liquid film thickness (h/R) against bubble capillary number. As a reference, the graph includes also the film thickness predictions obtained using the correlations of [27] for circular channels, and of Balestra et al. [118] for both 2D planar and 2D axisymmetric cases.

smaller than unity. In the numerical model, we consider both two-dimensional and axisymmetric ducts of semi-height (or radius) R and length $40R$, which is sufficient for the bubble to reach steady conditions. At the inlet, a fully-developed laminar profile is imposed to the fluid velocity, together with a null pressure gradient. No-slip is applied to the walls. At the outlet, a constant pressure is imposed, together with a null velocity gradient. As initial conditions, a long gas bubble with circular ends is set near the channel inlet; the bubble is long enough such that a flat film region establishes between the front and rear menisci. The liquid-to-gas density and viscosity ratios are set to $\rho_l/\rho_g = 1000$ and $\mu_l/\mu_g = 100$, to represent typical air-water cases or refrigerants used in two-phase cooling applications [44]. For this validation study, we have tested a wide range of liquid capillary numbers $Ca_l = \mu_l U_l/\sigma = 0.01 - 0.5$, which resulted into a range of bubble capillary numbers $Ca_b = \mu_l U_b/\sigma = 0.0105 - 1$, to cover the range investigated in the next sections for flow past pin-fins. The Reynolds number of the flow is set to a small reference number, $Re_l = 1$, for which inertial effects are expected to be small [119]. This enables comparison of results with literature data for the visco-capillary regime [27]. To achieve correct liquid film thickness values in the simulation, the computational mesh must be sufficiently fine to fully discretise the flow in the thin liquid film, with the smallest capillary number tested posing the most severe conditions. Using Aussillous and Quéré [27] correlation, we estimate a film thickness of about $h/R \approx 0.05$ for $Ca_l = 0.01$. Accordingly, we use a structured orthogonal mesh with 60 square cells in the radial direction, which are gradually refined in a boundary layer of thickness $0.05R$ near the wall, made of 14 cells with a minimum thickness of about $0.001R$. This guarantees that there are always more than 10 cells discretising the film region, in agreement with a previous study under similar conditions [120]. Overall, the computational domain includes nearly 200,000 cells and all the simulations were performed using a workstation. With 16 cores, the computational time required for each simulation to achieve steady-state was about 16 CPU hours. The total CPU (Central Processing Unit) time consumed by the simulation is equivalent to 16 hours of computation on a single CPU core.

Figure 5.1(a) illustrates a snapshot of bubble profile, velocity and pressure contours, at steady-state for $Ca_l = 0.03$ and a two-dimensional non-axisymmetric configuration. It can be seen that a thin liquid film is present next to the wall, where the flow is stagnant. This is expected, because there is no curvature gradient in the bubble profile that can drive flow by capillarity. Pressure is uniform within the bubble and

it is interesting to note that, while a pressure jump exists across the interface at the bubble nose and rear, no pressure change occurs across the interface in the film region. This can be explained by the fact that, in the two-dimensional geometry, there is only one interface curvature (in the $x-y$ plane), and thus where the film is flat the total curvature is zero and no Laplace pressure jump occurs. The situation differs in the axisymmetric case, because even though the interface profile appears flat along the film in the $x-y$ plane, there is a second curvature of the bubble in the cross-stream plane which establishes a nonzero pressure jump between gas and liquid in the film region. The liquid film thicknesses measured in the simulations for both 2D and 2D axisymmetric cases are reported in Fig. 5.1(b) as a function of the bubble capillary number. The graph includes also film thickness predictions obtained using the correlation of [27] for circular channels, $h/R = 1.34\text{Ca}^{2/3}/(1 + 3.35\text{Ca}^{2/3})$, and the correlations developed by Balestra et al. [118] for both planar and axisymmetric cases. Our numerical model is always very close to the reference data, with the largest deviation of about 5% as $\text{Ca}_\text{b} \to 1$ in the circular channel case. This can be ascribed to the appearance of inertial effects in the bubble dynamics as the Weber number approaches unity [119], and to uncertainty in the [27] correlation in this range of values; for example, if the film thickness correlation of [30] is utilised, the deviation with the simulation results in this range falls below 5%.

5.2   Model setup and mesh convergence analysis

This section introduces the model geometry and mesh for the study of the flow of long bubbles translating between pin fin arrays. We consider the flow of an isolated long gas bubble that travels through the channel formed by two arrays of in-line cylindrical pin-fins of circular cross-section in cross-flow, under the effect of a liquid flow parallel to the arrays; Fig. 5.2 provides a schematic representation of the geometry and flow configuration. In the numerical model, the flow domain is represented with a three-dimensional geometry, as illustrated in Fig. 5.2(a). To describe the flow, a Cartesian reference frame is adopted, where x expresses the streamwise coordinate, y is the width-wise cross-stream coordinate and z is the height-wise cross-stream coordinate, parallel to the cylinders axes. The reference frame is centred half-way along the domain height and width, so that $z = 0$ identifies the domain's horizontal centreplane and $y = 0$ a vertical centreplane. The radius of the circular pin-fins R is kept con-

stant throughout the study; for convenience, all other dimensions are rescaled with R. Figure 5.2(b) provide a schematic representation of the geometry on a horizontal centreplane ($z = 0$). The flow domain has a length of $L = 60R$. The domain cross-section has a width $W = 8R$ and height $H = 2R$, so that the cylinders' height and diameter coincide. Two arrays of in-line cylindrical pin-fins, illustrated as full white circles in Fig. 5.2(b), are positioned along the x direction, symmetric with respect to the vertical centreplane $y = 0$. The cross-stream pitch of the cylinders is maintained constant in this work, $d_y = 4R$, so that the cross-stream gap between the cylinders identifies a square channel of width $s_y = d_y - 2R = 2R$. The choice of maintaining s_y fixed and equal to $2R$ enables us to reduce the number of geometrical variables. The streamwise pitch of the cylinders is indicated as d_x, with the corresponding gap being $s_x = d_x - 2R$, and this will be changed during the study, with the baseline configuration being $s_x = 0.5R$. As boundary conditions, a liquid-only flow of uniform velocity magnitude is imposed at the domain inlet, where the streamwise coordinate origin $x = 0$ is set, together with a zero-gradient pressure condition. Due to the symmetry of the flow, only one-quarter of the domain cross-section is resolved and symmetry
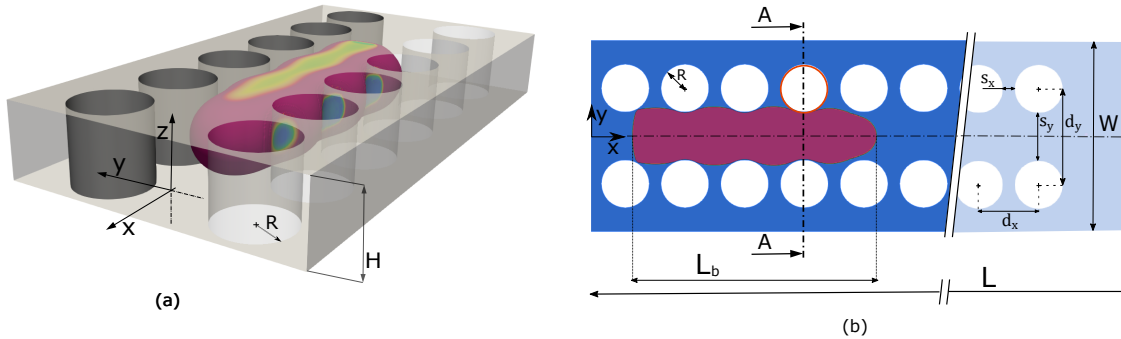
Figure 5.2: Illustration of the flow configuration under study. An elongated bubble propagates through the gap formed by two arrays of in-line cylindrical pins. The rainbow-tinted contour identifies the bubble surface at a given time instant, coloured by the non-dimensional value of the interface curvature $\kappa^* = \kappa R$. (b) Illustration of the computational domain on a horizontal centreline plane ($z = 0$). The domain width and length are indicated with W and L, respectively. R denotes the radius of the cylindrical pins. The flow is from left to right. The streamwise (along x) and cross-stream (along y) distance between the cylinder centres are indicated as d_x and d_y. The streamwise and cross-stream gap between the pins are denoted as s_x and s_y, with $s_x = d_x - 2R$ and $s_y = d_y - 2R$. The red area identifies the bubble at a given time instant, and its length is denoted as L_b.

boundary conditions are adopted at the sides of the domain margins, corresponding to planes $y = 0$ and $y = W/2$, and on the horizontal centreplane $z = 0$. On the top $(z = H/2)$ domain boundary, a no-slip condition is imposed. At the outlet boundary $(x = L)$, pressure is set to a zero reference value together with a zero-gradient velocity condition. On the pin fin walls, a no-slip condition is applied. Since the lubricating film trapped between the bubble and cylinders is always discretised with the mesh, no contact line forms and thus the contact angle boundary condition is not necessary. As initial condition, a long gas bubble of initial length L_b is patched along the domain centre, with the shape of a cylinder (of radius $0.9R$) with spherical rounded ends; the initial length of the bubble will be varied during the study to investigate its impact on the flow dynamics, with the baseline configuration being $L_b = 12R$. Note that this flow model, i.e. long gas bubbles travelling through arrays of pin-fins, applies well to boiling in micro-pin fin evaporators where long vapour bubbles are generated upon nucleation within the superheated fluid [42], but can also be a model for the dynamics of carbon dioxide bubbles propagating through porous subsurface reservoirs in geological CO_2 sequestration [88].

At the onset, the bubble propagates downstream and its shape and velocity evolve

(a)   (b)
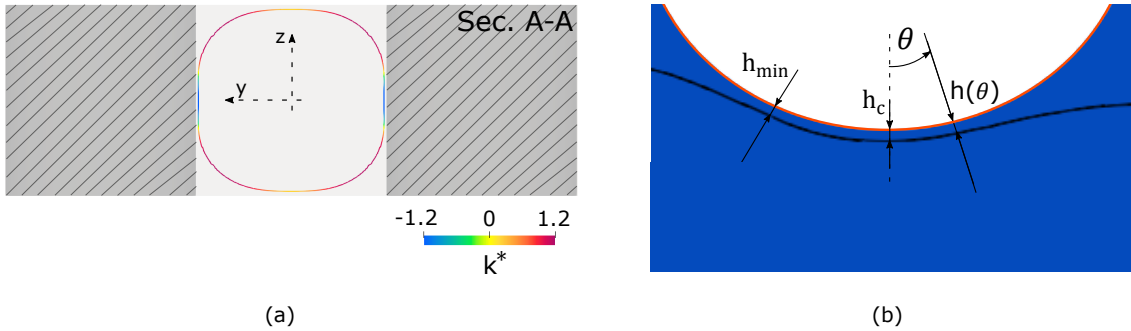
Figure 5.3: (a) Cross-section of the bubble extracted on Section A-A in Fig. 5.2(b), coloured by the value of the nondimensional interface curvature. The colour legend in (a) applies also to Fig. 5.2(a). (b) Close-up view of the liquid film profile on the horizontal centreline plane $(z = 0)$, near the cylinder coloured in red in (b). The liquid film thickness is measured on a local reference frame centred on the cylinder centre, and $h(\theta)$ denotes the film thickness measured along the radial direction at an angle θ from the y axis. h_c and h_{min} denote, respectively, the film thickness at $\theta = 0$ and its minimum value around the cylinder. The images above refer to a case run with $Ca_l = 0.04$, $Re_l = 1$, $s_x = 0.5R$, and initial bubble length $L_b = 12R$.

towards a steady-periodic configuration; the domain length was chosen sufficiently long in order for such regime to be achieved by the propagating bubble. Figure 5.3(a) and (b) show examples of the liquid film morphology identified during the bubble transit and introduce the notation that will be later used to report liquid film thickness measurements. Surface tension forces redistribute the liquid surrounding the bubble into thin films covering the cylinders and top/bottom channel walls, similarly to what observed in square channels [121], while static menisci are formed in the gap between two consecutive cylinders. Figure 5.3(b) shows a close-up view of the liquid film profile on a horizontal centreplane ($z = 0$), near the cylinder coloured in red in (b), with the black solid line identifying the liquid-gas interface. For convenience, the thickness of this film is described as the radial distance between the cylinder surface and the liquid-gas interface, measured on a local reference frame centred with the cylinder. For each cylinder, different film thickness parameters will be extracted and presented in the next sections: a local film thickness $h(\theta)$, which varies in the circumferential direction with the reference $\theta = 0$ coinciding with the $y-$axis; a film thickness at the cylinder centre, $h(\theta = 0) = h_c$; a circumferentially minimum film thickness value h_{min}, which does not necessarily occur at $\theta = 0$.

The aim of this work is to investigate the dynamics of long gas bubbles travelling across pin fin arrays by systematically varying capillary and Reynolds numbers, streamwise pitch of cylinders and bubble length. Capillary and Reynolds numbers based on the bubble velocity are defined as $\mathrm{Ca_b} = \mu_l U_b/\sigma$ and $\mathrm{Re_b} = 2\rho_l U_b R/\mu_l$, where R corresponds to the pin fin radius which in the present setup coincides with the half-height and half-width of the channel left between the in-line arrays of pin-fins. The corresponding groups based on the liquid speed are evaluated by considering as U_l the average liquid velocity in the channel bounded by the pin fin arrays, which is twice the average liquid speed set at the domain inlet due to the cross-section reduction induced by the cylinders. The range of conditions investigated in this study has been chosen to be relevant to two-phase flow in micro-pin fin heat exchangers [44], where $\mathrm{Ca} = 10^{-3} - 10^{-1}$ and $\mathrm{Re} = 10 - 10^2$, and flow in porous media [122, 83], where the capillary number may span several orders of magnitudes ($\mathrm{Ca} = 10^{-6} - 10^{-1}$) while $\mathrm{Re} \ll 1$. The capillary and Reynolds numbers, streamwise pitch of cylinders and bubble length will be varied independently in this study, within the following ranges: $\mathrm{Ca_l} = 0.04 - 1$, $\mathrm{Re_l} = 1 - 1000$, $s_x = 0.125R - 2R$, and $L_b = 2.5R - 12R$.

Smaller values of Ca_l are disregarded due to the computational cost of resolving very thin liquid films. Liquid-to-gas density and viscosity ratios in this work are fixed to 1000 and 100, respectively, which are representative of air-water combinations or two-phase flow of refrigerants.

OpenFOAM solves the fluid flow equations in dimensional form and thus requires input parameters in dimensional units. All our simulation cases are parameterised using hard-coded values of $R = 1\,\mathrm{m}$ for the pin fin radius, $\rho_l = 1\,\mathrm{kg/m^3}$ for the liquid density, and $U_l = 2\,\mathrm{m/s}$ as the average velocity of the liquid between the pin fin arrays; since the pin fin arrays occupy half of the domain cross-section, the velocity boundary condition set at the domain inlet is $1\,\mathrm{m/s}$. The bubble density is set to $\rho_b = 0.001\,\mathrm{kg/m^3}$ to achieve a liquid-to-gas density ratio of 1000. The liquid dynamic viscosity depends on the liquid Reynolds number of the simulation, $\mu_l = 2\rho_l U_l R/\mathrm{Re_l}$. The surface tension coefficient is calculated from the liquid capillary number, $\sigma = \mu_l U_l/\mathrm{Ca_l}$. For example, the case run with $\mathrm{Ca_l} = 0.04$ and $\mathrm{Re_l} = 1000$ was obtained by using $\mu_l = 0.004\,\mathrm{kg/(m\,s)}$ and $\sigma = 0.2\,\mathrm{N/m}$. Last, the bubble dynamic viscosity is calculated from μ_l to achieve a liquid-to-gas dynamic viscosity ratio of 100, thus $\mu_b = 0.00004\,\mathrm{kg/(m\,s)}$ for the case indicated above. The typical end time of the simulation in these units is of about 10 seconds.

The decision to conduct investigations at a characteristic scale of meters, larger than the micro-scale target applications, is both strategic and well-founded. The fluid dynamics studied in this work is governed by the Navier-Stokes equations, which remain consistent under scaled conditions. By maintaining key dimensionless numbers (such as Reynolds, Capillary, and Weber numbers), it is observed that the physical behaviours at the meter scale can be directly compared to those at the micro-scale. This scaling ensures that the fundamental dynamics observed in the simulations effectively represent those at the micro-scale, allowing for reliable extrapolation of the findings. Furthermore, the use of larger scales is shown to significantly reduce the computational cost of the simulations and simplify the calculations, as everything is scaled by the radius of the pins. Through the analysis at this scale, an extensive parametric study was able to be conducted more efficiently and across a wider range of conditions, which is often impractical at the micro-scale due to computational constraints. Additionally, validating and testing the numerical models are more achievable with this strategy.

Our interest is to fully resolve the flow in the thin liquid film trapped between the

pin-fins and the long bubble, and therefore the computational mesh must be suffi-
ciently fine to discretise this film with an adequate number of cells under all conditions
simulated. The domain is meshed in three successive steps, using OpenFOAM's li-
brary *snappyHexMesh*. First, the domain block without pin-fins is discretised with
a uniform structured mesh made of cubes of side Δ, with the parameter R/Δ indi-
cating the number of cells per radius of the cylinders. Then, the mesh is recursively
refined n times near the cylinders surface, by splitting a cube into eight equal smaller
cubes for each refinement cycle. We identify as $\Delta_{min} = \Delta/2^n$ the size of the smallest
cubic cells obtained after n refinements, with the number of smallest cubic cells per
cylinder radius quantified as R/Δ_{min}. Finally, a thin boundary layer composed of 5
cells and overall thickness $2\Delta_{min}$ is generated over the surface of the cylinders, where
cells are progressively refined radially towards the cylinders surface, from Δ_{min} on
the outer edge of this layer down to an absolute minimum cell thickness of $\Delta_{min}/2^4$
on the cylinder surface. A representative image of the grid arrangement for a mesh
built with $R/\Delta = 40$ and $n = 2$ is shown in Fig. 5.4(a).

The mesh analysis was performed for a base case run with $Ca_l = 0.04$, $Re_l = 1$,
$s_x = 0.5R$, and $L_b = 12R$. This has the smallest capillary number of the range that
will be investigated, and thus represents the most severe case due to the very thin
liquid film expected. Four different computational meshes were created, by fixing the
background mesh size to $R/\Delta = 40$ and applying four different levels of refinement
near the cylinders, $n = 0, 1, 2, 3$. Further details for these four meshes are provided
in Tab. 5.3.

Figure 5.4(b) displays the results of the mesh convergence analysis, presented
in terms of the film thickness measured around cylinder number 12 from the domain
inlet. We consider the film thickness at the cylinder centre h_c measured on a horizontal
centreplane as indicated in Fig. 5.2(d). It will be shown in the next sections that the
film thickness does never reach a constant value as the bubble is transiting, similarly
to what observed in square channels by [121], and thus the film thickness reported
in Fig. 5.4(b) is taken at an instant where the bubble nose is $9R$ downstream the
cylinder centre. In the graph, the film thickness is plotted as a function of R/Δ_{min},
where Δ_{min} denotes the size of the smallest cubic cell in the domain.

All the meshes tested yield a film thickness value close to $h_c/R = 0.02$, and no
major differences are observed in the results obtained with the different meshes. This
can be explained by the fact that even the coarsest mesh ($R/\Delta = 40$, $n = 0$) dis-

cretises the film with about 4 computational cells thanks to the very thin boundary layer of cells generated around the cylinder surface, which is at the bottom limit of the threshold suggested by [123] to adequately resolve thin liquid films. Results seem to converge towards a value close to 0.019 as $R/\Delta_{min} > 150$, with less than 2% difference in the film thicknesses detected with the two most refined meshes (identified as mesh c and d in Tab. 5.3). Therefore, the mesh characterised by $R/\Delta = 40$ and $n = 2$, displayed in Fig. 5.4(a) and identified as case c in Tab. 5.3, is the one selected for the remainder of this work. Simulations were run on the high-performance computing cluster Sulis at HPC Midlands+ (https://warwick.ac.uk/research/rtp/sc/sulis). Using typically 256 cores and OpenFOAM's scotch domain decomposition, the com-
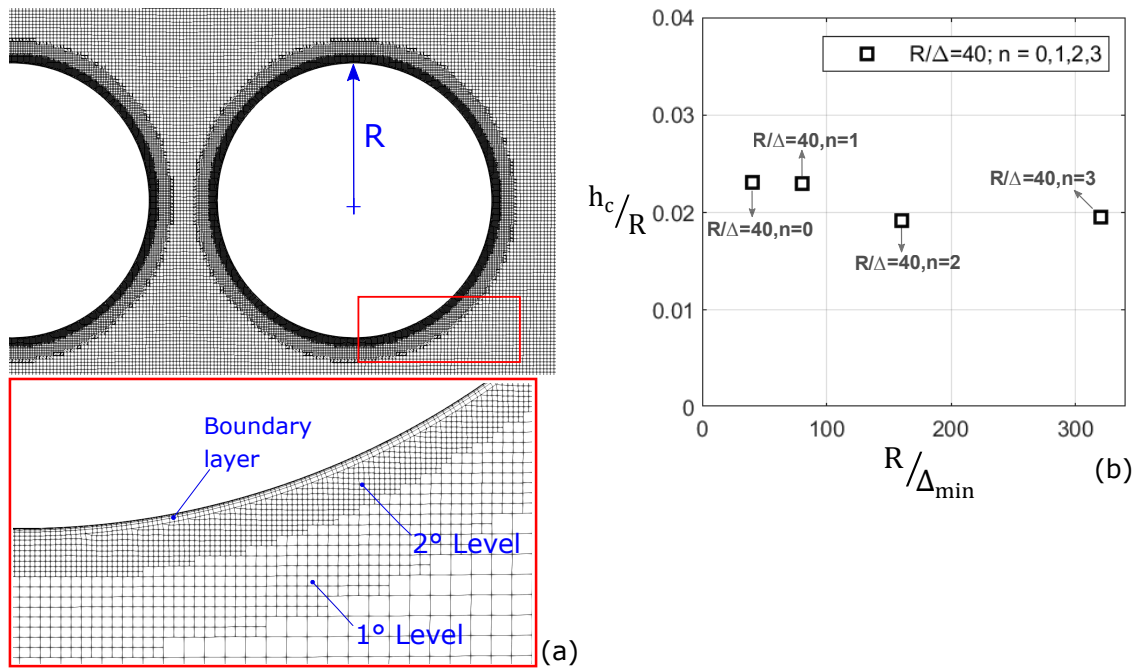
Figure 5.4: Results for the mesh convergence analysis for a long bubble translating through micro-pin fin arrays. (a) Example of computational mesh and close-up view of the refined regions near a cylinder, for the grid arrangement with $R/\Delta = 40$ and $n = 2$; Δ indicates the largest size of the cubic cells far from the cylinder, while n indicates the maximum level of refinement near the pins, which identifies the size of the smallest cubic cell as $\Delta_{min} = \Delta/2^n$. (b) Dimensionless liquid film thickness h_c/R, measured in the correspondence of the 12th cylinder from the inlet, as indicated in Fig. 5.2(d), for increasing values of mesh resolution. Further details about the grids are provided in Tab. 5.3.

Mesh convergence analysis					
Mesh	R/Δ	n	cells number	$\Delta_{min} = \Delta/2^n$	$\Delta_{min}/2^4$
a	40	0	11197384	$0.025R$	$0.0016R$
b	40	1	18966336	$0.0125R$	$0.0008R$
c	40	2	30341952	$0.0062R$	$0.0004R$
d	40	3	52916544	$0.0031R$	$0.0002R$

Table 5.3: Details of the four computational grids tested, characterised with the number of cells per cylinder radius in the bulk flow region (R/Δ), number of recursive refinements near the cylinders walls (n), smallest size of the cubic cells in the refined region $\Delta_{min} = \Delta/2^n$ and thickness of the thinnest cell ($\Delta_{min}/2^4$) in the boundary layer surrounding the cylindrical pin-fins.

putational time for each simulation ranged from 10,000 (high Ca_l) to 50,000 CPU hours (low Ca_l).

5.3 Results

The results of the systematic analysis of the flow of long bubbles between arrays of in-line cylindrical pin-fins are presented below, organised in subsections. Section 5.3.1 reports in detail the findings for a reference case run with $Ca_l = 0.04$, $Re_l = 1$, $s_x = 0.5R$ and $L_b = 12R$. Section 5.3.2 presents the results of the visco-capillary regime, where the Reynolds number is fixed to a very small number ($Re_l = 1$) so that inertial effects are negligible, and the liquid film thickness and bubble dynamics are studied by systematically varying Ca_l in the range $Ca_l = 0.04 - 1$. Section 5.3.3 describes the results of the simulations performed by changing the streamwise gap between the pins s_x for three selected values of capillary number ($Ca_l = 0.04, 0.1$ and 0.2) and $Re_l = 1$. Section 5.3.4 investigates the results obtained by varying the initial bubble length L_b for one value of the capillary number ($Ca_l = 0.1$). The last Sec. 5.3.5 presents the results of the visco-inertial regime, where simulations were run by varying the Reynolds number in the range $Re_l = 1 - 1000$; this was done for two different configurations of streamwise gap between the fins ($s_x = 0.5R, 2R$) and one selected value of the capillary number ($Ca_l = 0.04$).

5.3.1   Bubble and liquid film dynamics for reference case

This section presents the results for the reference case run with $Ca_l = 0.04$, $Re_l = 1$, $s_x = 0.5R$, and $L_b = 12R$. Figure 5.5(a) displays a snapshot of bubble profile, velocity and pressure contours, extracted on a horizontal centreplane ($z = 0$), when the bubble flows in the terminal steady-periodic regime. It can be seen that the cylinders modify the shape of the bubble that indents under the effects of the cylinders, while it extends towards the liquid in the gap between the cylinders. The velocity is higher inside the bubble because the gas flows downstream at a higher speed than the liquid, and localised velocity maxima are visible in the centreline between cylinders. The pressure decreases in the liquid in the streamwise direction due to the friction and pressure drag generated by the cylinders. The pressure in the bubble is larger than that in the liquid regions next to convex interface profiles, e.g. near bubble nose, rear, and in the gap between the cylinders. However, in the correspondence of concave interface regions, such as in the liquid films formed between the bubble and the cylinders, the interface curvature becomes negative (see also Fig. 5.2(a) and (c)) and thus the pressure in the film is larger than that in the bubble and the surrounding liquid regions, as revealed by Fig. 5.5(b) where the contours of the pressure field in the film region around cylinder 13 are depicted. This generates circumferential draining flows that drive liquid out of the thin film region as the bubble translates downstream, as demonstrated by the velocity vectors in Fig. 5.5(b), and contributes to the monotonic thinning of the liquid film as time elapses.

The liquid film and bubble dynamics as the bubble travels through the domain are explained by means of Fig. 5.5(c) and (d). Figure 5.5(d) plots the velocity of the bubble front, centre of mass and rear, evaluated respectively as $U_{b,N} = dx_N/dt$, $U_{b,c-m} = dx_{c-m}/dt$ and $U_{b,R} = dx_R/dt$, with x_N, x_{c-m}, and x_R being the streamwise coordinates of bubble nose tip, centre of mass, and rear tip; the velocity values are reported as a function of the bubble nose position. The bubble does never achieve a steady terminal velocity, but the two velocities experience oscillations due to the influence of the cylinders. Every time the bubble nose or rear pass through a new set of pins, the bubble experiences a restriction on the cross-section, leading to an increase in velocity; by contrast, when the bubble leaves the set of pins, the cross-section increases, which results in a reduction of the bubble velocity. The bubble nose quickly reaches a steady-periodic dynamics as $x_N/R > 20$, identified by velocity
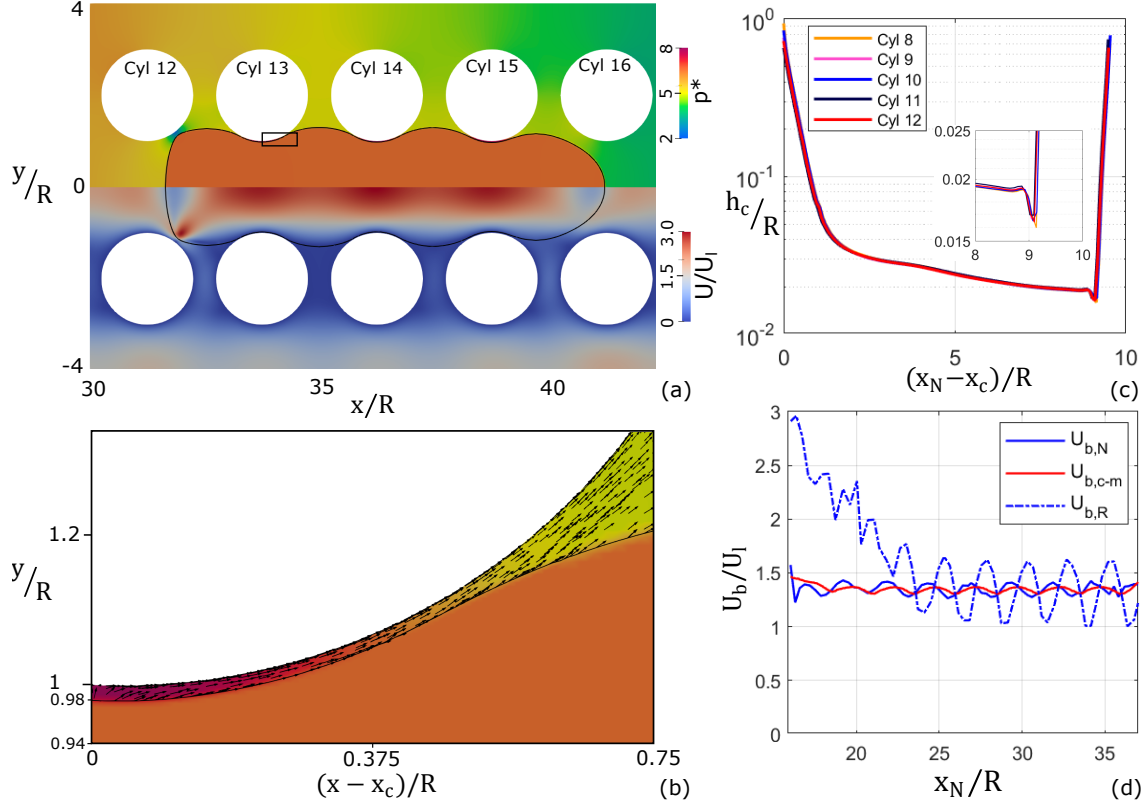
Figure 5.5: Results for reference case run with $Ca_l = 0.04$, $Re_l = 1$, $s_x = 0.5R$, and $L_b = 12R$. (a) Sketch of bubble profile, velocity (bottom half) and pressure (top half) on a horizontal centreplane ($z = 0$), extracted at nondimensional time $t^* = tU_l/R = 18.8$. The velocity field is rescaled by the average liquid speed in the channel formed between the arrays of pin-fins (U_l); the pressure field is rescaled by the capillary pressure $p_{ref} = \sigma/R$; the black solid line identifies the bubble profiles. Flow is from left to right. (b) Close-up view of the pressure field and velocity vectors in the thin film region around cylinder 13, indicated with the black rectangle in (a). (c) Evolution of the dimensionless liquid film thickness h_c/R during the transit of the bubble, measured over 8th to 12th cylinders, and reported as a function of the bubble nose streamwise distance from the cylinders centres, $x_N - x_c$. The inset shows a close-up view of the data near the bubble rear. (d) Evolution of the bubble nose ($U_{b,N}$), centre of mass ($U_{b,c-m}$) and rear ($U_{b,R}$) velocity while the bubble flows downstream the channel.

oscillations exhibiting a constant average value. The bubble rear achieves a steady-periodic regime slightly later, when the bubble nose is past the coordinate $x_N/R \approx 25$. At this instant, the tip of the bubble rear is located at about $x_R/R \approx 15$ (the bubble is about $10R$ long under these conditions), which corresponds to cylinder number

6 under the present setup. Therefore, the whole bubble achieves a steady-periodic regime after the rear has passed cylinder 6; this is verified by the film thickness plots in Fig. 5.5(c).

Figure 5.5(c) reports the dimensionless liquid film thickness, measured on the horizontal centreplane $z = 0$ along the y direction in the point where the distance between the cylinders is the smallest, which corresponds to $\theta = 0$ in Fig. 5.2(d). The film thickness is reported as a function of the bubble nose streamwise distance from the cylinder centre, $x_N - x_c$, and it is measured over five consecutive cylinders (cylinders 8th-12th) to verify that the thin film dynamics has reached a steady regime. This is verified by the fact that all film thickness curves overlap. The liquid film thickness decreases quickly during the initial stages of thin film formation around the cylinder, $(x_N - x_c)/R < 2$. After this initial film has formed, its thickness continues decreasing monotonically as the bubble nose travels further downstream the channel, although at a slower rate than that detected during the initial stages. The monotonic thinning of the film when $(x_N - x_c)/R > 2$ can be ascribed to draining flows driven by capillarity both in the circumferential direction, as explained in the paragraph above, and in the cross-stream $z-$direction owing to the gas-liquid interface curvature gradients established in the $y - z$ plane, see Fig. 5.5(c), where the latter has been observed already in square and rectangular channels [22, 124, 76]. However, this thinning trend subsides as $(x_N - x_c)/R \gg 2$ because the drainage flow rate scales with h^3 and thus quickly drops as the area available for the liquid to escape the thin film reduces. An undulation of the liquid film profile can be observed in the proximity of the bubble rear meniscus in the inset of Fig. 5.5(c), where the film thickness exhibits a global minimum, similarly to what observed in straight channels [119].

We now look at the details of the pressure field along the flow domain. Figure 5.6 shows pressure profiles along four lines aligned with the $x-$axis: line A is aligned with the centre of the channel not occupied by the bubble (coordinates $y = 4R$, $z = 0$), while line B is located in the same channel but tangent to the cylinder surface ($y = 3R$, $z = 0$); line C ($y = R$, $z = 0$) is the corresponding line tangent to the cylinder surface but in the channel occupied by the bubble, whereas line D is the centreline of the channel occupied by the bubble ($y = 0$, $z = 0$). The pressure profiles are extracted at a selected time instant within the steady-periodic regime. Pressure decreases uniformly within the channel not occupied by the bubble as suggested by the values extracted along lines A and B and reported in Fig. 5.6(b), with some undulations related to the

periodic fluid acceleration and deceleration across the pin-fin matrix. The pressure at the centre of the channel occupied by the bubble (line D) follows an analogous trend, although it exhibits a sharp increase in the correspondence of the rear meniscus of the bubble, followed by a constant value when measured within the bubble, and finally by a sharp drop when crossing the front meniscus. These sudden pressure changes are due to the capillary jump in pressure across the liquid-gas interface and the pressure jump is larger at the bubble front than the rear, because the curvature of the front meniscus is larger than that at the rear as observed already in straight channels by [125]. The pressure extracted along line C shows regular peaks in the region occupied by the bubble, which occurs where line C enters the zones occupied by the thin film. Here, the pressure is larger than that inside the bubble owing to the negative interface curvature. It is interesting to note than, on the capillary pressure scale used in Fig. 5.6(b), $p^* = p/(\sigma/R)$, the max pressure difference between $p_C - p_D$ evaluated over every peak of p_C is on the order of 1, because the main contribution to the interface curvature in these points comes from that established on the $x - y$ plane, which is of magnitude $\kappa_{xy} \approx 1/R$ as the interface profile follows closely the cylinder surface.
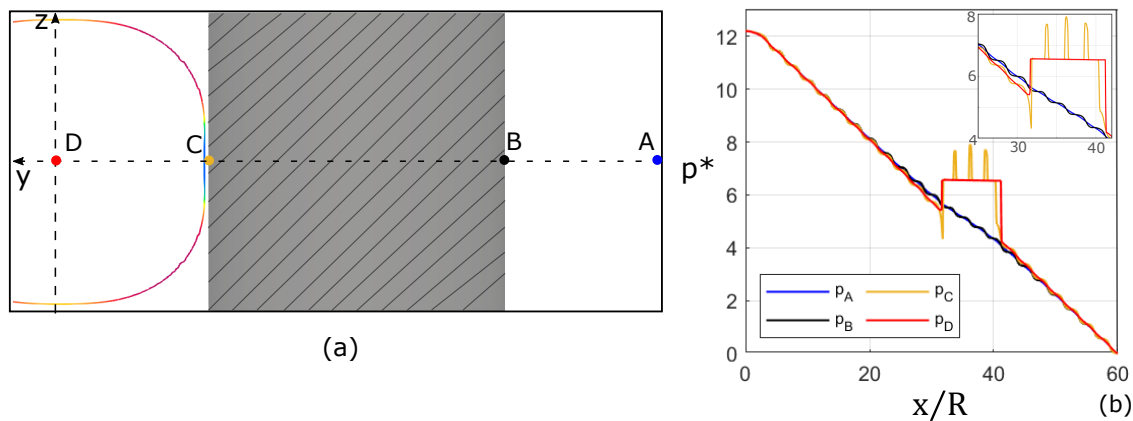
Figure 5.6: Results for reference case run with $Ca_l = 0.04$, $Re_l = 1$, $s_x = 0.5R$, and $L_b = 12R$. (a) Illustration of pressure measurement points on the domain cross-section. The liquid-gas interface profile is also shown, extracted on the same section of the domain as indicated in Fig. 5.2(b). (b) Streamwise evolution of the pressure field along the axial lines passing through the four points indicated in (a), extracted at time $t^* = 18.8$, when the bubble flows in the steady-periodic regime.

5.3.2 Effect of the capillary number

This section presents a systematic analysis of the effect of the capillary number on the bubble and liquid film dynamics in the visco-capillary regime. The capillary number is varied in the range $Ca_l = 0.04 - 1$, while the Reynolds number is set to a small value, $Re_l = 1$, for which inertial effects are expected to be negligible [125].

Figure 5.7 illustrates different features of the liquid-gas interface extracted in the correspondence of cylinder 12, when the bubble nose is $9R$ downstream the cylinder centre, e.g. $(x_N - x_c)/R = 9$ in Fig. 5.5(c). Figure 5.7(a) shows the bubble cross-sectional profiles taken at $x = x_c$, with x_c being the coordinate of the cylinder centre, for different capillary numbers. The cross-sectional interface profile is nearly axisymmetric for $Ca_l \geq 0.1$, whereas for smaller capillary numbers the profile flattens near the top wall and the cylinder surface. Along the cylinder surface, $y/R = 1$ in Fig. 5.7(a), a very thin film forms and as the capillary number is reduced this film extends further on the vertical (z) direction, forming a dimple similarly to what observed in square channels [121]. However, in square channels the critical capillary number at which the dimple is formed is about $Ca_l = 0.01$, which is one order of magnitude smaller than the pin-fin case. Figure 5.7(b) presents the dimensionless liquid film thickness around a cylinder as a function of a local circumferential coordinate θ, for different capillary numbers, measured on the horizontal centreline plane ($z = 0$). As the capillary number is reduced starting from the highest value tested, $Ca_l = 1$, the liquid-gas interface approaches the cylinder surface and the shortest distance between interface and solid wall is detected at $\theta = 0$, i.e. in the correspondence of a line connecting the cylinders centres along the width-wise direction, where we identify $\theta = 0$. When the liquid capillary number decreases below 0.1, a thin liquid film forms around the cylinder surface in the circumferential direction. As the capillary number is reduced further, the liquid film thins at a slower rate but it tends to cover a wider portion of the cylinder wall. The curvature of the liquid film, observed from a $(r = R, \theta, z = 0)$ line on the cylinder wall, changes sign and two dimples are formed identifying a minimum film thickness value at symmetric circumferential positions with respect to $\theta = 0$. The dimples move sideways as the capillary number decreases and at the lowest capillary number tested, $Ca_l = 0.04$, these are located at about $\theta = \pm 30$ degrees. A similar liquid film dynamics over a curved surface was observed by [126] on the top surface of long bubbles travelling in horizontal channels under Bond numbers slightly

above unity, where an asymmetrical thinning of the liquid film was observed as an effect of draining downward flows triggered by gravity. All the data for centre (h_c) and minimum film thickness values (h_{min}) extracted on the $z = 0$ centreplane for cylinder number 12 at different capillary numbers are compiled in Fig. 5.7(c,d). As
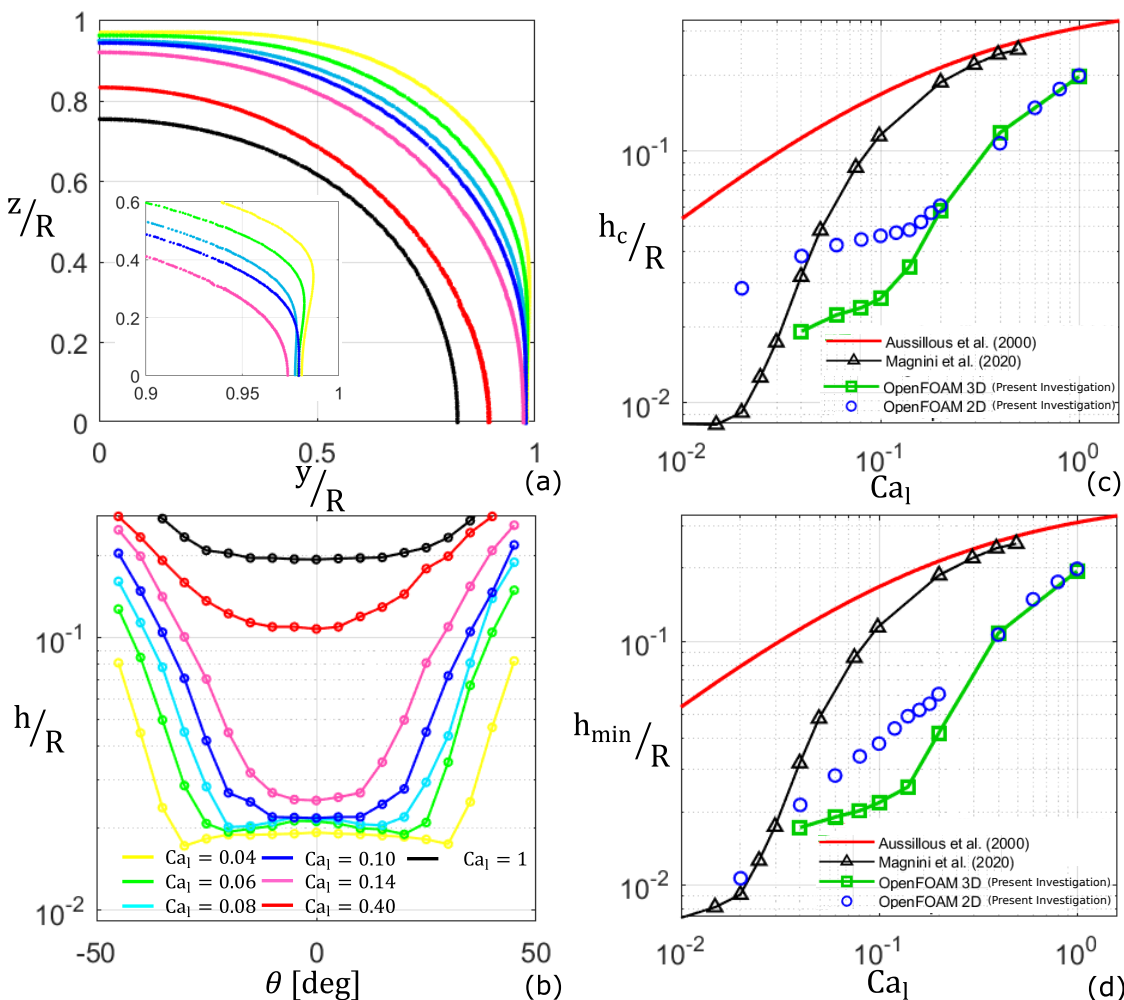
Figure 5.7: (a) Cross-sectional ($y - z$ plane) liquid-gas interface profiles for different capillary numbers measured in correspondence of the centre of the cylinder; the inset gives a close-up view near the cylinder wall, where $y/R = 1$. (b) Dimensionless local liquid film thickness (h/R) measured on the centreplane ($z = 0$) around the cylinder; see Fig. 5.2(d) for the notation. The legend in (b) applies also to (a). (c-d) Dimensionless liquid film thickness measured on the plane $z = 0$ (c) at the cylinder centre (h_c/R) and (d) minimum film thickness (h_{min}/R), versus liquid capillary number (Ca_l).

a reference, the graphs include also the film thickness predictions obtained using [27] correlation for circular channels and the results of the numerical simulations of [121] for square channels. Furthermore, the graphs report also the results of the simulations of a preliminary study that we conducted in the same conditions, but using a two-dimensional geometry which disregarded the z direction. Both the centre and minimum film thicknesses decrease quickly as the capillary number is decreased until the critical capillary number $Ca_l = 0.1$ is reached, and a thin film begins coating the cylinder surface. Below this critical value, the reduction of h subsides similarly to what is observed in square channels but below $Ca_l = 0.01$. In general, the film thickness around the cylinders is always significantly smaller than that achieved in circular and square channels, in the range of capillary numbers investigated; however, extrapolation of the trends in the figures suggest that when $Ca_l < 0.04$ liquid films in square channels may be smaller than those around pin-fins. It is interesting to note that the two-dimensional simulations yield values of the film thickness that agree well with the three-dimensional simulations at larger capillary numbers, $Ca_l \geq 0.2$, where surface tension is less important, whereas the agreement worsens at lower capillary numbers. This is expected, as two-dimensional simulations cannot account for the interface curvature on the $y - z$ cross-sectional plane and thus are missing the associated contribution to the capillary force. Further insight into the dynamics of the whole bubble when varying capillary numbers is provided with Fig. 5.8. As the capillary number increases and viscous forces become more important, the bubbles elongate in the flow direction and expand less in the gap between the cylinders. The shape of the bubble rear, emphasised with the close-up view in Fig. 5.8(b), is rounded as long as surface tension forces remain important, $Ca_l \leq 0.1$, whereas it flattens for large capillary numbers as previously observed for circular tubes [128] and eventually exhibits time-dependent patterns and fragmentation when $Ca_l = 1$; note that, as $Re_l = 1$, the Weber number of the flow becomes of the order of unity for $Ca_l = 1$, and therefore inertial effects triggering time-dependent patterns at the bubble tail may become relevant in these conditions [129]. Figure 5.8(c) shows the values of the bubble-to-liquid velocity ratio when varying the capillary number. The bubble speed is always larger than the average liquid speed in the channel formed between the pin fin arrays, so that $U_b/U_l > 1$ for the entire range of conditions studied. The bubble speed is very close to the values reported for square channels in previous studies [121, 127], although bubbles travelling through pin fin arrays are slightly faster, in
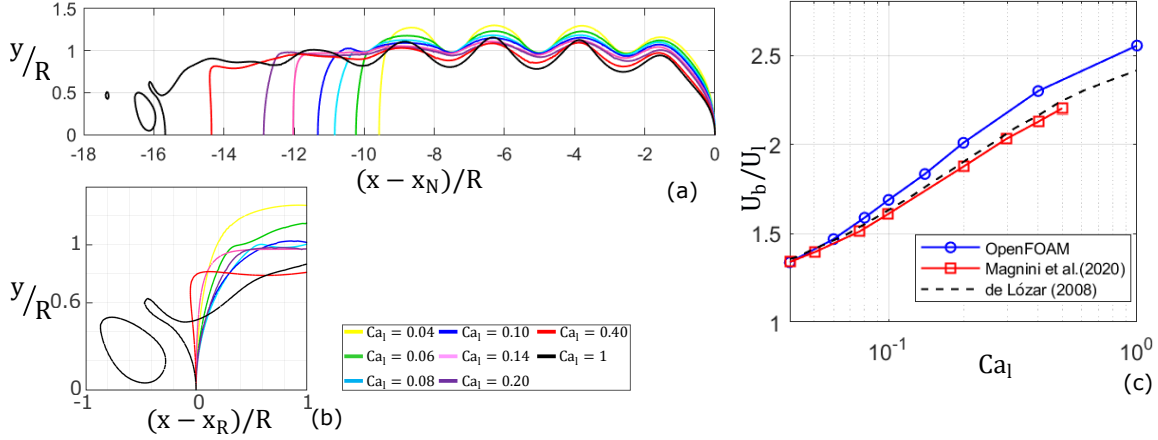
Figure 5.8: Systematic analysis of the capillary number effect, for $Ca_l = 0.04 - 1$, on the bubble shape and speed; other conditions are $Re_l = 1$, $s_x = 0.5R$, and $L_b = 12R$. (a) Liquid-gas interface profiles on the centreplane $z = 0$ extracted at steady-state, for different capillary numbers. All profiles are extracted at the instant where the bubble nose (x_N) is about $9R$ downstream the centre of cylinder number 12. The profiles in (a) are shifted to have same x_N. (b) Close-up view of the profiles in (a) near the bubbles rear, now shifted to have the same position of the bubble rear x_R. (c) Dimensionless velocity of the bubble nose $(U_{b,N} = dx_N/dt)$ against liquid capillary number (Ca_l). As a reference, the graph contains the results of the numerical simulations of [121] and [127] for square channels.

particular in the higher range of the Ca_l tested. This can be explained by the fact that as the bubble nose progresses between two consecutive pin-fins, the liquid can be displaced sideways across the gap between the cylinders, thus offering less resistance to the bubble advancement.

5.3.3 Effect of the streamwise distance between pin-fins

This section investigates the influence of the streamwise gap between the pins on the dynamics of the flow. The results of simulations performed varying the pitch in the range $s_x = 0.125R - 2R$ are reported, for three selected values of the capillary number, $Ca_l = 0.04, 0.1$ and 0.2, while $Re_l = 1$, and $L_b = 12R$. The different gaps between the pins can also be converted into porosity values for the geometry. The porosity can be estimated as $\phi = 1 - \pi R^2/(d_x d_y)$, with d_y being constant $(d_y = 4R)$ and $d_x = s_x + 2R$. The range of porosity obtained for $s_x = 0.125R - 2R$ is $\phi = 0.63 - 0.8$, with the reference case $s_x = 0.5R$ corresponding to a porosity of 0.69. For all the
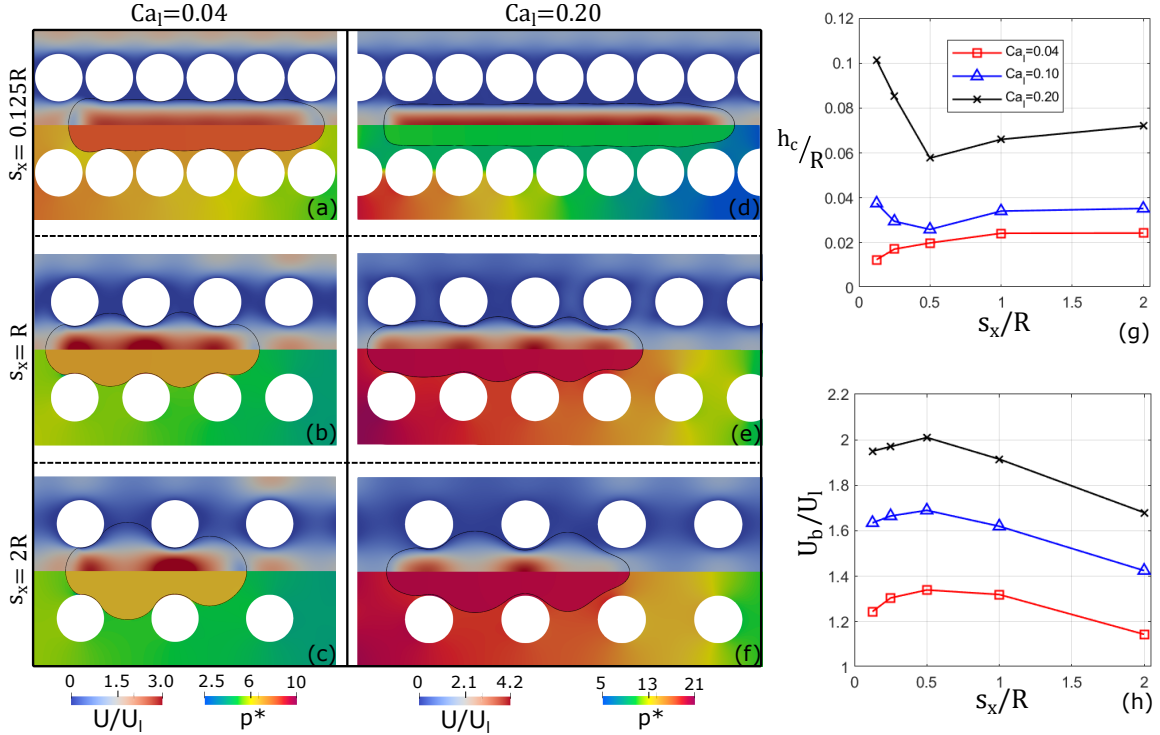
Figure 5.9: Systematic analysis of the effect of the streamwise distance between the pin-fins, for $s_x = 0.125R - 2R$; other conditions are $Ca_l = 0.04, 0.1, 0.2$, $Re_l = 1$ and $L_b = 12R$. (a-f) Snapshots of bubble profiles (black lines), velocity (top half) and pressure contours (bottom half) for different values of s_x. (g) Dimensionless liquid film thickness (h_c/R) and (h) bubble velocity ($U_{b,N} = dx_N/dt$) against streamwise gap between the pins (s_x) for different capillary numbers (Ca_l). The legend in (g) applies also to (h).

other studies previously shown, a reference configuration $s_x = 0.5R$ was adopted, which is a typical setup in micro-pin fin heat exchangers [38, 130]. In Fig. 5.9(a-f), snapshots of bubble profiles, velocity and pressure contours for cases with different geometry are reported. It can be observed that the cylinders setup modifies strongly the shape of the bubble. The increase of the pitch between the fins favours the bubble to expand between the gaps, as a consequence the bubble is shorter. We observed that $s_x = 2R$ was a limit configuration in the present setup. For $s_x > 2R$, the bubble expanded excessively in the cross-stream direction and eventually remained trapped in the region bounded between four adjacent pin-fins, with the incoming liquid bypassing it through the neighbour channels. As s_x is reduced, the bubble exhibits smaller bulges and indentations, taking a more slender profile between the

pin fin arrays similarly to what would be expected in a straight wall configuration. Therefore, we can consider the straight wall configuration as an asymptotic case where $s_x \rightarrow 0$.

Liquid film thickness and bubble speed trends for different values of s_x and Ca_l are summarised in Fig. 5.9(g) and (h). Overall, we can observe that the distance between the cylinders has a significant influence on the film thickness established between the bubble and the cylinders walls. There is a systematic trend of h_c/R to increase as $s_x/R > 0.5$, which can be ascribed to a larger portion of the cylinders surface becoming covered by the liquid film. The leading and trailing edge of the meniscus formed around the cylinders get farther from the $\theta = 0$ location where h_c is measured, as s_x is increased above 0.5. This causes a slight increase in h_c, similarly to what is observed in square channels as the capillary number is reduced and a dimple forms over the channel walls [121]. The bubble speed decreases as s_x increases in the same range, because the bubble tends to expand in the cross-stream direction as the channelling effect of the cylinders on the flow is reduced. As $s_x \rightarrow 0$, we would expect h_c to converge towards the value for a square channel, which is larger than the thicknesses observed for $s_x = 0.5$ over the entire range of Ca_l studied in this work, see Fig. 5.7(c). This is in agreement with the increasing trend of h_c/R as s_x is reduced below 0.5 in Fig. 5.9(g) for $Ca_l = 0.1$ and 0.2, which identifies a minimum film thickness value at $s_x = 0.5R$ for both capillary numbers. However, this trend is not observed for the smallest capillary number tested, $Ca_l = 0.04$, where h_c decreases monotonically in the range of s_x investigated. It is plausible that the expected increase of h_c towards the square channel values is shifted towards lower values of s_x than those investigated in this work at small Ca_l, where surface tension becomes dominant and the liquid-gas interface is to a larger extent impacted by the topography of the domain walls.

In summary, the liquid film thickness is very sensitive to the streamwise pitch of the pin-fins, and for a constant value of the liquid flow rate (or liquid capillary number) h_c may change by a factor of 2 when s_x is varied in the range $s_x = 0.125R - 2R$.

5.3.4 Effect of the bubble length

Multiphase flow within microchannels presents different flow regimes depending on the volume of gas being mobilised and on the relative velocity between the liquid

and gas phases [131]. In the case of bubbles, flow regimes can be separated into bubbly flows, when the equivalent diameter of a bubble is smaller than the channel size, and elongated bubbles when bubbles are larger. Within straight channels, it has been verified in numerous studies that when the bubble length is more than twice the channel diameter, the bubble length has no impact on the speed of the bubble [120]. Within circular channels, the bubble length has no effect on the liquid film thickness provided that $L_b/R > 4$ [120], although the bubble length necessary to achieve an annular film may increase with capillary and Reynolds numbers [119]. In noncircular
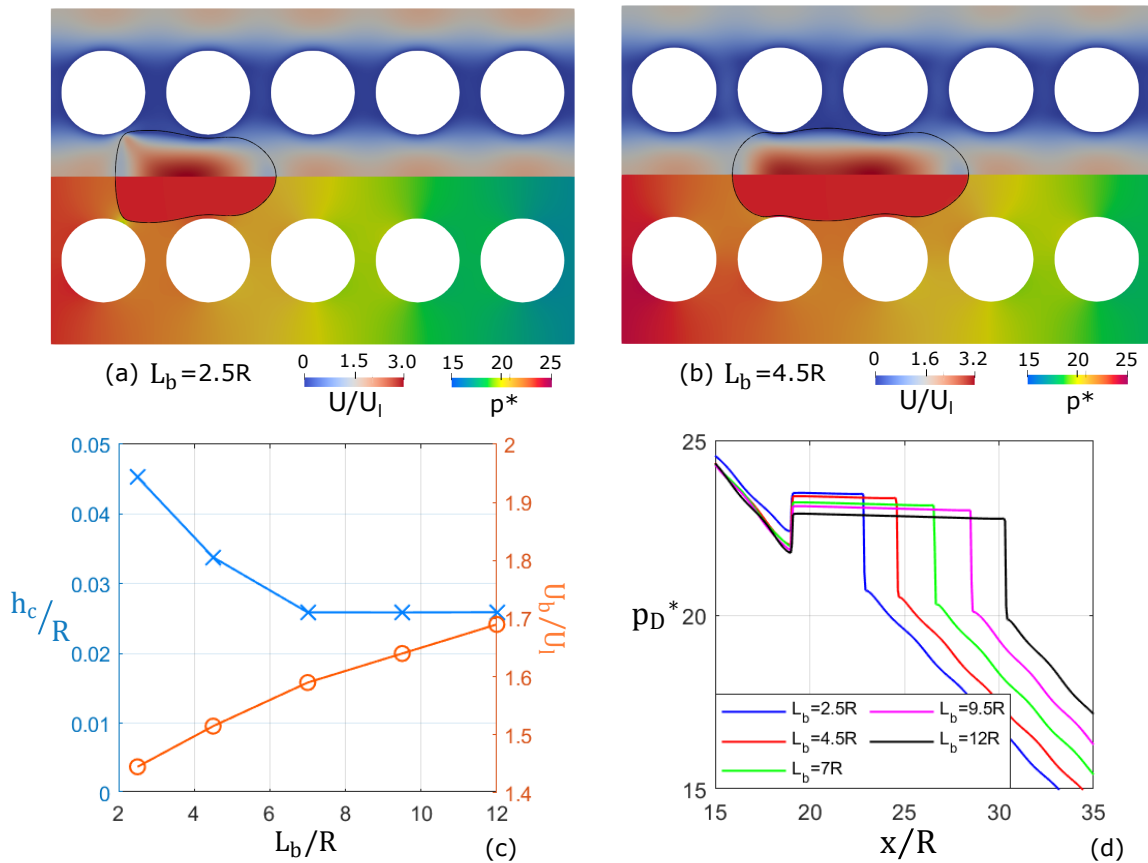
Figure 5.10: Systematic analysis of the effect of the initial bubble length, for $L_b/R = 2.5 - 12$; other conditions are $Ca_l = 0.1$, $Re_l = 1$ and $s_x = 0.5R$. (a-b) Snapshots of bubble profiles (black lines), velocity (top half) and pressure (bottom half) contours, for (a) $L_b = 2.5R$ and (b) $L_b = 4.5R$. (c) Liquid film thickness and bubble velocity against initial bubble length (L_b). (d) Streamwise pressure profiles extracted along the centerline of the channel, as indicated in Fig. 5.6(a), when the bubble flows in the steady-periodic regime.

channels, the bubble length may have an impact on the liquid film thickness due to the capillary-induced drainage flows in the liquid film, depending on the capillary number and channel aspect-ratio [111]. Therefore, this section presents the results of an analysis of the bubble length. The initial bubble length is varied within the $L_b = 2.5R - 12R$, while fixing $Ca_l = 0.1$, $Re_l = 1$ and $s_x = 0.5R$.

Figure 5.10(a,b) provide snapshots of the bubble dynamics during the steady-periodic regime, for relatively short bubbles. Although no significant differences emerge between the two figures, the liquid film deposited around the cylinder for the shortest bubble, $L_b = 2.5R$ in Fig. 5.10(a), is evidently thicker than that established for $L_b = 4.5R$ in Fig. 5.10(b). Note that for $L_b = 2.5R$ the bubble length is similar to the streamwise distance between the centres of two consecutive pins, and therefore only one or two cylinders maximum are simultaneously engaged by the bubble during its flow, making the dynamics of the rear meniscus more dependent on that of the front meniscus.

This qualitative information is supported by the liquid film thickness data presented in Fig. 5.10(c). In this section, the liquid film thickness is still measured around cylinder number 12, but now it is measured at the time instant when the bubble nose is only $2.5R$ downstream the cylinder centre so that the same measurement point is available for all bubble lengths. In the previous sections, where $L_b = 12R$, the measurement point was at a distance of $9R$ behind the bubble nose, but this was not possible when testing shorter bubbles. When bubbles are shorter than $7R$, the liquid film thickness seems to increase monotonically when reducing the bubble length. This can be ascribed to the fact that there is no sufficient time for the liquid in the film to drain, thus leaving a thicker liquid layer over the cylinder surface. When $L_b/R > 7$, a threshold slightly larger than that reported for circular channels, the bubble length no longer impacts the liquid film thickness for the capillary number studied. Note that the difference in liquid film thickness between the two limiting cases $L_b/R = 2.5$ and $L_b/R = 12$ is significant, as it amounts to a factor of 2. The bubble speed increases monotonically with the bubble length, although the difference in bubble speed between $L_b/R = 9.5$ and 12 is only about 5%. Last, Fig. 5.10(d) shows the pressure profiles along the channel centreline for the different cases. Shorter bubbles exhibit shorter regions where the pressure increases due to the capillary contribution, but no other differences are apparent among the different configurations.

5.3.5   Effect of the Reynolds number

Inertial forces are typically regarded as secondary effects in microfluidics, however, there exist engineering applications where flows in sub-millimetric channels can still achieve Reynolds numbers as high as 10^3 [132, 133]. This happens in particular in heat transfer elements, where high flow rates are utilised to achieve high convective heat transfer. In two-phase flow, there is general consensus that inertia has a considerable impact on the bubble dynamics and shape when $\mathrm{Re} > 100$ [125, 30], and generally inertial forces impact the bubble dynamics by thinning the liquid film thickness for Reynolds numbers in an intermediate range of $\mathrm{Re} = 100 - 500$, and thickening it at higher Reynolds numbers.

In this section, we present the results of simulations run by systematically varying the Reynolds number in the range $\mathrm{Re_l} = 1 - 1000$, which resulted in a range of bubble Reynolds numbers $\mathrm{Re_b} = 1 - 1600$. The capillary number is fixed to a value of
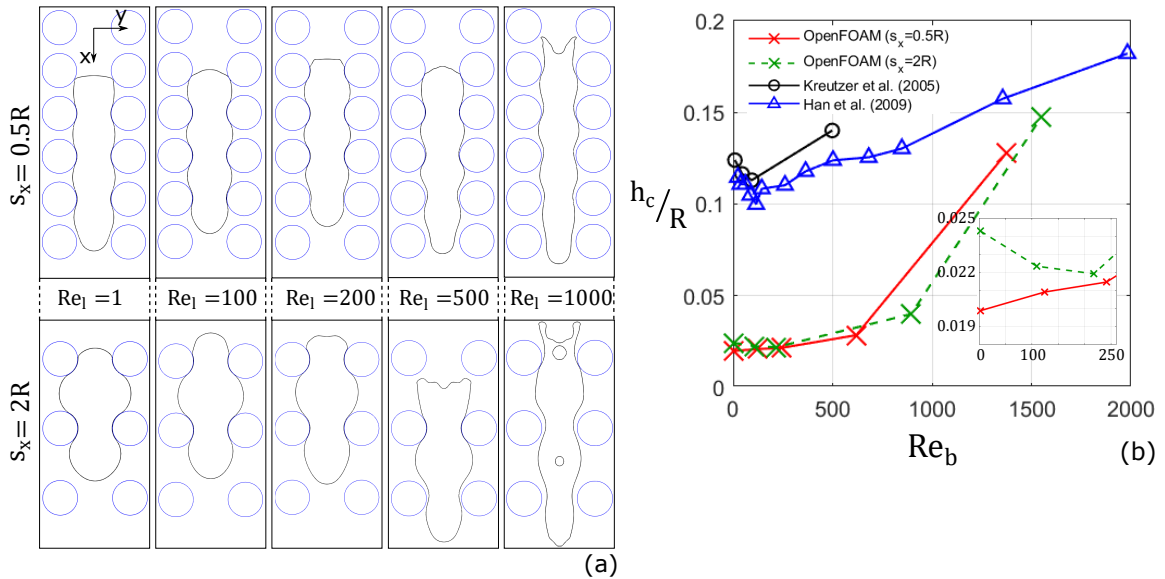
Figure 5.11: Systematic analysis of the effect of the Reynolds number, for $\mathrm{Re_l} = 1 - 1000$, in two different geometrical configurations $s_x = 0.5R, 2R$; other conditions are $\mathrm{Ca_l} = 0.04$ and $L_b = 12R$. (a) Snapshots of bubble profiles for different Reynolds numbers and different streamwise gap between the pins. (b) Dimensionless liquid film thickness (h_c/R) against Reynolds number of the bubble ($\mathrm{Re_b} = 2\rho_l\mathrm{U_b}\mathrm{R}/\mu_l$); the inset shows a close-up view of the data at small Reynolds numbers. As a reference, the plot also includes the liquid film thickness results of [125] and [30] for $\mathrm{Ca_l} = 0.04$.

$Ca_l = 0.04$, and two different values of streamwise distance between the pin-fins were taken into account $s_x = 0.5R, 2R$, with a constant initial bubble length of $L_b = 12R$.

Since cross-flow past arrays of cylinders may exhibit time-dependent patterns known as von Kármán vortex streets, all simulations were first run in single-phase for a long time (up to $t^* = tU_l/R = 150$) to verify whether vortex shedding appeared in the conditions investigated, for both $s_x = 0.5R$ and $2R$. No time-dependent patterns were observed in the entire range of Reynolds numbers tested. [134] performed experiments of flow past one confined cylinder in a microfluidic channel and observed that the critical Reynolds number at which vortex shedding appeared, evaluated as Re $= \rho U_m D/\mu$ with U_m being the maximum velocity upstream of the cylinder and D the cylinder diameter, increased from 200 to 550 when decreasing the channel height-to-diameter ratio from 3 to 1, while maintaining the same width-to-diameter ratio of 3. In our case, the height-to-diameter ratio of the channel is 1 and the width-to-diameter can be considered as 1. Furthermore, the maximum liquid speed upstream the cylinders bank is about half that used to calculate the Reynolds number in this work, and therefore the range of Reynolds numbers considered in our study and the level of confinement are well within the range where [134] observed no vortex shedding. We attempted tests for larger gaps between the cylinders, $s_x = 3R$, and in this case we observed the appearance of time-dependent vortices at Reynolds numbers of about 500, but these conditions were not eventually studied in two-phase regime.

Figure 5.11(a) shows snapshots of the bubble dynamics for all values of s_x and Re_l investigated. For values of Re_l up to about 500, the bubble retains the capillary-driven shape with a rounded nose and tail, although the nose becomes more slender as already reported by [135]. When $Re_l = 1000$, bubbles are considerably longer and the interface exhibits time-dependent patterns that cause fragmentation of the rear meniscus and entrainment of liquid within the gas. Liquid films are apparently thicker, and the profile of the film around the cylinders in the circumferential direction is strongly asymmetric, with thinner films on the downstream quarter of the cylinder surface ($\theta > 0$ in Fig. 5.2(d)) and thicker films on the upstream quarter ($\theta < 0$).

The film thickness data versus Re_l are compiled in Fig. 5.11(b), where experimental data from the literature for circular channels are also included as a reference. In the low-Reynolds number range, the film thickness is little sensitive to Re_l and the values for flow past pin-fins are much smaller than those in tubes, as already discussed previously. However, at the largest Reynolds number tested, $Re_l = 1000$,

h_c/R increases by a factor of 5 from the value achieved in the visco-capillary regime, also approaching the values measured in tubes. As observed in Fig. 5.11(a), there is a distinct change in bubble dynamics from $Re_l = 500$ to $Re_l = 1000$, where inertial forces have a strong impact on the bubble shape and film topology. Therefore, the presence of the cylinders seems to amplify the effect of inertia as compared to two-phase flow in straight channels, and the impact of the Reynolds number on the bubble dynamics, film morphology and film thickness becomes of primary importance.

5.4 Conclusions

The shape and dynamics of long gas bubbles propagating through circular pin fin arrays have been examined in detail for a range of liquid capillary numbers $Ca_l = 0.04 - 1$, streamwise pitch of the cylinders $s_x = 0.125R - 2R$, bubble length $L_b = 2.5R - 12R$ and Reynolds numbers $Re_l = 1 - 1000$, thus covering both the visco-capillary and visco-inertial regimes, conditions that may be relevant both for flow in porous media and micro-pin fin heat exchangers. The study is based on the results of three-dimensional numerical simulations conducted adopting a geometric VOF method as implemented in the TwoPhaseFlow library for OpenFOAM released by [60]. The computational mesh is always sufficiently fine to fully capture the thin liquid film trapped between the bubble and the obstacles, thus allowing to quantify its thickness and morphology at all conditions investigated. The main conclusions of this study are as follows:

- The bubble nose and rear menisci experience periodic accelerations and decelerations as the bubble propagates through the arrays, but eventually achieve a steady-periodic flow regime where their time-averaged values are the same.

- As the bubble propagates through the arrays of pin-fins, it wraps around their surface leaving a thin liquid film in between. This film exhibits some of the features characteristic of film deposition in straight channels; it thins monotonically towards the bubble rear, and its thickness varies as a function of the capillary number. Under the conditions investigated, the film thickness is always smaller than those reported for circular and square channels.

- When $Ca_l < 0.1$, interfacial dimples form over the flat channel walls and the pin-fins surfaces, causing localised peaks of capillary pressure that induce strong drainage flows that push liquid out of the film.

- Bubble and film dynamics are very sensitive to the streamwise distance between the cylinders s_x. As $s_x \to 0$, the configuration converges to that of a straight channel and the liquid film thickness increases. As s_x increases, the bubble is less guided in the downstream direction and tends to expand in the gap between the cylinders, giving way to thicker liquid films. In between these two limiting situations, a minimum film thickness condition is identified.

- Bubbles shorter than $L_b/R = 7$ exhibit increasing values of the film thickness as their length is decreased, but for $L_b/R > 7$ the bubble length has a negligible impact on its dynamics.

- Inertial effects are mild when $\mathrm{Re_l} \leq 500$ but, for larger Reynolds numbers, the bubble shape exhibits strong time-dependent patterns leading to fragmentation of its rear meniscus and to liquid films that are more than 5 times thicker than those observed in the visco-capillary regime.

This work emphasises that the morphology and thickness of liquid films deposited by long bubbles flowing in non-straight and complex confined geometries are profoundly different from those reported for circular and non-circular straight channels. As such, models and correlations specific to the geometrical configuration of interest should be used to predict relevant liquid-gas interface features. The observations made and the results collected in this study will be valuable in subsequent analyses involving heat transfer in Ch. 6 and 7, as they provide detailed insights into the flow development within these intricate geometries. This allows for a better understanding of the phenomena when phase change is also considered, thereby making the examination of results more straightforward.

Chapter 6

Dynamics of bubbles and liquid film during flow boiling in a micro-pin evaporator

This chapter of the thesis presents the results of a comprehensive investigation into flow boiling within a micro-pin fin evaporator [1]. The primary objective of this investigation is to acquire a comprehensive understanding of the heat transfer mechanisms during flow boiling in micro-pin fin heat exchangers. Building upon the findings extracted from the prior chapter under isothermal conditions, the study rigorously examines the behaviours exhibited by bubbles and thin liquid films and the interplay influenced by heat transfer in these complex geometries. Consequently, a focal point of this exploration is the detailed analysis of how bubbles propagate and evolve in size as they propagate through the micro-pin fin arrays. The flow is studied by means of numerical simulations, performed using a customised boilingFoam solver in OpenFOAM v2106, which adopts the built-in geometric Volume of Fluid method to capture the liquid-vapour interface dynamics. The numerical model of the evaporator includes in-line arrays of pin-fins of diameter of $50\,\mu$m and height of $100\,\mu$m, streamwise pitch of $91.7\,\mu$m and cross-stream pitch of $150\,\mu$m. The fluid utilised is refrigerant R236fa at a saturation temperature of $30\,^\circ$C. The range of operating conditions simulated includes values of mass flux $G = 500 - 2000\,\text{kg}/(\text{m}^2\text{s})$, heat flux $q = 200\,\text{kW}/\text{m}^2$, and inlet subcooling $\Delta T_{sub} = 0 - 5\,\text{K}$. This study shows that bubbles

---

[1]The results presented in this chapter have been published by El Mellas et. al [136].

nucleated in a pin-fin evaporator tend to travel along the channels formed in between the pin-fin lines. Bubbles grow due to liquid evaporation and elongate in the direction of the flow, leaving thin liquid films that partially cover the pin-fin surface. The main contributions to heat transfer arise from the evaporation of this thin liquid film and from a cross-stream convective motion induced by the bubbles in the gap between the cylinders, which displace the hot fluid otherwise stagnant in the cylinders wakes. When the mass flow rate is increased, bubbles depart earlier from the nucleation sites and grow more slowly, which results in a reduction of two-phase heat transfer. Higher inlet subcooling yields lower two-phase heat transfer coefficients because condensation becomes important when bubbles depart from the hot pin-fin surfaces and reach highly subcooled regions, thus reducing the two-phase heat transfer.

Solver option

The solver boilingFoam has been adopted for this study, implemented in OpenFOAM v.2106 [77]. These simulations rely on a geometric Volume of Fluid method to capture the interface dynamics. OpenFOAM's PIMPLE algorithm is used for the pressure-velocity coupling, with three correction steps (nCorrectors). The different discretisation methods selected for the various terms of the governing equation solved are reported in Tab. 6.1.

The main difference between the schemes adopted during the previous investigation on adiabatic conditions (Chap. 5), is that for the time derivative term the Euler scheme is adopted. When dealing with phase change the complexity of the problem

Term		Scheme
Time derivative	$\partial \phi / \partial t$	Euler
Gradient	$\nabla \phi$	Gauss linear
Divergence	$\nabla \cdot (\rho \vec{u} \vec{u})$	Gauss limitedLinearV (1)
Divergence	$\nabla \cdot (\alpha \vec{u})$	Gauss vanLeer
Divergence	$\nabla \cdot \mu [\nabla \vec{u} + (\nabla \vec{u})^T]$	Gauss linear
Divergence	$\nabla \cdot (\rho \vec{u} c_p T)$	Gauss limitedLinearV (1)
Laplacian	$\nabla \cdot (\lambda \nabla T)$	Gauss linear orthogonal
Interpolation		Linear
Surf-norm Grad		orthogonal

Table 6.1: Discretisation methods for the solver boilingFoam.

Field	Solver	smooter/precond.	Tolerance
α	smoothSolver	symGaussSeidel	10^{-8}
p	GAMG	DICGaussSeidel	10^{-8}
u	smoothSolver	symGaussSeidel	10^{-8}
T	PBICGStab	DILU	10^{-10}
$\dot{m}$	PCG	DIC	10^{-10}
momentumPredictor	yes		
nCorrectors	3		

Table 6.2: Solution methods for the solver boilingFoam.

increases due to the additional physical processes involved, which can significantly impact the stability and convergence of the numerical solution. In scenarios where phase change has a great influence on the simulation, moving to a more stable and straightforward scheme of the first order like the implicit Euler method for time integration can help avoid these stability issues, ensuring that the simulation remains convergent and provides physically meaningful results.

6.1 Simulation setup

The geometry and conditions for the simulations are taken from the work of Falsetti et al. [42], where the thermohydraulic performances of a micro-pin fin evaporator were experimentally characterised, using the refrigerant R236fa as working fluid with an outlet saturation temperature maintained constant at $T_{sat} = 30.5 \pm 0.5\,^{\circ}\mathrm{C}$. The

Figure 6.1: (a) Micro-pin fin evaporator bottom side with aluminium film heaters. (b) Inlet restrictions before the micro-pin fin array, from Falsetti et al. [42].

working conditions analysed by the experiments involved a range of mass fluxes of $G = 500 - 2500 \, \text{kg}/(\text{m}^2\text{s})$ and heat fluxes of $q = 200 - 480 \, \text{kW}/\text{m}^2$. The micro-evaporator was traversed by 66 in-line rows of circular micro-pin fins, covering a total heated area of $1 \, \text{cm}^2$. The test section of the silicon micro-evaporator (from the bottom) is shown in Fig. 6.1(a). Two versions of the micro-evaporator were tested, one with and one without inlet restrictions. The inlet restrictions consisted of an additional row of pin-fins with a larger diameter placed before the heated area to suppress flow instabilities, such as vapour backflow [42], see Fig. 6.1(b). In the present numerical work, the geometrical configuration of the micro-pin fin evaporator is simulated by considering up to three arrays of pin-fins and the adjacent channels, depending on the study being performed; a schematic of the flow configuration and notation in this work is provided in Fig. 6.2- 6.3. The flow domain is represented with a three-dimensional geometry. A Cartesian coordinate system is adopted to describe
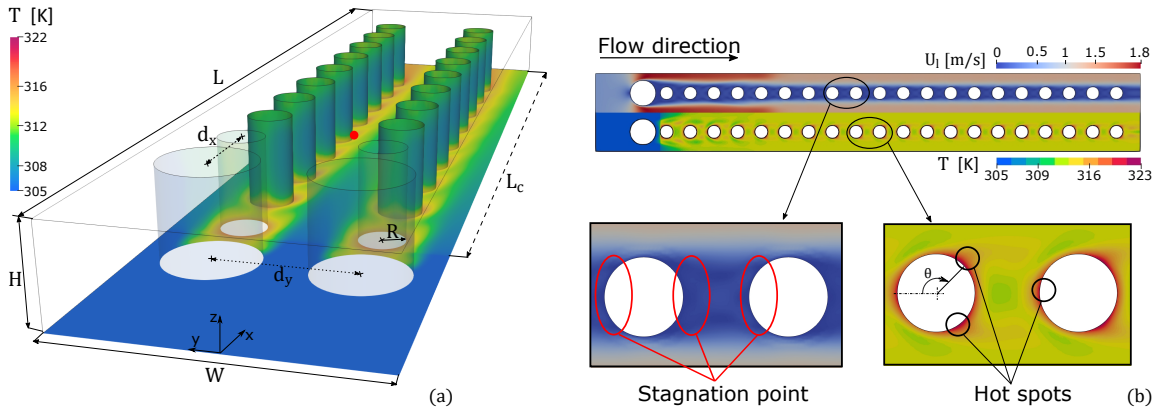
Figure 6.2: (a) Illustration of the flow domain and notation used in this work. The temperature contours of the heated surfaces are shown, extracted at the start of a two-phase simulation. The domain width, length, and height are indicated with W, L and H, respectively. For visualisation, a short domain of length $L = 50R$ is displayed. R denotes the radius of the cylindrical pins. The streamwise (along x) and cross-stream (along y) distances between the cylinders' centres are indicated as d_x and d_y. The length of the heated area is denoted with L_c. The flow is in the direction of positive x. The red dot identifies a plausible nucleation site for the two-phase simulation. (b, top half) Velocity contours on a horizontal plane halfway through the domain height ($z = H/2$) and (b, bottom half) temperature contours of the heater ($z = 0$) at the start of the two-phase simulation. Simulation conditions: $G = 1000 \, \text{kg}/(\text{m}^2\text{s})$, $q = 200 \, \text{kW}/\text{m}^2$, $T_{sat} = 30 \, °\text{C}$ and no inlet subcooling.

the flow, where x indicates the streamwise coordinate, y is the width-wise cross-stream coordinate, and z is the height-wise cross-stream coordinate. The coordinate system is centred between two pin-fin arrays, and $z = 0$ identifies the bottom surface of the evaporator, where heat is applied.

Fig. 6.2(a) shows an illustration of the flow domain used for the two-phase simulations described in Sec. 6.3.2 and 6.3.3, where two arrays of pin-fins are included in the geometry. The circular micro-pin fins have a radius and height of respectively $R = 25\,\mu$m and $H = 100\,\mu$m; the pitch between the cylinders in the streamwise and cross-stream directions are respectively $d_x = 91.7\,\mu$m and $d_y = 150\,\mu$m. The cross-stream gap between the cylinders identifies a square channel of width $W_{ch} = d_y - 2R = 100\,\mu$m. The hydraulic diameter of the channels d_h is identified as the hydraulic diameter of this square cross-section, i.e. $d_h = 100\,\mu$m [42]. Larger cylinders, of radius of $50\,\mu$m, are positioned upstream to the channel to serve as inlet restrictions [42]. In the example of Fig. 6.2(b), the domain width is $W = 300\,\mu$m, which incorporates two arrays of cylinders and half of the adjacent channels. The domain length will be varied in this work in the range $L = 2 - 10$ mm, depending on the flow conditions investigated. The working fluid tested is the refrigerant R236fa, which will be studied for a saturation temperature of $30\,^\circ$C; the thermophysical properties of the fluid at the conditions of interest are listed in Tab. 6.3.

Boundary conditions

A liquid-only flow of uniform velocity is imposed (U_l), together with a zero-gradient condition for the pressure; the fluid velocity is calculated from the target value of the mass flux as $U_l = GW_{ch}/[\rho_l(W_{ch} + 2R)]$. The temperature of the working fluid at the inlet is set to a value of $T_{inl} = T_{sat} - \Delta T_{sub}$, with ΔT_{sub} being the target value of the inlet subcooling. At the fluid outlet $(x = L, y, z)$, a zero-gradient condition

Phase	ρ [kg/m^3]	λ [W/(m K)]	μ [kg/(m s)]	σ [N/m]	h_{lv} [kJ/kg]
liquid	1342.4	0.0714	2.675×10^{-4}	0.008933	142.42
vapour	21.57	0.01436	1.119×10^{-5}		

Table 6.3: Thermophysical properties of the refrigerant R236fa at $T_{sat} = 30\,^\circ$C ($p_{sat} = 320$ kPa).

is imposed for the velocity and the temperature, with a reference pressure value. Periodic boundary conditions are adopted at the sides of the domain $(x, |y| = W/2, z)$ to model the presence of adjacent channels. In the experiment, the heat load was applied through the evaporator base and transferred to the operating fluid through the pin-fins and bottom channel surface. Since the numerical model does not account for conjugate heat transfer, a constant heat flux q is applied to the cylinders' surface and the bottom boundary of the evaporator $(x, y, z = 0)$. The heat load is not applied to the entire domain length but only along a length L_c measured starting from the centre of the larger cylinders at the inlet; this emulates the experimental setup, where heat was applied via Aluminium heaters covering only the channel area of the evaporator and not the inlet and outlet manifolds. In the experiment, the top of the evaporator was covered with a glass lid to allow optical access. This is reproduced in the numerical model by setting an adiabatic condition to the top of the domain $(x, y, z = H)$. On the channel and pin-fin walls, a no-slip condition is applied. The contact angle formed by the liquid-vapour interface and the solid walls is set to a static value of $\beta = 5°$ (hydrophilic wall). In the experiment, the contact angle of R236fa on silicon was not measured. Since R236fa is an almost perfectly wetting fluid, the contact angle was arbitrarily set to a small value.

The assumption of a constant contact angle was made primarily to simplify the model. Including the effects of a dynamic contact angle would significantly increase the complexity of the problem and increase the simulation time. The focus of the study was on the overall heat transfer performance, bubble dynamics, and design optimisation, where the contact angle plays a secondary role. However, it is acknowledged that this assumption is a limitation concerning the prediction of liquid film thickness and morphology. As noted, no experimental data are available for the dynamic contact angle in scenarios like the one investigated, making the simplification to a constant contact angle a reasonable approximation.

The working conditions investigated in the present numerical study involve a range of mass fluxes of $G = 500 - 2000 \, \text{kg/(m}^2\text{s)}$, a range of inlet subcooling values of $\Delta T_{sub} = 0 - 5 \, \text{K}$, while the heat flux is fixed to $q = 200 \, \text{kW/m}^2$.

Note that the solver, boilingFoam, used during the investigation accounted for Conjugate Heat Transfer (CHT), but the transient conduction in the solid domain during the analysis was neglected. The micro-pin fin heat exchanger featured a relatively simple geometry with no significant variations in material properties, and
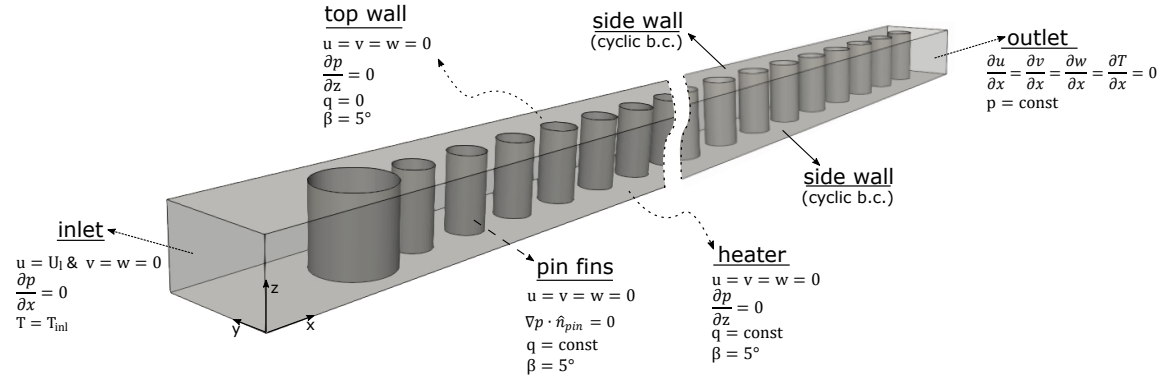
Figure 6.3: Schematic of the simulation geometry and boundary conditions; for convenience, only one row of pins is shown.

temperature gradients within the solid were expected to be minimal. Therefore, treating the solid as an isothermal surface may be sufficient. In systems such as the one investigated, the heat transfer coefficient of the working fluid dominated over the thermal resistance of the solid parts. As a consequence, neglecting CHT is expected to have a minimal impact on the overall results. The final reason for this approach was limited computational resources. Incorporating CHT would have required solving an additional equation and accounting for the entire solid domain, which was computationally expensive in this scenario.

Initial conditions

Two-phase flow simulations require seeding an initial bubble and suitable initial velocity and temperature fields. The latter can be obtained from a preliminary single-phase simulation run under the same conditions, which emulates the initial stage of the experiment where heat is applied to the evaporator and the fluid temperature increases over time until nucleation begins. Due to the high heat flux applied in the flow boiling experiments, this preliminary single-phase simulation cannot be run until steady-state, because the wall temperature would increase by more than $100\,\mathrm{K}$ above saturation. Therefore, the single-phase simulation was run in time until the wall temperature reached a prescribed target value at a specified nucleation point, both identified as explained below.

The velocity and temperature contours displayed in Fig. 6.2(a) and (b) show an example of initial conditions for a two-phase simulation taken from a single-phase

simulation that was not run until steady-state. The exact locations of the nucleation points of the bubbles are generally not known a priori. However, potential sites can be identified where micro-cavities are present in the walls due to the microfabrication process [92] has introduced in Sec. 3.1. One plausible location is at the edge where the pin-fin surface meets the base surface of the channel [41, 42], because temperatures are higher due to the presence of the hydrodynamic boundary layers and the photolithography manufacturing procedure may leave some surface imperfections at the connecting point between the flat base surface and the cylinder, which will act as nucleation spots. This point is highlighted in Fig. 6.2(a) with a red dot at the base of the fifth pin-fin on the left-hand side array. The fifth cylinder was adopted as the nucleation point in the simulations with no inlet subcooling, whose results are discussed in Sec. 6.3.2, 6.3.3 and 6.3.4. The choice of the fifth cylinder was arbitrary and made as a compromise between placing the nucleation point too close to the inlet restrictions and the computational cost of increasing the length of the domain. The circumferential location of the nucleation spot around the selected pin-fin was chosen upon inspection of the single-phase temperature fields; see, for example, Fig. 6.2(b). The hottest zone of each pin-fin was identified as a spot located at about 135° from the stagnation point at the cylinder upstream, which coincides with the point where the hydrodynamic boundary layer separates from the cylinder surface. Therefore, this circumferential location was identified as the most suitable for nucleation; interestingly, this location around the cylinder corresponds qualitatively to the point where Falsetti et al. [44] observed streams of bubbles being generated by the nucleation process.

The nucleation temperature is a result of the topography of the surface over which boiling occurs and of the hydraulic and thermal boundary layers developing over the wall, which impact the near-wall temperature profile. The nucleation temperature was not measured in the experiment, and thus, an estimation must be extracted from the available experimental data. Falsetti et al. [42] reported curves of the heat transfer coefficient as a function of the vapour quality for a few selected values of the mass flux G and heat flux q. For a given G and q pair, the heat transfer coefficient corresponding to a zero vapour quality can be assumed as the heat transfer coefficient at the boiling onset. From this value of the heat transfer coefficient, a wall temperature at the boiling onset can be back-calculated from $h = q/(T_w - T_{sat})$, with h being the heat transfer coefficient from the experiment and T_w the unknown nucleation temperature.

In summary, the general procedure to obtain suitable initial velocity and temperature conditions for a two-phase simulation is as follows: (i) from the working conditions set G and q, a nucleation temperature is estimated from the knowledge of the heat transfer coefficient from the experimental data in Falsetti et al. [42]; (ii) a nucleation location is arbitrarily defined as a point at the edge between the fifth pin-fin and the base surface, forming an angle of 135° from the leading edge of the cylinder; (iii) a preliminary single-phase simulation is run until the temperature at the nucleation point reaches the nucleation temperature. Any variation to this procedure will be explained in the relevant sections.

Once the initial conditions are identified, the boiling process in the two-phase simulation is initiated by seeding a spherical bubble of initial diameter of $10\,\mu$m at the nucleation point. The two-phase simulation then evolves in time until the bubble reaches the outlet section of the channel, which takes about 1 millisecond; the time-step of the simulations ranged from $10^{-8}\,$s to $10^{-7}\,$s.

6.2   Mesh convergence analysis

The mesh convergence analysis was performed for a representative case run with inlet restrictions, $G = 1000 \, \text{kg}/(\text{m}^2\text{s})$, $q = 200 \, \text{kW/m}^2$, $T_{sat} = 30 \, °\text{C}$ and no inlet subcooling. The computational domain utilised is analogous to that depicted in Fig. 6.2(a); it incorporates two rows of pin-fin arrays with their adjacent channels ($W = 300 \, \mu\text{m}$), and it has a length of 2.1 mm, corresponding to about 20 pin-fins being modelled in the streamwise direction.

The domain is discretised with an arbitrary polyhedral grid structure with mainly hexahedral elements. The domain is meshed in two successive steps, using Open-FOAM's tool snappyHexMesh. First, the entire domain block with no pin-fins is meshed using uniform cubes with cell size Δ. Then, the mesh is recursively refined $n = 2$ times near the cylinder surface by splitting a cube into eight smaller cubes for each refinement cycle. Finally, the cubes are clipped to fit the surface of the cylinders and the cylinders are subtracted from the computational domain. Three different meshes were tested, starting with varying values of the largest cubic cells. The representative parameters of the mesh are listed in Tab. 6.4, and a close-up view of the mesh near one pin-fin is shown in Fig. 6.4(a). Note that for all three meshes employed in the grid independence analysis, the smallest cell near the cylinder surface has a size below $1 \, \mu\text{m}$.

The identification of the suitable initial conditions for the simulation follows the procedure outlined in Sec. 6.1. For $G = 1000 \, \text{kg}/(\text{m}^2\text{s})$ and $q = 200 \, \text{kW/m}^2$, Falsetti et al. [42] measured a heat transfer coefficient of about $12.5 \, \text{kW}/(\text{m}^2\text{K})$ at zero vapour quality, which corresponds to a nucleation superheat of 16 K and a wall temperature of

Mesh convergence analysis				
Mesh	R/Δ	n	cells number	$\Delta_{min} = \Delta/2^n$
M1	7.5	2	5841352	$0.033R = 0.83 \, \mu\text{m}$
M2	10	2	11101302	$0.025R = 0.62 \, \mu\text{m}$
M3	12.5	2	18557950	$0.02R = 0.5 \, \mu\text{m}$

Table 6.4: Details of the three computational grids tested, characterised with the number of cells per cylinder radius in the bulk flow region (R/Δ), number of recursive refinements near the cylinders walls (n), and smallest size of the cubic cells in the refined region $\Delta_{min} = \Delta/2^n$.
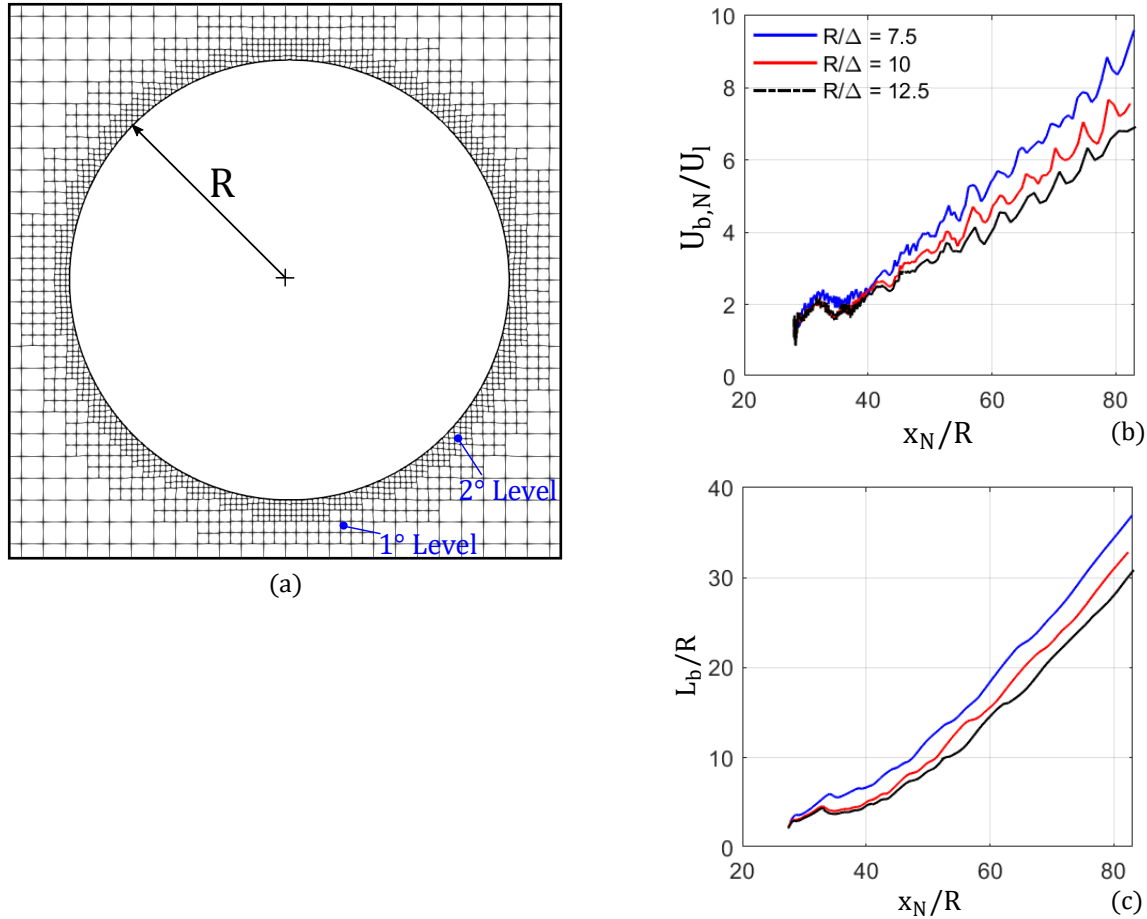
Figure 6.4: Results for the mesh convergence analysis. (a) Example of computational mesh near a cylinder, for a grid arrangement with $R/\Delta = 10$ and $n = 2$ (mesh M2 in Tab. 6.4). (b-c) Evolution of the bubble nose velocity and bubble length while the bubble flows downstream the channel; x_N indicates the streamwise location of the bubble nose. The legend in (b) applies also to (c). The results refer to a case run with inlet restrictions, $G = 1000 \, \text{kg}/(\text{m}^2\text{s})$, $q = 200 \, \text{kW}/\text{m}^2$, $T_{sat} = 30 \, °\text{C}$ and no inlet subcooling.

319 K. Therefore, the preliminary single-phase simulation is run until the temperature at the nucleation point reaches this value, after which a small bubble is seeded and the two-phase simulation begins.

Upon boiling onset, the bubble grows quickly due to the superheated liquid surrounding the cylinder. Figure 6.4(b) and (c) display the temporal evolution of the velocity of the bubble nose and the bubble length as the bubble grows and accelerates downstream the evaporator. Both bubble speed and length increase over time and
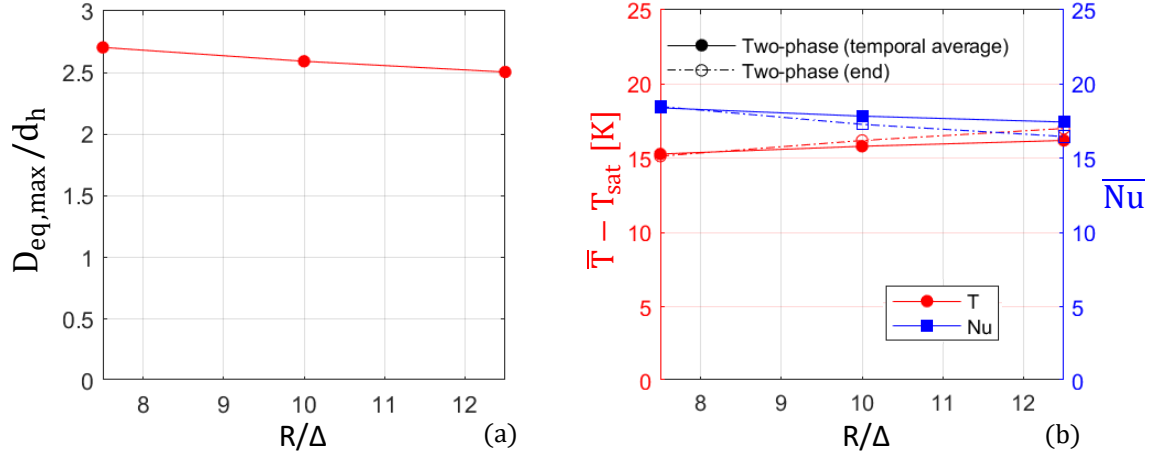
Figure 6.5: Results for the mesh convergence analysis. (a) Maximum bubble equivalent diameter at the instant when the bubble approaches the outlet section, rescaled by the channel hydraulic diameter $d_h = 100\,\mu$m. (b) Spatially-averaged temperature ($\overline{T}_s$) and Nusselt number ($\overline{\text{Nu}}$) of the heated surfaces (heater and pins). The data are presented as a time-average over the entire simulation and as an instantaneous value at the end of the simulation. The results refer to a case run with inlet restrictions, $G = 1000\,\text{kg/(m}^2\text{s)}$, $q = 200\,\text{kW/m}^2$, $T_{sat} = 30\,°\text{C}$ and no inlet subcooling.

achieve a linear trend as a function of the position of the bubble nose in agreement with those observed for bubbles propagating in straight microchannels [121, 137]. The presence of the cylinders acting as periodic obstacles for the flow of the bubble is manifested in Fig. 6.4(b) by the periodic oscillations of the bubble nose speed. The bubble dynamics and heat transfer for this case will be analysed in detail in Sec. 6.3.2. All computational grids tested yield similar values of bubble speed and length, with a systematic trend towards lower evaporation rates as the mesh is refined which was already previously observed in boiling simulations employing the phase-change model of Hardt and Wondra [65]. Nonetheless, the relative differences between the equivalent bubble diameter at the end of the simulation for the different grids, plotted in Fig. 6.5(a), is less than 7%. This suggests that all grids capture the bubble dynamics well. Figure 6.5(b) shows the average surface temperature and Nusselt number ($\text{Nu} = qd_h/[\lambda_s(\overline{T}_s - T_{sat})]$), calculated as a spatial average over all heated surfaces (base and pin-fins). The differences between the three meshes are minimal, with mesh M2 ($R/\Delta = 10$) exhibiting a temporally-averaged Nusselt number which is only 3% smaller than M1 ($R/\Delta = 7.5$), and less than 3% higher than that measured with

the finest mesh M3. The instantaneous values of average temperature and Nusselt number at the end of the simulation are also very similar, with less than 5% difference between M2 and M3. Hence, mesh M2 was the mesh used to perform the simulations presented in the next sections. Simulations were run on the high-performance computing cluster Sulis (https://warwick.ac.uk/research/rtp/sc/sulis). Using typically 128 cores and OpenFOAM's scotch domain decomposition, the computational time for each simulation ranged from 5000 (low Re) to 7000 CPU hours (high Re).

6.3 Results

The results of this work are presented below, organised in subsections. Section 6.3.1 reports the results of a validation study. Section 6.3.2 presents a detailed analysis of the two-phase hydrodynamics and heat transfer for one representative case. The effect of the inlet flow rate is analysed in Section 6.3.3. Section 6.3.4 describes the simulation results performed by changing the nucleation site location. The last Section 6.3.5 illustrates the analysis of the effect of the inlet subcooling.

6.3.1 Validation

Single-phase validation

The numerical framework was first validated versus the single-phase pressure drop and heat transfer data obtained by Falsetti et al. [42], who performed single-phase experiments at low heat fluxes to validate their experimental and measurement setup against established correlations for friction factor and Nusselt number across pin-fins and tube banks. Single-phase numerical simulations were run on a longer domain matching the experimental setup, i.e. 1 cm, but modelling only one row of pin-fins and the surrounding channels ($W = 150 \, \mu$m). Simulations were performed by varying the mass flux in the range of $G = 500 - 2500 \, \text{kg/(m}^2\text{s)}$, while keeping the heat flux fixed at $q = 50 \, \text{kW/m}^2$, and were run until velocity and temperature fields achieved steady-state regimes. The Reynolds number is calculated using the hydraulic diameter of the straight channel formed between the pin-fin arrays, $d_h = 100 \, \mu$m, as Falsetti et al. [42]:

$$\text{Re} = \frac{G d_h}{\mu_l} \tag{6.1}$$

The range of Reynolds numbers corresponding to $G = 500 - 2500 \, \mathrm{kg/(m^2 s)}$ is $\mathrm{Re} = 187 - 935$.

The results of the single-phase validation study are presented in Fig. 6.6. Figure 6.6(a) shows the pressure profile along the channel centreline ($y = 0$, $z = H/2$) for different mass fluxes, while Fig. 6.6(b) shows the corresponding velocity and pressure fields near the inlet. The pressure profiles reveal a sudden pressure drop immediately after the larger pin serving as inlet restriction, followed by a gradual pressure recovery. For $G = 500 \, \mathrm{kg/(m^2 s)}$, the pressure increase due to pressure recovery is approximately $100 \, \mathrm{Pa}$, extending over a length of $x \approx 12R$. For $G = 2500 \, \mathrm{kg/(m^2 s)}$, the pressure increase is $2700 \, \mathrm{Pa}$, extending over a length of $x \approx 40R$. At low values of the mass flux, $G < 1000 \, \mathrm{kg/(m^2 s)}$ ($\mathrm{Re} < 374$), the flow field achieves steady-state along the whole length of the evaporator. The recirculating regions downstream each pin-fin remain stationary and form two sets of counter-rotating vortices; see, for example, Fig. 6.7(c), where streamlines are reported on a horizontal mid-plane ($z = H/2$) far from the inlet section ($x/R \approx 200$). Steady recirculating patterns for flow past cylinders at Reynolds numbers much larger than 100 in the presence of strong confinement were also reported by Zhang et al. [134]. At $G = 1000 \, \mathrm{kg/(m^2 s)}$, some weak
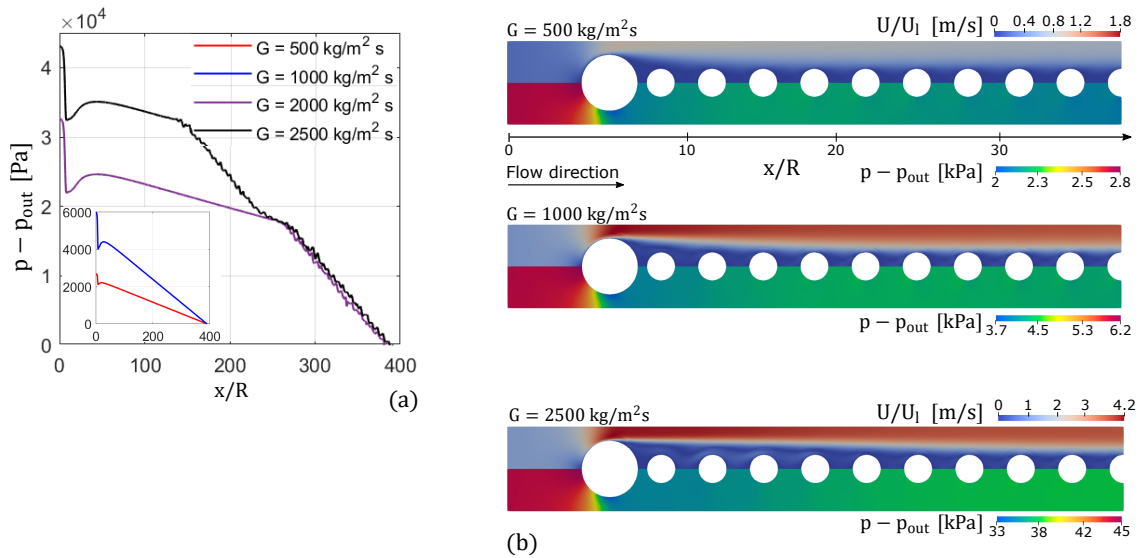
Figure 6.6: Results of the single-phase validation study. (a) Pressure drop profile along the channel ($p - p_{\mathrm{out}}$). (b) Snapshots of velocity (top half) and pressure contours (bottom half), extracted at steady-state in the mid-height plane ($z = H/2$) near the inlet section for different mass flux (G) at the inlet.

unsteadiness on the flow in the pin-fins wake becomes apparent, which gives rise to asymmetric wakes. However, the recirculating region remains bounded in the gap between consecutive cylinders. The flow field always reaches nearly steady-state conditions for $G < 2000 \, \text{kg}/(\text{m}^2\text{s})$, and the axial pressure profile exhibits a uniform linear decay along x as observed for $G = 500 \, \text{kg}/(\text{m}^2\text{s})$ and $1000 \, \text{kg}/(\text{m}^2\text{s})$ in Fig. 6.6(a). As the mass flux is increased to $G = 2000 \, \text{kg}/(\text{m}^2\text{s})$, to which it corresponds Re = 748, strong vortex shedding begins appearing from a certain axial location in the evaporator, $x/R \approx 270$, see Fig. 6.7(c). The transition to the vortex shedding regime induces a significant change in trend in the axial pressure profiles displayed in Fig. 6.6(a), causing a sharp change in the slope of the curve and thus increasing the pressure drop. Upon a further increase of the mass flux to $G = 2500 \, \text{kg}/(\text{m}^2\text{s})$, the slope of the pressure profile does not exhibit significant changes. Still, the transition to vortex shedding occurs earlier within the evaporator, and thus, the total pressure drop increases considerably.

In the experiments of Falsetti et al. [42], the total pressure drop Δp_{tot} in the test section was measured using a differential pressure transducer between the inlet and outlet manifold plenums. To obtain the pressure drop along the pin-fin array, Δp_{fin}, they subtracted the contributions of the inlet and outlet pressure drop Δp_{in} and Δp_{out} from Δp_{tot}, so that $\Delta p_{fin} = \Delta p_{tot} - \Delta p_{in} - \Delta p_{out}$. The inlet pressure drop Δp_{in} was estimated by summing the contributions of two sudden contractions from the inlet manifold plenum to the test section inlet plenum, a third contraction across the inlet restrictions, and subtracting the pressure recovery due to the sudden expansion after the restrictions. The outlet pressure drop Δp_{out} was estimated by summing up the pressure recoveries due to three sudden expansions from the channels outlet to the outlet manifold plenum. All these seven contributions were calculated using empirical correlations [138]. From Δp_{fin}, the friction factor for the pin-fin array was calculated as follows:

$$f = \frac{\Delta p_{fin}\rho_l d_h}{2L_c G^2} \tag{6.2}$$

The uncertainty on the friction factor was calculated using the Kline and McClintock method of propagation of error and returned a value of $\pm 15\%$. However, the uncertainties introduced by the use of correlations to estimate the inlet and outlet pressure drops were not included. The correlations were originally developed for sud-

den restrictions and expansions within long channels, as such their use to estimate pressure drops in configurations where the flow cannot become fully developed between consecutive area changes, is expected to constitute another source of error. By estimating as 25% the uncertainty associated to each predicted contraction and expansion pressure drops, the overall uncertainty in the friction factor increases to about 20%. For a coherent comparison with the experiment, where the contribution of the pressure recovery after the inlet restrictions was incorporated into Δp_{in} (and thus excluded from Δp_{fin}), the friction factor in the simulations is calculated by considering as Δp_{fin} the pressure drop between the local maximum in pressure after the restrictions and the channel outlet.

The values of the friction factor for experiments and simulations are reported in Fig. 6.7(b). Evaporators with and without inlet restrictions were tested by tested by Falsetti et al. [42] and the results for both configurations are included in Fig. 6.7(b). The figure includes also predictions obtained using an empirical correlation developed by Brunschwiler et al. [139] for water flowing across in-line circular pin-fins; this was developed by fitting experimental data measured at Reynolds numbers below 300, and thus the curve for Re > 300 is displayed as a dashed line. Trends and magnitudes of the friction factor in experiments and simulations are in good agreement across the entire range of flow rates examined, with deviations that remain always below the uncertainty in the experimental values. The friction factor first reduces upon an increase in the Reynolds number. In the experiment, this trend exhibits a transition at about $\mathrm{Re} = 200 - 400$, after which f slightly increases reaching a value of $f = 0.045 - 0.05$ that becomes approximately independent of Re. This transition was attributed to the establishment of vortex shedding in the wake of the pin fins. The friction factor in the simulations exhibits the same trend, with the transition in f occurring at $\mathrm{Re} = 400$. Analysis of the flow patterns in the simulations confirms that the change of trend in f happens when the vortices in the wake of the cylinders become unsteady. As the flow rate is further increased, such that full vortex shedding is established, the friction factor attains asymptotically constant values which are weakly dependent on Re. Since in the simulations the inlet boundary condition sets a perfectly unidirectional flow at the test section inlet, it is reasonable that flow instabilities occur at slightly higher Reynolds number than the experiment, where the flow enters the channels after a series of changes in direction and cross-sectional area.

The results presented in this work were performed without using any turbulence model in the simulations. This is justified by the relatively small Reynolds number and by the fact that turbulence models for interface-resolved two-phase simulations are not well established. Single-phase flow past a cylinder may become weakly turbulent at the highest flow rates tested in this work, however, the flow model adopted is expected to remain suitable provided that the mesh is sufficiently fine to capture the smallest scales of the flow. The Kolmogorov scale η associated to the flow past the cylinders can be estimated as $\eta/D = \mathrm{Re_D}^{-3/4}$, with D being the diameter of the pin-fins and $\mathrm{Re_D} = GD/\mu_l$. This yields $\eta = 0.5\,\mu\mathrm{m}$ at the highest flow rate tested, which is on the order of the smallest cell size near the cylinders surface, as such it is expected that the smallest flow structures are captured by the mesh. Furthermore, the results of the mesh independence analysis and the good agreement between the experimental and computational values of the friction factor across the range of flow rates tested, provide confidence that the present numerical setup is sufficiently accurate to model the flow configuration under investigation.

For the experimental validation of the heat transfer performance, the average Nusselt number $(\overline{\mathrm{Nu}})$ is calculated from the numerical results. Following common practice for flow across banks of tubes [140, 141], the Nusselt number in the simulations is calculated from a wall heat transfer coefficient which is computed by dividing the heat flux by the log-mean temperature as follows:

$$\overline{\mathrm{Nu}} = \frac{\overline{h}_w d_h}{\lambda_l}, \qquad \overline{h}_w = \frac{q}{\Delta T_{LM}} \tag{6.3}$$

where $\overline{h}_w$ is the average wall heat transfer coefficient and ΔT_{LM} is the log-mean temperature difference:

$$\Delta T_{LM} = \frac{T_{out} - T_{inl}}{ln\left(\frac{\overline{T}_s - T_{inl}}{\overline{T}_s - T_{out}}\right)} \tag{6.4}$$

where T_{out} is the average bulk temperature measured at the outlet, T_{inl} is the average bulk temperature at the inlet and $\overline{T}_s$ is the average temperature of the heated walls (base evaporator wall and pin-fins). The use of the log-mean temperature instead of the temperature difference becomes important in particular at low Re, where the fluid may experience a large change in temperature as it moves through the pin-fin arrays Incropera [141].

The results are reported in Fig. 6.7(c), where the average single-phase Nusselt

number ($\overline{\mathrm{Nu}}$) is plotted as a function of Re. The graph also includes the experimental results of Falsetti et al. [42] and the Nu predicted using Zukauskas correlation for tube bundles [142]. The results exhibit an approximately linear trend versus the Reynolds number and are in good agreement with the experimental data, both with and without inlet restrictions. The heat transfer performance increases with a higher Reynolds number, which is expected due to the promotion of the flow mixing and generation of vortex shedding along the channel. Experimental and computational Nusselt numbers match very well for Re $= 500 - 600$, whereas for higher flow rates the simulations underpredict the experimental data by about 15%, which is on the order of the experimental uncertainty on $\overline{\mathrm{Nu}}$. This deviation may be also due to the different data reduction procedures adopted to obtain heat transfer coefficients from raw data. The log-mean temperature difference method is used in the simulation,
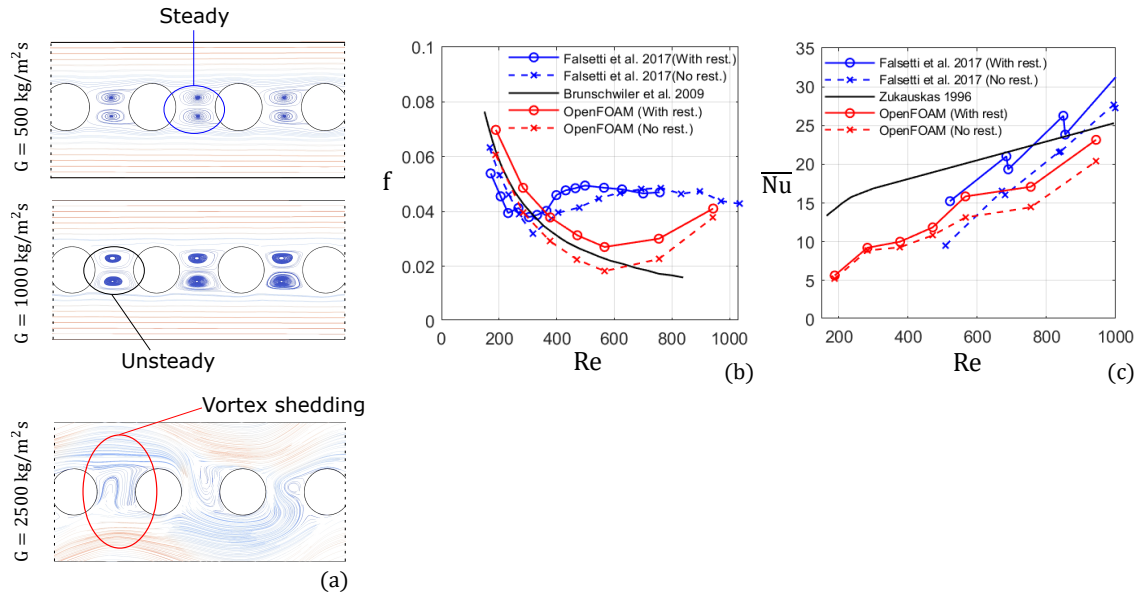
Figure 6.7: Results of the single-phase validation study. (a) Local velocity contours for different values of G, farther from the inlet section ($x/R \approx 200$). (b) Single-phase friction factor (f) as a function of the liquid Reynolds number (Re) for geometries with and without inlet restrictions. As a reference, the chart presents also the friction factor data reported by Falsetti et al. [42] and the f prediction using Brunschwiler et al. [139] correlation. (c) Spatially-averaged Nusselt number ($\overline{\mathrm{Nu}}$) of the heated surfaces (heater and pins) at steady-state versus Reynolds number (Re) for both geometries. As a reference, the graph contains also the Nusselt number results of Falsetti et al. [42] and the predictions for tube bundles using Zukauskas [142] correlation.

which is common practice for fluid flow across tube banks. In the experiment, the wall temperature was calculated from the two-dimensional temperature and heat flux maps measured on the outer surface of the evaporator base by infrared thermography. An inverse three-dimensional heat conduction problem was then solved to estimate the footprint heat transfer coefficient and Nusselt number. This indirect measurement method is likely affected by an additional uncertainty that cannot be quantified.

A quantitative validation of the two-phase numerical framework against the experimental flow boiling results of Falsetti et al. [42], e.g. pressure drop and heat transfer coefficient, cannot be easily achieved. The main reason is that the experimental data were measured at steady-state conditions after the flow was left to stabilise for a few minutes. In contrast, such a long time cannot be achieved in the numerical simulation owing to the time-step restriction. Furthermore, even if this could be achieved, it would require setting an arbitrary bubble generation frequency, as this parameter is not known from the experiment. Also, the heat transfer coefficient from the experiment is already utilised to set the initial conditions in the two-phase simulation, as explained in Sec. 6.1. As such, numerical and experimental heat transfer coefficients are essentially the same at the beginning of the simulation, and thus their comparison is not indicative. Therefore, for the two-phase validation, we rely on the previous work of Municchi et al. [77], who utilised the present solver to simulate flow boiling in straight microchannels and successfully compared their numerical simulations with selected experimental data from the literature. Nonetheless, in the next sections, a qualitative comparison with the experimental data of Falsetti et al. [42] will still be conducted where possible.

Two-phase validation

A flow boiling simulation at conditions matching one selected configuration from Falsetti et al. [42] was performed to validate the two-phase numerical setup. The simulation is run for an evaporator with inlet restrictions, $G = 1000 \, \text{kg/(m}^2\text{s)}$, $q = 200 \, \text{kW/m}^2$, $T_{sat} = 30 \, ^\circ\text{C}$. Two arrays of pin-fins with their adjacent channels are included in the numerical model, with the domain length limited to 2.1 mm to maintain an affordable computational cost. As initial condition, a small vapour bubble is generated on the fifth pin-fin when the local temperature reaches 319 K, as explained in Sec. 6.1. In the experiment, boiling gives rise to the nucleation of multiple bubbles and this behaviour must somehow be reproduced for a coherent comparison of heat

transfer coefficients. The bubble generation frequency is not known from the experiment, however, Falsetti et al. [143] estimated it to be within the range $6000-8000\,1/\mathrm{s}$ for R236fa in the conditions under investigation. Hence, the validation simulation was run by generating bubbles from the same nucleation spot with a frequency of $7000\,1/\mathrm{s}$, corresponding to a time interval of 0.14 ms between the nucleation events. It takes about 1 ms for the generated bubbles to reach the outlet of the channel, as such there are always about 4-5 bubbles simultaneously present in the simulated domain. Since the outlet boundary condition becomes unsuitable when bubbles are crossing the outlet boundary, bubbles are eliminated as soon as they reach the outlet section. This way, the numerical model is able to reproduce a continuous two-phase flow within the channels. The spatially-averaged wall heat transfer coefficient obtained in the two-phase simulation is plotted as a function of time in Fig. 6.8. The figure also includes the benchmark value measured in the experiment [42] for vapour qualities in the range $0-0.05$, $\overline{h}_{w,exp} = 12300\,\mathrm{W}/(\mathrm{m}^2\mathrm{K})$, which corresponds to the bubbly-slug flow regime simulated. The yellow area in the figure identifies the uncertainty in the
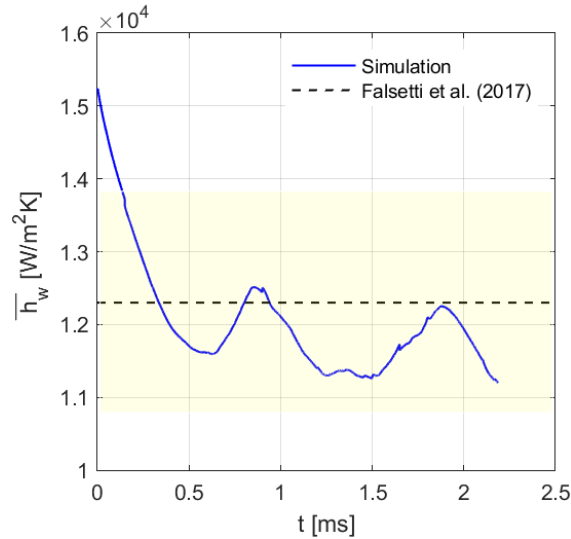
Figure 6.8: Results of the two-phase validation study. The conditions simulated are $G = 1000\,\mathrm{kg}/(\mathrm{m}^2\mathrm{s})$, $q = 20\,\mathrm{W}/\mathrm{cm}^2$, $T_{sat} = 30\,^\circ\mathrm{C}$, evaporator with inlet restrictions. The time-dependent spatially-averaged heat transfer coefficient of the heated surfaces (heater and pins) from the simulation is compared to corresponding data from the experiments of Falsetti et al. [42]. The yellow band identifies the $\pm 12\%$ uncertainty in the experimental value.

experimental value, which was calculated as 12%. At the onset of the two-phase simu-
lation, the heat transfer coefficient is higher than the experiment owing to the initial
condition set. As time elapses, the heat transfer coefficient decreases because the
wall is still heating up, however, as the two-phase flow develops and more bubbles are
generated, the surface area covered by the bubbles increases benefitting heat transfer.
The sequential generation and removal of bubbles as they reach the outlet induces
a periodic trend on the heat transfer coefficient versus time as observed in Fig. 6.8.
The heat transfer coefficient tends to an asymptotically steady-periodic trend with
average value of about $\overline{h}_w = 11800\,\text{W/(m}^2\text{K)}$ in the simulation, which agrees well
with the experiment as deviations remain well within the experimental uncertainty.

6.3.2 Base case

In this section, we provide a detailed analysis of the results obtained for a reference
case run with inlet restrictions, $G = 1000\,\text{kg/(m}^2\text{s)}$, $q = 200\,\text{kW/m}^2$, $T_{sat} = 30\,°\text{C}$
and no inlet subcooling; this was the case used for the mesh independence study in
Sec. 6.2. The bubble nucleation point is set on the fifth cylinder, at $135°$ from the
stagnation point at the cylinder upstream as indicated in Fig. 6.2(b). The nucleation
temperature is set to $319\,\text{K}$, for the heat transfer coefficient at the nucleation point
to coincide with that measured by Falsetti et al. [42] under the same conditions, as
explained in Sec. 6.1.

The discussion will primarily focus on the following aspects: the development of
the bubble shape, the flow dynamics, the morphology of the liquid film thickness,
and their impact on the heat transfer performance of the micro-pin fin evaporator.
Figure 6.9(a) shows the evolution of the bubble equivalent diameter as time elapses
and panels (b) and (c) illustrate corresponding bubble shapes at selected time instants
during the simulation. The bubble equivalent diameter is calculated at each time-step
as the diameter of a spherical bubble of volume equivalent to that of the simulation.
When the ratio of equivalent diameter to channel hydraulic diameter, D_{eq}/d_h, grows
above 1, the bubble becomes strongly confined by the channel walls. As the bubble
nucleates (instant A), it grows very rapidly in size owing to the superheat accumulated
by the liquid in the neighbourhood of the nucleation spot, which is the hottest zone
of the evaporator due to the recirculating fluid in the cylinder wake. The bubble
departs quickly from the cylinder where it nucleated due to the drag exerted by the

incoming liquid and migrates towards the centre of the channel (instants B and C). Its growth rate subsides during this stage due to the cooler liquid far from the heated surfaces.

At about $t = 0.4\,\text{ms}$ (instant D), the bubble has grown in size to occupy the whole channel cross-section and comes in contact with the second array of cylinders (in $y < 0$). At this point, the growth of the bubble is restricted by the pin-fins, which act as bounding walls, the bubble predominantly expands in the flow direction and tends to elongate as observed in straight channels [144]. However, unlike straight channels, the bubble tends to expand also in the width-wise cross-stream direction in the gap between the cylinders. These are hot regions in the evaporator, and thus the sensible heat accumulated in the recirculating fluid in the wakes of the cylinders directly contributes to the evaporation rate of the bubble. Figure 6.9(d) depicts the bubble and the velocity and temperature contours extracted on a horizontal mid-
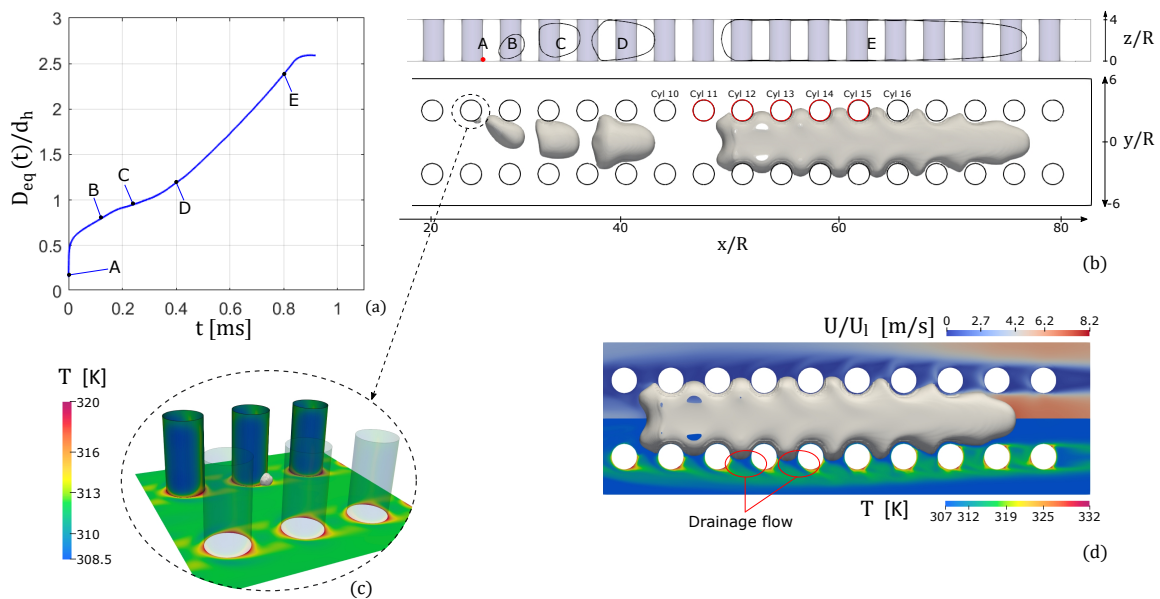
Figure 6.9: Results for reference case run with inlet restrictions, $G = 1000\,\text{kg/(m}^2\text{s)}$, $q = 200\,\text{kW/m}^2$, $T_{sat} = 30\,°\text{C}$ and no inlet subcooling. (a) Dimensionless bubble equivalent diameter versus time. (b) Liquid-vapour interface profiles on a vertical mid-plane $y = 0$ and top view of the bubble profile extracted at different instants indicated in (a). (c) Close-up view near the nucleation site of the bubble, in grey, and temperature contours of the cylinders and heater taken at the boiling onset. (d) Sketch of bubble profile, velocity (top half) and temperature (bottom half) on a horizontal mid-plane ($z = H/2$), extracted at the time instant E.

plane $z = H/2$ at instant E, shortly before the bubble nose reaches the end of the channel. It is interesting to observe that the expansion of the bubble in the gap between the cylinders pushes liquid sideways, away from the cylinder wake. This is not only hot liquid from the stagnation zone but also cooler liquid draining out of the thin liquid film region trapped between the pin-fins and the bubble interface. El Mellas et al. [115] showed that the capillary pressure gradient established between the concave bubble region indented by the cylinder, where pressure is higher, and the convex region formed in the gap between two cylinders, where pressure is lower, causes continuous drainage of the thin film trapped between bubble and cylinder. This drainage flow, emphasised with the red ellipses in Fig. 6.9(d), is composed of cooler liquid at near-saturation conditions due to the thin-film evaporation process, which is manifested by the blue streaks apparent in the temperature contours of Fig. 6.9(d).

To further illustrate the bubbly dynamics during its growth, Fig. 6.10 displays selected profiles of the liquid-vapour interface and temperature field extracted at the time instants labelled as D and E in Fig. 6.9. For each time instant, the figures show the interface profiles and temperature contours on the vertical mid-plane at $y = 0$ and two selected cross-sectional planes in the $y - z$ direction. The two cross-stream planes for each time instant are chosen to be in a region occupied by the bubble ($x/R = 38 - 42$ for instant D; $x/R = 50 - 78$ for E), with one plane centred on a specific cylinder and a second plane located half-way between the same cylinder and the previous one. For time instant D, the selected cylinder is the 9th, corresponding to the planes $x/R \approx 38$ and 40. For time instant E, the selected cylinder is the 15th, corresponding to $x/R \approx 60$ and 62. Surface tension forces, together with the effect of the evaporation, redistribute the liquid surrounding the bubble into thin films covering the cylinders and the top and bottom channel walls, similar to what is observed in square channels [76]. At time instant D, the bubble is not large enough to completely fill the channel and the bubble's cross-sectional shape is still approximately circular, see Fig. 6.10(a) and (b), with the minimum film thickness being detected in the correspondence of the half-height of the channel ($z = H/2$) on the cylinders' surface. As the bubble grows and fills the channel cross-section, the film changes its shape; see instant E in Fig. 6.10(c) and (d). The liquid film becomes thinner, which can be attributed to the gradual evaporation and drying out of the film over time. The position of the minimum film thickness from the mid-height shifts towards the top
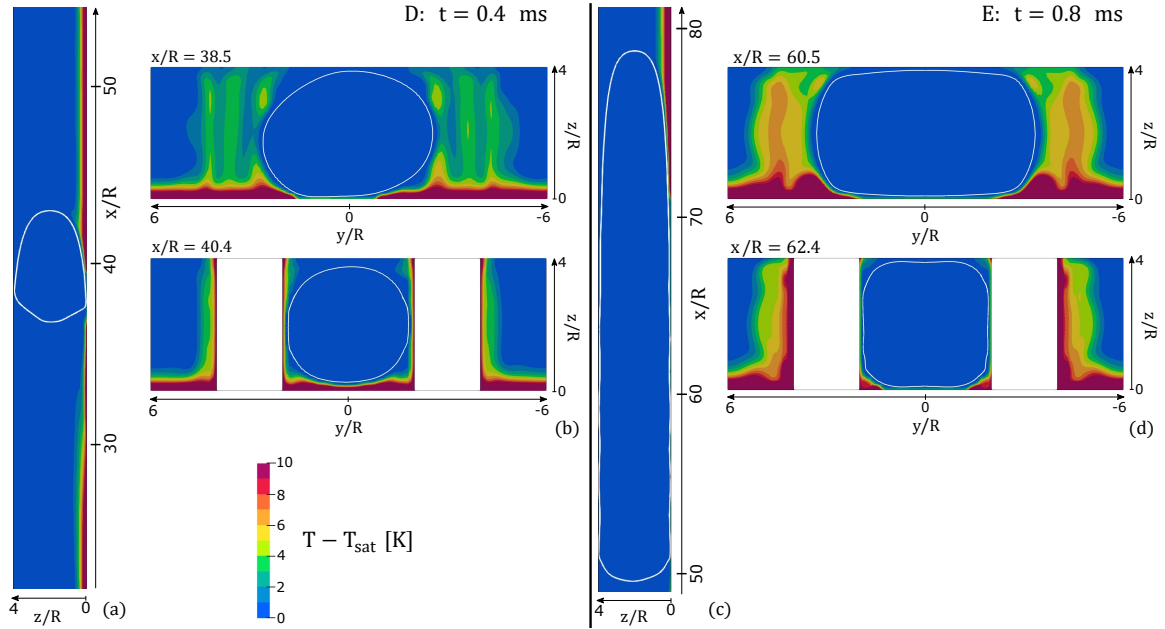
Figure 6.10:   Results for the reference case run with inlet restrictions, $G = 1000 \, \text{kg/(m}^2\text{s)}$, $q = 200 \, \text{kW/m}^2$, $T_{sat} = 30 \, ^\circ\text{C}$ and no inlet subcooling. (a) Liquid-vapour interface profiles and temperature contours on a vertical mid-plane $y = 0$ extracted at the time instant D. (b) Liquid-vapour interface profiles and temperature contours on the cross-section at planes $x/R \approx 38$ and 40, extracted at the time instant D. (c-d) Liquid-vapour interface profiles and temperature contours on the vertical mid-plane $y = 0$ and cross-sections on planes $x/R \approx 60$ and 62, extracted at the time instant E.

and bottom walls, where two dimples appear, identifying two minimum film thickness regions. Where it is not constrained by the fins, the bubble expands remarkably in the cross-stream direction until about $y/R = \pm 3$, and film evaporation contributes to the cooling of the heater surface in the gap between the cylinders.

To better analyse the impact of the two-phase flow on the heat transfer in the evaporator, Fig. 6.11(a,b) provides axial profiles of temperature and Nusselt number, both averaged for each pin-fin. These profiles were extracted at different time instants, as indicated in Fig. 6.9(a). The solid markers represent the pin-fins on the side of positive y of the geometry, where the bubble is initially positioned, while the empty markers represent the pin-fins on the opposite side ($y < 0$). Note that at instant A (boiling onset), the two arrays of pin-fins have the same temperature, and thus a single set of symbols (crosses) is used. The chart also includes time-

averaged results obtained from the entire two-phase simulation. As time elapses, temperatures increase, as the bubble is initialised not at steady-state but once the nucleation conditions are achieved at the heated walls, and thus, Nusselt numbers decrease as the evaporator heats up over time. The highest temperature is detected on the second set of pin-fins, right after the inlet restriction, because the restriction
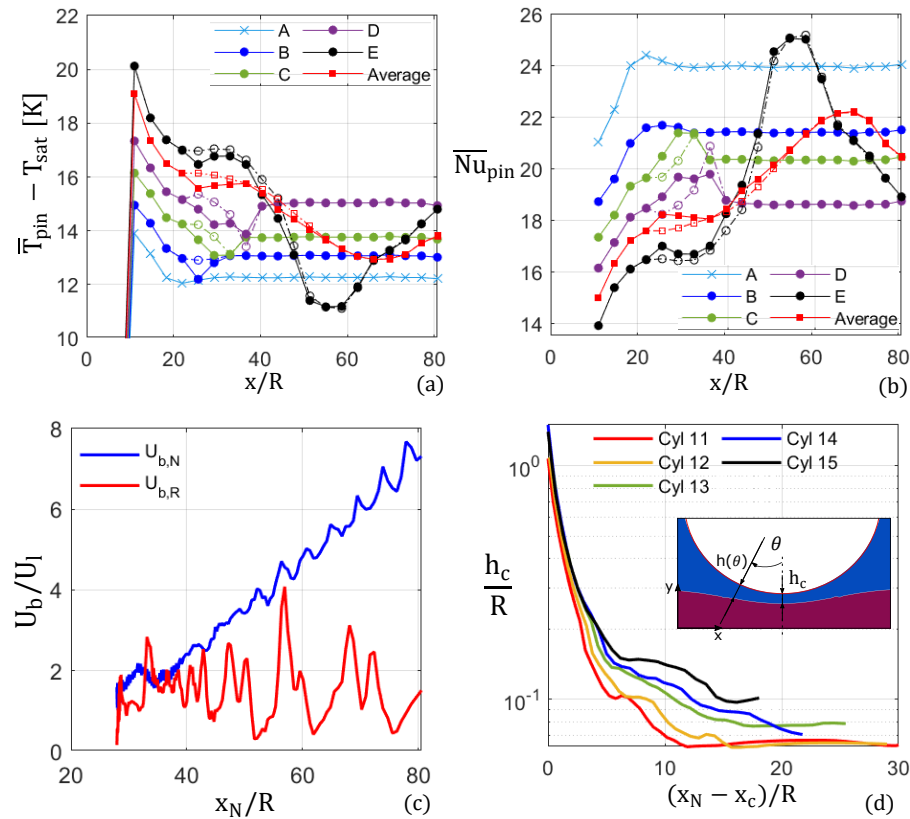
Figure 6.11: Results for the reference case run with inlet restrictions, $G = 1000 \, \mathrm{kg/(m^2 s)}$, $q = 200 \, \mathrm{kW/m^2}$, $T_{sat} = 30 \, ^\circ\mathrm{C}$ and no inlet subcooling. (a-b) Instantaneous two-phase spatially-averaged temperature ($\overline{T}_{pin}$) and Nusselt number ($\overline{\mathrm{Nu}}_{pin}$) of the pin-fins over the streamwise direction, taken at the time instants indicated in Fig. 6.9(a). The full markers indicate the results of the array of pin-fins on the side of positive y, where the bubble nucleates, while the empty markers refer to the array of pin-fins on the opposite side ($y < 0$). The graph also shows the time-average results during the entire two-phase simulation. The legend in (a) applies also to (b). (c) Evolution of the bubble nose ($U_{b,N}$) and rear ($U_{b,R}$) velocity as the bubble travels through the channel. (d) Evolution of the dimensionless liquid film thickness (h_c/R) while the bubble flows downstream, measured over the 11th to 15th cylinders; these were coloured in red in Fig. 6.9(b).

generates a large recirculation region. During the initial stages, when the bubble equivalent diameter is smaller than or on the order of the channel hydraulic diameter (instants B, C and D), the increase of the Nusselt number brought by the two-phase flow is still marginal and mostly felt only by the array of cylinders where nucleation occurs. At the stage when the bubble is elongated (instant E), the beneficial effect of the two-phase flow is considerable and the pin-fin Nusselt number grows from about $\overline{\mathrm{Nu}}_{pin} = 16.5$ in the single-phase region of the channel to $\overline{\mathrm{Nu}}_{pin} = 25$ in the region occupied by the bubble and by the thin evaporating liquid film. At this stage, the cooling effect is relatively uniform between the two arrays of cylinders. The time-average Nusselt number reported with red squares in Fig. 6.11(b) emphasises the beneficial effect of the two-phase flow in causing a localised increase of the heat transfer performance in the region of the evaporator covered by the elongated bubble, as exemplified by the monotonically increasing trend of $\overline{\mathrm{Nu}}_{pin}$ along the evaporator. A qualitatively similar heat transfer trend was observed by Falsetti et al. [42] under the same conditions ($G = 1000\,\mathrm{kg/(m^2s)}$, $q = 200\,\mathrm{kW/m^2}$), which was ascribed to the formation of extended evaporating film regions as the flow pattern developed from slug to annular flow.

Last, Fig. 6.11(c) and (d) report the bubble speed and thickness of the evaporating film formed over the pin-fins surfaces as the bubble grows downstream in the channel. The velocity of the bubble front and rear, denoted as $U_{b,N} = dx_N/dt$ and $U_{b,R} = dx_R/dt$, respectively, are shown as a function of the bubble nose position. Here, x_N and x_R represent the streamwise coordinates of the nose and rear tips of the bubble. The bubble does not reach a steady terminal velocity, but experiences oscillations due to the influence of the pin-fins. The front of the bubble experiences higher velocities compared to the rear due to the evaporation process that makes the bubble longer as time elapses.

The liquid film thickness h_c in Fig. 6.11(d) is measured as the distance between the liquid-vapour interface and cylinder surface evaluated on a horizontal mid-plane ($z = H/2$) along a cross-stream $y-$axis passing through the cylinder centre, as sketched in the figure inset. The film thickness is plotted as a function of the axial distance of the bubble nose (x_N) from the centre of the cylinder (x_c). As the bubble nose flows past the cylinder, h_c decreases due to the combined effect of draining flows [115] and thin-film evaporation. The minimum film thickness values range from about $h_c = 0.06R$ to $0.1R$ (i.e. from 1.5μm to 2.5μm), with progressively thicker films being established on

cylinders downstream the channel due to the rising speed of the bubble nose. These thicknesses compare well with those measured by El Mellas et al. [115] for isothermal flows at similar values of the bubble capillary number, $Ca_b = \mu_l U_{b,N} \sigma \approx 0.2$. The thin-film regions provide a remarkable contribution to heat transfer. The local Nusselt number can estimated by assuming one-dimensional steady-state heat conduction across the film such that the heat transfer coefficient is calculated as $h = \lambda_l / h_c$ and thus $Nu = d_h / h_c$, which yields $Nu = 40 - 67$ for $h_c = 1.5 - 2.5 \, \mu m$. This explains the sudden increase of $\overline{Nu}_{pin}$ observed in Fig. 6.11(b) at instant E in the region where the thin liquid film is formed, i.e. $x/R = 50 - 60$. No liquid film dryout is observed on the pin-fins. The time necessary for evaporation to deplete the liquid film can be estimated as $t_{dry} = h_c \rho_l h_{lv} / q$, which yields $t_{dry} \approx 1.4 - 2.4 \, ms$ for $h_c = 1.5 - 2.5 \, \mu m$. Therefore, the time necessary for evaporation to dry the film is larger than the residence time of the film over the cylinder, which explains why dryout does not occur under the present conditions.

6.3.3   Effect of mass flux

In this section, the impact of the mass flux on the two-phase dynamics and heat transfer performances is investigated. Within micro-heat exchangers, inertial forces can still be relevant despite the small channel sizes, because the use of low-viscosity refrigerants and the need for efficient convective cooling may result in values of the Reynolds number approaching 10^3. Two-phase simulations are run for $G = 500, 1000, 1500, 2000 \, \text{kg}/(\text{m}^2\text{s})$, $q = 200 \, \text{kW}/\text{m}^2$, and no inlet subcooling. Falsetti et al. [42] did not perform measurements for $G = 500 \, \text{kg}/(\text{m}^2\text{s})$ and $G = 2000 \, \text{kg}/(\text{m}^2\text{s})$, and thus the boiling onset temperature for the two-phase simulations cannot be estimated as explained in Sec. 6.1. In order to facilitate a comparison of the numerical results obtained at different flow rates, for all cases the nucleation temperature is set to 319 K for all cases, as it was calculated previously based on the experimental results with $G = 1000 \, \text{kg}/(\text{m}^2\text{s})$.

The bubble equivalent diameter versus time for the different cases is displayed in Fig. 6.12(a). As the mass flux increases, the bubble growth rate during the early stages reduces due to the thinner thermal boundary layers established around the
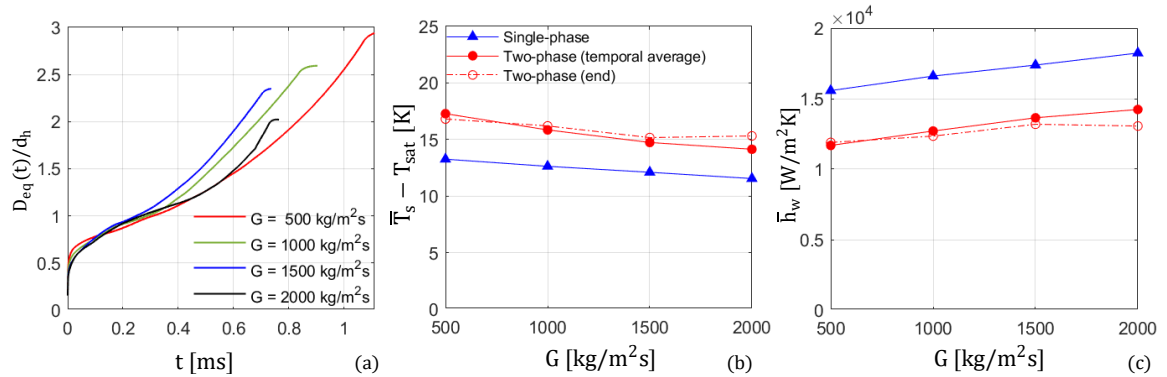
Figure 6.12: Systematic analysis of the effect of the liquid mass flux at the inlet. (a) Dimensionless bubble equivalent diameter (D_{eq}/d_h) versus time. (b-c) Spatially-averaged single- and two-phase temperature $(\overline{T}_s)$ and heat transfer coefficient $(\overline{h}_w)$ of the heated surfaces (heater and pins). The single-phase data refer to the instant of boiling onset; for the two-phase results, data are presented as a time-average over the entire simulation and as instantaneous values at the end of the simulation, when the bubble nose reaches the outlet section. The legend in (b) applies also to (c). The results refer to a case run with inlet restrictions and $q = 200 \, \text{kW}/\text{m}^2$, $T_{sat} = 30 \, °\text{C}$ and no inlet subcooling.

pin-fins. At larger time instants, Fig. 6.12(a) suggests that the growth rate increases with increasing mass flux for $G = 500 - 1500 \, \text{kg}/(\text{m}^2\text{s})$, which is due to the fact that the bubble travels faster along the channel under the increased drag force exerted by the fluid, and thus it covers a larger heated area in the unit time resulting in higher evaporation rates. The bubble grows significantly less for $G = 2000 \, \text{kg}/(\text{m}^2\text{s})$. This can be explained by the high shear force exerted by the incoming liquid that tends to detach the bubble from the hot cylinders already at early stages and by the reduced thickness of the thermal boundary layers that are feeding the liquid evaporation process. Further insight can be gained by inspection of the snapshots of the bubble dynamics at different mass fluxes provided in Fig. 6.13. For $G = 500 \, \text{kg}/(\text{m}^2\text{s})$ and $G = 1000 \, \text{kg}/(\text{m}^2\text{s})$ the process of bubble growth, departure from the nucleation point and elongation appear in a well-ordered sequence, with the bubble exhibiting a rounded rear meniscus and a slender front meniscus as expected in flows governed by capillary forces. Already at $G = 1500 \, \text{kg}/(\text{m}^2\text{s})$, to which it corresponds a Reynolds number of the incoming liquid of $\text{Re} = G d_h / \mu_l = 561$, the process of bubble elongation begins when the bubble is smaller than the channel size due to the high-shear hydrodynamic boundary layers formed by the cylindrical obstacles. The bubble eventually grows to occupy the entire channel cross-section and elongates in the flow direction, although the rear meniscus loses the spherical shape observed at lower mass fluxes and wobbles as the bubble propagates downstream. This is due to the high inertial forces that tend to produce an unsteady dynamic of the tail of long bubbles, as already reported for slug flows in circular channels [120, 119]. At the highest mass flux tested, $G = 2000 \, \text{kg}/(\text{m}^2\text{s})$ ($\text{Re} = G d_h / \mu_l = 748$), the high-shear forces overcome surface tension and cause high deformation and eventually fragmentation of the bubble. Owing to the thinner thermal boundary layers and the high fluid speed, the bubbles quickly reach the end of the channel without growing to a sufficient size to occupy the channel cross-section. Therefore, they are less in contact with the hot cylinder surfaces and are thus characterised by a reduced growth rate, which explains the trend observed in Fig. 6.12(a).

Figure 6.12(b,c)presents the results of single- and two-phase spatially-averaged temperatures and heat transfer coefficients obtained for different mass flow rates. The single-phase data refer to the instant of boiling onset, whereas two sets of two-phase data are plotted, one averaged in time during the entire two-phase simulation, and one evaluated at the end of the two-phase simulation, when the bubble nose reaches the
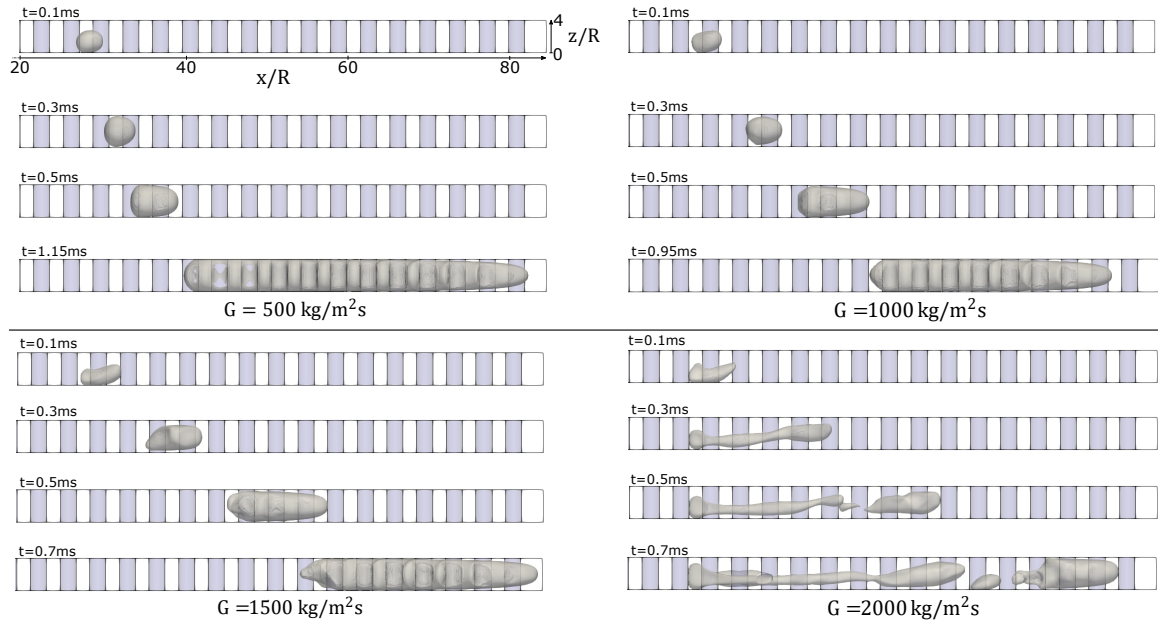
Figure 6.13: Side view of snapshots of bubble growth for different values of the liquid mass flux at the inlet. To aid visualisation, the array of pins in $y < 0$ is removed. The figures show the bubble contour in grey and the cylindrical pin-fins are depicted in violet.

outlet section. Note that the two-phase temperatures are higher than the single-phase ones, with the heat transfer coefficients correspondingly lower, because the evaporator temperature increases over time. As a general trend, the heat transfer performances improve by increasing the mass flow rate, mainly due to the enhanced convective heat transfer between fluid and solid walls. However, the four-fold increase in mass flux from $G = 500 \, \text{kg/(m}^2\text{s)}$ to $G = 2000 \, \text{kg/(m}^2\text{s)}$ only results in a few per cent increase of the heat transfer coefficient, from $\overline{h}_w = 12 \, \text{kW/(m}^2\text{K)}$ to $\overline{h}_w = 14 \, \text{kW/(m}^2\text{K)}$ when considering time-averaged values in Figure 6.12(c). Furthermore, this increasing trend seems to saturate as the mass flux approaches $G = 2000 \, \text{kg/(m}^2\text{s)}$, suggesting that a further increase in the mass flow rate may no longer improve two-phase heat transfer. This is related to the change in the two-phase flow pattern explained above with the aid of Fig. 6.13. Since the bubbles lose their bullet shape due to the high inertial forces and grow to a lesser extent due to the reduced contact time with the heated walls, the surface area of the evaporator covered by a thin evaporating film is significantly reduced, which has a detrimental impact on heat transfer. A comparison with the

trends observed by Falsetti et al. [42] at varying mass fluxes for the same heat load is difficult because non-monotonic trends of h_w versus G were reported, depending on the vapour quality. Nonetheless, in the low vapour quality range which applies well to the present simulations, they detected a generally increasing trend of h_w with G from $G = 750\,\text{kg/(m}^2\text{s)}$ to $G = 1750\,\text{kg/(m}^2\text{s)}$, in agreement with the trend of the present numerical simulations for $G < 2000\,\text{kg/(m}^2\text{s)}$.

6.3.4 Effect of the location of the nucleation site

The position of the nucleation sites in an evaporator is not usually known beforehand, unless nucleation cavities are artificially manufactured. To investigate the effect of the nucleation site location on the bubble dynamics and two-phase heat transfer, we have tested different nucleation positions while keeping these constant conditions: $G = 1000\,\text{kg/(m}^2\text{s)}$ and $q = 200\,\text{kW/m}^2$, with no inlet subcooling. In the cases
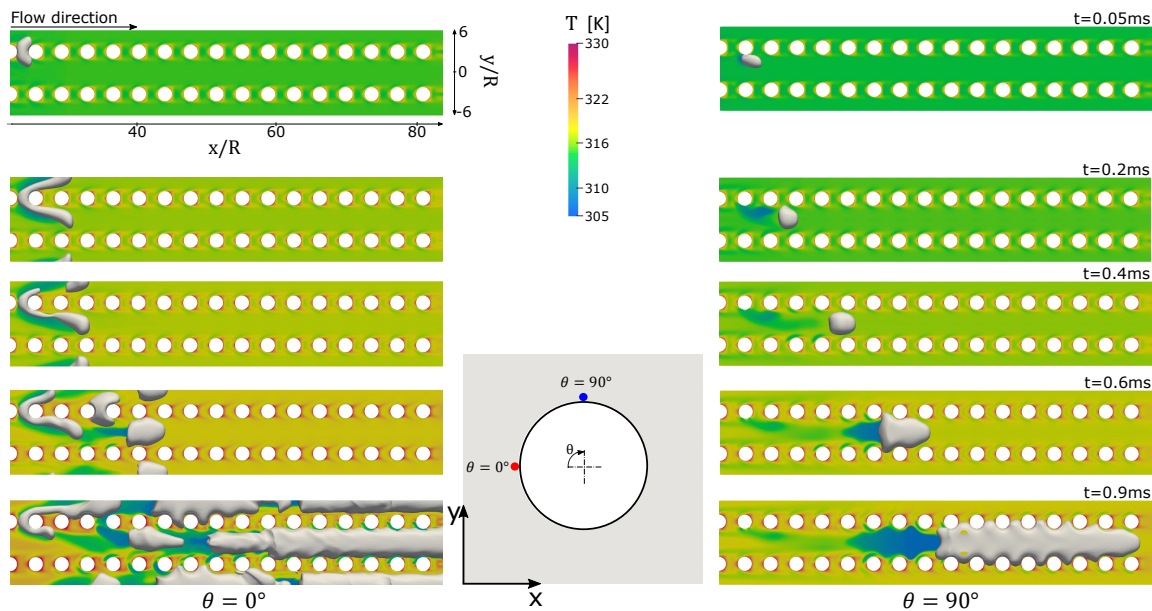
Figure 6.14: Systematic analysis of the effect of the location of the nucleation site. Each set of five figures shows snapshots of the bubble profile and temperature field of the base wall $(z = 0)$ as time elapses, extracted at the same time instants, for the location of the nucleation $\theta = 0°$ and $\theta = 90°$. The nucleation circumferential position around the cylinder is identified by its angle θ calculated as indicated in the inset at the centre of the figure. The results refer to a case run with inlet restrictions, $G = 1000\,\text{kg/(m}^2\text{s)}$, $q = 200\,\text{kW/m}^2$, $T_{sat} = 30\,°\text{C}$ and no inlet subcooling.
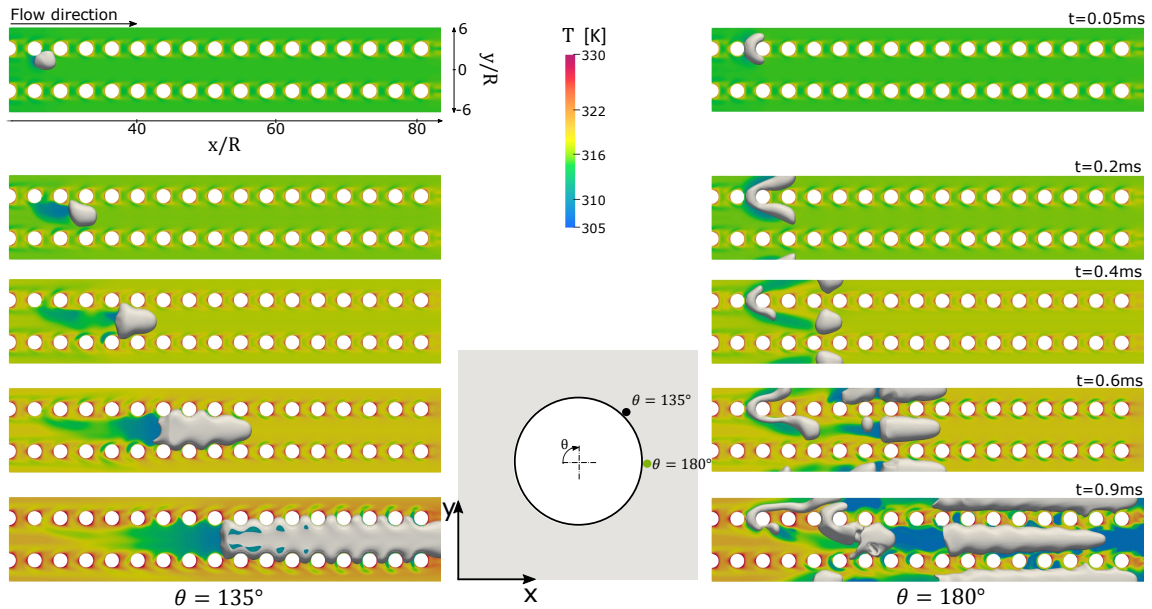
Figure 6.15: Systematic analysis of the effect of the location of the nucleation site. Each set of five figures shows snapshots of the bubble profile and temperature field of the base wall $(z = 0)$ as time elapses, extracted at the same time instants, for the location of the nucleation $\theta = 135°$ and $\theta = 180°$. The results refer to a case run with inlet restrictions, $G = 1000\,\mathrm{kg/(m^2s)}$, $q = 200\,\mathrm{kW/m^2}$, $T_{sat} = 30\,°\mathrm{C}$ and no inlet subcooling.

presented in the previous sections, the nucleation spot was set on the fifth pin-fin at an angle of $\theta = 135°$ from the leading edge of the cylinder. Here, we tested $\theta = 0$, which coincides with the upstream stagnation point on the cylinder surface, its diametrically opposed downstream point $\theta = 180°$, and $\theta = 90°$ which is outside of the flow recirculation region between the pin-fins arrays; in all cases, the bubbles are initialised at the edge between the cylinder surface and the base wall of the evaporator. The locations of the nucleation spots tested are shown in Fig. 6.14- 6.15, together with snapshots of the bubble dynamics and temperature fields. The images provide a top view of the geometry, where the top wall has been removed to aid visualisation. These snapshots capture the growth of the bubble and the evolution of the temperature field of the heater $(z = 0)$, taken at the same time instants for the various nucleation sites tested. When the bubble is initially positioned in the stagnation regions, $\theta = 0, 180°$, there is a more substantial bubble growth. This can be attributed to the bubble being trapped within the static flow region where the fluid
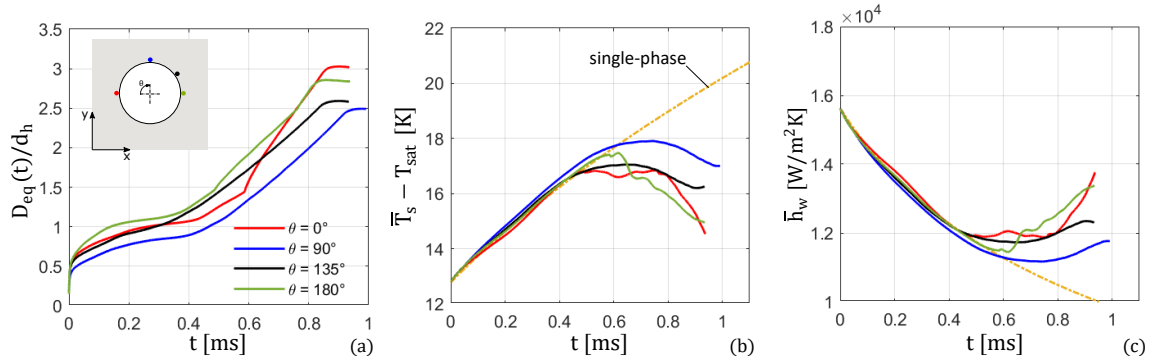
Figure 6.16: Systematic analysis of the effect of the location of the nucleation site. (a) Dimensionless bubble equivalent diameter (D_{eq}/d_h) versus time. (b-c) Spatially-averaged temperature ($\overline{T}_s$) and heat transfer coefficient ($\overline{h}_w$) of the heated surfaces (heater and pins) as time elapses. The legend in (a) applies also to (b-c). The results refer to a case run with inlet restrictions, $G = 1000\,\mathrm{kg/(m^2s)}$, $q = 200\,\mathrm{kW/m^2}$, $T_{sat} = 30\,^\circ\mathrm{C}$ and no inlet subcooling.

is warmer, allowing for an extended period of contact with the walls and, consequently, a more significant growth. The bubble continues to expand symmetrically around the downstream cylinder, and eventually a portion of it escapes from the stagnant region. The high shear exerted by the fluid flowing through the evaporator channels breaks up the bubble into smaller units, which occupy all the channels available and grow until they become elongated bubbles. On the other hand, when the bubble is initialised in a point exposed to the flow outside the stagnant regions, $\theta = 90^\circ$, it detaches quickly from the pin-fin surface due to shear, and thus it grows more slowly. The bubble dynamics observed in Fig. 6.15 for $\theta = 90^\circ$ resemble those for $\theta = 135^\circ$, where break-up does not occur, and a single elongated bubble unit flows through the channel. It is interesting to note that, although the flow rate is the same for all cases, the elongated bubbles present different shapes depending on the initial position of the nucleation spot. When $\theta = 0$ and 180° multiple bubbles flow through adjacent channels, they do not seem able to expand in the cross-stream gap between the cylinders, while they do so in the cases where $\theta = 90^\circ$, 135° and only one bubble is present. This may be due to the fact that when multiple bubbles are present in adjacent channels, the bubbles cannot displace the liquid out of the recirculation regions as they flow downstream the channel.

Plots of the bubble volume versus time and resulting temperature and heat trans-

fer coefficients are displayed in Fig. 6.16. As expected, the bubble growth rates are higher when initialised in the stagnation regions. In contrast, the case with $\theta = 90°$ exhibits the slowest growth rate because the bubble departs early from the nucleation spot. Figure 6.16(b) and (c) report the spatially-averaged temperatures and heat transfer coefficients for the whole heated surfaces (pin-fins and base wall) as a function of time. For reference, the figure also shows the temporal evolution of temperature and heat transfer coefficient that would be achieved in single-phase, in the absence of nucleation. The heat transfer performance is closely related to the bubble growth rate. When the bubbles grow substantially in the recirculation regions and break up, eventually distributing evenly among the parallel channels, the heat transfer coefficient grows quickly because a larger portion of the heated area is covered by the two-phase flow, and thus, it benefits from more efficient heat transfer mechanisms. The heat transfer coefficient achieved at the end of the simulation for bubbles nucleating at 0 and 180° is about 15% higher than that obtained for bubbles nucleating at 90° or 135°. The beneficial effect of two-phase cooling over single-phase cooling becomes evident at the later time instants, for $t > 0.6$ ms, when the bubbles have grown sufficiently large to cover larger areas of the heated surface. As the two-phase flow develops, temperatures drop significantly, and the heat transfer coefficient increases steeply over time, while heat transfer performances deteriorate in single-phase flow as velocity and temperature fields develop towards the steady-state regime.

6.3.5   Effect of inlet subcooling

In this section, we investigate the impact of the inlet subcooling on the two-phase flow and heat transfer. It is common to have subcooled conditions at the entrance of two-phase heat sinks to prevent boiling onset at the inlet of the evaporator. This may cause backflow of vapour bubbles into the inlet manifold, triggering flow instabilities and maldistribution. Falsetti et al. [42] set the inlet subcooling to 5 ± 1.5 K by adjusting the fluid temperature at the inlet manifold plenum of the evaporator using a pre-heater. Using numerical simulations, we study values of inlet subcooling up to $\Delta T_{sub} = 5$ K, while keeping mass flux and heat flux constant to $G = 1000$ kg/(m²s) and $q = 200$ kW/m². In this case, a wider domain ($W = 450 \, \mu$m) with three arrays of pin-fins is utilised, and bubbles are nucleated on the central array. Due to subcooling, the location of boiling onset changes along the evaporator depending on ΔT_{sub}, e.g.

boiling onset is expected to shift downstream for increasing values of ΔT_{sub}. The procedure adopted to identify the nucleation location for each ΔT_{sub} is explained below.

As a subcooled liquid enters the heat sink, the fluid temperature increases along the flow direction while its pressure and associated saturation temperature decrease due to pressure drop. When the fluid temperature increases above its saturation temperature, boiling is assumed to begin and we define as x_{act} the axial location where this occurs. The pressure and temperature at the inlet of the evaporator were not measured by Falsetti et al. [42], and thus these need to be estimated. In the experiment, the outlet saturation temperature of the fluid was maintained at $T_{sat} = 30.5\,°\mathrm{C}$ ($\pm 0.5\,°\mathrm{C}$), to which it corresponds a saturation pressure of about $p_{sat} = 325\,\mathrm{kPa}$. The total pressure drop in the evaporator measured between inlet and outlet manifold plenums for $G = 1000\,\mathrm{kg/(m^2 s)}$ and $q = 200\,\mathrm{kW/m^2}$ in the experiment in flow boiling conditions was of about $25\,\mathrm{kPa}$. This can be used to estimate the inlet pressure giving $p_{sat,inl} = 350\,\mathrm{kPa}$, which corresponds to a saturation temperature of about $T_{sat,inl} = 32.8\,°\mathrm{C}$. This is the value considered as the inlet saturation temperature in the present simulations. We study three values of the inlet subcooling, $\Delta T_{sub} = 2\,\mathrm{K}, 4\,\mathrm{K}, 5\,\mathrm{K}$, by setting the inlet temperature in the simulations to $T_{inl} = 30.8\,°\mathrm{C}, 28.8\,°\mathrm{C}, 27.8\,°\mathrm{C}$. Figure 6.17 shows the axial profiles of the bulk fluid temperature obtained in single-phase for these three values of ΔT_{sub}. To find the locations of the nucleation sites for each ΔT_{sub}, it is necessary to cross each profile with the profile of the saturation temperature along the evaporator. This is obtained from the single-phase pressure drop in the simulation, giving the red dashed curve in Fig. 6.17. The three nucleation site locations highlighted with blue points in Fig. 6.17 correspond to the x_{act} locations used in the simulations. Table 6.5 summarises the coordinates of the nucleation spots and corresponding saturation temperatures.

Hence, three different simulations were performed with three different values of inlet subcooling by initialising the vapour bubble at different axial locations along the channel. The bubbles are always initialised on the surface of the nearest pin-fin to the location identified in Tab. 6.5, and placed at the edge between the pin-fin surface and bottom wall of the evaporator, at an angle of 135° with the leading edge of the cylinder. An initial single-phase simulation is run for all cases to obtain partially developed velocity and temperature fields. The single-phase simulation terminates when the temperature at the nucleation spot reaches a superheat of $16\,\mathrm{K}$, calculated
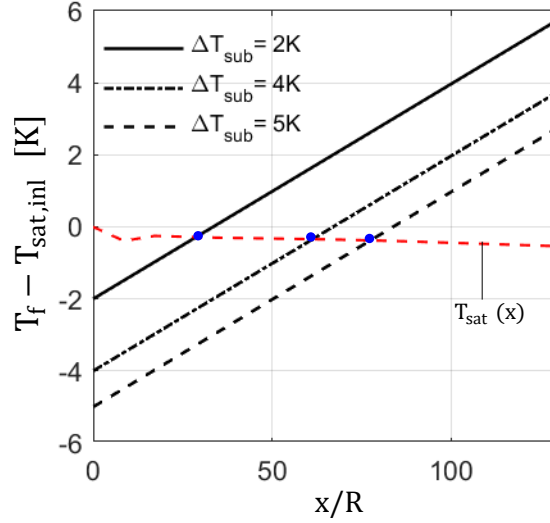
Figure 6.17: Evolution of the bulk temperature (T_f) and locations of the nucleation spots (x_{act}) as a function of the subcooling degree at the inlet.

from the experimental heat transfer coefficient value of $12.5\,\text{kW}/(\text{m}^2\text{K})$ as explained in Sec. 6.2. All simulations were run with a domain length of $3.2\,\text{mm}$. Figure 6.18(a) illustrates the evolution of the dimensionless bubble equivalent diameter over time. Initially, the growths of the bubbles appear to be similar among different subcooling degrees. However, once the bubbles depart from the pin-fin walls, different behaviours emerge. Snapshots of the bubble dynamics at different time instants are displayed in Fig. 6.18(c) and (d) for $\Delta T_{sub} = 2\,\text{K}$ and $4\,\text{K}$, respectively. Upon detachment from the pin-fin walls, the bubbles tend to move towards the centre of the channel, outside the thermal boundary layer. This motion brings them into a region where the surrounding fluid is highly subcooled, particularly near the top surface of the

ΔT_{sub} [K]	$T_{sat,inl}$ [K]	T_{inl} [K]	$\Delta p_{inl-act}$ [kPa]	T_{sat}[K]	x_{act} [m]
2	305.95	303.95	1.1	305.8	8.375×10^{-4}
4	305.95	301.95	2.1	305.55	16.75×10^{-4}
5	305.95	300.95	2.5	305.5	20.94×10^{-4}

Table 6.5: Simulation parameters for the analysis of the effect of subcooling. ΔT_{sub} denotes the inlet subcooling, $\Delta p_{inl-act}$ indicates the single-phase pressure drop between the inlet and the nucleation point, which is located at x_{act}, T_{sat} is the saturation temperature at the nucleation point.
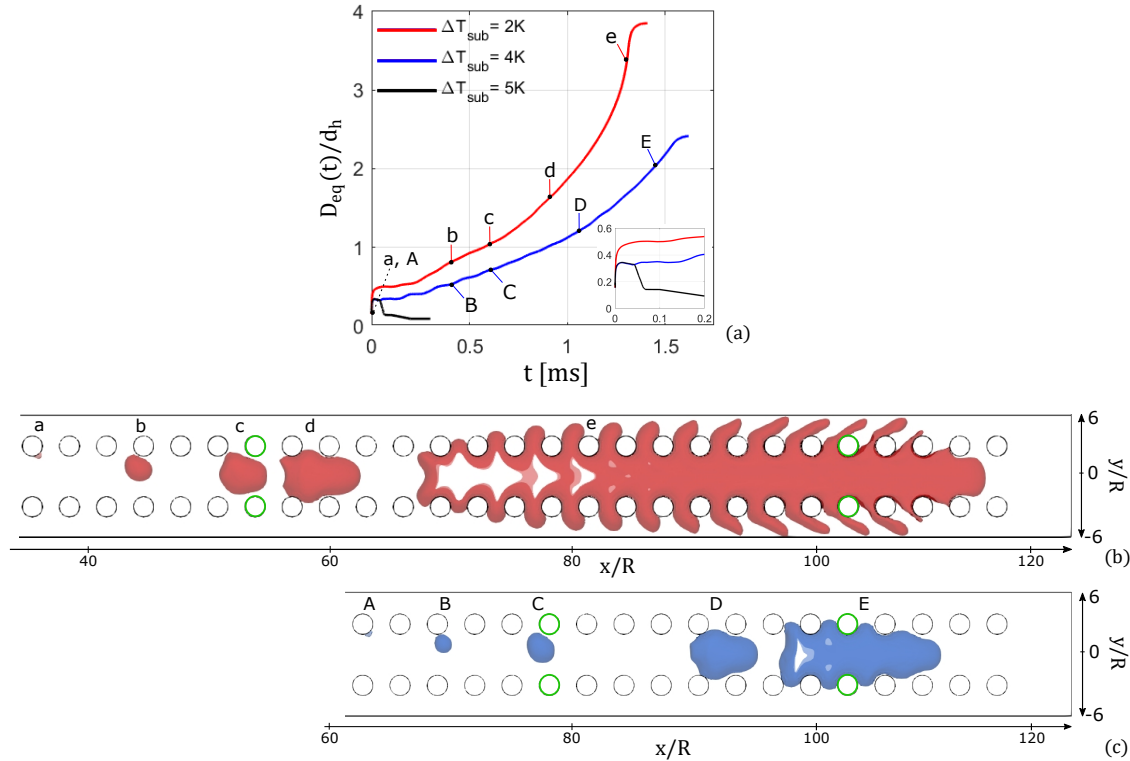
Figure 6.18: Systematic analysis of the effect of the subcooling of the fluid at the inlet. (a) Dimensionless bubble equivalent diameter versus time. The inset shows a close-up view of the first instants of the simulations until the detachment of the bubble occurs. (b) Top view of the bubble profile extracted at the different instants indicated in (a), for subcooling at the inlet $\Delta T_{sub} = 2$ K. (c) Top view of the bubble profile extracted at different instants indicated in (a), for subcooling at the inlet $\Delta T_{sub} = 4$ K. The green cylinders in (b) and (c) identify the cross-sections analysed in Fig. 6.19 and 6.21. Other conditions are: $G = 1000 \, \text{kg}/(\text{m}^2\text{s})$ and $q = 200 \, \text{kW}/\text{m}^2$.

evaporator. Condensation occurs in these regions of the bubble surface and its intensity becomes more significant with higher degrees of subcooling. Every time the bubble approaches a new set of warm pins propelled by the fluid flow, an increase in size is observed, with evaporation becoming dominant over condensation. On the other hand, when the bubble moves away from the set of pins, the surrounding fluid temperature is lower, and the growth of the bubble is arrested until a new set of pins is encountered. This induces oscillations on the plots of the bubble volume over time during the initial stages as manifested by the curves in Fig. 6.18(a). This oscillatory behaviour becomes more evident as the degree of subcooling increases. For example,

in the case of $\Delta T_{sub} = 4\,\text{K}$, this oscillatory phase occurs for a longer duration. A subcooling degree of $4\,\text{K}$ requires nearly double the time compared to the case with a subcooling of $2\,\text{K}$ for this oscillatory stage to terminate. This pattern continues until the bubble reaches a length of approximately $L_b \approx 2R$, which is the minimum size that ensures that the bubble always remains in close contact with the pin-fins. Note that for the highest degree of subcooling studied, $\Delta T_{sub} = 5\,\text{K}$, condensation overcomes evaporation, and the bubble condenses completely after departing from the pin-fin surface. Therefore, no snapshots are presented for this case as the bubble immediately condensate and disappears. For $\Delta T_{sub} = 2\,\text{K}$ and $4\,\text{K}$, the development of the bubble shape as it travels through the channel follows a similar pattern to that observed in the previous sections at saturation conditions. The bubble primarily grows in the direction of the flow, driven by the heat transfer from the heater and pin-fins. Once the bubble becomes large enough to fill the square channel cross-section between the cylinders, it expands into the gaps between them. This expansion can be visualised particularly at the time instant e for the test case with a subcooling of $\Delta T_{sub} = 2\,\text{K}$, see Fig. 6.18(c), where an additional effect becomes apparent. Due to the low subcooling and thus high evaporation rate, the bubble begins creating vapour branches penetrating the neighbouring channels. The fluid flow in the empty channels is considerably stronger because the presence of the bubble restricts the free flow of fluid within the channel. Consequently, these vapour branches are pushed and elongated in the direction of the flow. For both $\Delta T_{sub} = 2\,\text{K}$ and $4\,\text{K}$, as the bubble approaches the outlet section, dry patches start to form on the surface of the bubble. These are identified as white regions within the bubble in Fig. 6.18(b) and (c). In the case of a subcooling of $2\,\text{K}$, the area covered by these dry patches is significantly larger, as expected, leading to a decrease in heat transfer performance. Increasing the degree of subcooling results in a reduction in bubble nose velocity and, consequently, the length of the bubble.

Figures 6.19 and 6.21 present snapshots of the liquid-vapour interface profiles and temperature contours at selected times and over selected planes for the cases run with $\Delta T_{sub} = 2\,\text{K}$ and $\Delta T_{sub} = 4\,\text{K}$. Each figure includes the liquid-vapour interface profiles and temperature contours on the vertical mid-plane $y = 0$ and on two cross-sectional planes orthogonal to the flow direction, for two different time instants, similarly to those previously shown in Fig. 6.10 for the case with no inlet subcooling. The cylinders near which the $y-z$ cross-sectional planes are extracted are highlighted
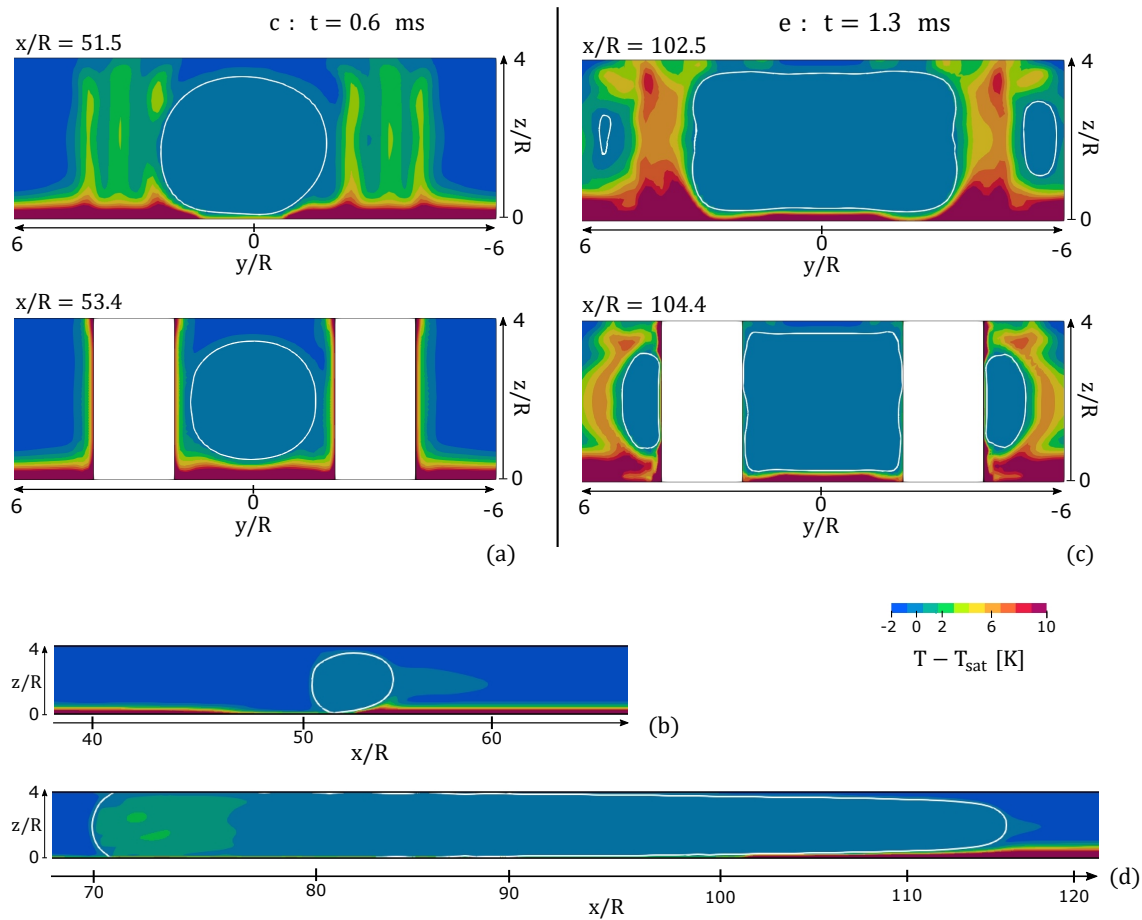
Figure 6.19: Simulation results for the simulation case run with an inlet subcooling of $\Delta T_{sub} = 2\,\text{K}$. (a) Liquid-vapour interface profiles and temperature contours on the vertical mid-plane $y = 0$, extracted at time instant c. (b) Liquid-vapour interface profiles and temperature contours on the cross-section at planes $x/R \approx 51$ and 53, extracted at time instant c. (c,d) Liquid-vapour interface profiles and temperature contours on the vertical mid-plane $y = 0$ and cross-sections on planes $x/R \approx 102$ and 104, extracted at time instant e. The results refer to a case run with inlet restrictions, $G = 1000\,\text{kg/(m}^2\text{s)}$ and $q = 200\,\text{kW/m}^2$.

in green in Fig. 6.18(b,c). For $\Delta T_{sub} = 2\,\text{K}$, Fig. 6.19(a,b) reveals that at time instant c, the bubble is already slightly elongated, although thick liquid films are still present around the pin-fins surfaces, the top and the bottom walls of the evaporator. Figure 6.20(a,b) depict the axial profiles of the average temperature and heat transfer coefficient for each pin-fin at different time instants, and a slight dip in temperature appears at $x/R \approx 50$ at time c, owing to the presence of the bubble. At time e,
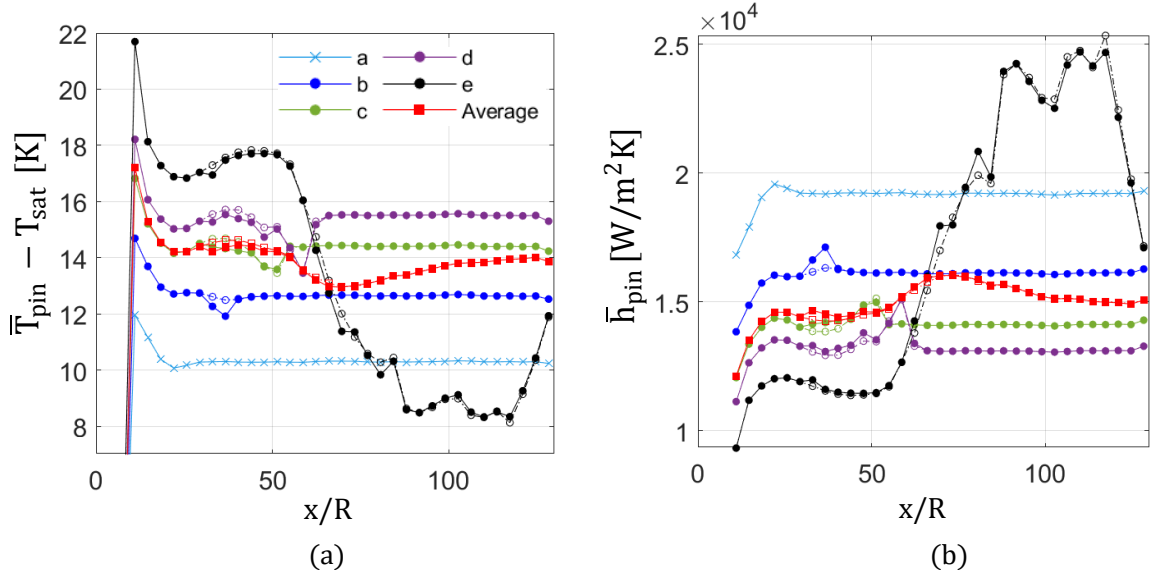
Figure 6.20: Simulation results for the simulation case run with an inlet subcooling of $\Delta T_{sub} = 2\,\text{K}$. (a,b) Instantaneous two-phase spatially-averaged temperature $(\overline{T}_{pin})$ and heat transfer coefficient $(\overline{h}_{pin})$ of the pin-fins over the streamwise direction, taken at the time instants indicated in Fig. 6.18(b). The full markers indicate the results of the array of pin-fins on the side of positive y, where the bubble nucleates, while the empty markers refer to the array of pin-fins on the opposite side $(y < 0)$. The graph also shows the time-average results over the entire two-phase simulation. The legend in (a) applies also to (b). The results refer to a case run with inlet restrictions, $G = 1000\,\text{kg}/(\text{m}^2\text{s})$ and $q = 200\,\text{kW}/\text{m}^2$.

Fig. 6.19(c,d), the bubble has expanded in the cross-stream direction with vapour branches extending in the neighbouring channels. Being now confined by the pin-fins and the top/bottom surfaces of the evaporator, the cross-sectional shape of the liquid-vapour interface takes a square or rectangular shape with thin liquid films covering all surfaces. The temperature field on the vertical mid-plane $y = 0$ reveals that the vapour region near the bubble tail has become superheated, this is due to the vapour contact with the heated surface of the evaporator established at the bubble tail, owing to the dryout of the liquid film that was apparent in Fig. 6.18(c) for $x/R = 70 - 80$. The axial profile of the heat transfer coefficient at time e reported in Fig. 6.20(b) shows a two-fold increase in the zone occupied by the bubble, reaching peak values of $\overline{h}_{pin} = 25\,\text{kW}/(\text{m}^2\text{K})$ for $x/R = 80 - 115$, whereas slightly lower values are detected near the bubble tail due to liquid film dryout occurring around the pin-fins.
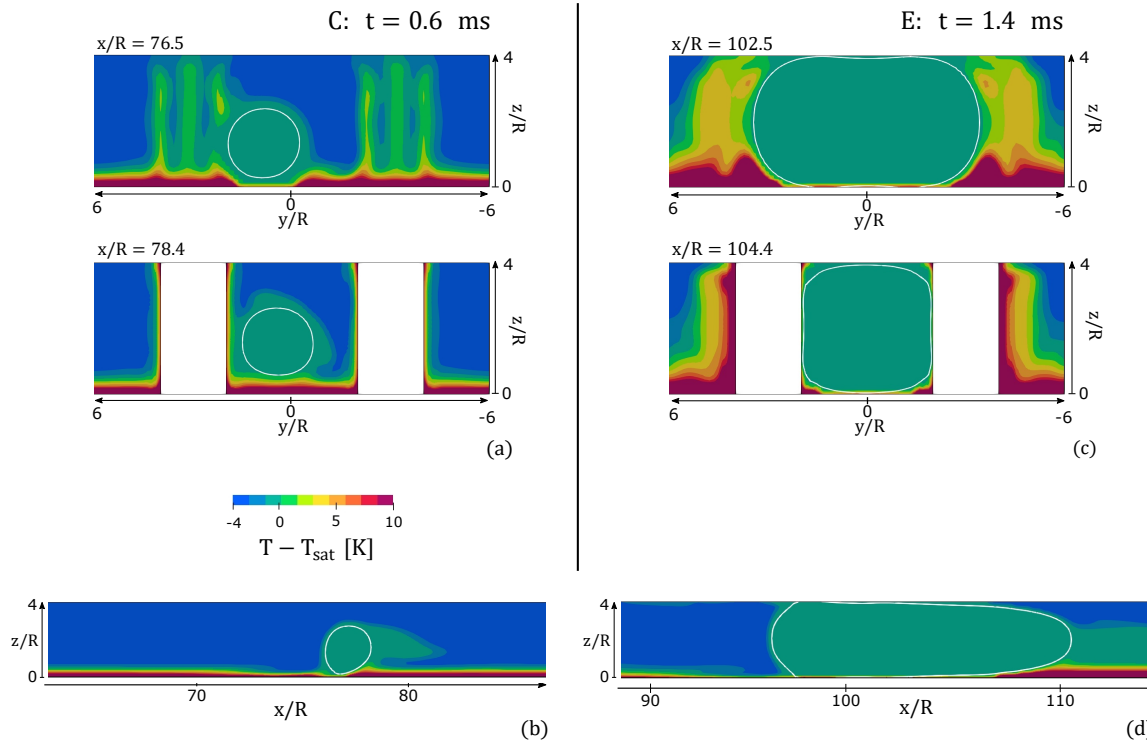
Figure 6.21: Simulation results for the simulation case run with an inlet subcooling of $\Delta T_{sub} = 4\,\text{K}$. (a) Liquid-vapour interface profiles and temperature contours on the vertical mid-plane $y = 0$, extracted at time instant c. (b) Liquid-vapour interface profiles and temperature contours on the cross-section at planes $x/R \approx 76$ and 78, extracted at time instant C. (c,d) Liquid-vapour interface profiles and temperature contours on the vertical mid-plane $y = 0$ and cross-sections on planes $x/R \approx 102$ and 104, extracted at time instant E. The results refer to a case run with inlet restrictions, $G = 1000\,\text{kg/(m}^2\text{s)}$ and $q = 200\,\text{kW/m}^2$.

The situation differs when a higher degree of subcooling, $\Delta T_{sub} = 4\,\text{K}$, is considered. A comparison of the bubble sizes in Fig. 6.18(b) and (c) for time instants b ($\Delta T_{sub} = 2\,\text{K}$) and B ($\Delta T_{sub} = 4\,\text{K}$), both at $t = 0.4\,\text{ms}$ after nucleation, demonstrates that the bubble diameter at the departure from the nucleation site becomes smaller as subcooling increases. Inspection of the liquid-vapour interface profiles in Fig. 6.21 indicates that at time instant C ($t = 0.6\,\text{ms}$, coincident with time c for $\Delta T_{sub} = 2\,\text{K}$), the bubble is still smaller than the channel size. Thus, its presence is barely perceptible from the temperature and heat transfer coefficients plots in Fig. 6.22(a) and (b). At time instant E, shortly before reaching the end of the simulation domain, the bubble has become elongated so that very thin liquid films are established around

(a)   (b)
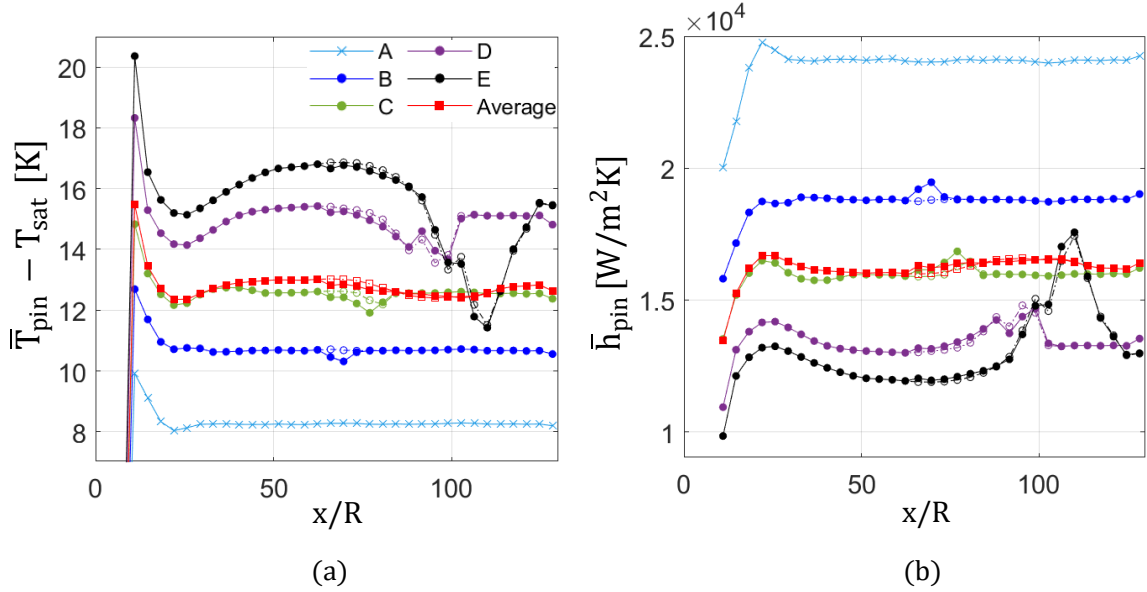
Figure 6.22: Simulation results for the simulation case run with an inlet subcooling of $\Delta T_{sub} = 4$ K. (a,b) Instantaneous two-phase spatially-averaged temperature ($\overline{T}_{pin}$) and heat transfer coefficient ($\overline{h}_{pin}$) of the pin-fins over the streamwise direction, taken at the time instants indicated in Fig. 6.18(b). The full markers indicate the results of the array of pin-fins on the side of positive y, where the bubble nucleates, while the empty markers refer to the array of pin-fins on the opposite side ($y < 0$). The graph also shows the time-average results over the entire two-phase simulation. The legend in (a) applies also to (b). The results refer to a case run with inlet restrictions, $G = 1000$ kg/(m^{2}s) and $q = 200$ kW/m^2.

the pin-fins and on the top and bottom evaporator walls, with Fig. 6.18(d) indicating that film dryout is initiating near the bubble tail. Temperature and heat transfer coefficient at time E exhibit a rapid increase from $x/R = 90$, despite the tip of the bubble tail being located at $x/R = 95$. This is because the bubble transit cooled down the wall and reduced the thickness of the thermal boundary layer over the pin-fins and bottom surface of the evaporator, as it is visible in Fig. 6.21(c). A peak on the heat transfer coefficient of $\overline{h}_{pin} = 17.5$ kW/(m^{2}K) at $x/R \approx 104 - 108$ is apparent, which corresponds to the two most downstream pin-fins that are fully covered by a thin evaporating film. Since with $\Delta T_{sub} = 4$ K the bubble is shorter, and the pin-fin surface area covered by the evaporating film is smaller than that achieved for $\Delta T_{sub} = 2$ K, the maximum value of the two-phase heat transfer coefficient calculated at instant E is about 30% lower. However, the time-average value calculated over

the entire two-phase simulation (red squares in Fig. 6.20(b) and 6.22(b)) is slightly higher due to the larger subcooling.

In summary, the results discussed above indicate that a higher degree of subcooling tends to decrease the overall two-phase heat transfer coefficient. This effect arises because bubbles grow more slowly under these conditions, thereby delaying the beneficial effects of two-phase heat transfer. This observation is in agreement with the experimental findings reported by Chang et al. [45]. It is important to note that subcooling requires additional energy to cool the fluid below its saturation temperature. Despite this energy requirement, subcooling is still commonly employed in practical applications. This frequent use is partly because two-phase systems are not as widely adopted as single-phase systems, due in part to their complexity and the challenges associated with managing them effectively.

6.4 Conclusions

This chapter presented the results of a computational study of flow boiling in a micro-pin fin evaporator. The numerical model of the evaporator included in-line arrays of pin-fins of diameter of $50\,\mu$m and height of $100\,\mu$m, streamwise pitch of $91.7\,\mu$m and cross-stream pitch of $150\,\mu$m, to reproduce the micro-pin fin evaporator studied experimentally by Falsetti et al. [42]. The fluid utilised is refrigerant R236fa at a saturation temperature of $30\,°$C. The range of operating conditions simulated covers values of mass flux $G = 500 - 2000\,$kg/(m²s), heat flux $q = 200\,$kW/m², and inlet subcooling of $\Delta T_{sub} = 0 - 5\,$K. The numerical simulations were performed using boiligFoam solver in OpenFOAM v2106 with a geometric Volume Of Fluid method to capture the interface dynamics. The dynamics of the bubbles and thin evaporating liquid films as they evolve through the pin-fin arrays and the corresponding heat transfer mechanisms were studied in detail. The main conclusions of this work are as follows:

- In single-phase flow, the flow past the arrays of pin-fins becomes weakly unsteady when the Reynolds number, calculated as $\text{Re} = Gd_h/\mu_l$ with d_h being the hydraulic diameter of the straight channel formed between the arrays, grows above about 400, with vortex shedding visible when $\text{Re} > 600$. While the single-phase friction factor decreases when increasing Re up to $\text{Re} \approx 600$, it increases

when Re is above 600 due to the additional pressure drop induced by vortex shedding.

- In single-phase flow, the cylinders exhibit hot spots at circumferential locations identified at 135° from the upstream stagnation point. These hot spots may act as potential nucleation sites, in agreement with existing experimental evidence [44].

- Vapour bubbles nucleated at 135° from the upstream stagnation point detach early from the pin-fin surface and, at saturated conditions, quickly elongate along the channel formed between the pin-fin arrays. Thin liquid films form around the cylinders, and heat transfer is enhanced by a combination of film evaporation and heat convection in the gaps between the cylinders, with up to +50% increase in Nusselt number compared to the single-phase case for $G = 1000 \, \text{kg}/(\text{m}^2\text{s})$.

- Higher flow rates yield higher heat transfer coefficients in the single-phase flow regions of the evaporator but lower heat transfer coefficients in the two-phase flow region because the thinner thermal boundary layers reduce the evaporation rates. When G is increased to $2000 \, \text{kg}/(\text{m}^2\text{s})$, the overall effect is a reduction in the average heat transfer performance of the evaporator.

- The location of the nucleation site influences the subsequent bubble dynamics and heat transfer significantly. When the bubble nucleates in the stagnation region between consecutive pin-fins (0° and 180°), it grows faster and eventually fragments into smaller bubbles. This increases the surface area covered by the two-phase flow and leads to an average heat transfer coefficient that is about 16% higher than that observed for bubbles nucleating at 90°.

- Higher inlet subcooling decreases the two-phase heat transfer coefficients due to condensation occurring when bubbles depart from the hot pin-fin surfaces. At a subcooling of 5 K, bubbles collapse completely once they depart from the pin-fins.

In conclusion, the dynamics of bubbles and flow boiling in micro-pin fin evaporators are significantly different from those observed in straight microchannels. Based on observations from the previous investigation on adiabatic conditions (Ch. 5), the study

was simplified by identifying similar behaviours. This aspect allowed for a more direct analysis of the dynamics involved. This work also includes the first accurate validation of boiling models in microchannels against experimental data, thus establishing a benchmark for boiling studies at the micro-scale. The results gathered in this study, can be considered as a validation, and will be beneficial in the next analysis, where the effects of the variation of the pin-fins geometry and configuration of the evaporator on the flow dynamics and heat transfer performance are investigated in Ch. 7. Computational heat transfer prediction models would benefit from the availability of finely resolved experimental data for film thickness, bubble dynamics and local heat transfer measurements, which are becoming increasingly available for straight channels but are not yet available for two-phase flows across pin-fin geometries.

Chapter 7

Analysis of micro-pin fin evaporators with different shape

This final chapter of the thesis presents a comprehensive study examining the impact of pin-fin shapes on flow dynamics and heat transfer[1]. The primary objective is to elucidate the intricate interplay between pin shapes and their influence on both flow dynamics and heat transfer efficiency. The configuration and arrangement of pin-fins are recognised as pivotal factors in shaping flow dynamics and optimising heat transfer performance. As illustrated in the literature review [1, 33, 34, 35, 36], the selection of pin-fin shapes offers a diverse range of possibilities. Therefore, this chapter undertakes a comparative analysis of various pin-fin shapes. The shapes under scrutiny include the conventional cylindrical, cubic, diamond, triangular, and drop-shaped fins. Additionally, the investigation explores scenarios involving a staggered arrangement of pins, specifically focusing on cylindrical shapes. The chapter is organised in two parts. The initial part presents the outcomes of a single-phase study, accompanied by a thorough examination of mass flux effects. Subsequently, the second part focuses on the results of a two-phase investigation, considering a single value of mass flux.

---

[1]A manuscript is in preparation to present the results of this chapter.

7.1 Single-phase investigation

In general, the primary objective when the pin shape is changed is to augment the heat transfer coefficient without causing an undesirable increase in pressure drop. In this section, we present comparative results for different pin-fin shapes, and the simulations also encompass a comprehensive single-phase mass flux study. It is important to note that in the experiment conducted by Falsetti et al. [42], used in the previous Ch. 6 as a comparison, only cylindrical-shaped pins were utilised, rendering a direct qualitative comparison with their study unfeasible for non-cylindrical shapes. In the process of generating geometries, careful consideration of various parameters such as pin dimensions and the total heated area is crucial to ensure a fair and meaningful comparison. To achieve this, we adopted a methodology similar to that employed by Falsetti et al. [42] in constructing a micro-evaporator. The initial step involved considering an equivalent straight square micro-channel with walls formed by a cross-stream gap of $W_{ch} = 100\,\mu$m and pin-fin thickness of $d = 50\,\mu$m. Following this criterion, the cross-stream gap and the total heated surface area are fixed, and the micro-pin evaporator can be constructed, resulting in the stream-wise pitch between the fins d_x. Adopting a similar approach, we generated different geometries featuring various pin shapes while maintaining a constant cross-stream gap and total surface area. The three-dimensional computational flow domain used in the study is analogous to the one depicted in Fig. 6.2(a). It includes two rows of pin-fin arrays with adjacent channels ($W = 300\,\mu$m), with a total length of $L = 2.1$ mm. This corresponds to approximately 14 to 22 pin-fins, depending on the shape of the obstacles (and relative pitch) modelled in the stream-wise direction. All the pin-fins have a height of $H = 100\,\mu$m. Figure 7.1 provides a schematic representation of the geometry on a horizontal plane ($z = 0$). From the previous study, the inlet restriction (with a larger pin at the inlet) has been removed from the geometry to avoid obstacles being too close, particularly when considering the configuration with drop-shaped fins. The configurations with cylindrical inline and staggered arrays have the same characteristics, pin dimensions, and pitch between fins as in the previous study; however, in the staggered configuration, the pin-fins are arranged in an offset pattern. Each row of pins is shifted relative to the adjacent row, of a length corresponding to $d_{x,cyl}/2$, creating a staggered layout; see Fig. 7.1(b). The cubic pins configuration consists of cubes with sides of equal length. To adhere to the constraint on the cross-stream gap, the

external surface area of a cubic pin is larger compared to a cylindrical one. As a result, the stream-wise distance between the pins is greater, leading to a lower number of pins per array (17) compared to the case with cylinders (21). The diamond configuration is constructed similarly to the cubic one but rotated by 45°, resulting in shorter sides to maintain the same W_{ch}, as illustrated in Fig. 7.1(d). This configuration features arrays with 22 pins. The configuration with triangular pins is designed with sides of equal length, and the triangles are oriented such that one of their corners aligns
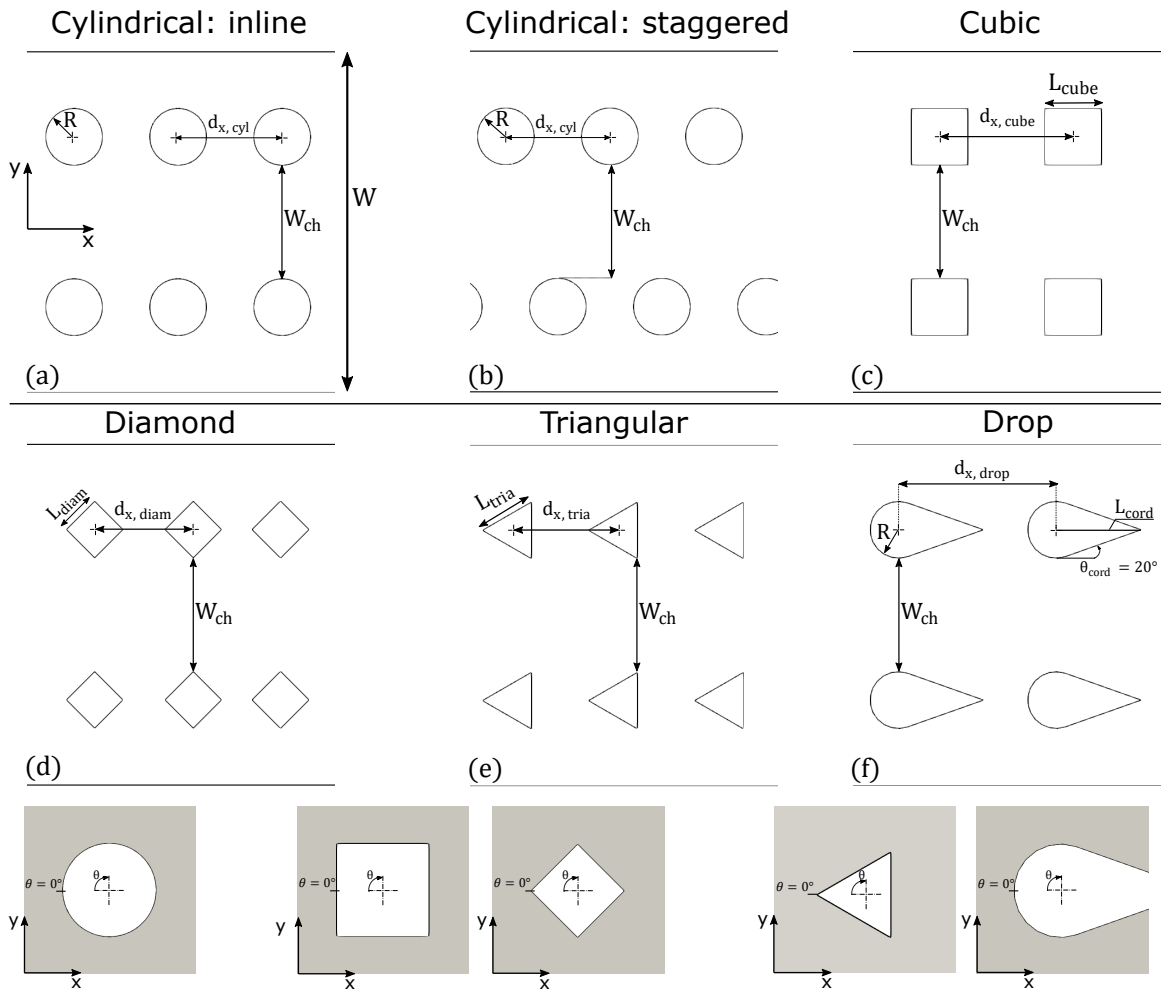
Figure 7.1: Illustration of the computational domain for the different configurations of the micro-evaporator tested. The domain width and the cross-stream gap between the pins are kept constant in all the configurations and are indicated with W and W_{ch}, respectively. The different streamwise (along x) distances between the pins' centres are indicated as $d_{x,*}$.

Shape	Specific length	d_x	$n°$ pins
Cylindrical (in-line)	$R = 25\,\mu$m	$91.7\,\mu$m	21
Cylindrical (staggered)	$R = 25\,\mu$m	$91.7\,\mu$m	21
Cubic	$L_{cube} = 50\,\mu$m	$117.64\,\mu$m	17
Diamond	$L_{diam} = 35.36\,\mu$m	$86.96\,\mu$m	22
Triangular	$L_{trian} = 43.3\,\mu$m	$93.46\,\mu$m	21
Drop shape	$R_{drop} = 25\,\mu$m, $L_{drop} = 75\,\mu$m	$138.88\,\mu$m	14

Table 7.1: Pin-fin shape specific lengths and total number of pins per array.

orthogonally with the direction of the fluid flow, as depicted in Fig. 7.1(e). Finally, the configuration featuring drop-shaped fins is constructed with the cusp positioned upstream and the tail extending downstream. The cups share the same dimensions as the cylindrical pin (same radius), and the length of the chord (L_{chord}) is set at three times the radius, leading to a chord angle of $\theta_{chord} = 20°$, as showed in Fig. 7.1(f). All the specific dimensions and the total number of pins per array are summarised in Tab. 7.1. The working fluid tested is the refrigerant R236fa, which will be studied for a saturation temperature of $30\,°$C; the thermophysical properties of the fluid at the conditions of interest are listed in Tab. 6.3. The same boundary conditions of the previous investigation are being adopted, as depicted in Fig. 6.3. The working conditions examined in the present numerical study involve a range of mass fluxes of $G = 500 - 1500\,$kg/(m^{2}s), no inlet subcooling, while the heat flux at the walls (heater and fins) is set at $q = 50\,$kW/m^2. The domain is discretised with an arbitrary polyhedral grid structure with mainly hexahedral elements. The domain is meshed in two successive steps, using OpenFOAM's tool snappyHexMesh. The two-phase simulations require a suitable initial velocity and temperature field to seed the initial bubble. This is achieved with a preliminary single-phase run. As we imposed a lower heat flux at the walls ($q = 50\,$kW/m^2) compared to the one set in the previous studies in Ch. 6, this allows us to run the single-phase simulations until steady-state conditions are achieved. The velocity and temperature contours displayed in Fig. 7.2(a-f) show an example of initial conditions for the two-phase simulation, extracted from a single-phase simulation run until steady-state, similarly to those previously shown in Fig. 6.2(b), for the various configurations. Examining the results of the configuration with cylindrical inline fins in Fig. 7.2(a), it is observed that discarding the inlet restriction from the heat exchanger has a minimal impact on the flow dynamics. Nu-
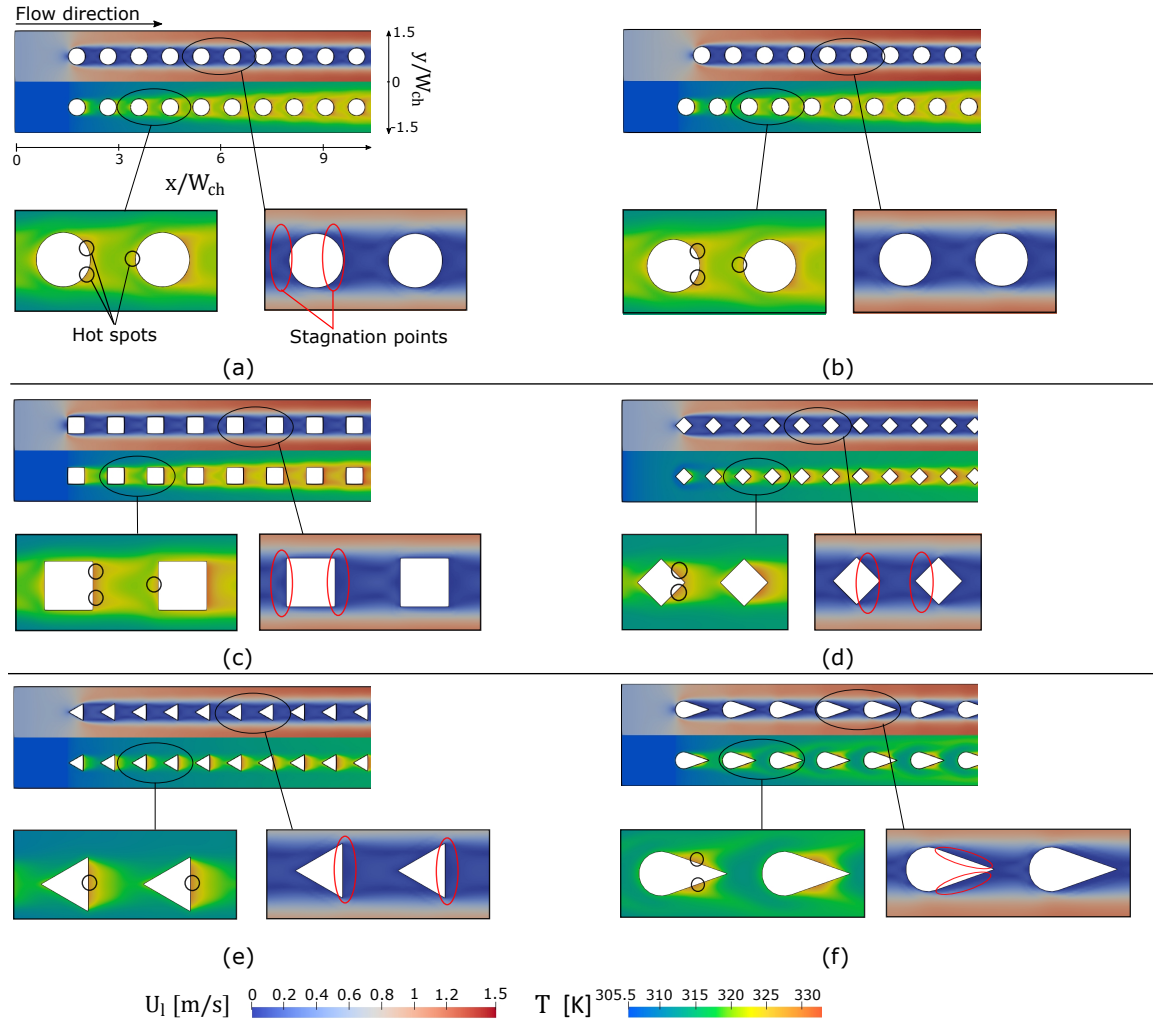
Figure 7.2: (top half) Velocity contours on a horizontal plane halfway through the domain height ($z = H/2$) and (bottom half) temperature contours of the heater ($z = 0$) at steady-state, for the different pin-fin shapes studied in the investigation. Simulation conditions: $G = 1000\,\mathrm{kg/(m^2s)}$, $q = 50\,\mathrm{kW/m^2}$, $T_{sat} = 30\,^{\circ}\mathrm{C}$ and no inlet subcooling.

cleation sites with potential for bubble formation are identified at the pin-fin base's edge, where it intersects with the base surface, as the temperatures are higher due to the presence of the hydrodynamic boundary layers. These points are highlighted with black circles in Fig. 7.2. The third cylinder was selected as the nucleation point in the simulations for the inline cylindrical case; for all the other configurations, we adopted the closest pin at that streamwise length ($X^* = x/W_{ch} \approx 3.5$). The choice

of that particular location was arbitrary. In configurations featuring cylindrical pins, whether inline or staggered, the hottest zone on each pin-fin is consistently identified at approximately 135° from the stagnation point at the cylinder upstream. This location corresponds to where the hydrodynamic boundary layer separates from the cylinder surface. However, it is crucial to note that this specific position may not be universally applicable to other shapes, as different geometries influence the boundary layer differently. Using a local coordinate system centred on the pin-fin centre, θ identifies the angle formed by a point in the pin-fin surface and the horizontal line, we can identify the exact location of the hottest zone around the different shapes. A better visualisation of these spots is illustrated in Fig. 7.3, which reports three-dimensional views of the temperature contour for the different configurations extracted at the end of the single-phase simulations, where the hottest zones are highlighted. To provide further insight, Fig. 7.4(a-c) display the single-phase temperature profile around the selected pin-fins on a horizontal plane ($z = 0$). This visualisation aids in easily identifying the hottest zones at the specified locations. The figure also presents examples of the reference frames θ, centred in the pin centres. The description of the profile is given from the upstream point at $\theta = 0°$ to the downstream point at $\theta = 180°$, as the results are then symmetric. For the cylindrical inline geometry, at $\theta = 0°$ the temperature is about 17 K. This configuration witnesses an initial temperature decrease as we leave the stagnant region until reaching a minimum at 90° (13 K), where fresh fluid interacts with the pin's surface. Upon re-entry into the downstream stagnation region, a temperature peak at $\theta = 135°$ (21 K) is observed, followed by a gradual decline until 180°. The pattern for the cylindrical staggered configuration is the same as the inline configuration, suggesting that the offset of the pins has no major influence on the overall temperature of the heated surfaces. For the cubic configuration, at $\theta = 0°$ we can observe the highest temperature for all the shapes (19 K). This can be ascribed to the larger recirculation region created by the shape. A gradual decrease in temperature occurs until the first corner ($\theta = 45°$), where the lowest temperature is measured at about 14 K, due to the free-stream of the liquid, followed by a sudden increase that flattens until 135°, where a decisive rise leads to the hottest point $\theta = 155°$ (24 K). Subsequently, there is a subtle decrement of temperature until the downstream point. Rotating the cube to have the diamond shape alters the trend abruptly. At upstream, the temperature is considerably lower (15 K) than the cubic one, as the configuration reduces the area characterised by stagnant fluid. The min-
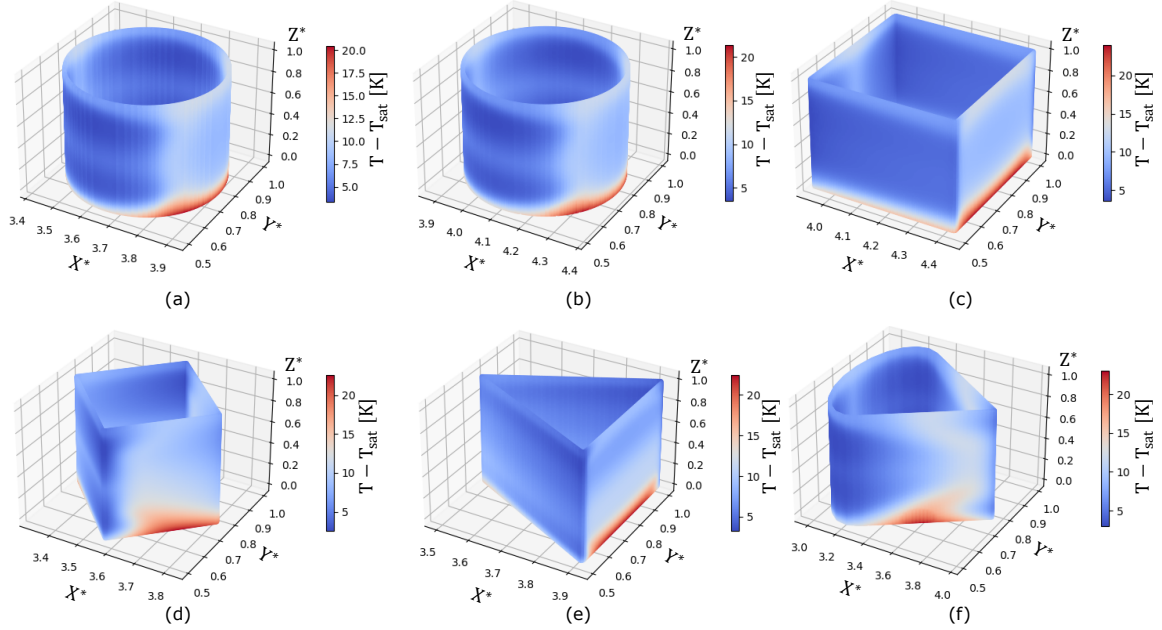
Figure 7.3: Three-dimensional views of temperature contour for the different pin-fin configurations tested, extracted at steady-state. The flow is in the direction of positive x (from left to right). The coordinates are scaled by the width of the channel (W_{ch}), such as $X^* = x/W_{ch}$, $Y^* = y/W_{ch}$ and $Z^* = z/W_{ch}$. Simulation conditions: $G = 1000\,\text{kg}/(\text{m}^2\text{s})$, $q = 50\,\text{kW}/\text{m}^2$, $T_{sat} = 30\,°\text{C}$ and no inlet subcooling.

imum temperature is measured at 90°, after which the temperature increases until $\theta = 150°$, where the maximum is observed, followed by a decrease until the downstream position. The triangular pin shape exhibits a pattern similar to the diamond until the first corner at 150°. Then the temperature remains constant in the stagnant region downstream. On the other hand, the drop-shaped fin manifests a similar trend to the cylindrical shape in the first part; however, the temperatures are significantly lower as the drop shape helps in better distribution of the fluid flow around the pin, reducing the chances of flow separation and promoting more uniform heat transfer. Flow separation is observed only at $\theta = 160°$, where the peak of temperature is measured, then a considerable drop in temperature is observed in correspondence to the tail. The point characterised by the highest temperature is highlighted by a red dot for all the configurations investigated in Fig. 7.4. The single-phase Nusselt number profiles around the pin-fins for the various configurations, extracted on a horizontal plane ($z = 0$) at steady-state, are presented in Fig. 7.4(d-f).
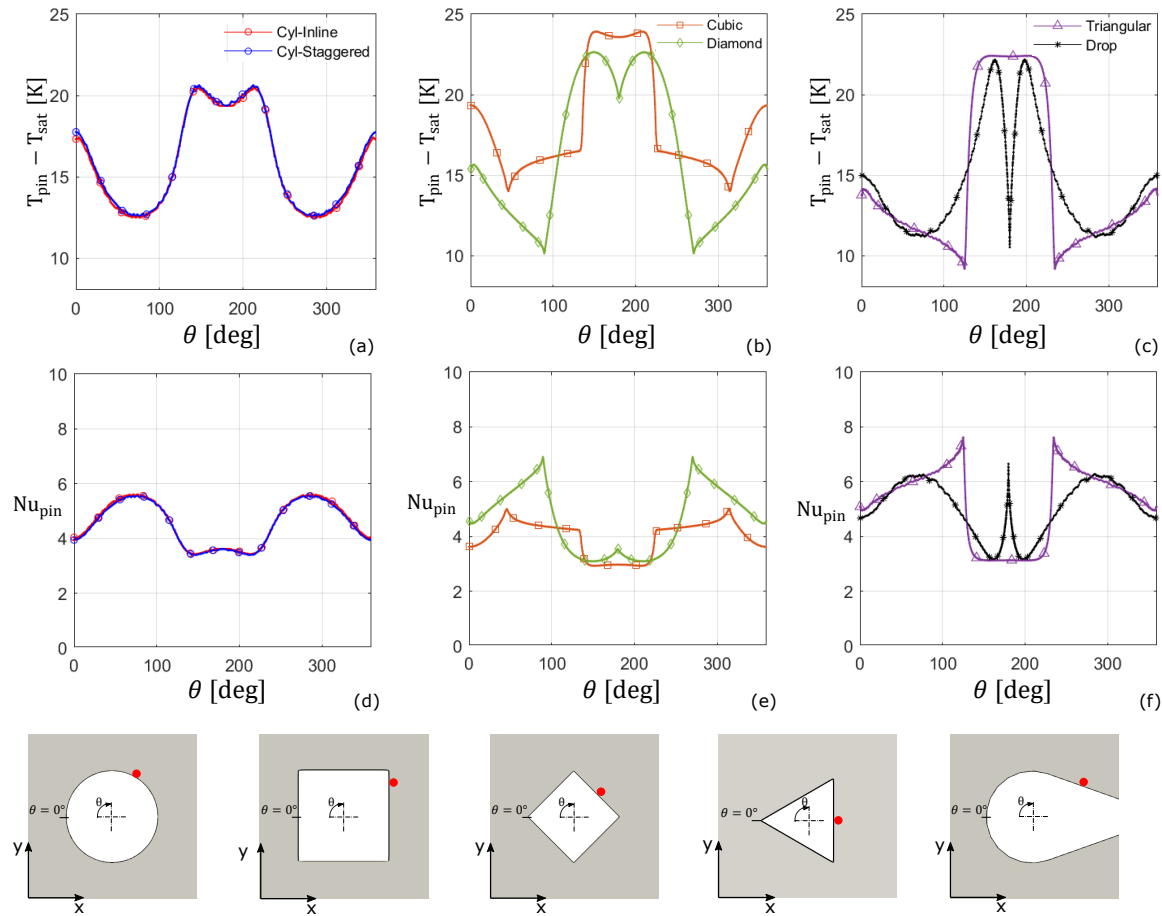
Figure 7.4: Results for the single-phase simulations. (a-c) Single-phase temperature profile and (d-f) single-phase Nusselt number (Nu) around the pin-fins, extracted on a horizontal plane ($z = 0$) at steady state, for the different configurations investigated. The profiles are measured on a local reference frame θ centred on the pin-fin centres. Examples of the reference frames are shown for the various shapes. Simulation conditions: $G = 1000 \, \text{kg/(m}^2\text{s)}$, $q = 50 \, \text{kW/m}^2$, $T_{sat} = 30 \, ^\circ\text{C}$ and no inlet subcooling.

The overall results of the single-phase investigation are presented in Fig. 7.5. Figure 7.5(a) illustrates the pressure profile along the channel centreline ($y = 0$, $z = H/2$) for $G = 1000 \, \text{kg/(m}^2\text{s)}$ for the different configurations tested. The profiles reveal a sudden pressure drop immediately after the first set of pins, acting as a restriction, followed by a gradual decline. Notably, the pressure recovery observed in the previous investigation in Ch. 6 is no longer evident due to the absence of the inlet restriction. Comparing the configurations, there is no significant disparity in terms of pressure drop. Cubic pin-fins exhibit the highest pressure drop ($\Delta p \approx 1670 \, \text{Pa}$), while drop-
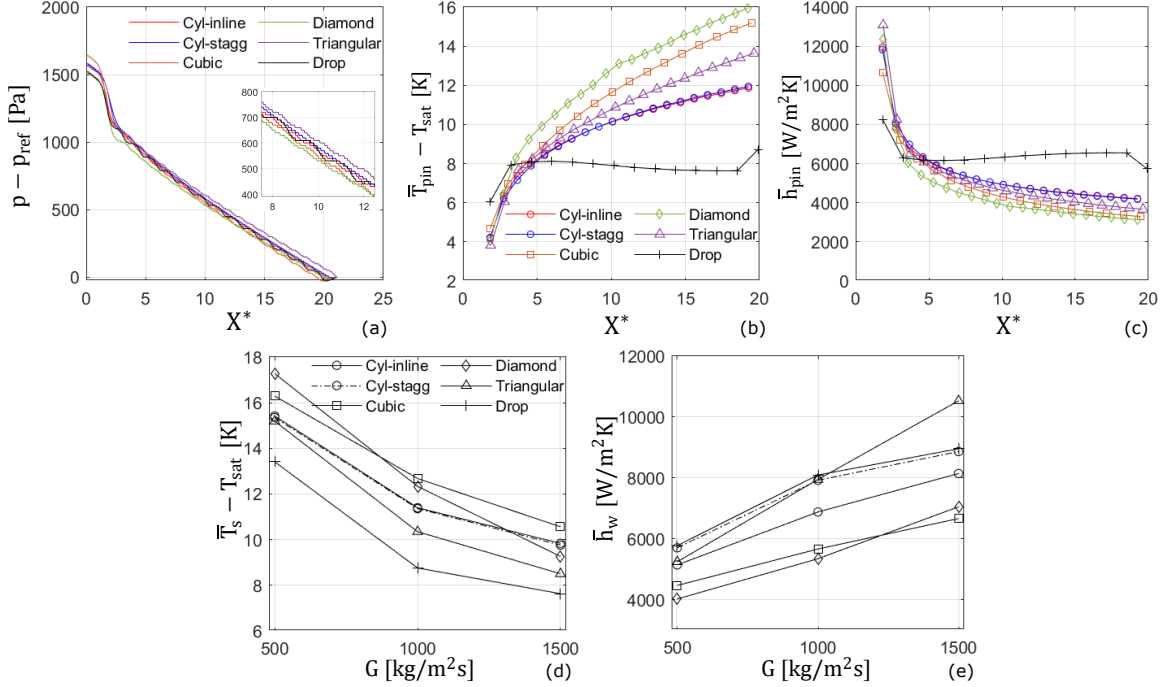
Figure 7.5: Results of the single-phase simulations. (a) Pressure drop along the channel ($p - p_{out}$) for the different configurations tested. (b-c) Instantaneous single-phase spatially-averaged temperature ($\overline{T}_{pin}$) and heat transfer coefficient ($\overline{h}_{pin}$) of the pin-fins over the streamwise direction, taken at steady-state. The legend in (a) also applies to (b) and (c). Simulation conditions: $G = 1000 \, \text{kg/(m}^2\text{s)}$, $q = 50 \, \text{kW/m}^2$, $T_{sat} = 30 \, ^\circ\text{C}$ and no inlet subcooling. (d-e) Spatially-averaged single-phase temperature ($\overline{T}_s$) and heat transfer coefficient ($\overline{h}_w$) of the heated surfaces (heater and pins) versus mass flux. The data are extracted at the end of the simulation. The legend in (d) applies also to (e). Simulation conditions: $q = 50 \, \text{kW/m}^2$, $T_{sat} = 30 \, ^\circ\text{C}$ and no inlet subcooling.

shaped fins demonstrate the lowest ($\Delta p \approx 1540 \, \text{Pa}$). To better analyse the impact of the pin shapes on heat transfer in the evaporator, Fig. 7.5(b,c) provides axial profiles of temperature and heat transfer coefficient ($\overline{h}_{w,pin}$). These profiles were extracted at the end of the single-phase simulation, once it reached steady-state. As we move along the streamwise direction, the temperature increases for all configurations, except the drop-shaped fins. These fins reach a maximum temperature at the 4$^{\text{th}}$ pin (corresponding to $X^* \approx 7.5$), after which the average temperature remains constant, slightly decreasing, with a sudden jump at the end of the channel, attributed to the vicinity of the last pin to the outlet section. This can explained by the fact that the

drop shape helps in better distribution of the fluid flow around the pin, the thermal resistance is lower, as the fluid hardly separate, promoting more uniform heat transfer.

Figure 7.5(d,e) presents the results of single-phase spatially-averaged temperatures and heat transfer coefficients measured on the heated surfaces (heater and pins) for different mass flow rates. The data pertain to the end of the simulation. As a general trend, heat transfer performance improves with increasing mass flow rate, primarily due to enhanced convective heat transfer between the fluid and the heated surfaces as mixing increases. The results exhibit an approximately linear trend as a function of the mass flow rate. The poorest performance is observed in both the cubic and diamond configurations. This can be explained by the fact that these configurations present multiple sharp corners, which can lead to flow separation and increased flow resistance. The best performances are achieved when drop-shaped pins are adopted; however, for high flow rates, the triangular pin surpasses all other shapes. The higher capability of the drop-shaped configuration can be explained by the fact that the pin surface area is greater compared to the other shapes. This increased surface area allows for more efficient heat transfer by providing more contact points for heat exchange with the surrounding fluid. The triangular shape has fewer sharp corners compared to the cubic and diamond shapes, reducing flow separation and minimising flow resistance. The high performance at high flow rates can be ascribed to the promotion of vortex shedding, which improves the overall efficiency of the system. It is interesting to note that the spatially-averaged temperature of the solid walls for both configurations with cylindrical pin-fins remains essentially identical as the mass flow rate varies. However, when examining the heat transfer coefficient, the staggered configuration outperforms the inline one. This can be explained by the fact that the heat transfer coefficient is based on the log-mean temperature difference, as explained in Eq. (**??**). The staggered configuration promotes better heat transfer by disrupting the flow and creating more opportunities for convective heat exchange between the fluid and the pin surfaces and also promotes vortex shedding between adjacent pins, leading to complex flow patterns.

7.2   Two-phase flow investigation

In this section, we present the two-phase results for a representative case with $G = 1000\,\mathrm{kg/(m^2 s)}$, $q = 50\,\mathrm{kW/m^2}$, $T_{sat} = 30\,^\circ\mathrm{C}$, and no inlet subcooling. The two-phase simulation initiates once steady-state is reached, and the bubble nucleation is triggered at the nearest pin-fin to the position $X^* \approx 3.5$, as shown in Sec.7.1. This position aligns with the angle described earlier, as indicated in Fig. 7.2, coinciding with the hottest region at the edge where the pin-fin meets the evaporator base. The discussion will predominantly focus on the advancement of the bubble shape, flow dynamics, morphology of the liquid film thickness, and their impact on the heat transfer performance of the micro-pin fin evaporator as the configuration is altered. Figure 7.6(a) illustrates the evolution of the bubble equivalent diameter over time. The bubble equivalent diameter is computed at each time-step as the diameter of a spherical bubble with a volume equivalent to that of the simulation. Figures 7.7 and 7.8 depict the corresponding bubble shapes at selected time instants during the simulations. The shape evolution of the bubbles for the cubic and triangular configuration are presented in Fig. 7.8 as a single figure to present the development was unfeasible. From a broader perspective, the evolution of the bubble shape as it progresses through the channel closely imitates the observed pattern in the previous chapter for both configurations featuring cylindrical pins (inline and staggered), including diamond and drop-shaped pins. Upon nucleation, the bubble experiences rapid growth in the direction of the flow, driven by heat transfer from the heated walls (heater and pin-fins). Subsequently, the growth rate diminishes after the initial phase as the bubble leaves the nucleation region, influenced by the incoming liquid flow, and migrates towards the centre of the channel, where the liquid is no longer superheated, farther from the walls. Once the equivalent diameter to channel hydraulic diameter, D_{eq}/d_h, reaches 1, the bubble comes into contact with the second array of pin-fins (in $y < 0$). At this point, the bubble is strongly confined by the channel walls, predominantly expanding in the flow direction. Additionally, the bubble tends to spread sideways between the pins. Upon closer inspection, the overall shape of the bubble is significantly influenced by the micro-heat exchanger configuration, particularly when it starts to be restricted by the pins. The outcomes for configurations with cubic and triangular pins differ significantly. The bubble is initiated downstream of the pin, inside the flow recirculation region between the pin-fin arrays, resulting in more
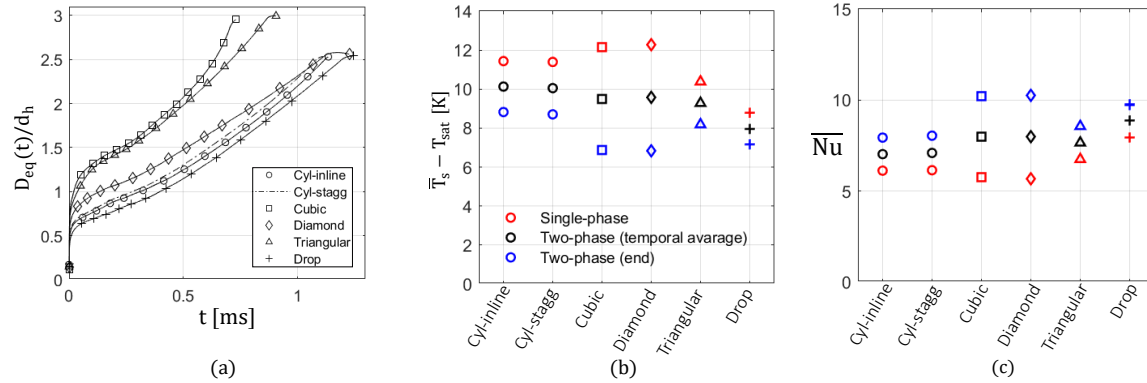
Figure 7.6: Systematic analysis of the effect of the pin-fin shape. (a) Dimensionless bubble equivalent diameter (D_{eq}/d_h) versus time. (b-c) Spatially-averaged single- and two-phase temperature ($\overline{T}_s$) and Nusselt number ($\overline{Nu}$) of the heated surfaces (heater and pins). The single-phase data refer to the instant of boiling onset; for the two-phase results, data are presented as a time-average over the entire simulation and as instantaneous values at the end of the simulation, when the bubble nose reaches the outlet section. The legend in (b) applies also to (c). The results refer to a case run with $G = 1000 \, \text{kg}/(\text{m}^2\text{s})$, $q = 50 \, \text{kW}/\text{m}^2$, $T_{sat} = 30 \, °\text{C}$ and no inlet subcooling.

substantial growth. This can be attributed to the bubble's confinement within the stagnant region, where the fluid is hotter, allowing for an extended interaction with the heated walls. As the bubble enlarges, it reaches the next pin, extending symmetrically around it. Eventually, a portion of the bubble escapes from the stagnant region. The high shear forces exerted by the fluid in the evaporator channels fragment the bubble into smaller units, occupying all available channels and evolving into elongated shapes. It is noteworthy that, with triangular pins, the bubble is unable to extend in the cross-stream direction gap due to the presence of multiple bubbles in adjacent channels. This observation aligns with findings in the previous study, where bubbles were seeded in the downstream ($\theta = 150°$) region between the cylindrical pins, see Sec. 6.3.4. However, this effect is not observed for the configuration with cubic pins. This discrepancy may be explained by the fact that the bubble is not initialised exactly downstream of the pin, as done for the triangular configuration, but at $150°$ from the stagnation point at the pin upstream, see Fig. 7.4. This results in the bubble growing disproportionately in one direction once it starts to extend around the next pin. As the bubble breaks, one of the resulting bubbles is larger than the other and, consequently, propagates faster through the channel. This leads
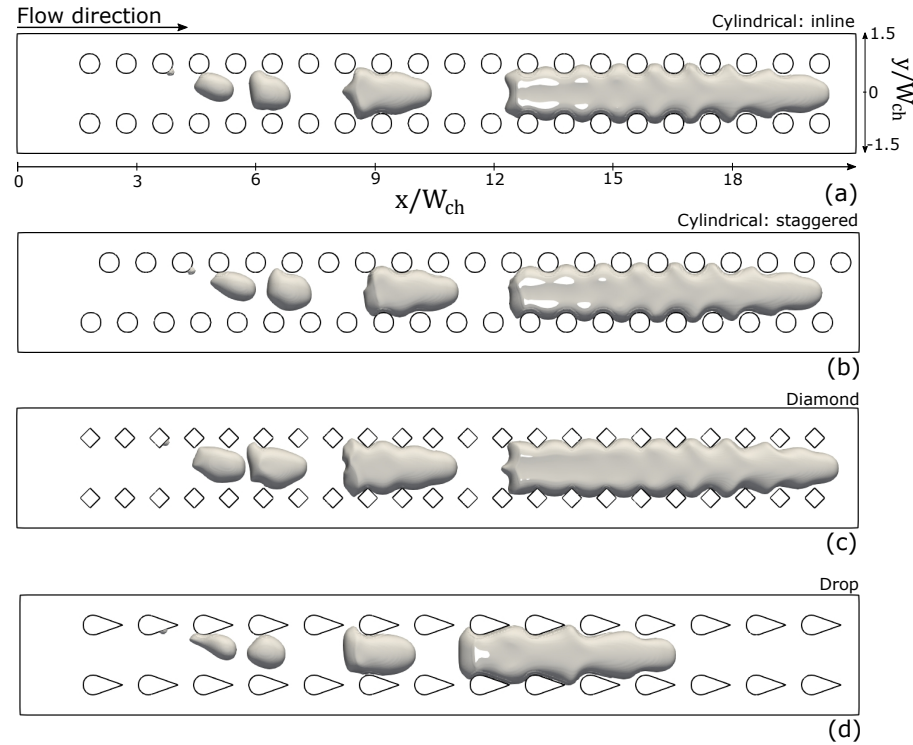
Figure 7.7: Top view of the bubble profile extracted at different instants for the various pin-fin shapes tested. The bubble shapes are extracted at $t = 0\,\mathrm{ms}$, $t = 0.15\,\mathrm{ms}$, $t = 0.30\,\mathrm{ms}$, $t = 0.6\,\mathrm{ms}$ and the last one when the bubble nose is close the outlet section. The results for the configuration cases with cubic and triangular pins are reported in Fig. 7.8. The results refer to a case run with $G = 1000\,\mathrm{kg/(m^2s)}$, $q = 50\,\mathrm{kW/m^2}$, $T_{sat} = 30\,°\mathrm{C}$ and no inlet subcooling.

to a scenario where the bubble in the central channel at the front is able to expand in the cross-stream direction without being limited by a secondary bubble in the adjacent channel, while the rear is constrained by the presence of the adjacent bubble.

Quantifying the liquid film thickness for direct comparison among different shapes poses challenges due to the lack of a universal measurement method, particularly given the significant dimensional variations around different pins. Therefore, a more qualitative overview is provided. Snapshots of the bubble profile, and temperature contours of the base wall ($z = 0$), extracted at the last time instant indicated in Fig. 7.7 and 7.8, for the different shapes are presented in Fig. 7.9. The black solid line identifies the bubble profile taken at the mid-height plane ($z = H/2$). Examining
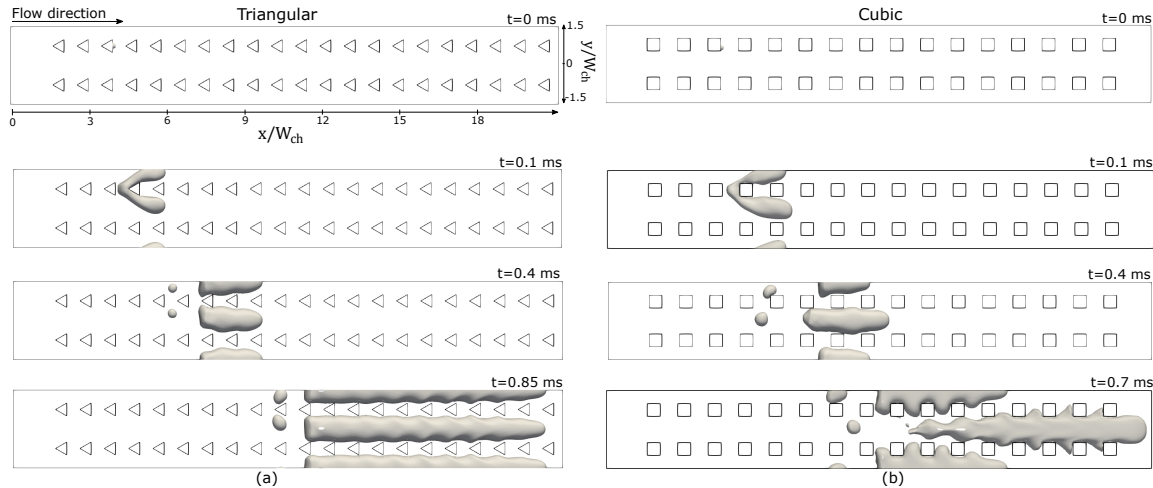
Figure 7.8: Top view of the bubble profile extracted at the different instants for configuration cases with cubic and triangular pins. The results refer to a case run with $G = 1000\,\text{kg/(m}^2\text{s)}$, $q = 50\,\text{kW/m}^2$, $T_{sat} = 30\,^\circ\text{C}$ and no inlet subcooling.

the film thickness as the distance between the liquid-vapour interface and the pin-fin surface ($Y^* = 1$), both cylindrical configurations (inline and staggered) exhibit a similar morphology, see Fig. 7.9(a,b). The minimum film thickness values range from approximately $1.75\,\mu$m to $2.25\,\mu$m, with thicker films observed on downstream pins, due to the higher velocity of the bubble front. The film thickness around the diamond pins is shown in Fig. 7.9(c). A liquid film with 0 thickness was measured in the corner at $\theta = 90^\circ$, suggesting dry-out of the film. As we move along the sides of the pin the thickness increases. For the triangular configuration thick liquid film can be observed in Fig. 7.9(d), with the minimum film thickness measured at the correspondence of the corner that aligns orthogonally with the direction of the fluid flow, ranging from approximately $1.9\,\mu$m to $5\,\mu$m. No film thickness can be measured on the sides of the pins, as the bubble is unable to expand in the cross-stream direction. For the configuration with drop-shaped pins, the film is depicted in Fig. 7.9(e); the minimum film thickness can be measured in correspondence of $\theta = 90^\circ$, and it ranges between $1.75\,\mu$m and $2.9\,\mu$m. Last, the film thickness around the cubic pins is more difficult to evaluate due to the complex dynamic of the bubble. At the rear of the bubble, thick liquid films are present as the bubble is strongly influenced by the bubble in the neighbour channel. Near the front region, as depicted in Fig. 7.9(f), we can observe film thickness of $2 - 4\,\mu$m at the centre of the cube ($\theta = 90^\circ$), while the minimum
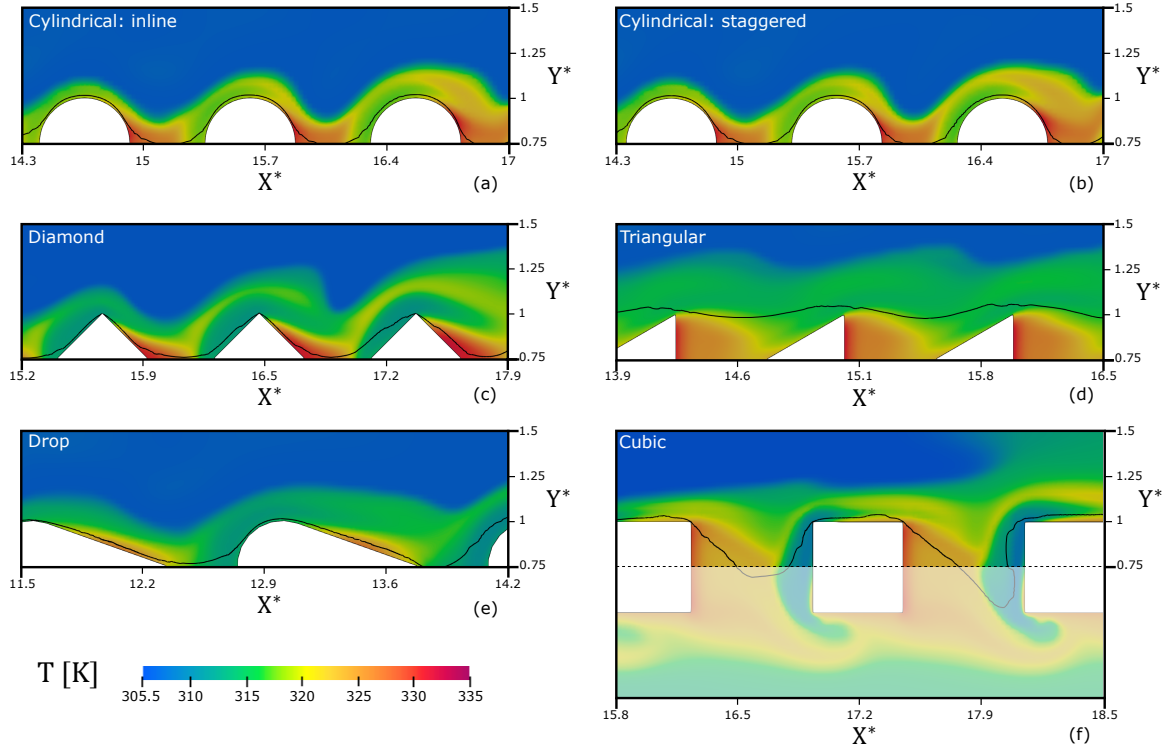
Figure 7.9: Sketch of the bubble profile extracted at the last instant indicated in Fig. 7.7 and 7.8, and temperature field of the bottom surface ($z = 0$) for the different configurations investigated. The results refer to a case run with $G = 1000 \, \mathrm{kg/(m^2 s)}$, $q = 50 \, \mathrm{kW/m^2}$, $T_{sat} = 30 \, °\mathrm{C}$ and no inlet subcooling.

is detected close to the sides of approximately $1 \, \mu$m. To analyse the effects of the pin-fin configuration on heat transfer, Fig. 7.6(b,c) presents the results of single- and two-phase spatially-averaged temperatures and Nusselt numbers for different configurations. The single-phase data refer to the instant of boiling onset, whereas two sets of two-phase data are plotted: one averaged over time during the entire two-phase simulation and one evaluated at the end of the two-phase simulation when the bubble nose reaches the outlet section. The results for both cylindrical configurations (inline and staggered) are identical, explained by the overall similarity in the development of the bubble. The data suggest that the drop-shaped fin outperforms all the other shapes in terms of time-average. However, examining the outcomes extracted at the end of the simulations, the cubic and diamond-shaped configurations excel. For the case with cubic pins, the higher surface area occupied by the two-phase flow due to bubble fragmentation leads to an average Nusselt number approximately 14% higher

than that measured for the configuration with inline cylindrical pins (28% higher when measured at the end of the simulation). The fragmentation of bubbles also occurs in the configuration with triangular pins; however, there is no similar enhancement in heat transfer performance, as observed in the cubic case. This can be attributed to the fact that the bubble splits symmetrically, and the resulting bubbles are identical and propagate at the same velocity, as seen in Fig. 7.8(a). The interaction between two bubbles in adjacent channels significantly influences each other, preventing them from extending into the cross-stream direction gap between two pins. This is supported by the thick liquid film measured around the walls, as depicted in Fig. 7.9(d). Consequently, the bubble is unable to efficiently cover the obstacles, resulting in a notable limitation in heat transfer performance (less than a 25% increase in Nusselt number compared to the single-case). In contrast, the high heat transfer coefficient observed for the case with diamond pins can be attributed to the diamond geometry, which facilitates the bubble's expansion in the lateral direction of the channel. This leads to an average Nusselt number approximately 13% higher (29% higher at the end of the simulation) than that measured for the configuration with inline cylindrical pins.

7.3   Conclusion

This chapter presented the results of a computational study of flow boiling in micro-pin-fin evaporators, where the influence of the pin geometry and configuration has been investigated. The numerical model of the evaporator included arrays of cylindrical, cubic, diamond, triangular, and drop-shaped pin-fins in an inline arrangement. The effects of the staggered arrangement, for cylindrical pins, have also been investigated. The dimensions of the pin-fins are evaluated while keeping the cross-stream pitch constant at $150\,\mu$m and maintaining the total surface area. This design is based on arrays of cylindrical inline pins, as adopted in the experimental work performed by Falsetti et al. [42], resulting in variations in the streamwise pitch. The fluid utilised is refrigerant R236fa at a saturation temperature of $30\,°$C. The range of simulated operating conditions covered mass flux values $G = 500 - 1500\,\mathrm{kg/(m^2 s)}$ and a heat flux of $q = 50\,\mathrm{kW/m^2}$. The numerical simulations were performed using the boilingFoam solver in OpenFOAM v2106 [77], employing a geometric Volume Of Fluid method to capture interface dynamics. The study delves into the detailed dynamics of bubbles and thin evaporating liquid films as they evolve through the pin-fin arrays, along with the corresponding heat transfer mechanisms.

The main conclusions of this work are as follows:

- In the single-phase regime, the geometry affects the boundary layer greatly, resulting in various hot spots, typically in the downstream stagnant region. These hot zones act as plausible nucleation spots. Notably, the cylinders feature hot spots at circumferential positions located at 135° from the upstream stagnation point, in agreement with existing experimental evidence [44]. The hot spots for the other configurations can be identified in the range of 135° to 180°.

- No great disparity among the different shapes is measured in terms of pressure drop. The lowest value of pressure drop is measured in the configuration with drop-shaped pins.

- For cylindrical pins the staggered configuration outperforms the inline configuration with regard to heat transfer performance, as the offset layout disturbs the fluid flow leading to more complex flow patterns and enhancing the mix-

ing. Shapes characterised by multiple sharp corners present higher thermal resistance and result in lower heat transfer capacity.

- The location of the nucleation site influences the following bubble dynamics and heat transfer significantly. Cylindrical, diamond, drop-shaped geometries have bubble nucleated between 135° to 160° from the upstream stagnation point, resulting in early detachment from the pin-fin surface, quickly elongating along the channel formed between the pin-fin arrays. Thin liquid films form around the cylinders, and heat transfer is enhanced by a combination of film evaporation and heat convection in the gaps between the obstacles. Higher performance is observed for the diamond configuration as the bubble expands more efficiently in the gaps.

- Vapour bubbles nucleate within the stagnant region for the cubic and triangular geometries, they grow faster and eventually split into smaller bubbles. When the fragmentation of the bubble is symmetric considerable influence of the bubbles between each other is observed, limiting the improvement of the heat transfer performance.

The study unveils the intricate relationship between pin geometry and heat transfer dynamics in micro-pin fin evaporators, emphasising the significance of subtle design complexities. Interestingly, the superior heat transfer performance in the single-phase regime of the staggered configuration for cylindrical pins underscores the importance of disrupting flow patterns. The identification of specific nucleation sites adds a practical dimension to understanding how bubble behaviour influences heat transfer, with potential applications in optimising system efficiency.

Chapter 8

Conclusion and outlook

The work presented in this thesis on the modelling of two-phase flows across micro-pin fins evaporators can be subdivided into two main parts, which will be summarised in the following subsections.

8.1 Adiabatic flow

In the adiabatic part of the study, an investigation was conducted into the dynamics of gas bubbles propagating across circular pin-fins. Various conditions were investigated, including different liquid capillary numbers $Ca_l = 0.04 - 1$, streamwise pitch of the cylinders $s_x = 0.125R - 2R$ (with R representing the radius of the pin-fins), initial bubble lengths $L_b = 2.5R - 12R$, and Reynolds numbers $Re = 1 - 1000$. Advanced numerical simulations were employed, with a focus on capturing the thin liquid film between the bubble and the pin-fins, revealing several noteworthy insights.

- Periodic accelerations and decelerations were identified in the dynamics of the bubble's nose and rear menisci, ultimately reaching a steady-periodic flow regime.

- As the bubble traversed the pin-fin arrays, it tended to cover the surfaces of the fins, resulting in the formation of a thin liquid film between the bubble and the obstacles. This film exhibited characteristics similar to straight channels, consistently maintaining a smaller thickness compared to other straight channel shapes. The minimum film thickness ranged from about $h_{min} = 0.02R$ to $0.2R$, approximately 4 times smaller than circular channels for small capillary numbers ($Ca_l = 0.04$).

- The morphology of the liquid film and bubble shape was found to be significantly influenced by the capillary number. The study observed the formation of interfacial dimples when the capillary number is decreased ($Ca_l < 0.1$), causing local peaks of capillary pressure that induced drainage flows, expelling liquid from the film.

- The sensitivity of bubble and film dynamics to the streamwise distance between cylinders was highlighted, with a decrease in this distance, $s_x \to 0$, leading the configuration towards that of a straight channel and an increase in liquid film thickness. Conversely, larger distances allowed the bubble to expand, resulting in thicker liquid films.

- The study also noted the impact of bubble length on film dynamics, revealing a significant difference by a factor of 2 between the limiting cases. Bubbles shorter than $L_b = 7R$ exhibited an increase in film thickness as their length decreased, while longer bubbles showed negligible length-related impacts.

- For low Reynolds numbers $Re < 500$, inertial effects were found to be mild but became prominent at higher Reynolds numbers, leading to time-dependent patterns, fragmentation of the rear meniscus, and significantly thicker liquid films, about 5 times thicker than those measured in the visco-capillary regime ($Re = 1$).

8.2 Flow boiling study

In the second part of the study, the modelling of boiling flows in micro-pin fins was performed to investigate the impact of pins on flow dynamics and heat transfer performance. Several conditions were tested within the range of liquid mass flow rates $G = 500 - 2000 \, \text{Kg/(m}^2\text{s)}$, heat flux $q = 50 - 200 \, \text{kW/m}^2$, subcooling degree $\Delta T_{sub} = 0 - 5 \, \text{K}$, and different nucleation spot. The study also investigates the influence of pin-fin shape and their arrangement on flow dynamics. It includes tests with cylindrical pins in both inline and staggered arrangements, as well as cubic, diamond, triangular, and drop-shaped fins in an inline structure. Referring to the configuration with cylindrical pins of radius $R = 25 \, \mu\text{m}$ and cross-stream distance of $d_y = 150 \, \mu\text{m}$, taken from the experimental work of Falsetti et al. [42], the other

pin geometries were constructed while maintaining constant d_y and the total heated area. The fluid used was refrigerant R236fa at a saturation temperature of 30° C. The intricacies of these phenomena were unveiled through meticulous analysis of bubble behaviour, liquid film morphology, and heat transfer performance, revealing different insights.

- In the single-phase regime, the flow past pin-fin arrays undergoes a transition to weakly unsteady patterns beyond a Reynolds number of approximately 400, with vortex shedding becoming more pronounced at Reynolds numbers exceeding 600. This transition leads to enhanced mixing, resulting in an up to +15% increase in the Nusselt number for the case with cylindrical pins.

- No major influence was observed in pressure drop among the different configurations. However, the various shapes have a significant impact on how the boundary layer separates from the fin surface, leading to distinct locations of the hottest zone where plausible nucleation can occur. Shapes with multiple sharp corners, such as cubic and diamond, exhibit higher thermal resistance compared to smoother shapes like cylindrical and drop-shaped pins. The optimal performance is achieved with drop-shaped pins; however, for high flow rates ($G = 1500\,\text{kg}/(\text{m}^2\text{s})$), the configuration with triangular pins outperforms all others, with up to +30% increase in heat transfer coefficient compared to cylindrical inline pins.

- In the two-phase flow regime, the bubble exhibits unique characteristics depending on the nucleation spot. When the bubble nucleates outside or partially outside the stagnant region between two consecutive fins, early detachment from the pin-fin surface is observed. This leads to quick elongation along the channel formed between pin-fin arrays, generating a thin liquid film around the pins. This process enhances heat transfer through a combination of film evaporation and heat convection in the gaps between obstacles. There is an up to +50% increase in the Nusselt number compared to the single-phase case for $G = 1000\,\text{kg}/(\text{m}^2\text{s})$.

- When nucleation occurs in the stagnation region, faster bubble growth and eventual fragmentation result in increased surface coverage, with bubbles being

up to $+20\%$ larger. This phenomenon contributes to a higher heat transfer coefficient.

- The staggered configuration with cylindrical pin-fins has been observed to enhance performance only in the single-phase regime compared to the inline configuration, as mixing is improved. However, no major impact was observed in the two-phase regime, as the bubble's growth and flow dynamics remain very similar.

- The influence of flow rates on heat transfer is revealed for the configuration with inline cylindrical pins, showcasing a trade-off between enhanced heat transfer coefficients in single-phase flow regions and reduced coefficients in the two-phase flow region. This intricate balance results in an overall increase in heat transfer performance at a flow rate of $1000\,\mathrm{kg/(m^2s)}$, while a further increase to $2000\,\mathrm{kg/(m^2s)}$ leads to an overall reduction.

- In the comparison between pin shapes for $G = 1000\,\mathrm{kg/(m^2s)}$, the best performances are achieved by the cubic and diamond configurations, exhibiting up to a $+29\%$ increase in the Nusselt number compared to the configuration with cylindrical inline pins. In the cubic configuration, bubble fragmentation occurs, leading to an increase in the total surface area covered by the two-phase flow. In the diamond geometry, the bubble can expand more efficiently in the lateral direction.

- While triangular pins experience bubble fragmentation, they do not exhibit the same enhancement observed in the cubic configuration. This discrepancy is attributed to the strong influence of bubbles in the adjacent channels, hindering efficient bubble expansion and leading to the formation of thicker films (up to 3 times thicker than those measured for cylindrical pins). Consequently, only a limited improvement in heat transfer performance from single-phase to two-phase cases is observed.

- Higher inlet subcooling is found to decrease two-phase heat transfer coefficients for the configuration with inline cylindrical pins. This is primarily because condensation occurs after bubbles depart from the hot pin-fin surfaces, resulting in smaller bubbles. For $\Delta T_{sub} = 4\,\mathrm{K}$, the heat transfer coefficient measured at

the end of the simulation was -30% lower than the case with a subcooling of 2 K. At a subcooling of 5 K, bubbles collapse entirely upon departure from the pin-fins.

8.3   Outlook on ongoing work

In light of these findings, it is clear that the dynamics of bubbles and flow boiling in micro-pin fin evaporators significantly deviate from those observed in straight microchannels. The diverse observations, particularly concerning the substantial impact of pin shape and the interconnection of nucleation sites with resulting bubble behaviour, hold immense potential for optimising system efficiency.

In this thesis, I have advanced the understanding of two-phase flows in micro-pin fin evaporators, making a significant contribution to both theoretical and practical knowledge in the field. An important aspect of my work includes performing the first accurate validation of boiling models in microchannels against experimental data, establishing a new benchmark for phase change heat transfer studies at the micro-scale. Through detailed numerical simulations, I have elucidated the dynamics of gas bubbles interacting with pin-fin arrays under various conditions, providing crucial insights into film thickness variations and bubble behaviour, which are key informations for optimising thermal management systems in compact electronics and other industrial applications.

Despite these advancements, the research encountered considerable challenges, primarily due to the lack of comprehensive experimental data. Indeed, despite significant interest in the topic, there remains high uncertainty in evaluating flow characteristics with sufficient resolution. As previously introduced, heat transfer trends in all experimental work vary significantly under different operational conditions, which increase the challenge. Another problem is that is practical impossible with the current technology to study and measure the liquid film thickness in this geometries. This lack of consensus poses a significant obstacle to developing universally accepted correlations for this flow type. However, the results presented in this investigation takes the first step to close this gap.

Additionally, the simulations, based on idealised conditions, may not fully capture the complexities of real-world phenomena. Furthermore, the current computational costs limit the feasibility of simulating the entire micro-channel. While the configura-

tions simulated serve as good approximations of the actual evaporator, they remain approximations. This discrepancy underscores the need for future studies to refine these models to ensure their robust applicability across diverse applications.

Further investigation is recommended to refine the research. Two potential advancements are envisioned:

- An advancement in the research involves considering conjugate heat transfer. This could potentially facilitate testing higher heat loads and extending simulations until steady-state is achieved, to have initial conditions more similar to the experiments.

- A second potential advance is the implementation of a sub-model for nucleation, which could allow for a more detailed and physically accurate representation of the boiling process. The criteria for activating specific nucleation sites and their dependence on the geometry pose challenges that require careful consideration.

Bibliography

[1] J. F. Tullius, R. Vajtai, and Y. Bayazitoglu. A Review of Cooling in Microchannels. In: *Heat Transf. Eng.* 32 (2011), pp. 527–541.

[2] T. G. Karayiannis and M. M. Mahmoud. Cramming more components onto integrated circuits. In: *Eletronics* 38 (1965), pp. 114–117.

[3] G. E. Moore. A Method for Capturing Sharp Fluid Interfaces on Arbitrary Meshes. In: *J. Comput. Phys.* 153.1 (1999), pp. 26–50.

[4] E. Masanet, A. Shehabi, N. Lei, S. Smith, and J. Koomey. Recalibrating global data center energy-use estimates. In: *Science* 367 (2020), pp. 367–374.

[5] T. Swallow. *Top 10: Green Energy Data Centres.* https://energydigital.com/top10/top-10-green-energy-data-centres. 2023.

[6] S. Anders. Hypotheses for primary energy use, electricity use and CO2 emissions of global computing and its shares of the total between 2020 and 2030. In: *WSEAS Trans. Power Syst.* (2021).

[7] A. Capozzoli and G. Primiceri. Cooling Systems in Data Centers: State of Art and Emerging Technologies. In: *Energy Procedia* 83 (2015), pp. 484–493.

[8] Techpowerup. *Intel Core i9-13900K.* https://www.techpowerup.com/cpu-specs/core-i9-13900k.c2817. 2023.

[9] A. M. Haywood, J. Sherbeck, P. Phelan, G. Varsamopoulos, and S. K. S. Gupta. The Relationship Among CPU Utilization, Temperature, and thermal Power for Waste Heat Utilization. In: *Energ. Convers. Manage.* 95 (2015), pp. 297–303.

[10] D. B. Tuckerman and R. F. W. Pease. High-performance heat sinking for VLSI. In: *Electron Device Lett.* 2 (1981), pp. 126–129.

[11] C. Baldassari and M. Marengo. Flow boiling in microchannels and microgravity. In: *Prog. Energy Combust. Sci.* 39 (2013), pp. 1–36.

[12] M. Asadi, G. Xie, and B. Sunden. A review of heat transfer and pressure drop characteristics of single and two-phase microchannels. In: *Int. J. Heat Mass Transf.* 79 (2014), pp. 34–53.

[13] L. Cheng and G. Xia. Fundamental issues, mechanisms and models of flow boiling heat transfer in microscale channels. In: *Int. J. Heat Mass Transf.* 108 (2017), pp. 97–127.

[14] J. Park. Critical Heat Flux in Multi-Microchannel Copper Elements with Low Pressure Refrigerants. PhD thesis. EPFL, 2008.

[15] Y. Peles, A. Kosar, C. Mishra, C. Kuo, and B. Schneider. Forced convective heat transfer across a pin fin micro heat sink. In: *Int. J. Heat Mass Transf.* 48 (2005), pp. 3615–3627.

[16] S. Nukiyama. The maximum and minimum values of the heat Q transmitted from metal to boiling water under atmospheric pressure. In: *Journal of Japaneese Society of Mechanical Engineers* 37 (1934), pp. 367–374.

[17] T. Chen and S. V. Garimella. Measurements and high-speed visualizations of flow boiling of a dielectric fluid in a silicon microchannel heat sink. In: *Int. J. Multiph. Flow* 32 (2006), pp. 957–971.

[18] D. Wu, J. B. Marcinichen, and J. R. Thome. Experimental evaluation of a controlled hybrid two-phase multi-microchannel cooling and heat recovery system driven by liquid pump and vapor compressor. In: *Int. J. Refrig.* 36 (2013), pp. 375–389.

[19] S. G. Kandlikar. Similarities and Differences Between Flow Boiling in Microchannels and Pool Boiling. In: *Heat Transf. Eng.* 31 (2010), pp. 159–167.

[20] Q. Liu. Numerical study of flow boiling in micro/mini channels. PhD thesis. KTH Royal Institute of Technology, 2017.

[21] F. P. Bretherton. The motion of long bubbles in tubes. In: *J. Fluid Mech.* 10 (1961), pp. 166–188.

[22] H. Wong, C. J. Radke, and S. Morris. The motion of long bubbles in polygonal capillaries. Part 1. Thin films. In: *J. Fluid Mech.* 292 (1995), pp. 71–94.

[23] D. Picchi and P. Poesio. Dispersion of a passive scalar around a Taylor bubble. In: *J. Fluid Mech.* 951 (2022), A22.

[24] J. R. Thome, V. Dupont, and A. M. Jabobi. Heat transfer model for evaporation in microchannels. Part I: Presentation of the model. In: *Int. J. Heat Mass Transf.* 47 (2004), pp. 3375–3385.

[25] M. Magnini and J. R. Thome. An updated three-zone heat transfer model for slug flow boiling in microchannels. In: *Int. J. Multiph. Flow* 91 (2017), pp. 296–314.

[26] G. I. Taylor. Deposition of a viscous fluid on the wall of a tube. In: *J. Fluid Mech.* 10 (1960), pp. 161–165.

[27] P. Aussillous and D. Quéré. Quick deposition of a fluid on the wall of a tube. In: *Phys. Fluids* 12 (2000), pp. 2367–2371.

[28] M. T. Kreutzer, F. Kapteijn, J. A. Moulijn, and J. J. Heiszwolf. Multiphase monolith reactors: Chemical reaction engineering of segmented flow in microchannels. In: *Chem. Eng. Sci.* 60 (2005), pp. 5895–5916.

[29] A. de Lózar, A. L. Hazel, and M. Heil. Scaling properties of coating flows in rectangular channels. In: *Phys. Rev. Lett.* 99 (2007), p. 234501.

[30] Y. Han and N. Shikazono. Measurement of liquid film thickness in micro square channel. In: *Int. J. Multiph. Flow* 35 (2009), pp. 896–903.

[31] A. Mohammadi and A. Kosar. Review on Heat and Fluid Flow in Micro Pin Fin Heat Sinks underSingle-phase and Two-phase Flow Conditions. In: *Nanoscale Microscale Thermophys. Eng.* 22 (2018), pp. 153–197.

[32] D. Deng, L. Zeng, and W. Sun. A review on flow boiling enhancement and fabrication of enhanced microchannels of microchannel heat sinks. In: *Int. J. Heat Mass Transf.* 175 (2021), p. 121332.

[33] R. Ricci and S. Montelpare. An experimental IR thermographic method for the evaluation of the heat transfer coefficient of liquid-cooled short pin fins arranged in line. In: *Exp. Therm. Fluid Sci.* 30 (2006), pp. 381–391.

[34] W. Wan, D. Deng, Q. Huang, T. Zeng, and Y. Huang. Experimental study and optimization of pin fin shapes in flow boiling of micro pin fin heat sinks. In: *Appl. Therm. Eng.* 114 (2017), pp. 436–449.

[35] R. Sun, J. Hua, X. Zhang, and X. Zhao. Experimental study on the effect of shape on the boiling flow and heat transfer characteristics of different pin-fin microchannels. In: *Int. J. Heat Mass Transf.* 57 (2021), pp. 2081–2095.

[36] X. Yu, C. Woodcock, Y. Wang, J. Plawsky, and Y. Peles. Enhanced Subcooled Flow Boiling Heat Transfer in Microchannel With Piranha Pin Fin. In: *Int. J. Heat Mass Transf.* 139 (2017), p. 112402.

[37] M. Khoshvaght-Aliabadi, S. Deldar, and S. M. Hassani. Effects of pin-fins geometry and nanofluid on the performance of a pin-fin miniature heat sink (PFMHS). In: *Int. J. Mech. Scien.* 148 (2018), pp. 442–458.

[38] A. Kosar and Y. Peles. Convective flow of refrigerant (R-123) across a bank of micro pin fins. In: *Int. J. Heat Mass Transf.* 49 (2006), pp. 3142–3155.

[39] A. Kosar and Y. Peles. Boiling heat transfer in a hydrofoil-based micro pin fin heat sink. In: *Int. J. Heat Mass Transf.* 50 (2007), pp. 1018–1034.

[40] S. Krishnamurthy and Y. Peles. Flow boiling of water in a circular staggered micro-pin fin heat sink. In: *J. Heat Transfer* 51 (2008), pp. 1349–1364.

[41] M. Law and P. Lee. A comparative study of experimental flow boiling heat transfer and pressure characteristics in straight- and oblique-finned microchannels. In: *Int. J. Heat Mass Transf.* 85 (2014), pp. 797–810.

[42] C. Falsetti, H. Jafarpoorchekab, M. Magnini, N. Borhani, and J. R. Thome. Two-phase operational maps, pressure drop, and heat transfer for flow boiling of R236fa in a micro-pin fin evaporator. In: *Int. J. Heat Mass Transf.* 107 (2017), pp. 805–819.

[43] C. Falsetti, M. Magnini, and J. R. Thome. Flow boiling heat transfer and pressure drops of R1234ze(E) in a silicon micro-pin fin evaporator. In: *J. Electron. Packag.* 139 (2017), p. 031008.

[44] C. Falsetti, M. Magnini, and J. R. Thome. Hydrodynamic and thermal analysis of a micro-pin fin evaporator for on-chip two-phase cooling of high density power micro-electronics. In: *Appl. Therm. Eng.* 130 (2018), pp. 1425–1439.

[45] W. R. Chang, C. A. Chen, J. H. Ke, and T. F. Lin. Subcooled flow boiling heat transfer and associated bubble characteristics of FC-72 on a heated micro-pin-finned silicon chip. In: *Int. J. Heat Mass Transf.* 53 (2009), pp. 5605–5621.

[46] R. C. Kharangate and I. Mudawar. Review of computational studies on boiling and condensation. In: *Int. J. Heat Mass Transf.* 1081 (2017), pp. 1164–1196.

[47] Z. Guo, D. F. Fletcher, and B. S. Haynes. A Review of Computational Modelling of Flow Boiling in Microchannels. In: *Int. J. Multiph. Flow* 6 (2014), pp. 79–177.

[48] S. Popinet. Numerical Models of Surface Tension. In: *Annu. Rev. Fluid Mech.* 50 (2018), pp. 49–75.

[49] J. E. Welch, F. H. Harlow, J. P. Shannon, and B. J. Daly. *The MAC method.* Tech. rep. LA-3425. Los Alamos National Laboratory, 1965.

[50] A. Esmaeeli and G. Tryggvason. Computations of film boiling. Part I: Numerical method. In: *Int. J. Heat Mass Transf.* 47 (2004), pp. 5451–5461.

[51] A. Esmaeeli and G. Tryggvason. Computations of film boiling. Part II: Multimode film boiling. In: *Int. J. Heat Mass Transf.* 47 (2004), pp. 5463–5476.

[52] G. Tryggvason, A. Esmaeeli, and N. Al-Rawahi. Direct numerical simulations of flows with phase change. In: *Computers Structures* 83.6 (2005), pp. 445–453.

[53] C. W. Hirt, A. A. Amsden, and J. L. Cook. An arbitrary Lagrangian-Eulerian computing method for all flow speeds. In: *J. Comput. Phys.* 14 (1974), pp. 227–253.

[54] V. E. Badalassi, H. D. Ceniceros, and S. Banerjee. Computation of multiphase systems with phase field models. In: *J. Comput. Phys.* 190 (2003), pp. 371–397.

[55] M. Sussman, P. Smereka, and S. Osher. A Level Set Approach for Computing Solutions to Incompressible Two-Phase Flow. In: *J. Comput. Phys.* 114 (1994), pp. 146–159.

[56] C. W. Hirt and B. D. Nichols. Volume of fluid VOF method for the dynamics of free boundaries. In: *J. Comput. Phys.* 39 (1981), pp. 201–225.

[57] S. J. Cummins, M. M. Francois, and D. B. Kothe. Estimating curvature from volume fractions. In: *Comput. Struct.* 83 (2005), pp. 425–434.

[58] J. Roenby, H. Bredmose, and H. Jasak. A computational method for sharp interface advection. In: *R. Soc. Open Sci.* 3 (2016), pp. 160–405.

[59]   H. Scheufler and J. Roenby. Accurate and efficient surface reconstruction from volume fraction data on general meshes. In: *J. Comput. Phys.* 383 (2019), pp. 1–23.

[60]   H. Scheufler and J. Roenby. TwoPhaseFlow: An OpenFOAM based framework for development of two phase flow solvers. In: *arXiv* (2021). DOI: `https://doi.org/10.48550/arXiv.2103.00870`.

[61]   M. Sussman and E.G.Puckett. A Coupled Level Set and Volume-of-Fluid Method for Computing 3D and Axisymmetric Incompressible Two-Phase Flows. In: *J. Comput. Phys.* 162 (2000), pp. 301–337.

[62]   Y. Y. Yan and Y. Q. Zu. A lattice Boltzmann method for incompressible two-phase flows on partial wetting surface with large density ratio. In: *Int. J. Comput. Phys.* 25 (2007), pp. 763–775.

[63]   S. W. J. Welch and J. Wilson. A Volume of Fluid Based Method for Fluid Flows with Phase Change. In: *J. Comput. Phys.* 160 (2000), pp. 662–682.

[64]   S. W. J. Welch and T. Rachidi. Numerical computation of film boiling including conjugate heat transfer. In: *Numerical Heat Transfer, Part B* 42 (2002), pp. 35–53.

[65]   S. Hardt and F. Wondra. Evaporation model for interfacial flows based on a continuum-field representation of the source terms. In: *J. Comput. Phys.* 227 (2008), pp. 5871–5895.

[66]   R. W. Schrage. *A theoretical study of interphase mass transfer.* New York: Columbia University Press, 1953.

[67]   A. Mukherjee and S. G. Kandlikar. Numerical simulation of growth of a vapor bubble during flow boiling of water in a microchannel. In: *Microfluidics and Nanofluidics* 1 (2005), pp. 137–145.

[68]   C. Kunkelmann and P. Stephan. CFD Simulation of Boiling Flows Using the Volume-of-Fluid Method within OpenFOAM. In: *Numerical Heat Transfer, Part A: Applications* 56 (2009), pp. 631–646.

[69]   M. Magnini, B. Pulvirenti, and J. R. Thome. Numerical investigation of hydrodynamics and heat transfer of elongated bubbles during flow boiling in a microchannel. In: *Int. J. Heat Mass Transf.* 59 (2013), pp. 451–471.

[70] K. Ling, G. Son, D. Sun, and W. Tao. Three dimensional numerical simulation on bubble growth and merger in microchannel boiling flow. In: *Int. J. Therm. Sci.* 98 (2015), pp. 135–147.

[71] M. Nabil and A. S. Rattner. interThermalPhaseChangeFoam—A framework for two-phase flow simulations with thermally driven phase change. In: *SoftwareX* 5 (2016), pp. 216–226.

[72] A. Georgoulas, P. Koukouvinis, M. Gavaises, and M. Marengo. Numerical investigation of quasi-static bubble growth and detachment from submerged orifices in isothermal liquid pools: The effect of varying fluid properties and gravity levels. In: *Int. J. Multiph. Flow* 74 (2015), pp. 59–78.

[73] A. Georgoulas, M. Andredaki, and M. Marengo. An Enhanced VOF Method Coupled with Heat Transfer and Phase Change to Characterise Bubble Detachment in Saturated Pool Boiling. In: *Energies* 10 (2016), p. 70.

[74] M. Andredaki, A. Georgoulas, N. Miché, and M. Marengo. Accelerating Taylor bubbles within circular capillary channels: Break-up mechanisms and regimes. In: *Int. J. Multiph. Flow* 134 (2021), p. 103488.

[75] M. Andredaki, K. Vontas, A. Georgoulas, N. Miché, and M. Marengo. The effect of channel aspect ratio on flow boiling characteristics within rectangular micro-passages. In: *Int. J. Heat Mass Transf.* 183 (2021), p. 122201.

[76] M. Magnini and O. K. Matar. Numerical study of the impact of the channel shape on microchannel boiling heat transfer. In: *Int. J. Heat Mass Transf.* 150 (2020), pp. 119–322.

[77] F.Municchi, I.El Mellas, O.K.Matar, and M.Magnini. Conjugate heat transfer effects on flow boiling in microchannels. In: *Int. J. Heat Mass Transf.* 195 (2022), p. 123166.

[78] M. Muradoglu and H. A. Stone. Motion of large bubbles in curved channels. In: *J. Fluid Mech.* 570 (2007), pp. 455–466.

[79] M. Sauzade and T. Cubaud. Bubble deformations and segmented flows in corrugated microchannels at large capillary numbers. In: *Phys. Rev. Fluids* 3 (2018), p. 034202.

[80] T. Patel, D. Patel, N. Thakkar, and A. Lakdawala. A numerical study on bubble dynamics in sinusoidal channels. In: *Phys. Fluids* 31 (2019), p. 052103.

[81]   G. R. Anjos. Numerical Investigation of Two-Phase Flows in Corrugated Channel with Single and Multiples Drops. In: *Fluids* 6 (2021), p. 13.

[82]   D. Lorenzini and Y. Joshi. Flow boiling heat transfer in silicon microgaps with multiple hotspots and variable pin fin clustering. In: *Phys. Fluids* 31 (2019), p. 102002.

[83]   A. Ferrari and I. Lunati. Direct numerical simulations of interface dynamics to link capillary pressure and total surface energy. In: *Adv. Water Resour.* 57 (2013), pp. 19–31.

[84]   Y. Yang, S. Cai, J. Yao, J. Zhong, K. Zhang, W. Song, L. Zhanga, H. Suna, and V. Lisitsac. Pore-scale simulation of remaining oil distribution in 3D porous media affected by wettability and capillarity based on volume of fluid method. In: *Int. J. Multiph. Flow* 143 (2021), p. 103746.

[85]   Z. Guo, D. F. Fletcher, and B. S. Haynes. Implementation of a height function method to alleviate spurious currents in CFD modelling of annular flow in microchannels. In: *Appl. Math. Model.* 39.16 (2015), pp. 4665–4686.

[86]   M. A. Safi, N. I. Prasianakis, J. Mantzaras, A. Lamibrac, and F. B. Büchi. A pore-level direct numerical investigation of water evaporation characteristics under air and hydrogen in the gas diffusion layers of polymer electrolyte fuel cells. In: *Int. J. Heat Mass Transf.* 129 (2019), pp. 1250–1262.

[87]   S. Rooij, M. Magnini, O. K. Matar, and S. Haussener. Numerical optimization of evaporative cooling in artificial gas diffusion layers. In: *Appl. Therm. Eng.* 186 (2021), p. 116460.

[88]   C. Soulaine, S. Roman, A. Kovscek, and H. A. Tchelepi. Pore-scale modelling of multiphase reactive flow: application to mineral dissolution with production of CO_2. In: *J. Fluid Mech.* 855 (2018), pp. 616–645.

[89]   C. Gomes Suarez, J. Noordmans, H. C. van der Mei, and H. J. Busscher. Removal of Colloidal Particles from Quartz Collector Surfaces As Stimulated by the Passage of Liquid-Air Interfaces. In: *Langmuir* 15 (1999), pp. 5123–5127.

[90]   J. Shang, M. Flury, G. Chen, and J. Zhuang. Impact of flow rate, water content, and capillary forces onin situ colloid mobilization during infiltration in unsaturated sediments. In: *Water Resour. Res.* 44 (2008), W06411.

[91] G. Tryggvason. A Front-tracking/Finite-Volume Navier-Stokes Solver for Direct Numerical Simulations of Multiphase Flows. In: (2012), p. 5.

[92] S. F. Jones, G. M. Evans, and K. P. Galvin. Bubble nucleation from gas cavities — a review. In: *Adv. Colloid Interface Sci.* 80 (1999), pp. 27–50.

[93] M Gallo, F. Magaletti, A. Georgoulas, M. Marengo, J. Coninck, and C. M. Casciola. A nanoscale view of the origin of boiling and its dynamics. In: *Nature Communication* 14 (2023).

[94] V. P. Carey. *Liquid-Vapor Phase-Change Phenomena: An Introduction to the Thermophysics of Vaporization and Condensation Processes in Heat Transfer Equipment (3rd ed.)* CRC Press, 2020.

[95] B. P. Leonard. The ULTIMATE conservative difference scheme applied to unsteady one-dimensional advection. In: *Comput. Methods Appl. Mech. Eng.* 88.1 (1991), pp. 17–74.

[96] W. F. Noh and P. Woodward. *The SLIC (Simple Line Interface Calculation) method.* Tech. rep. UCRL-52111. Lawrence Livermore Laboratory, 1976.

[97] Y. Li and M. Rudman. Assessment of high-order upwind schemes incorporating FCT for convection-dominated problems. In: *Numerical Heat Transfer: Part B* 27.1 (1995), pp. 1–9.

[98] O. Ubbink and R. I. Issa. A Method for Capturing Sharp Fluid Interfaces on Arbitrary Meshes. In: *J. Comput. Phys.* 153.1 (1999), pp. 26–50.

[99] H. G. Weller. A new approach to VOF-based interface capturing methods for incompressible and compressible flows. In: *OpenCFD Ltd. Report TR/HGW/04* (2008).

[100] S. S. Deshpande, L. Anumolu, and M. F. Trujillo. Evaluating the performance of the two-phase flow solver interFoam. In: *Comput. Sci. Discov.* 5 (2012), p. 014016.

[101] D. L. Youngs. Time-dependent multi-material flow with large fluid distortion. In: *Numerical Methods for Fluid Dynamics.* Ed. by K. W. Morton and M. J. Baines. Academic Press, 1982, pp. 273–285.

[102] J. U. Brackbill, D. B. Kothe, and C. Zemach. A continuum method for modeling surface tension. In: *J. Comput. Phys.* 100 (1992), pp. 335–354.

[103] M. Owkes and O. Desjardins. A mesh-decoupled height function method for computing interface curvature. In: *J. Comput. Phys.* 281 (2015), pp. 285–300.

[104] Basilisk. *Basilisk.* `http://basilisk.fr/`.

[105] I. Tanasawa. Advances in Heat Transfer. In: *Advances in Condensation Heat Transfer.* Ed. by J. P. Hartnett, T. F. Irvine, and Y. I. Cho. Vol. 21. San Diego: Elsevier, 1991, pp. 55–139.

[106] H. Wang, S. V. Garimella, and J. Y. Murthy. Characteristics of evaporating thin film in a microchannel. In: *Int. J. Heat Mass Transf.* 50 (2007), pp. 3933–3942.

[107] C. Kunkelmann. Numerical Modelling and Investigation of Boiling Phenomena. PhD thesis. Technischen Universität Darmstadt, 2011.

[108] OpenFOAM. *OpenFOAM guide.* `https://www.openfoam.com/documentation/user-guide`.

[109] T. Abadie, J. Aubin, and D. Legendre. On the combined effects of surface tension force calculation and interface advection on spurious currents within Volume of Fluid and Level Set frameworks. In: *J. Comput. Phys.* 297 (2015), pp. 611–636.

[110] S. Popinet. An accurate adaptive solver for surface-tension-driven interfacial flows. In: *J. Comput. Phys.* 228 (2009), pp. 5838–5866.

[111] M. Magnini, F. Municchi, I. El Mellas, and M. Icardi. Liquid film distribution around long gas bubbles propagating in rectangular capillaries. In: *Int. J. Multiph. Flow* 148 (2022), p. 103939.

[112] L. E. Scriven. On the dynamics of phase growth. In: *Chem. Eng. Sci.* 10 (1959), pp. 1–13.

[113] L. Gamet, M. Scala, J. Roenby, H. Scheufler, and J.-L. Pierson. Validation of volume-of-fluid OpenFOAM isoAdvector solvers using single bubble benchmarks. In: *Comput. Fluids* 213 (2020), p. 104722.

[114] M. Magnini, B. Pulvirenti, and J. R. Thome. Characterization of the velocity fields generated by flow initialization in the CFD simulation of multiphase flows. In: *Appl. Math. Model* 40 (2016), pp. 6811–6830.

[115] I. El Mellas, F. Municchi, M. Icardi, and M. Magnini. Dynamics of long bubbles propagating through cylindrical micro-pin fin arrays. In: *Int. J. Multiph. Flow* 163 (2023), p. 104443.

[116] R. I. Issa. Solution of the implicitly discretized fluid flow equations by operator-splitting. In: *J. Comput. Phys.* 62 (1985), pp. 40–65.

[117] L. S. Caretto, A. D. Gosman, S. V. Patankar, and D. B. Spalding. Two calculation procedures for steady, three-dimensional flows with recirculation. In: *Proceedings of the Third International Conference on Numerical Methods in Fluid Mechanics*. Berlin, Heidelberg, Germany, 1973, pp. 60–68.

[118] G. Balestra, L. Zhu, and F. Gallaire. Viscous Taylor droplets in axisymmetric and planar tubes: from Bretherton's theory to empirical models. In: *Microfluid Nanofluid* 22.10 (2018).

[119] M. Magnini, A. Ferrari, J. R. Thome, and H. A. Stone. Undulations on the surface of elongated bubbles in confined gas-liquid flows. In: *Phys. Rev. Fluids* 2 (2017), p. 084001.

[120] S. Khodaparast, M. Magnini, N. Borhani, and J. R. Thome. Dynamics of isolated confined air bubbles in liquid flows through circular microchannels: an experimental and numerical study. In: *Microfluid Nanofluidics* 19 (2015), pp. 209–234.

[121] M. Magnini and O. K. Matar. Morphology of long gas bubbles propagating in square capillaries. In: *Int. J. Multiph. Flow* 129 (2020), p. 103353.

[122] R. Lenormand, E. Touboul, and C. Zarcone. Numerical models and experiments on immiscible displacements in porous media. In: *J. Fluid Mech.* 189 (1988), pp. 165–187.

[123] R. Gupta, D. F. Fletcher, and B. S. Haynes. On the CFD modelling of Taylor flow in microchannels. In: *Chem. Eng. Sci.* (2009), pp. 2941–2950.

[124] A. L. Hazel and M. Heil. The steady propagation of a semi-infinite bubble into a tube of elliptical or rectangular cross-section. In: *J. Fluid Mech.* 470 (2002), pp. 91–114.

[125] M. T. Kreutzer, F. Kapteijn, J. A. Moulijn, C. R. Kleijn, and J. J. Heiszwolf. Inertial and interfacial effects on pressure drop of Taylor flow in capillaries. In: *AIChE J.* 51 (2005), pp. 2428–2440.

[126] H. Moran, M. Magnini, C. N. Markides, and O. K. Matar. Inertial and buoyancy effects on the flow of elongated bubbles in horizontal channels. In: *Int. J. Multiph. Flow* 135 (2021), p. 103468.

[127] A. de Lózar, A. Juel, and A. L. Hazel. The steady propagation of an air finger into a rectangular tube. In: *J. Fluid Mech.* 614 (2008), pp. 173–195.

[128] M. Magnini, A. Beisel, A. Ferrari, and J. R. Thome. Pore-scale analysis of the minimum liquid film thickness around elongated bubbles in confined gas-liquid flows. In: *Adv. Water Resour.* 109 (2017), pp. 84–93.

[129] E. L. Sharaborin, O. A. Rogozin, and A. R. Kasimov. Computational Study of the Dynamics of the Taylor Bubble. In: *Fluids* 6 (2021), p. 389.

[130] S. A. Isaacs, Y. J. Kim, A. J. McNamara, Y. Joshi, Z. Yue, and M. S. Bakir. Two-phase flow and heat transfer in pin-fin enhanced micro-gaps. In: *13th InterSociety Conference on Thermal and Thermomechanical Phenomena in Electronic Systems.* Hong Kong, China, 2012.

[131] K. A. Triplett, S. M. Ghiaasiaan, S. I. Abdel-Khalik, and D. L. Sadowski. Gas-liquid two-phase flow in microchannels Part I: two-phase flow patterns. In: *Int. J. Multiph. Flow* 25 (1999), pp. 377–394.

[132] A. Kosar, Y. Peles, and C. Mishra. Laminar Flow Across a Bank of Low Aspect Ratio Micro Pin Fins. In: *J. Fluids Eng.* 127 (2005), pp. 419–430.

[133] H. Zhao, Z. Liu, C. Zhang, N. Guan, and H. Zhao. Pressure drop and friction factor of a rectangular channel with staggered mini pin fins of different shapes. In: *Exp. Therm. Fluid Sci.* 71 (2016), pp. 57–69.

[134] S. Zhang, N. Cagney, S. Balabani, C. P. Naveira-Cotta, and M. K. Tiwari. Probing vortex-shedding at high frequencies in flows past confined microfluidic cylinders using high-speed microscale particle image velocimetry. In: *Phys. Fluids* 31 (2019), p. 102001.

[135] R. K. Edvinsson and S. Irandoust. Finite-element analysis of Taylor flow. In: *AIChE J.* 42 (1996), pp. 1815–1823.

[136] I. El Mellas, N. Samkhaniani, C. Falsetti, A. Stroh, M. Icardi, and M. Magnini. Numerical investigation of bubble dynamics and flow boiling heat transfer in cylindrical micro-pin-fin heat exchangers. In: *Int. J. Heat Mass Transf.* 228 (2024), p. 125620.

[137]   M. Magnini and J. R. Thome. Computational study of saturated flow boiling within a microchannel in the slug flow regime. In: *J. Heat Transf.* 138 (2016), p. 021502.

[138]   P.-S. Lee and S. V. Garimella. Saturated flow boiling heat transfer and pressure drop in silicon microchannel arrays. In: *Int. J. Heat Mass Transf.* 51 (2008), pp. 789–806.

[139]   T. Brunschwiler, B. Michel, H. E. Rothuizen, U. Kloter, B. Wunderle, H. Oppermann, and H. Reichl. Interlayer cooling potential in vertically integrated packages. In: *Microsyst. Technol.* 15 (2008), pp. 57–74.

[140]   VDI Gesellschaft. *VDI Heat Atlas.* Springer Berlin Heidelberg, 2010.

[141]   F. Incropera. *Fundamentals of Heat and Mass Transfer 6th Edition.* John Wiley and Sons, 2011.

[142]   A. Zukauskas. Some aspects of heat transfer from tubes in crossflow. In: *The 1996 4 th International Symposium on Heat Transfer, ISHT, Beijing, China, 10/07-11/96.* 1996, pp. 82–93.

[143]   C. Falsetti, M. Magnini, and J. R. Thome. A new flow pattern-based boiling heat transfer model for micro-pin fin evaporators. In: *Int. J. Heat Mass Transf.* 122 (2018), pp. 1425–1439.

[144]   A. Ferrari, M. Magnini, and J. R. Thome. Numerical analysis of slug flow boiling in square microchannels. In: *Int. J. Heat Mass Transf.* 123 (2018), pp. 928–944.

Publications

Journal articles

- M. Magnini, F. Municchi, I. El Mellas, and M. Icardi. Liquid film distribution around long gas bubbles propagating in rectangular capillaries. In: *Int. J. Multiph. Flow* 148 (2022), p. 103939

- F.Municchi, I.El Mellas, O.K.Matar, and M.Magnini. Conjugate heat transfer effects on flow boiling in microchannels. In: *Int. J. Heat Mass Transf.* 195 (2022), p. 123166

- I. El Mellas, F. Municchi, M. Icardi, and M. Magnini. Dynamics of long bubbles propagating through cylindrical micro-pin fin arrays. In: *Int. J. Multiph. Flow* 163 (2023), p. 104443

- I. El Mellas, N. Samkhaniani, C. Falsetti, A. Stroh, M. Icardi, and M. Magnini. Numerical investigation of bubble dynamics and flow boiling heat transfer in cylindrical micro-pin-fin heat exchangers. In: *Int. J. Heat Mass Transf.* 228 (2024), p. 125620